To the Graduate Council:

I am submitting a dissertation written by Cara Lynn Nygren entitled "Experimental studies of intra- and intermolecular chemical structure." I have examined the final paper copy of this dissertation for form and content and recommend that it is accepted in partial fulfillment of the requirements for the degree of Doctor of Philosophy, with a major in Chemistry.

John F.C. Turner, major professor

We have read this dissertation
and recommend its acceptance:

Acceptance for the Council:

Vice Chancellor and Dean of Graduate Studies

Thesis
2005b
.N94

EXPERIMENTAL STUDIES OF INTRA- AND INTERMOLECULAR CHEMICAL STRUCTURE

A Dissertation
Presented for the
Doctor of Philosophy Degree
The University of Tennessee, Knoxville

Cara Lynn Nygren
May 2005

DEDICATION

This body of work is dedicated to my parents.

ACKNOWLEDGEMENTS

First and foremost, I would like to thank my advisor, Dr. J.F.C. Turner, for his excellent supervision and support and for giving me such amazing opportunities.

I would like to thank the members of my committee: Dr. Craig E. Barnes, Dr. Fred M. Schell, Dr. Claudia J. Rawn, Dr. Bryan Chakoumakos, and Prof. Chick C. Wilson.

I would like to thank Prof. Chick C. Wilson for his interest in my research and for allowing me the opportunity to spend some time studying at the University of Glasgow. I would like to thank Prof. Jennifer C. Green for her invitation to spend time working under her supervision at Oxford to learn DFT.

I would like to thank Dr. Laura E. Pence for her help and encouragement during her sabbatical at UT. I would like to thank Dr. Linda H. Doerrer for her last minute calculations and understanding when my refinements just weren't going fast enough.

I would like to thank the members, past and present, of the Turner research group for helping me through these last few years and for their understanding while I was writing this. I would especially like to thank Dr. Sylvia E. McLain, without whom I would have lost my mind and Jamie Molaison for taking me to lunch when I had to get away from everyone.

I would also like to thank my family and friends for their undying support and encouragement and for understanding, most of the time, that I had to go to work.

ABSTRACT

The purpose of this study was two fold. The determination of hydrogen atom positions by X-ray diffraction methods is widely underused. With advances in instrument and computing technology, the use of X-ray diffraction experiments to accurately image the electron density associated with a hydrogen bond has become feasible. Secondly, general crystallographic computing programs analyze diffraction data by employing a spherical atom model. However, no such atom can be defined solely by a sphere when bound in a molecule. The use of spherical harmonics to model diffraction data enables a more complete description of the electron density in a molecular system. The use of these types of programs has allowed a detailed analysis of a variety of both hydrogen bonded and non-hydrogen bonded systems.

This dissertation details the experimental information for charge density and hydrogen bonding studies. The experimental results are analyzed in depth to yield a more complete understanding of a variety of bonding motifs. In some cases, the DFT calculations were performed to augment the experimental results. A series of other experimental components are added to yield a more complete structural model of each molecular system.

Chapter one presents a solid background to X-ray diffraction and the solid state. The information presented in the chapter describes the development of X-ray diffraction, various techniques and the experimental methods available to model diffraction data. Chapter one also develops the basic concepts for understanding the crystalline solid state.

Chapter two gives a detailed introduction to hydrogen bonding and the use of diffraction techniques to model the electron and nuclear density as well as define the

distribution of these densities in a three-center four-electron bond. The first molecule analyzed is urotropine-*N*-oxide·formic acid, which consists of a short, strong, symmetric hydrogen bond. Variable temperature X-ray diffraction studies were used to model the total electron density in the hydrogen bond through the use of Fourier difference maps, while neutron diffraction experiments were used to confirm the proton position in the hydrogen bond. The second system analyzed was para-iodobenzoic acid. Variable temperature X-ray diffraction experiments revealed a split-site population of the electron density associated with the proton position, as is evident by the use of difference Fourier maps.

Chapter three contains the detailed charge density analysis of a material containing a short, strong, asymmetric hydrogen bond, namely cobaltocenium 3,5 bis(trifluoromethyl)phenoxide 3,5-bis(trifluoromethyl)phenol. High resolution X-ray diffraction data were collected to give insight into the chemical bonding both in the hydrogen bond as well as in the organometallic segment.

Chapter four focuses on the charge density studies on a novel heterocyclic alkene, 1,2,3,4,5,6,7,8-octahydro-2a,4a,6a,8a-tetraaza-cyclopenta[fg]acenaphthylene. Accurate determination of the electron density in this system demonstrates a delocalization of the electron density on the p orbitals on nitrogen over the π system.

Chapter five is a detailed experimental section for all material covered in this body of work.

TABLE OF CONTENTS

CHAPTER		PAGE
1	Introduction to X-ray diffraction and the solid-state	1
	1.1: Periodicity and the crystalline state	1
	1.2: Theory of X-ray diffraction	5
	1.3: Generation of X-rays	7
	1.4: Scattering of X-rays from a single electron and from a single atom	11
	1.5: Scattering from a periodic array of atoms	12
	1.6: Ewald sphere construction	15
	1.7: Debye-Waller temperature factor	15
	1.8: Development of X-ray scattering	17
	1.8.1: Discovery of X-rays and diffraction	17
	1.8.2: The Laue method	18
	1.8.3: Rotation method	18
	1.8.4: Further developments	19
	1.9: Refinement of scattering data	19
	1.9.1: Fourier methods	19
	1.9.2: Spherical atom approaches	21
	1.10: Accurate modeling of electron density	22
	1.10.1: Theoretical approaches to the aspherical atom model	22
	1.10.2: Experimental approaches to the aspherical atom model	24
	1.10.3: Bader's definition of atoms in molecules (AIM)	25
	1.10.4: Topological properties from aspherical atom refinements	26

2 Experimental and theoretical studies of the electronic structure in hydrogen bonded systems.....30

2.1: Introduction.....30

2.1.1: Characterization of the nuclear and electronic structure of the hydrogen bond.....37

2.1.2: Prior parameterization of the hydrogen bond.....38

2.2: Structural studies of urotropine-*N*-oxide·formic acid (I).....42

2.2.1: Molecular and crystal structure: urotropine-*N*-oxide·formic acid.....46

2.2.2: Hydrogen bond structure: urotropine-*N*-oxide·formic acid.....48

2.2.3: Nuclear structure of the hydrogen bond: urotropine-*N*-oxide·formic acid.....49

2.2.4: Discussion: urotropine-*N*-oxide·formic acid.....50

2.2.5: Conclusions: urotropine-*N*-oxide·formic acid.....62

2.3: Structural studies of para-iodobenzoic acid (II).....62

2.3.1: Temperature variation and structure of the lattice: para-iodobenzoic acid.....64

2.3.2: Molecular structure from spherical atom refinements: para-iodobenzoic acid.....64

2.3.3: Discussion: para-iodobenzoic acid.....68

2.3.4: Conclusions: para-iodobenzoic acid.....84

2.4: Experimental.....85

3 Characterization of the electron density in the short, strong hydrogen

bond in cobaltocenium 3,5 bis(trifluoromethyl)phenoxide 3,5-bis(trifluoromethyl)phenol.....91

3.1: Introduction.....91

3.1.1: The distribution of scattering density in the hydrogen bond.....94

3.1.2: Experimental investigations of the hydrogen bond.....96

3.2: Results and discussion.....98

3.2.1: Molecular and crystal structure of cobaltocenium 3,5 bis(trifluoromethyl)phenoxide 3,5-bis(trifluoromethyl)phenol.....98

3.2.2: Discussion of the hydrogen bonded anion.....103

3.2.3: Discussion of the electronic structure of the heavy atom moieties.....107

3.3: Conclusions.....114

3.4: Experimental.....116

4 The experimental and theoretical electronic structure of 1,2,3,4,5,6,7,8-octahydro-2a,4a,6a,8a-tetraaza-cyclopenta[fg]acenaphthylene and its derivatives.....118

4.1: Introduction.....118

4.2: Results.....122

4.2.1: Molecular and crystal structure of **IV**.....122

4.2.2: Molecular and crystal structure of $[\mathbf{IV}]^{2+}$.....125

4.2.3: Molecular and crystal structure of $[\mathbf{IVH}]^{+}$.....129

4.3: Description of the experimentally determined electronic density of **IV**.....138

4.4: Calculation of the electron densities in **IV**, $[\mathbf{IV}]^{2+}$ and $[\mathbf{IVH}]^{+}$.....144

4.5: Experimental measurement of the ionization energies of **IV**.....148

4.6: Conclusions.....153

4.7: Experimental.....153

5 Experimental section.....157

5.1: X-ray diffraction of non-hydrogen bonded systems.....157

5.2: X-ray diffraction of hydrogen bonded systems.....157

5.3: Charge density studies using the in-house X-ray diffractometer.....158

5.4: Charge density studies using synchrotron radiation.....159

5.5: Neutron diffraction.....161

5.6: Density Functional Theory.....163

5.7: Solid state nuclear magnetic resonance experiments.....163

5.8: Solution nuclear magnetic resonance experiments.....164

5.9: Differential Scanning Calorimetry.....164

Works cited.....165

Appendix 203

Vita.....245

LIST OF TABLES **PAGE**

Table 1.1: Definition of the 7 Bravais lattices.....5

Table 1.2: Ionization potentials for some commonly used elements in X-ray tubes.....9

Table 2.1: 'Cut-off criteria' for hydrogen bonds.....36

Table 2.2: Classification of the strength of a hydrogen bond.....39

Table 2.3: Intermolecular structural parameters at variable temperature from the spherical atom refinement. Neutron data is represented by an (N) and X-ray data by an (X) for urotropine-*N*-oxide·formic acid.....47

Table 2.4: Anisotropic displacement parameter tensors for H1 from neutron and X-ray diffraction data for urotropine-N-oxide·formic acid. The average U_{ansio} for the H atoms in the urotropine cage is 0.03404 $Å^2$ (neutron data) for urotropine-*N*-oxide·formic acid.....59

Table 2.5: Lattice parameters (reduced unit cell) for the collected data at variable temperature for para-iodobenzoic acid.....65

Table 2.6: Selected intramolecular structural parameters at variable temperature for para-iodobenzoic acid.....69

Table 2.7: Population of the major (A) configuration in the structure of para-iodobenzoic acid. The linear region is in the low temperature range, up to 198 K. The SOF, sight occupancy factor, refinements are less reliable for these split site H atoms than are the occupancies estimated from direct imaging from the Fourier maps. [X_A is the population of the

major configuration as determined from examination of the difference Fourier maps. $K = (X_A)/(1-X_A)$. ITF is the isotropic thermal factor.]……..78

Table 2.8: Selected refinement parameters for the collected data on urotropine-*N*-oxide·formic acid……..86

Table 2.9: Selected refinement parameters for the collected data on para-iodobenzoic acid……88

Table 2.10: Lattice parameters (reduced unit cell) for the collected data at variable temperature for urotropine-N-oxide·formic acid. The superscript in the reference column denoted X-ray (X) versus Neutron (N) data……..90

Table 3.1: d-orbital population summary for **III**……..112

Table 3.2: Selected refinement statistics for **III**……..117

Table 4.1: Selected bond properties for **IV** based on aspherical atom refinements……139

Table 4.2: Selected geometric parameters for the experimental and calculated structure of **IV**……145

Table 4.3: Comparison of selected geometric parameters of the experimental and calculated molecular structure of $[\mathbf{IV}]^{2+}$. *Indicates the average distance or angle in the calculations……..147

Table 4.4: Comparison of selected geometric parameters of the experimental and calculated molecular structure of $[IVH]^+$. *Indicates the average distance or angle in the calculations.....147

Table 4.5: Ionization energies for IV.....151

Table 4.6: Selected refinement statistics for IV.....154

Table 4.7: Selected refinement statistics for $[IV]^{2+}$ and $[IVH]^+$.....155

LIST OF FIGURES

Page

Figure 1.1: Schematic representation of lattice planes and fractional indices.....3

Figure 1.2: Wigner-Seitz cell.....4

Figure 1.3: Depiction of a 3_1 screw axis parallel to c.....6

Figure 1.4: Bremsstrahlung scattering.....8

Figure 1.5: Target spectrum for an X-ray source.....8

Figure 1.6: Schematic for a typical X-ray tube.....10

Figure 1.7: Derivation of Bragg's Law for X-ray diffraction.....15

Figure 1.8: Schematic representation of the Ewald sphere.....16

Figure 1.9: Definition of λ with respect to a pair of bonded atoms.....28

Figure 2.1: Graphical representation of hydrogen bond lengths versus angle from the CSD; X-H...Y, where X and Y are either C, N, O or F (a)defined as X-H-Y, (b) defined as X-H...Y^-, where H...Y^- is defined as a non-bonded contact.....32

Figure 2.2: Example of an intramolecular hydrogen bond.....35

Figure 2.3: Example of an intermolecular hydrogen bond in an acid-base pair.....35

Figure 2.4: Molecular orbital diagram on the bonding in the 3c-4e hydrogen bond.....35

Figure 2.5: Geometric parameters used to define a hydrogen bond.....38

Figure 2.6: The molecular structure of urotropine-*N*-oxide.....43

Figure 2.7: Potential equilibria involving both proton and electron redistribution in urotropine-*N*-oxide·formic acid.....45

Figure 2.8: The molecular structure of urotropine-*N*-oxide·formic acid at 123K (a) and a packing diagram (b).....48

Figure 2.9: Fourier difference maps showing the electron density associated with the proton position of the formic acid OH in urotropine-*N*-oxide·formic acid. Contour levels are drawn at 0.03 eÅ^{-3}.....51

Figure 2.10: Comparison of the variation of the C-O and C=O bond lengths of the formate segment by neutron diffraction and variable temperature X-ray diffraction experiments for urotropine-*N*-oxide·formic acid.....53

Figure 2.11: Comparison of the results from neutron (U_{aniso}) and X-ray (U_{iso}) data for the hydrogen bound H atom, H1, in urotropine-*N*-oxide·formic acid.....56

Figure 2.12: Comparison of the results from neutron (U_{aniso}) and X-ray (U_{iso}) data for the hydrogen bound H atom, H1, in urotropine-*N*-oxide·formic acid.....58

Figure 2.13: Comparison of X-ray and neutron data of urotropine-*N*-oxide·formic acid at 123K: (a) X-ray data with anisotropic refinement of H1 using GSAS, (b) X-ray data with isotropic refinement from Shelxtl, (c) Neutron data with anisotropic refinement of all H atoms from GSAS.....61

Figure 2.14: A schematic representation of a typical carboxylic acid dimer with the crystallographically generated atoms as X'.....63

Figure 2.15: (a) The molecular structure of para-iodobenzoic acid, corresponding to the asymmetric unit in the crystal, together with (b) the structure of the dimer at 103 K.....66

Figure 2.16: Packing diagram of para-iodobenzoic acid at 103K showing the orientation of the dimeric unit within the unit cell.....66

Figure 2.17: Representation of the asymmetric unit of para-iodobenzoic acid at 103K (top) and 298K (bottom).....67

Figure 2.18: ^{13}C CPMAS SSNMR variable temperature spectra for para-iodobenzoic acid.....70

Figure 2.19: DSC data for para-iodobenzoic acid, with the temperature transition centered around 230-233K.....71

Figure 2.20: Packing diagrams of para-iodobenzoic acid from the 103K data set demonstrating the stacking of the dimeric units as well as the I – I interactions.....74

Figure 2.21: Fourier difference map of para-iodobenzoic acid showing the residual electron density around the iodine position at 103 K ranging from –3.64 to 2.87 $e^-/Å^3$.....76

Figure 2.22: Fourier difference maps showing the carboxylate proton position in the dimeric unit from spherical atom refinements. Contour levels are drawn at 0.04 $eÅ^{-3}$.....77

Figure 2.23: Valence bond representations of the split-site equilibrium in para-iodobenzoic.....80

Figure 2.24: A plot of ln $K_{H,}$ vs inverse temperature for the split-site populations of the proton position in para-iodobenzoic acid, extracted from the integration of the Fourier map with a data cutoff of $F_{Obs}/\sigma(F) = 0$.....82

Figure 2.25: Comparison of the O-H vs. C-O and O-H vs. C=O (red) distances, r_{O-H} and r_{C-O} and $r_{C=O}$, extracted from the CCSD, showing no correlation between these structural parameters.....83

Figure 3.1: Example of a supported hydrogen bond between phenol and phenoxide moieties in di-tert-butyl-(phenolato)-(pyrazine) gallium, phenol solvate. The atoms involved in the hydrogen bond are labeled.....92

Figure 3.2: Representation of the asymmetric, short, strong hydrogen bond between 3,5-bis(trifluoromethyl)phenoxide and 3,5-bis(trifluormethyl)phenol.....93

Figure 3.3: Distribution of the O…H non-bonded contact distances versus O-H…O angle in a search of the CSD.....95

Figure 3.4: Schematic diagram of several different types of potential wells found in hydrogen bonds. From the top: symmetric double well; asymmetric double well; low-barrier symmetric double well; symmetric

double well with nearly no barrier; symmetric single well with a centered proton position.....97

Figure 3.5: Molecular structure of cobaltocenium 3,5 bis(trifluoromethyl) phenoxide 3,5-bis(trifluoromethyl)phenol, **III**, from a SHELXTL refinement of the data collected at 16 K.....99

Figure 3.6: ORTEP diagram of **III** demonstrating the bend of the phenol-phenoxide moiety around the $CoCp_2$ segment.....101

Figure 3.7: Difference Fourier map showing the electron density associated with the hydrogen bond in **III**. Contour levels are drawn at 0.03 $eÅ^{-3}$.....102

Figure 3.8: The Laplacian along the O-H-O bond in cobaltocenium 3,5-bis(trifluoromethyl)phenoxide 3,5-bis(trifluoromethyl)phenol (**III**). Contour levels are drawn at 2 $eÅ^{-5}$. Positive values are represented by solid blue lines, negative values by dotted red lines and the zero level contour is a green solid line.....104

Figure 3.9: Results of linear transit studies with DFT calculations on **III**.....106

Figure 3.10: Deformation density map of the O-H...O vector. Contour levels are drawn at 0.05 $eÅ^{-3}$. Positive values are represented by solid blue lines, negative values by dotted red lines and the zero level contour is a green solid line.....108

Figure3.11: Laplacian (top) and deformation density (bottom) maps of the Cp ring comprised of C1-C5. Contours levels are drawn at 2 $eÅ^{-5}$ in the Laplacian and at 0.05 $eÅ^{-3}$ in the deformation density map.

Positive values are represented by solid blue lines, negative values by dotted red lines and the zero level contour is a green solid line.....109

Figure 3.12: The Laplacian (left) in the plane of phenol system in **III**. Contour levels are drawn at 2 $eÅ^{-5}$. Deformation density map (right) of the phenol system. Contour levels are drawn at 0.05 $eÅ^{-3}$. Positive values are represented by solid blue lines, negative values by dotted red lines and the zero level contour is a green solid line.....111

Figure 3.13: Molecular orbital diagram of the $CoCp_2^+$ based on single point density functional theory calculations.....115

Figure 4.1: The general tetrazaamine framework and one of the simple, polar contributions to the ground state.....118

Figure 4.2: Schematic representations of the molecular structure of TDAE (left) and $[TDAE]^{2+}$(right).....120

Figure 4.3: Projections down the C-C vector of TDAE (left) and $TDAE^{2+}$ (right) demonstrating the difference in torsion angles in the two species.....120

Figure 4.4: The Wanzlick equilibrium.....121

Figure 4.5: Molecular structure of **IV**, with the asymmetric unit labeled. Thermal ellipsoids are drawn at the 50% probability level and all hydrogen atoms have been omitted for clarity.....123

Figure 4.6: Side view of **IV**, showing the chair-like conformation of the six

membered rings.....124

Figure 4.7: Distribution of bond distances in a search of the CSD on a NC=CN fragment.....126

Figure 4.8: Packing diagram of (IV).....127

Figure 4.9: ORTEP diagram of the dication, $[IV]^{2+}$, and a side view of the molecule. Hydrogen atoms have been omitted for clarity, thermal ellipsoids are drawn at the 50 % probability level and the asymmetric unit is labeled.....128

Figure 4.10: Distribution of angles and torsions angles in a NC=CN segment from a search of the CSD.....130

Figure 4.11: Valence bond description of $[IV]^{2+}$.....131

Figure 4.12: Valence bond description of IV.....132

Figure 4.13: ORTEP diagram of $[IVH]^{+}$. Most hydrogen atoms have been omitted for clarity. Thermal parameters are drawn at the 50 % probability level.....133

Figure 4.14: Description of the 98.16(8)° bend in $[IVH]^{+}$, which is defined by C2-C1-Ct01.....134

Figure 4.15: Diagram of $[IV]^{2+}$, which shows the non-bonded contacts between the iodine atoms and the heterocyclic structure.....136

Figure 4.16: Diagram of $[IVH]^{+}$, showing the possible non-bonded contacts present in the structure.....137

Figure 4.17: Deformation density map in the N-C-N plane. Contours are drawn

at 0.05 e $Å^{-3}$. Positive values are represented by solid blue lines, negative values by dotted red lines and the zero level contour is a green solid line.....141

Figure 4.18: Laplacian in the N-C-N plane. Contours are drawn at 2 e $Å^{-5}$. Positive values are represented by solid blue lines, negative values by dotted red lines and the zero level contour is a green solid line.....144

Figure 4.19: Geometry optimized molecular structure of **IV**, $[\mathbf{IV}]^{2+}$ and $[\mathbf{IVH}]^{+}$ from Density Functional Theory calculations.....146

Figure 4.20: He I photoelectron spectrum of **IV**.....149

Figure 4.21: He II photoelectron spectrum of **IV**.....150

Figure 4.22: Highest occupied molecular orbital of **IV** from density functional theory calculations.....152

NOMECLATURE

Units

Å	Angstrom, 10^{-10} m
e-Å^{-3}	electrons per angstrom cubed
$\in$	electric field
r_n	position of an electron
s	unit vector
E_0	amplitude of a primary X-ray beam
R	distance from an electron
m	mass of an electron
e	charge of an electron
ν	frequency of a primary X-ray beam
ρdV	charge of a volume element

List of Abbreviations

ADF	Amsterdam Density Functional Program
ANL	Argonne National Laboratory, Argonne, IL
APS	Advanced Photon Source
cif	crystallographic information file
CSD	Cambridge Structural Database
DFT	Density Functional Theory
ICL	Inorganic Chemistry Laboratory, Oxford University
IPNS	Intense Pulsed Neutron Source

pdb	protein database file
SCD	Single Crystal Diffractometer

Chapter 1: Introduction to X-ray diffraction and the solid state

1.1 Periodicity and the crystalline state

The theory of crystalline solids is simplified by translational symmetry, which means that there is a set of basis vectors, $\mathbf{a}_1$, $\mathbf{a}_2$, $\mathbf{a}_3$, in which the atomic structure is invariant under any translation which is an integer multiple of $\mathbf{a}_i$.[1] The theory of translational symmetry implies that periodic functions dominate the structure and properties of fully stoichiometric crystalline systems. A periodic function, $f(\mathbf{r})$, is defined as

$$f(\mathbf{r}) = f(\mathbf{r} + \boldsymbol{l}). \tag{1.1}$$

This holds true for all points in space, $\mathbf{r}$, given the translation $\boldsymbol{l}$.[1] Periodicity is an inherent physical property of crystalline materials. Crystalline materials are built up of a regular array of atoms in three dimensions in which all translationally identical points are termed lattice points. A vector drawn from one lattice point which is chosen as the origin to another lattice point is termed a lattice vector. A plane which contains the lattice point h_1, h_2, h_3 passes through an infinite number of lattice points as given by the Diophantine equation:[2]

$$x^i h_i = 1 \tag{1.2}$$

in which all planes with this property are called lattice planes. The summation over i is implied in equation (1.2) which is described by the Einstein summation convention.[2] In equation (1.2), x^i are the real space coordinates of any point X, which is the covariant quantity, and h_i are the reciprocal space Miller indices of the plane, which is the

contravariant quantity.[2] The distance between translationally identical planes is then given by the equation:

$$d = \frac{1}{\left|h_1\mathbf{a}_1 + h_2\mathbf{a}_2 + h_3\mathbf{a}_3\right|} \tag{1.3}$$

The lattice planes are numbered according to three numbers known as Miller indices. The three points that define a plane are represented by fractional indices, which are coordinates in the a_1, a_2, a_3 coordinate system, with a description of the fractional indices given in Figure 1.1. The planes defined by *hkl* are a set of equidistant planes, one of which passes through the origin. The equidistant planes are in turn given by the intercepts $\frac{a_1}{h}, \frac{a_2}{k}, \frac{a_3}{l}$, in which *h*, *k* and *l* are the Miller indices and the reciprocal of the fractional indices define the Miller indices of the lattice plane, (hkl). A set of planes which are equivalent, due to symmetry, are defined as {hkl}. If a line is drawn that passes through the origin which is parallel to the direction in question is given by [hkl]. The vector which is perpendicular to the *hkl* plane is given by $\mathbf{H}_{hkl}$, where magnitude is the reciprocal of the spacing, *d* given in equation (1.3).[3]

If the reciprocal lattice vectors, $b_1 b_2 b_3$, are directly related to the crystal axes by

$$\mathbf{b}_1 = \frac{\mathbf{a}_2 \times \mathbf{a}_3}{\mathbf{a}_1 \cdot \mathbf{a}_2 \times \mathbf{a}_3}, \mathbf{b}_2 = \frac{\mathbf{a}_1 \times \mathbf{a}_3}{\mathbf{a}_1 \cdot \mathbf{a}_2 \times \mathbf{a}_3}, \mathbf{b}_3 = \frac{\mathbf{a}_1 \times \mathbf{a}_2}{\mathbf{a}_1 \cdot \mathbf{a}_2 \times \mathbf{a}_3} \tag{1.4}$$

then it follows that the vector $\mathbf{H}_{hkl}$, in terms of the reciprocal lattice vectors is

$$\mathbf{H}_{hkl} = h\mathbf{b}_1 + k\mathbf{b}_2 + l\mathbf{b}_3 \tag{1.5}$$

The vector $\mathbf{H}_{hkl}$, is therefore normal to a set of *hkl* planes and the spacing of the planes, d_{hkl}, is perpendicular to the distance between planes, given by the equation[3]

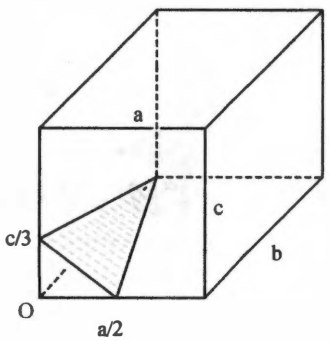


Figure 1.1. Schematic representation of lattice planes and fractional indices.

$$d_{hkl} = \frac{\mathbf{a}_1}{h} \cdot \frac{(h\mathbf{b}_1 + k\mathbf{b}_2 + l\mathbf{b}_3)}{|\mathbf{H}_{hkl}|} = \frac{1}{|\mathbf{H}_{hkl}|} \tag{1.6}$$

The repeat unit of the atoms or groups of atoms in a crystalline material is known as the unit cell, which is defined through translational symmetry and the repeat of the unit cell makes up the crystal as a whole. Representation of the unit cell may be conveniently defined in several different ways. If there is a center of symmetry at some point in the structure, it is often convenient to depict the center of the unit cell at a center of symmetry. This type of representation is called the *Wigner-Seitz* cell, which is constructed by drawing the perpendicular bisecting planes of the translation vectors from the chosen center to the closest equivalent lattice site in three-dimensional space.[1] The reciprocal lattice is most often dealt with in terms of the *Wigner-Seitz* cell, which is called the Brillouin zone, and is depicted in Figure 1.2.[1]

The three-dimensional unit cell is defined by one of seven crystal systems, which are triclinic, monoclinic, orthorhombic, tetragonal, trigonal (rhombohedral), hexagonal

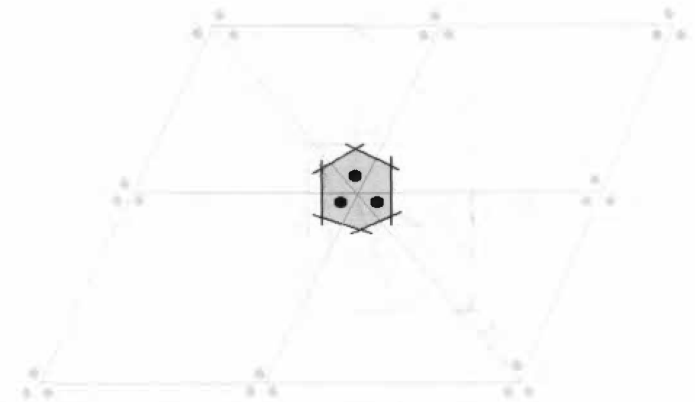


Figure 1.2. Wigner-Seitz cell.

and cubic and are constructed based on restrictions of lattice symmetry.[4] The definitions of the crystal systems are given in Table 1.1. These lattices may also be centered in 4 different ways. A primitive unit cell describes one in which the basis lies in an ordinary position in the unit cell. A face-centered unit cell describes one in which the lattice points are centered on faces of the unit cell. A body-centered unit cell describes one in which the lattice points are centered in the unit cell. A end-centered unit cell describes one in which the basis is centered on one of the opposing three sides, A, B or C. The combination of the lattice centering with the crystal system present defines the Bravais lattice, of which there are 14. The symmetry operations are subsequently used to describe the repeat of the basis throughout an infinite amount of space. There are three different types of point symmetry which are observed in crystalline materials; rotation axes (n), inversion axes ($\bar{n}$) and mirror planes (m), in which the value of n ranges from 1 to 6, with the exception of 5, which may occur individually or in combination. The combination of these symmetry elements leads to point groups, in which there are a total

Table 1.1. Definition of the 7 Bravais lattices.[4]

Crystal system		
Triclinic	$a \neq b \neq c$	$\alpha \neq \beta \neq \gamma$
Monoclinic	$a \neq b \neq c$	$\alpha = \gamma = 90^\circ, \beta \neq 90^\circ$
Orthorhombic	$a \neq b \neq c$	$\alpha = \beta = \gamma = 90^\circ$
Tetragonal	$a = b \neq c$	$\alpha = \beta = \gamma = 90^\circ$
Trigonal (rhombohedral)	$a = b = c$	$\alpha = \beta = \gamma$
Hexagonal	$a = b \neq c$	$\alpha = \beta = 90^\circ, \gamma = 120^\circ$
cubic	$a = b = c$	$\alpha = \beta = \gamma = 90^\circ$

of 32, crystallographically. The combination of the Bravais lattice and the symmetry operations present in the crystalline materials are all described by one of 230 possible space groups. Space group theory contains all of the elements of point group symmetry, with additional component operations due to the presence of translational symmetry. Due to translational symmetry, the additional symmetry operations present in space group theory include glide planes and screw axes. A glide plane is one in which the basis is translated through space. A screw axis is defined as an operation in which a point is rotated by $\frac{2\pi}{n}$ and translated by some distance r parallel to that axis and is shown in Figure 1.3.[4]

1.2 Theory of X-ray diffraction

Materials are capable of diffracting radiation when the radiation has a wavelength that is similar to the length scale of the distribution of scattering density in that material, approximately 1 Å. There are three such radiation sources which obey this criterion; X-

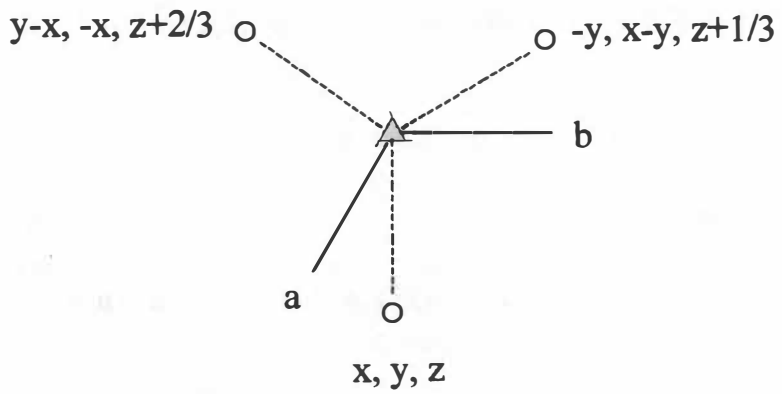


Figure 1.3. Depiction of a 3_1 screw axis parallel to c.

rays, neutrons and electrons. X-ray diffraction is the most widely used of these three applications due to the accessibility of X-ray sources.

Scattering can be broken down into two main types, inelastic and elastic scattering. Inelastic scattering occurs when the there is energy transferred either to or from the sample by the scattering probe, whereas elastic scattering results when both incident and scattered energies are equal, which leaves the wavelength constant after scattering from a sample. While inelastic scattering yields dynamical information about the system, elastic scattering is the most useful tool to probe the structure of the system. In an elastic scattering experiment, while there is no change in energy between the incident and scattered wavevector, there is a change in direction. The incident beam is represented by $\frac{s_0}{\lambda}$, with a length of $\frac{1}{\lambda}$, which terminates at the origin of the reciprocallattice. The scattering vector s may then be defined as

$$\mathbf{s} = \frac{(\mathbf{S} - \mathbf{S_0})}{\lambda} \tag{1.7}$$

in which S_0 is the incident scattering vector and S is the diffracted scattering vector. In equation (1.7), with a scattering angle equal to 2θ, the relationship between the scattering angle and the scattering vector becomes

$$\mathbf{s} = \frac{2\sin\theta}{\lambda} \tag{1.8}$$

The results of an X-ray diffraction experiment are a combination of the scattering by individual atoms as well as the interference that occurs between scattering from different atoms. The amplitude of a scattered wave from a single electron is given by the equation[5]

$$A = f\, A_0 \cos\left[2\pi\nu\left(t - \frac{r}{c}\right) - \varphi\right] \tag{1.9}$$

in which f is the atomic scattering factor, φ is the scattering phase shift and r is the distance from the origin. The intensity, I, in a diffraction experiment is given by the square of the modulus of the amplitude, or

$$I = |A|^2 = AA^* \tag{1.10}$$

where A^* is the complex conjugate of the scattering amplitude.

1.3 Generation of X-rays

X-rays are electromagnetic radiation with a wavelength of approximately 1 Å. They are typically generated when electrons are accelerated through a high voltage source and collide with matter. The electrons are then slowed down by this collision and the deceleration generates bremsstrahlung, which is depicted in Figure 1.4. This specific type of electromagnetic radiation is white radiation which is shown in Figure 1.5.[6] In

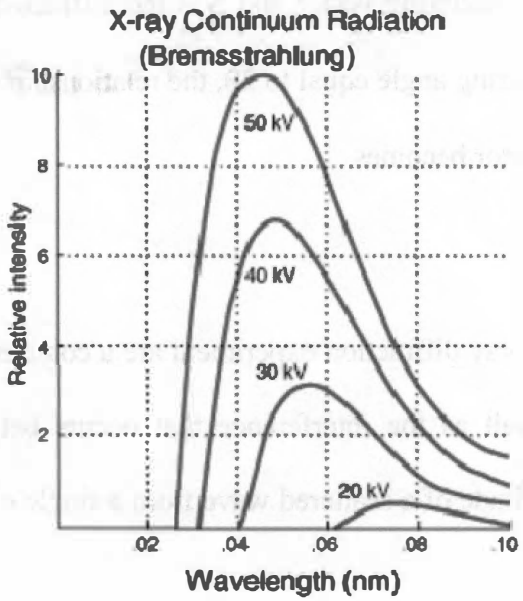


Figure 1.4. Bremsstrahlung scattering.[6]

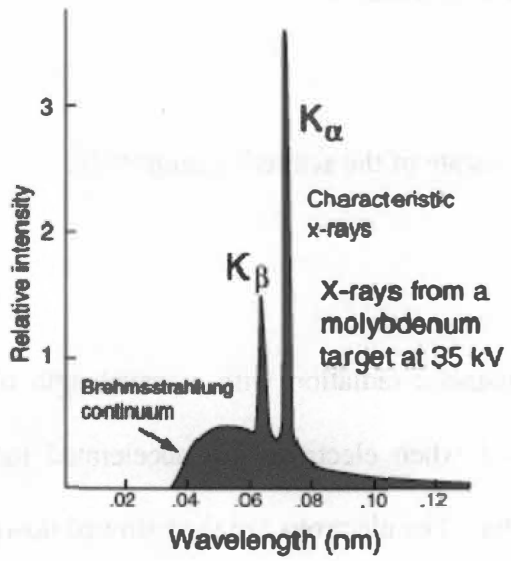


Figure 1.5. Target spectrum for an X-ray source.[6]

addition to bremsstrahlung, collision with a metal atom may ionize some 1s, or K shell, electrons of the metal. An electron from on outer orbital, in the case of transition metals, the 2p or 3p, then drops down to occupy the vacant 1s orbital. The energy that is released upon this transition is in the form of X-radiation. Depending on where the electron drops from, this radiation is called either α or β radiation. The wavelength of the emitted radiation is directly related to the atomic number, Z, of the ionized metal, such that

$$\upsilon = \left(\frac{c}{\lambda}\right) \propto Z^2 \tag{1.11}$$

where ν is the frequency and λ is the wavelength, as stated by Moseley's Law.[7] Table 1.2 lists the ionization potentials for some of the elements commonly used in X-ray tubes.[8]

In a typical X-ray tube, current is passed through a metal filament. The thermoelectric electrons produced are accelerated through a sealed tube, in a vacuum, towards an anode which has a potential difference of approximately 30 keV. The generated X-rays exit the tube through beryllium windows. Beryllium is used due to its low Z and therefore the X-rays may easily exit the sealed tube. A schematic representation of a typical X-ray tube is shown in Figure 1.6.

Table 1.2 Ionization potentials for some commonly used elements in X-ray tubes.

Element	$\lambda\left(K_{\bar{\alpha}}\right)$ /Å	***Ionization Potential /eV***
Cr	2.2909	5412
Mo	0.71069	17442
Cu	1.5418	8040
Fe	1.9373	6398

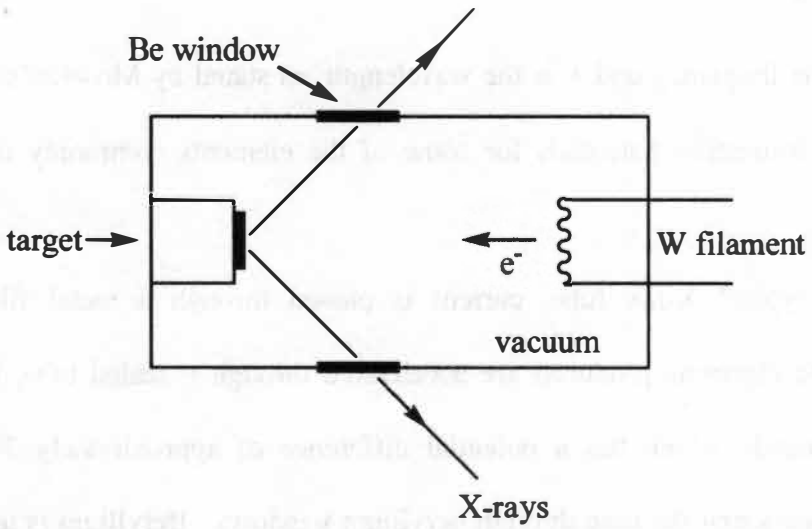


Figure 1.6. Schematic for a typical X-ray tube.[2]

1.4 Scattering of X-rays from a single electron and from a single atom

When an X-ray comes into contact with an atom, there are two processes which may occur. The X-ray beam may be absorbed or the beam may be scattered. Also, there are two ways in which electrons may scatter from an atom. In an elastic scattering event, the resulting scattered photon is emitted with the same wavelength and energy as the incident beam, resulting in elastic scattering. Inelastic scattering occurs when there is a change in energy between the incident and resulting beam and therefore a change in wavelength. If the scattered photon has a wavelength that is longer than the incident wavelength, the result is called Compton scattering. Compton scattering is completely incoherent and yields a diffuse background. In classical terms, the intensity of X-ray scattering by a free electron is given by Thomson's scattering equation[3]

$$I = I_0 \frac{e^4}{m^2 c^4 R^2}\left(\frac{1+\cos^2\theta}{2}\right) \tag{1.12}$$

where c is the velocity of light, e and m are the charge and mass of the electron, respectively, R is the distance from the scattered electron to the observation point and the term $\left(\frac{1+\cos^2\theta}{2}\right)$ is the polarization factor for an unpolarized primary beam.

However, scattering by an atom is more complex. There is an instantaneous electric field, $\in_e$, which is produced when an X-ray beam interacts with an atom, which is due to only one electron in that atom.

$$\in_e = \frac{E_0 e^2}{mc^2 R} e^{2\pi i\left[\upsilon t - \left(\frac{R}{\lambda}\right)\right]} \int e^{\left(\frac{2\pi i}{\lambda}\right)(s-s_0)r} \rho\, dV \tag{1.13}$$

The term defined by the integral in equation (1.13) is f_e, or the scattering factor per electron. By substituting

$$k = \frac{4\pi \sin\theta}{\lambda} \tag{1.14}$$

then the scattering factor per electron is

$$f_e = \int_{r=0}^{\infty} \int_{\phi=0}^{\pi} e^{ikr\cos\phi} \rho(r) 2\pi r^2 \sin\phi \, d\phi \, dr \tag{1.15}$$

and integrating with respect to φ, the scattering factor per free electron is equal to

$$f_e = \int_0^{\infty} 4\pi r^2 \rho(r) \frac{\sin kr}{kr} dr . \tag{1.16}$$

A more useful equation in X-ray diffraction is the atomic scattering factor, f, which is the sum over all electrons in the atom.

$$f = \sum_n f_{e,n} = \sum_n \int_0^{\infty} 4\pi r^2 \rho_n(r) \frac{\sin kr}{kr} dr \tag{1.17}$$

where the quantity $\sum_n \int_0^{\infty} 4\pi r^2 \rho_n(r) dr$ is equal to Z, the atomic number, it follows that f approaches Z at small values of $\frac{\sin\theta}{\lambda}$.

1.5 Scattering from a periodic array of atoms

X-ray diffraction by a single crystal is much more complex than the simplification that comes with assuming diffraction by a single electron or an atom. Because the electron density is periodic in a crystal, E is equal to the amplitude of the electron density

at a specific point of observation, given by the product of the electric field times its complex conjugate in the following equation:

$$E^2 = \epsilon_p \epsilon_p^* . \tag{1.18}$$

Multiplying the amplitude, A, by $\frac{c}{8\pi}$ provides the intensity at that point

$$I_p = \frac{E^2 c}{8\pi} . \tag{1.19}$$

The intensity at an observation point due to scattering by a single crystal is given by the summation of Thomson's scattering equation of a free electron, such that[3]

$$I_p = I_e F^2 \frac{\sin^2\left(\frac{\pi}{\lambda}\right)(s - s_0)\cdot N_1 \mathbf{a}_1}{\sin^2\left(\frac{\pi}{\lambda}\right)(s - s_0)\cdot \mathbf{a}_1} \frac{\sin^2\left(\frac{\pi}{\lambda}\right)(s - s_0)\cdot N_2 \mathbf{a}_2}{\sin^2\left(\frac{\pi}{\lambda}\right)(s - s_0)\cdot \mathbf{a}_2} \frac{\sin^2\left(\frac{\pi}{\lambda}\right)(s - s_0)\cdot N_3 \mathbf{a}_3}{\sin^2\left(\frac{\pi}{\lambda}\right)(s - s_0)\cdot \mathbf{a}_3} \tag{1.20}$$

where $N_n a_n$ are edges of the crystal which are parallel to the crystal axes a_n. The quantity F^2 is the product of FF^*, in which F is termed the structure factor, given by

$$F = \sum_n f_n e^{\left(\frac{2\pi i}{\lambda}\right)(s - s_0) r_n} \tag{1.21}$$

and is the summation over n atoms at positions r_n. The intensity of a reflection is conditioned by the structure factor. Thus, the structure factor, written where r_n is periodic with indices, *hkl*, $r_n = (hx_n + ky_n + lz_n)$, is given by

$$F_{hkl} = \sum_n f_n e^{2\pi i(hx_n + ky_n + lz_n)} . \tag{1.22}$$

Under various conditions in which $F_{hkl} = 0$, the lattice centering for the crystalline material is determined. These systematic absences give rise not only to the lattice centering, but also symmetry operations involving translation present in the lattice. The intensity, I, of any given reflection is equal to the square of the structure factor.

In the case of a periodic system, the analysis of scattering data is aided by the convolution of the unit cell structure which contains the molecular structure and the lattice. Scattering from a periodic system is described by Bragg's Law or the Laue equations and is a more specific use of general theory of scattering. Bragg's Law assumes crystalline materials to be built up of a series of layers. In an X-ray diffraction experiment, some X-rays are scattered off of these planes with an angle of reflection which is equal to the angle of incidence and the rest of the X-rays are transmitted through the planes, to be scattered by subsequent planes. A pictorial description of Bragg's Law is shown in Figure 1.7. As seen, the beam defined by 22' must travel an extra distance defined by the distance xyz. For 1' and 2' to be in phase, the distance xyz must be equal to a whole number integral of the incident wavelength, λ.

The distance which defines the interplanar spacing, d, is known as the d-spacing and the angle θ, the angle of incidence, is known as the Bragg angle. The mathematical description of Bragg's Law follows as

$$2d \sin \vartheta = n\lambda \tag{1.23}$$

In order for Bragg's Law to be satisfied, 1' and 2', the reflected beams, must be in phase and interfere constructively. When there is deviation from Bragg's angle, then either destructive interference or complete cancellation occurs.

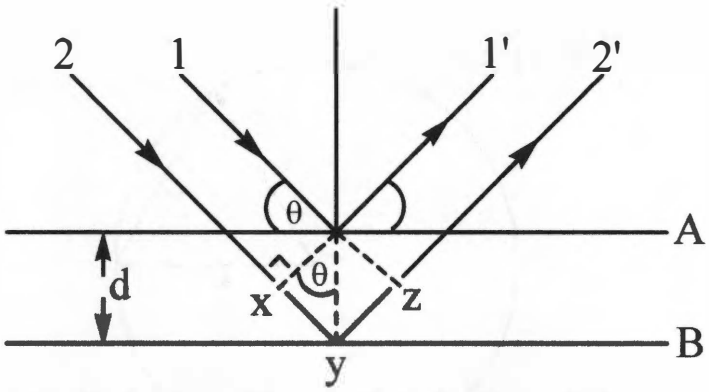


Figure 1. 7. Derivation of Bragg's Law for X-ray diffraction.

1.6 Ewald sphere construction

In reciprocal space, Bragg's Law may be represented by the sphere of reflection, also known as the Ewald sphere. A schematic representation of the Ewald sphere in two dimensions is shown in Figure 1.8. The incident beam, in reciprocal space is represented by $\frac{s_0}{\lambda}$, with a length of $\frac{1}{\lambda}$ which terminates at the origin of the reciprocal lattice. A reciprocal lattice point, hkl, which falls on the surface of the Ewald sphere represents a set of planes, (hkl), which satisfy Bragg's Law.

1.7. Debye-Waller temperature factor

At this point, variations in temperature have not been accounted for. However, the atomic position in a crystal is actually the average position around which the atoms oscillate. This is a result of the thermal vibrations of atoms. The average position, R, of atom *l* is given by

$$R_l' = R_l + \delta_l \tag{1.24}$$

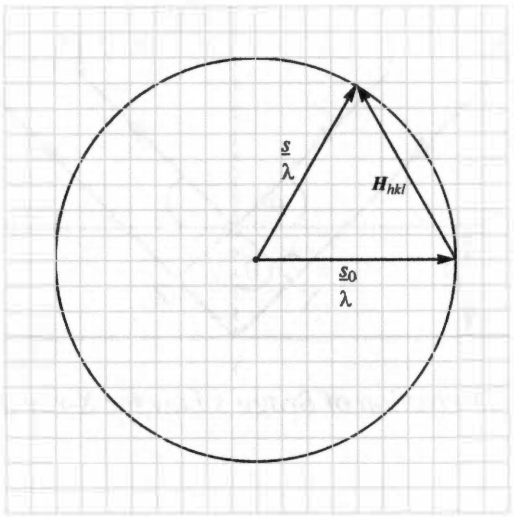


Figure 1.8. Schematic representation of the Ewald sphere.

where δ_l is defined as the instantaneous displacement due to thermal vibrations. The equation for the intensity is then given by

$$I = I_e \sum_l f_l e^{\left(\frac{2\pi i}{\lambda}\right)(s-s_0)(R_l+\delta_l)} \sum_{l'} f_{l'}^* e^{-\left(\frac{2\pi i}{\lambda}\right)(s-s_0)\left(R_{l'}+\delta_{l'}\right)} . \tag{1.25}$$

Although the results from the preceding equations imply that structural dynamics may be determined, all of the information in these equations results from an elastic scattering experiment in which the information available is on the Bragg average. The thermal vibrations of atoms increases with temperature and it is the time averaged information that is available in a diffraction experiment. To account for the temperature dependent displacement of atoms, the Debye-Waller temperature factor, W, is incorporated into the equation for the diffracted intensity, which is given by

$$W = \exp\left(-\frac{16\pi^2 \sin^2\theta}{\lambda^2}\frac{\Delta X^2}{3}\right) \tag{1.26}$$

where λ is the wavelength of the scattered X-ray and ΔX is the displacement. With the incorporation of the temperature factor, the structure factor may be modified as follows:[9]

$$F_{hkl} = \sum_j F_{hkl} \exp\left(-2W_j\right). \tag{1.27}$$

A physical representation of the thermal displacement of atoms is given by the displacement parameters. The isotropic displacement parameter is given by

$$B = 8\pi^2 \left\langle u^2 \right\rangle \tag{1.28}$$

in which $\left\langle u^2 \right\rangle$ is the mean displacement of the atom.[9] The six independent components of B, given as U_{ij}, are the anisotropic displacement parameters, or ADP's. These six parameters may be visualized using 'thermal ellipsoids' which are the three-dimensional representation of the six U_{ij} components.

1.8 Development of X-ray scattering

1.8.1. Discovery of X-rays and diffraction

X-rays were first discovered by William Röntgen in 1895[4] and applied to scattering experiments in 1912 with von Laue. M. von Laue theorized that crystalline materials could be used as natural diffraction gratings, which he proved by experimentation. His results showed that effects of X-rays diffracted by crystalline materials could be interpreted based on the diffraction of electromagnetic waves by the three-dimensional grating of the material. M. von Laue's development helped prove both the wave nature of X-rays as well as the concept of periodicity in crystalline materials. W.H. and W.L. Bragg further developed experimental techniques. Their initial

experiment on materials such as CaF_2 and NaCl provided a more complete understanding of diffraction of crystalline materials from a white beam.[10,11] Additionally in 1913, experiments on rock salt helped institute the concept of Bragg's Law.[10]

1.8.2 The Laue method

The method developed by von Laue is the oldest method of X-ray scattering. The Laue method can be divided into two subsets of experiments: transmission and back reflection. Both methods use a beam of continuous spectrum with a fixed crystal orientation. For a single orientation, the relationship between the incident beam and the hkl planes is fixed and only specific wavelengths satisfy Bragg's Law. The collimated primary beam passes through a slit in a piece of foil and strikes the sample and subsequently, the diffraction pattern is collected by a Laue camera. The Laue method is common for many single crystal neutron instruments, such as SXD (at the ISIS Facility located at Rutherford Appleton Laboratories in the United Kingdom) and SCD (at the Intense Pulsed Neutron Source located at Argonne National Laboratory in the United States).

1.8.3 Rotation method

The rotation method is useful in the determination of the unit cell dimensions as well as indexing of reflections for single crystal samples. The two available rotation methods include a stationary film or by use of a Weissenberg or precession photographs.

1.8.4 Further developments

With increasing advances in technology, including computer development and programming, the capabilities of diffraction equipment has dramatically increased over the last few decades. A data collection that just a few years ago would require a week, can now be completed in a few hours. The advent of ccd (charge coupled device) detectors is a large contributing factor in this change. These are area detectors that allow for a number of reflections to be collected and read by the computers in a matter of seconds, whereas the previous point detectors collected a significantly less amount of data in space.

1.9 Refinement of scattering data

1.9.1 Fourier methods

The general definition of a Fourier series which is periodic in the x direction and a period length of a, is given by[3]

$$f(x) = \sum_{n=-\infty}^{+\infty} \left\{ A_n \cos 2\pi n \frac{x}{a} + B_n \sin 2\pi n \frac{x}{a} \right\} \tag{1.29}$$

where A_n and B_n are the cosine and sine coefficients, respectively, for each value of n. One manner in which to represent the crystalline state is by a continuous electron density function, $\rho(xyz)$, which is triply periodic. Therefore, the function $\rho(xyz)$ may be expressed as a triple Fourier series with distances x, y, z which are perpendicular to the unit cell axes, **a**, **b** and **c**.

If the electron density is periodic in z but fixed in x and y, the function can be written as[3]

$$\rho(xyz) = \sum_{r=-\infty}^{+\infty} C_r(x,y)\exp\left(\frac{-2\pi irz}{z}\right) \tag{1.30}$$

where $C_r(x.y)$ is the coefficient. Analogous equations can be written assuming periodicity in x with fixed y and z as well as periodicity in y with fixed x and z. Combination of these three function yields the triply periodic function of the electron density which is written as:

$$\rho(xyz) = \sum_{p}\sum_{\substack{q\\-\infty}}^{+\infty}\sum_{r} C_{pqr}\exp\left(-2\pi i\left[p\left(\frac{x}{a}\right)+q\left(\frac{y}{b}\right)+r\left(\frac{z}{c}\right)\right]\right) \tag{1.31}$$

The periodic electron density may then be substituted into the general equation for the structure factor, with more common crystallographic notation, as[3]

$$F_{hkl} = \int_0^a\int_0^b\int_0^c \rho(xyz)\exp\left(2\pi i\left[h\left(\frac{x_n}{a}\right)+k\left(\frac{y_n}{b}\right)+l\left(\frac{z_n}{c}\right)\right]\right)dV \tag{1.32}$$

For axes which are not orthogonal, dV can be determined from

$$\frac{dV}{dxdydz} = \frac{V}{abc} \tag{1.33}$$

Combining equations (1.32) and (1.33) gives

$$VC_{hkl} = F_{hkl} \tag{1.34}$$

It can therefore be seen that the electron density, given in electrons per unit volume, is defined by a triple Fourier series, in which the coefficients are the structure factors, F_{hkl}.[3,12]

$$\rho(x,y,z) = \frac{1}{V}\sum_{h}\sum_{\substack{k\\-\infty}}^{+\infty}\sum_{l} F_{hkl}\exp\left(2\pi i\left[h\left(\frac{x_n}{a}\right)+k\left(\frac{y_n}{b}\right)+l\left(\frac{z_n}{c}\right)\right]\right) \tag{1.35}$$

In a diffraction experiment, it is the integrated intensity that is actually measured which is proportional to $F_{hkl}F_{hkl}^{*}$, the magnitude of the coefficients from equation (1.32) are determined but not the phase. This leads to a less obvious means of structure solution based on the Fourier series. However, if the phases of heavy atoms are known, then all of the phases can usually be determined for each F_{hkl}. It also holds true that all values for the electron density function are positive values and thus leaves restrictions on the phase of F_{hkl}. Combining these various restrictions allows the Fourier method to be useful in structure determination.

There is a lack of phase information that is inherent in most X-ray diffraction experiments.[13] As previously stated, the integrated intensity is equal to the square of the structure factor,

$$I = |F_{hkl}|^2 \tag{1.36}$$

where F_{hkl}^2 is the product of the real and imaginary structure factors. The structure factor is related to the electron density by Fourier transform, was seen in equation (1.35). Therefore, the scattering density in a diffraction experiment is obtained through the Fourier transform of the intensity, in which no phase information is present.

1.9.2 Spherical atom approaches

The most commonly used practice in the refinement of conventional X-ray diffraction data is the spherical atom approach. As the name indicates, all atoms in this type of refinement are assumed to be spherical. Atomic displacement parameters, or ADP's, are used in the refinement to account for "thermal motion" of the atoms. This

allows for a slight deviation from the sphericity of the atomic model in these refinements. In the Bragg averaged structure of these elastic diffraction experiments, there is no dynamical information about the molecular system in question. However, the ADP's are used to model what is considered to be the anisotropic movement of the atoms, on average, in the crystalline state.

1.10 Accurate modeling of electron density

1.10.1 Theoretical approaches to the aspherical atom model

The first improvements to the spherical atom, or independent atom model (IAM), developed when the κ-formalism was introduced in 1961.[14] This formalism allowed for charge transfer between atoms, in which the total electron density of an atom is given by

$$\rho_{atom} = \rho_{core} + \rho'_{valence}(\kappa r) = \rho_{core} + P_{valence}\kappa^3 \rho_{valence}(\kappa r) \tag{1.37}$$

where $P_{valence}$ is the valence shell population parameter and κ is the expansion/contraction parameter for the valence shell. The parameter κ scales the radial coordinate, r. Therefore, when $\kappa > 1$, the same amount of electron density is obtained at a smaller value of r, and thus the valence shell is contracted. In equation (1.37) the term κ^3 is introduced to satisfy the normalization function

$$N4\pi \int \rho_{valence}(\kappa r) r^2 dr = 1 \tag{1.38}$$

These normalization functions were introduced with an atom centered multipolar function which was an attempt to improve the 'complete' description of the charge density.[15-17]

Further developments to the accurate modeling of electron density were established in 1969 by Stewart, which introduced a generalized spherical harmonic

density function.[18] The definition of the multipolar density function included a radial function (r dependent) and an angular function (θ, ϕ dependent), in which the angular function is a spherical harmonic function $y_{lm\pm}(\vartheta,\varphi)$ and accordingly, $y_{lm\pm}(\vartheta,\varphi)$ is a linear combination of the complex spherical harmonics Y_{lm}. This linear combination of the spherical harmonic functions aids in interpretation of experimental electron density. From experiment, the observed electron density is necessarily real and therefore is best fit using a linear combination of spherical harmonic functions to produce a real function. The complex spherical harmonic functions are given by

$$Y_{lm}(\vartheta,\varphi) = (-1)^m \left[\frac{(2l+1)(l-|m|)!}{4\pi(l+|m|)!}\right]^{1/2} P_l^{|m|}\cos(\vartheta)exp(im\varphi) \tag{1.39}$$

where $(-1)^m$ is the Condon-Shortley phase factor and $P_l^{|m|}\cos(\vartheta)$ is the associated Legendre function.

The Hansen-Coppens multipolar density formalism was introduced in 1978,[19,20] which combined the κ-formalism and the atom centered multipolar density function. Using this formalism, the electron density of a single atom is[21]

$$\rho_{atom} = P_{core}\rho_{core}(r) + P_{valence}\kappa^3\rho_{valence}(\kappa r) + \sum_{l=0}^{l_{max}} \kappa'^3 R_l(\kappa' r)\sum_{m=0}^{l} P_{lm\pm} d_{lm\pm}(\vartheta,\varphi) \tag{1.40}$$

which is the current and most accurate way to model the total electron density in a system. P_{core} is the population of the core or valence electrons, ρ is the electron density of the core or valence shell, κ is the spherical expansion/contraction parameter, κ' is the

deformation expansion/contraction parameter, R_l is the radial term and $P_{lm\pm}d_{lm\pm}(\vartheta,\varphi)$ is the angular term of the spherical harmonic function.

1.10.2 Experimental approaches to the aspherical atom model

A basic definition of the anisotropic displacement parameter is, however, not sufficient in describing the actual aspherical nature of the atoms. By the nature of the covalent bond, in which electrons are shared between atoms, the distribution of electron density necessarily deviates from the standard "spherical" atom. Aspherical atom refinements have been implemented in a few programs, such as XD,[22] to utilize a mathematically accurate refinement method which allows for deviation from the spherical atom model approach. A combination of radial functions and spherical harmonics in combination with the kappa formalism, allow for an empirical description of the observed electron density in the molecular material, including the electron density formed in a chemical bond. Aspherical atom refinements begin with an input of data from the basic spherical atom refinement. These refinements are then built upon with an expansion of the spherical harmonic expressions which define experimental fit to the electron density.

There are several different ways to approach the deformation density model; however, there are two which are quite common. Given experimental considerations of the sample and temperature of the experiment, it is possible to calculate the deformation density based on the density obtained in a neutron diffraction experiment being subtracted from the electron density from an X-ray diffraction experiment, in which the deformation density is given by

$$\rho_{deformation}^{X-N}(r) = \frac{1}{V}\sum_{\mathbf{H}}\left(|F_{obs,X}|\frac{|F_{calc,N}|}{F_{calc,N}} - F_{calc,N}\right)\cos(2\pi\mathbf{H}\cdot r) \qquad (1.41)$$

where **H** is the lattice vector, V is the volume and F is the structure factor. The most widely used application of the deformation density is the difference between the total electron density and a calculated model from X-ray diffraction data. The deformation density is then given by

$$\rho_{deformation}^{X-X}(r) = \frac{1}{V}\sum_{\mathbf{H}}\left(F_{obs,X} - F_{calc,X,highorder}\right)\exp(-2\pi i\mathbf{H}\cdot r) \qquad (1.42)$$

The difference which results from equation (1.42) allows for a direct visualization of the electron density in a bond as well as lone pairs of electrons.

There are several topological properties which are accessible through the aspherical atom formalism which are well-behaved, functional forms. The deformation density is defined as the difference between the total density and the density which is calculated from a reference molecule based on unbiased positional and thermal parameters.

1.10.3 Bader's definition of atoms in molecules (AIM)

The definition of a bound atom in a molecule requires that its properties must be able to be defined by the average properties in a material. Atoms are objects in real space and therefore their topological properties are defined by space partitioning of the real space charge distribution. The charge density, $\rho(r)$, is a physical quantity which has a definite value, which is a scalar quantity in three-dimensional space.[23] These topological properties can be summarized by use of a bond critical point. The gradient field vector,

$\nabla\rho(r)$, is a convenient way to analyze these topological properties, which associate direction and magnitude to each point in space. The location of a bond critical point is found where $\nabla\rho(r)$ vanishes.[23] A gradient path begins at each critical point and terminates at an atom center, in which the line that connects these two points is termed the atomic interaction line.[23]

1.10.4 Topological properties from aspherical atom refinements

Important topological properties readily accessible through multipolar density formalism are the gradient of the density, $\nabla\rho$, and the Laplacian, $\nabla^2\rho$, and their applications in the definition of critical points. The gradient of the density is defined by

$$\nabla\rho(r) = i\frac{\partial\rho(r)}{\partial x} + j\frac{\partial\rho(r)}{\partial y} + k\frac{\partial\rho(r)}{\partial z} \tag{1.43}$$

which is equal to zero at a critical point. The bond critical points may be defined in terms of the Hessian matrix.[23] The Hessian matrix, $\mathbf{H}(r)$, is the symmetric matrix of the nine second derivatives of the density, $\frac{\partial^2\rho}{\partial x_i \partial x_j}$, in which the eigenvectors of $\mathbf{H}(r)$ may be obtained by the diagonalization of the matrix. The eigenvectors are the principal axes of the curvature at a point r. The number of non-zero eigenvalues of the curvature is termed the rank, *w*. The signature, σ, is the algebraic sum of the signs of the eigenvalues.[21] A critical point is then defined by (w,σ). [21,23] There are four possible types of critical points in this three-dimensional space. A (3,-3), or peaks, consists of all negative curvatures and the electron density is a local maximum. (3,-3) critical points are found at

the center of an atom. A (3,-1) critical point, termed passes or saddle points, consists of two negative curvatures at which ρ is a maximum in that plane as is defined by the aforementioned curvatures, and ρ is a minimum along the third curvature, perpendicular to the plane. (3,-1) critical points are located between every pair of atoms linked by a bond. A (3,+1) critical point, or pales, consist of two positive curvatures with ρ at a minimum in this plane and ρ is a maximum along the third curvature perpendicular to that plane. (3,+1) critical points are found at the center of a ring of atoms. The final type of critical point is a (3,+3), termed pits. All curvatures in a pit are positive and the electron density is a local minimum. This type of critical point is found at the center of a cage of atoms.

The Laplacian of the electron density is a topological property which may be extracted from the results of a multipolar formalism. The Laplacian is defined as

$$\nabla^2\rho(r)=\frac{\partial^2\rho(r)}{\partial x^2}+\frac{\partial^2\rho(r)}{\partial y^2}+\frac{\partial^2\rho(r)}{\partial z^2} \tag{1.44}$$

The numerical value of the Laplacian is indicative of the type of chemical bond present. In a typical C-O bond, the value for the Laplacian in found in the range of approximately -30 to -40 eÅ^{-5}, and in a typical C-C bond, this value ranges from -10 to -12 eÅ^{-5}.[21] For closed-shell, or ionic interactions, there is no accumulation of electron density along a bond path. Instead, there exists a minimum along the bond path connecting the two nuclei in which λ_3 has a positive value. However, λ_1 and λ_2 are negative because there is no contraction of electron density which is perpendicular to the bond. A diagram representing the paths of λ_i with respect to a pair of bonded atoms is shown in Figure 1.9.

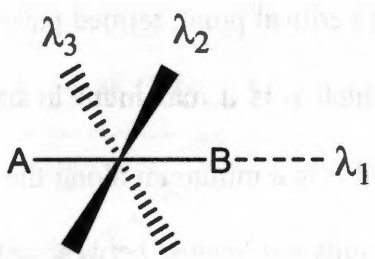


Figure 1.9. Definition of λ with respect to a pair of bonded atoms.

This results in a positive value for the Laplacian. For covalent bonds, the value of the Laplacian is negative, due to a strong dependence on λ_1 and λ_2. However, for second row elements, a large positive value of λ_3 dominates and may therefore lead to a positive value of the Laplacian. The Laplacian is useful in the classification of hydrogen bonds. For X-H...Y, the X-H bond is covalent; however, H...Y is a 'closed-shell' interaction. There is a small amount of electron density found along the H...Y vector. In a typical strong hydrogen bond, as is present in the $(H_2O)_2$ dimer, $\nabla^2\rho(r) = 0.42e\,\text{Å}^{-5}$ and for a very short, strong hydrogen bond, as in $(HF)_2$, $\nabla^2\rho(r) = 0.81e\,\text{Å}^{-5}$.[23]

The ellipticity, ε, is a measure of the amount of π-character present in a bond. The ellipticity is defined by

$$\varepsilon = \frac{\lambda_1}{\lambda_2} - 1 \tag{1.45}$$

where λ_1 is a contraction of the electron density perpendicular to the bond path. For a perfectly symmetric σ bond, the ellipticity equals zero. Any deviation from sphericity in a bond necessarily yields a value for the ellipticity which is greater than zero. Typical

values for the ellipticity of a bond are 0.0 for ethane, 0.23 for benzene and 0.45 for ethylene.[21]

Chapter 2: Experimental and theoretical studies of the electronic structure in hydrogen bonded systems

Part of the work reported in this chapter has been published in the *Journal of Physical Chemistry A*[24,25] and is included in its published form in the Appendix.

2.1 Introduction

The earliest reference to a hydrogen bonding interaction dates from the early 1900's,[26-28] and was used to explain simple inorganic systems such as ammonium salts. A formal definition of hydrogen bonding was not developed until 1960 by Pimentel and McClellan.[29]

> *"A hydrogen bond is said to exist when: 1) there is evidence of a bond, and 2) there is evidence that this bond specifically involves a hydrogen atom already bonded to another atom".*[30]

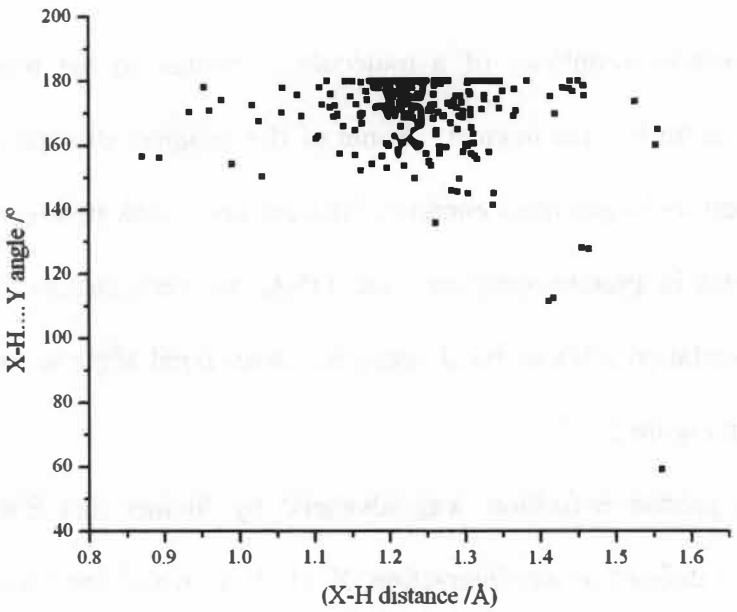
This is a loose definition that has been continually redeveloped and assessed since its advent. From this definition, it is clear that the definition of a hydrogen bond is unconventional with respect to the standard covalent two centered, two electron (2c-2e) bond. The hydrogen bond is a very complex interaction, spanning two orders of magnitude from the 'weak' hydrogen bond to HF_2 at 163 kJ mol^{-1}. At the lower extreme of energy, the hydrogen bond is equivalent to van der Waals and dispersion interaction (16.23 kJ mol^{-1} in 1,3,5,7-tetra-*tert*-butyl-s-indacene),[31] while at the higher extreme of energy, the very strong hydrogen bonds have energies in the range of some covalent interactions. For example, the bond strengths in F_2 and I_2 are 154.8(4) and 148.95(4) kJ

mol^{-1}, respectively,[32] in comparison to the hydrogen bond in $[FHF]^-$ which is 163 kJ mol^{-1}.[33]

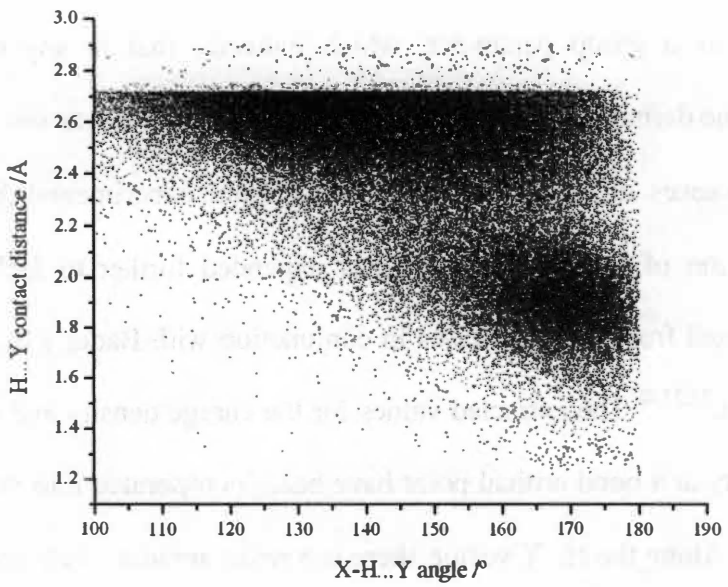
The structural simplicity of a molecule is related to the bond strength of a hydrogen bond in an inverse manner. Some of the simplest structures, such as HF_2,[33] have the strongest hydrogen bond energies, whereas very weak hydrogen bonds, such as those often found in protein structures and DNA, are very structurally complex. A graphical representation of these bond strengths versus bond angle as extracted from the CSD is shown in Figure 2.1.[34,35]

A more precise definition was advanced by Steiner and Saenger where the hydrogen bond is defined as any interaction, X–H···Y, in which the hydrogen atom has a partial positive charge and the atom Y has a partial negative charge.[36] The hydrogen bond is also defined as a group parameter, which indicates that in any description of a hydrogen bond the definition necessarily combines all three atoms as one 'entity'.

With advances in charge density analysis from experimental X-ray diffraction data, the definition of a hydrogen bond has expanded further to include topological properties extracted from these analyses in conjunction with Bader's theory of atoms in molecules (AIM).[21,37,38] The extracted values for the charge density and the Laplacian of the charge density at a bond critical point have been incorporated into the definition of a hydrogen bond. Along the H···Y vector, there is a small amount of electron density and a positive value for the Laplacian, which is characteristic of a closed-shell interaction.[21] Typical values for the Laplacian in a very strong hydrogen bond are 0.42 $e^-Å^{-5}$ for the water dimer and 0.81 $e^-Å^{-5}$ for $(HF)_2$.[21] However, some studies have shown in very short symmetric hydrogen bonds, the value for the Laplacian at the bond critical point along



(a)



(b)

Figure 2.1. Graphical representation of hydrogen bond lengths versus angle from the CSD; X-H...Y, where X and Y are either C, N, O or F.[9,10] (a) defined as X-H-Y, (b) defined as X-H...Y, where H...Y is defined as a non-bonded contact.

the H...Y vector indicates covalent character, with reported values between -5.9(9) and -7.1(9) $e^{-}Å^{-5}$.[21,39,40]

Hydrogen bonding is a common interaction in many areas of structural chemistry.[41-44] In chemically simple systems, such as the hydrides of the first row elements of the periodic table, hydrogen bonding is responsible for the strongly associated nature of water,[45-51] ammonia[52] and hydrogen fluoride,[53-55] as well as the excellent solvent properties of these fluids. The physical and chemical properties of more complex systems are also due to the presence of the hydrogen bond; highly complex examples occur in structural biology, where the generation and maintenance of protein secondary and tertiary structure are dependent on this interaction.[42-44,49] Protein-protein interactions,[44] enzymatic catalysis[42,43] and the structural chemistry of DNA are yet more complex examples.

The presence of a hydrogen bond is relatively simple to predict in the solid state. The presence of two electronegative atoms, usually N, O or F, one of which is bound to at least one hydrogen, normally ensures that a hydrogen bond will exist, assuming that there is no structural motif that prevents bond formation. The ease of formation and the predictability of the presence of hydrogen bonds have led to the exploitation of this interaction in the intelligent design of crystal structures – the field of crystal engineering.[56-61]

Apart from the importance and flexibility of the hydrogen bond as an important interaction in the solid state, it is also of theoretical interest in the study of proton transfer in several systems, notably carboxylic acid dimers, have been investigated theoretically and experimentally towards this end.[62-71] It has been demonstrated both through variable

temperature X-ray and neutron diffraction experiments, that in some molecular systems, the hydrogen atom migrates to the center of the X-H-Y bond as the temperature of the experiment is raised.[63,67,68,72,73] It is notable that proton migration may occur in both homonuclear (X-H-X) and heteronuclear (X-H-Y) systems.

Very strong hydrogen bonds are often intramolecular, as is shown in Figure 2.2, or found to occur between conjugate acid/base pairs, with an example shown in Figure 2.3, and are often referred to as short strong hydrogen bonds, or SSHB. SSHB's are very important in chemical reactivity and often play a dominant role in crystal packing when they are present and in this respect, it is a strong intermolecular interaction. As with all hydrogen bonds, they contain a significant electrostatic contribution, or charge transfer contribution.[29] However, based on the bond energies associated with SSHB's, the strength of these bonds are often equivalent to those with covalent character. The hydrogen bond may be defined as a 3-centered-4-electron (3c-4e) bond in which two electrons are from the X-H bond and two electrons are from the lone pair on Y. A simple molecular orbital diagram of the hydrogen bond is shown in Figure 2.4.

It has been stated that strong hydrogen bonds have very little covalent character and are predominantly defined by electrostatic forces.[29] Weak hydrogen bonds consist of very little or no covalent character and are only moderately electrostatic, although they are dominated by charge transfer components and dispersive forces. Some definitions of the hydrogen bond state that the distance between H and Y should be within the sum of the van der Waals radii.[74] However, a bond which is considered a weak hydrogen bond often does not fit this criteria. Desiraju and Steiner[29] developed a system to classify the 'cut-off criteria' for hydrogen bonding, which has an r^{-x} energy dependence that breaks

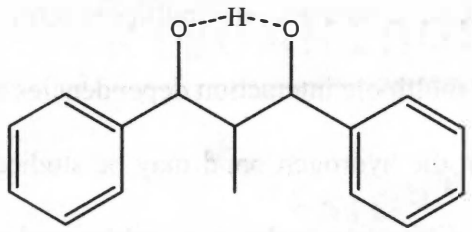


Figure 2.2. Example of an intramolecular hydrogen bond.

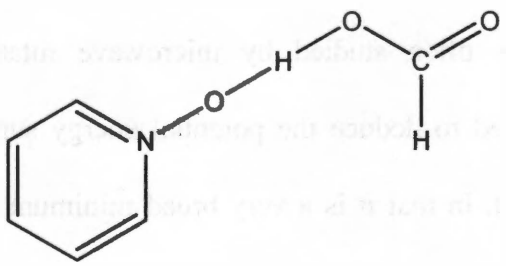


Figure 2.3. Example of an intermolecular hydrogen bond in an acid-base pair.

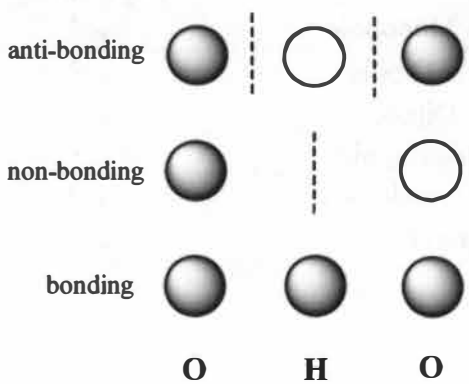


Figure 2.4. Molecular orbital diagram on the bonding in the 3c-4e hydrogen bond.

down the intermolecular interactions into multipole terms contributing to the energy of the bond. A list of the multipole interaction dependencies are given in Table 2.1.

Experimentally, the hydrogen bond may be studied by several different methods including a variety of diffraction techniques, vibrational spectroscopy for both solution and solid state,[75] gas phase rotational spectroscopy[76-78] and nuclear magnetic resonance spectroscopy (NMR).[79] In IR spectroscopy, hydrogen bonds are evidenced by the reduction in the X-H stretching frequency coupled with an increase in the band width and intensity as well as increasing the frequency of the X-H···Y bending vibration decreases, as compared to the non-hydrogen bonded system.[29,74,75] Evidence of the hydrogen bond in the gas phase is often studied by microwave rotational spectroscopy. These experiments were used to deduce the potential energy surfaces of a X-H···π hydrogen bond is relatively flat, in that it is a very broad minimum, and that for weak hydrogen

Table 2.1. 'Cut-off criteria' for hydrogen bonds.[6]

Interaction Type	r^{-x} *Energy Dependency*
Monopole – Monopole	r^{-1}
Monopole – Dipole	r^{-2}
Dipole – Dipole	r^{-3}
Dipole – Quadrupole	r^{-4}
Quadrupole - Quadrupole	r^{-5}
Dispersive	r^{-6}

bonds that exist in π systems, the donor is located at the center of the multiple bond, or the apparent center of the charge density, and not at an atom.[29] In both solid-state and solution NMR studies, when a hydrogen bond is present, there is chemical shift of the resonance.[74,80] As the strength of the hydrogen bond increases, the shielding decreases, resulting in an low field shift of the isotropic chemical shift.[81] In the solid-state, the presence of a hydrogen bond is evident by the broadening of the peak.[79]

2.1.1 Characterization of the nuclear and electronic structure of the hydrogen bond

Both X-ray and neutron diffraction techniques may be used to structurally characterize the hydrogen bond. However, the general distribution of scattering density differs between radiation sources, as is detailed in chapter 1. Neutron diffraction determines the distribution of nuclear density in the Bragg average, whereas X-ray diffraction reveals the distribution of electron density under the same prescription. In most structurally simple systems, defined here as 2-centered-2-electron bonded species (2c-2e), and therefore to understand the structure, there is a strong correlation between the nuclear density and the maxima in the electron density. It has been shown that the length of the hydrogen bond (X-H) as determined by neutron diffraction is slightly longer than in X-ray diffraction experiments. Motion of the H nucleus in an X-H hydrogen bond produces a foreshortening of the bond. This arises from the distribution of electron density relative to the instantaneous position of the nucleus. [82] It is common practice to normalize hydrogen bond lengths in X-ray diffraction experiments to the known neutron values, which is perhaps more accurate. However, these adjusted values are not necessarily more chemically meaningful.

2.1.2 Prior parameterization of the hydrogen bond

As was alluded to above, the hydrogen bond may be divided into three categories; very strong, strong and weak hydrogen bonds. However, to clarify the hydrogen bond, several methods of parameterization have been used. Figure 2.5 shows the relevant structural parameters used to describe the strength of a hydrogen bond. Early definitions were based on solely one geometric parameter, D, the distance between X and Y, due to the inaccurate location of the hydrogen atom in these bonds. With an increase in the accuracy of the location of the position of the hydrogen atom in the hydrogen bond, the strength of the bond is now often correlated with three geometric parameters d, θ and r. A summary of the classification of the strength of hydrogen bonds, as compared with van der Waals and dispersion forces, is represented in Table 2.2 given with examples.[31,33,41,83] A van der Waals interaction is said to be present when the distance from H to Y is less than the sum of the van der Waals radii.[29] This implies that strong and very strong hydrogen bonds contain van der Waals forces, though the distance in a weak hydrogen bond is on the same order as that in a van der Waals interaction. The difference between a van der Waals interaction and a weak hydrogen bond is that van der Waals interactions

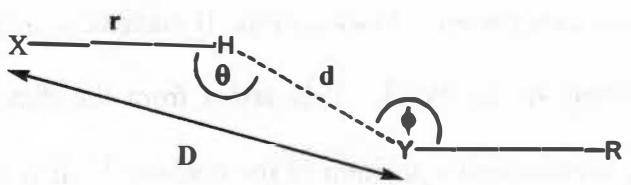


Figure 2.5. Geometric parameters used to define a hydrogen bond.[29]

Table 2.2. Classification of the strength of a hydrogen bond.[29]

	Very strong	*Strong*	*Weak*	*Van der Waals*
Bond energy /kJ mol^{-1}	62 – 167	16 – 62	< 16	~4-21
Relative IR shift	> 25 %	5 – 25 %	< 5 %	
D /Å	2.2 – 2.5	2.5 – 3.2	3.0 – 4.0	
d /Å	1.2 – 1.5	1.5 – 2.2	2.0 – 3.0	< Σ vdw radius H + vdw radius Y
θ /°	175 – 180	130 – 180	90 - 180	
Example[12,13,61]	FH...F$^-$ 163 kJ mol^{-1}	HOH…Cl$^-$ 56 kJ mol^{-1}	NH_3…benzene 9 kJ mol^{-1}	C-H…H-C ~4.18-20.9 kJ mol^{-1}

are isotropic in that the interaction energy is independent of the angle θ (Figure 2.5), whereas hydrogen bonds are directional.[84]

For many chemical systems, the determination of structure is based on the assumptions of the existence of atoms within the molecules; in this sense, a molecule may be defined as a bound ensemble of atoms and is therefore an extra hierarchical layer over and above the structure of the atom in the description of matter. Though this assumption is widespread in chemistry, a comprehensive definition of the atom within this hierarchical structure that is quantum mechanically satisfactory has only been derived in the last 25 years or so, predominantly due to the work of Bader.[23,37,85-88] More concisely,[89]

> *[t]he molecular structure hypothesis - that a molecule is a collection of atoms linked by a network of bonds - was forged in the crucible of nineteenth century experimental chemistry. It has continued to serve as the principal means of ordering and classifying the observations of chemistry.*

An issue arises when considering the structure of a crystalline material that derives from the bipartile nature of the atom itself: it is not possible, by a single experimental method to determine the structure of an atom or any ensemble of atoms. One may determine the electron density *or* the nuclear density, but not both, using the same radiation source. If the nuclear position of the atom and the electron density associated with the atom are very strongly correlated, then it is certainly reasonable to assert that the either the distribution of the nuclear positions or the distribution of total electron density are good measures of the position of any atom within the system. It is notable that for the

vast majority of atoms, the total electron density is dominated by the core electron density.

There are at least two areas where this last generality is not true in molecular systems: the electrides[90-92] and those systems that contain the hydrogen bond. In the latter case, the valence density of hydrogen is also the 'core' density and in the hydrogen bond, the delocalized nature of the electron density ensures that the normally strong correlation between the distribution of nuclear density and the distribution of electron density breaks down. Consequentially, the 'atomic' definition of a hydrogen bond is more problematic.

It is well accepted that the most common diffraction technique for the location of H atoms in a hydrogen bond is neutron diffraction. However, an important distinction must be made, in that a neutron diffraction experiment simply describes the nuclear density in the hydrogen bond and the distribution of electron density in a molecular system is only measurable by X-ray diffraction experiments. In many heavy atom systems, the nuclear and electron densities are strongly correlated; however, the density in a hydrogen bond is not correlated in the same manner.[25] The distribution of density in a 3-centered-4-electron bond such as the hydrogen bond, is often diffuse and anisotropic in nature; however, the nuclear density is generally not diffuse in a 3c-4e bond. Therefore, the only way to clearly demonstrate the distribution of electron density in a bond is through a series of extensive X-ray diffraction experiments.

This chapter includes extensive experimental and theoretical studies of two hydrogen bonded systems, which include urotropine-*N*-oxide·formic acid (**I**) and para-iodobenzoic acid (**II**). Direct imaging of the electron density associated with the short,

strong hydrogen bond is emphasized by the use of difference Fourier maps which are the results of X-ray diffraction experiments performed at variable temperature, exploring the possible methods of refinement of the electron density associated with the hydrogen bond which is a useful method that is complementary to other, more usual methods of refinement.[93] A neutron diffraction experiment is performed on urtropine-*N*-oxide·formic acid to ensure the exact location of the nuclear density associated with the hydrogen bond. By using both radiation sources, we thereby define all the scattering density in the Bragg average associated with the hydrogen bond. It is notable that the neutron diffraction data are not essential or even necessary in an *a priori* sense to define the electron density distribution in the hydrogen bond, but as we shall show, the inclusion of information about the distribution of nuclear density is instructive. The chemical ramification of the results in an 'atomistic', chemical sense is explored and shows that such a description of the hydrogen bond is not particularly illuminating. Both solution and solid state NMR data were obtained to further enhance the crystallographic results. In the case of para-iodobenzoic acid, thermodynamic data were collected to give insight into the phase transition centered about 230.77 K.

2.2 Structural studies of urotropine-N-oxide·formic acid (I)

Urotropine is a molecular system that has had an important role in crystallography, due in part to the similarity of this molecule to adamantane.[94-107] Whereas adamantane is of great interest as an archetype for plasticity, urotropine is brittle,[108] despite the apparent similarity between the molecular structures. Urotropine crystallizes in the cubic space group $I4_3/m$, with one nitrogen atom, one carbon atom and two hydrogen atoms in the

asymmetric unit, and is structurally related to adamantane. Due to the high tetrahedral symmetry of the molecule, there is only one set of unique bond lengths for urotropine and that bond length is C-N bond length is 1.4715(14) Å. The simplicity of the asymmetric unit and the lattice has ensured that urotropine has been investigated as a model for lattice dynamics,[102] molecular vibrations in the solid state[96,98,99,101,102,105,109] and for multipole refinements,[102,106,107] to name a few. Urotropine-*N*- oxide is a potentially polybasic, polar molecule, and its adducts are interesting systems for the investigation of hydrogen bonding. The molecule has two potential sites at which hydrogen bonding may occur; the tertiary nitrogen centers and the *N*-oxide O atom, offering the potential for the "engineering" of intermolecular interactions with appropriate adducts.

The molecular structure of urotropine-*N*-oxide, shown in Figure 2.6, has previously been investigated by single crystal X-ray diffraction.[110] It is notable that the N-O bond length is particularly short at 1.3951(12) Å, in comparison to the normal range for the N-O distance in hydroxylammonium cations which is 1.396 – 1.436 Å.[34,35,110] It is a neutral molecule, though there is a formal charge separation between the nitrogen and oxygen atoms. The structure of several adducts of urotropine-*N*-oxide have also been

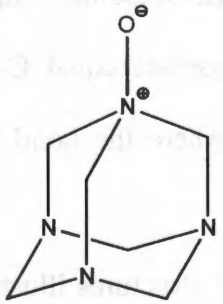


Figure 2.6. The molecular structure of urotropine-N-oxide.

reported;[111-115] where the first molecular and crystal structure determination of urotropine-*N*-oxide·formic acid was first determined by Mak in 1978, from data accumulated at room temperature.[114,115]

There is a potential coupling between the distribution of electron density associated with the hydrogen position and the structure of the formic acid residue in urotropine-*N*-oxide·formic acid wherein a valence bond, atomistic description, this correlation automatically is present. This possibility was alluded to by Mak in 1978 in an inverted manner, by asserting that, due to the asymmetry in the C-O and C=O bond lengths, there was no formal proton transfer, though the quality of data collected at that time precluded a detailed analysis of the structural behavior of the hydrogen atom. Correlation of the bond lengths in the formic acid residue to the structure of the electron density, and therefore the proton position, can occur in this material as full H atom transfer to the N-O bond should result in the formation of a delocalized formate ion. Retention of $O_{formate}$-H bond order should make the delocalization less likely in the formate ion. Possible equilibria of this type are shown in Figure 2.7.

Using a valence bond formalism, in principle, the *N*-oxide·formic acid adduct **1a** can equilibrate with **1b**, the hydroxylammonium – formate salt, where the formate ion is fully delocalized and therefore possesses equal C-O bond lengths or with **1c/d**, the hydroxylammonium formate salts where the bond lengths in the formate ion are not resonance delocalized.

It is notable that the resonance structures illustrated in Figure 2.7 as intermediates only have formal meaning within a valence bond description and that the description of many main group and organic molecules is inadequate when the description is based on a

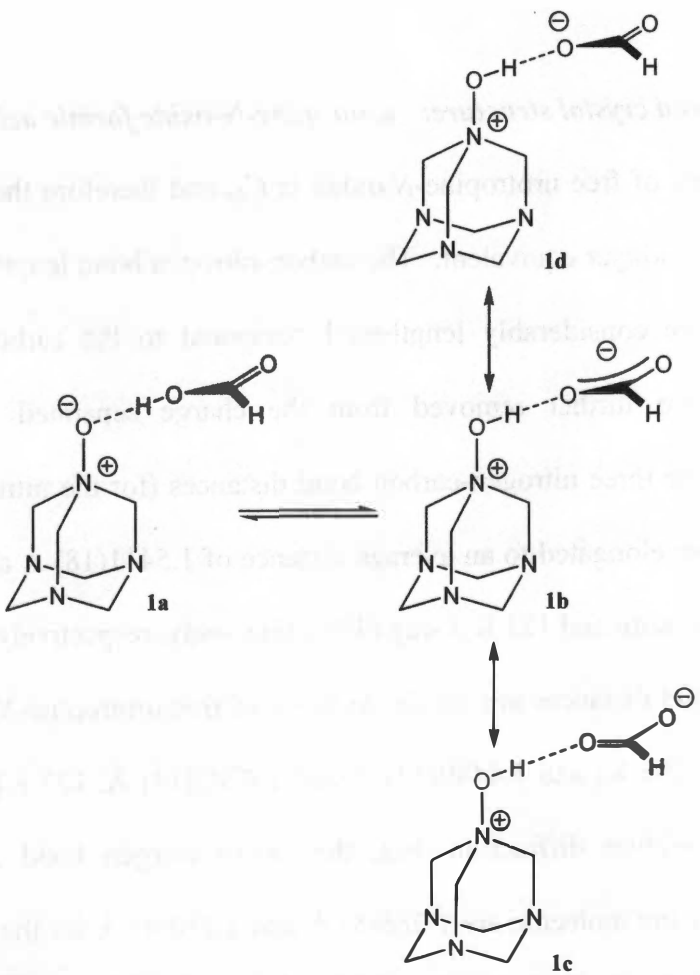


Figure 2.7. Potential equilibria involving both proton and electron redistribution in urotropine-N-oxide·formic acid.

hybridizational or valence bond approach.[116-123] Herein, the method of analysis used expressly employs a delocalized description of the electron density in order to shed light on the precise nature of the hydrogen bonding network in urotropine-*N*-oxide·formic acid.

2.2.1 Molecular and crystal structure: urotropine-N-oxide·formic acid

The symmetry of free urotropine-*N*-oxide is C_{3v} and therefore the carbon-nitrogen bond lengths are no longer equivalent. The carbon-nitrogen bond lengths adjacent to the *N*-oxide portion are considerably lengthened compared to the carbon-nitrogen bond distances which are further removed from the charge separated segment of the molecule.[34,35,114] The three nitrogen-carbon bond distances (for the nitrogen atom of the *N*-oxide portion) are elongated to an average distance of 1.5411(18) Å and 1.5249(13) Å for the room temperature and 123 K X-ray diffraction study, respectively. The remaining nitrogen-carbon bond distances are similar to those of free urotropine-*N*-oxide [1.441(2) Å and 1.473(2) Å, 298 K; and 1.4480(14) Å and 1.4783(14) Å, 123 K].[110,114] Based on the experimental neutron diffraction data, the carbon-oxygen bond distances in the formate segment of the molecule are 1.286(5) Å and 1.230(4) Å for the C7-O2 and C7-O3 bonds, respectively, and these distances are compiled in Table 2.3. These distances coincide with the results extracted from the X-ray diffraction experiment at 123K, 1.2862(14) Å and 1.2228(13) Å, respectively. The C-N bond distances in the cage correspond well with the distances obtained in the X-ray diffraction experiment, differing by less than one thousandth of an angstrom.

Table 2.3. Intermolecular structural parameters at variable temperature from the spherical atom refinement. Neutron data is represented by an (N) and X-ray data by an (X) for urotropine-N-oxide·formic acid.

T / K	$r_{N_1O_1}$ / Å	$r_{O_1H_1}$ / Å	$r_{O_2H_1}$ / Å	$r_{O_1O_2}$ / Å	$r_{O_2C_7}$ / Å	$r_{O_3C_7}$ / Å	$\angle_{O_1H_1O_2}$ / o	$\angle_{O_2C_7O_3}$ / o	
123	1.3727(33)	1.221(7)	1.211(7)	2.428(6)	1.286(5)	1.230(4)	173.3(6)	126.28(34)	*(N)*
123	1.3984(11)	1.24(4)	1.19(7)	2.435(1)	1.2862(14)	1.2228(13)	173.1(5)	125.17(10)	*(X)*
148	1.3956(11)	1.25(3)	1.21(3)	2.443(1)	1.2818(15)	1.2252(15)	170.0(6)	125.62(11)	*(X)*
173	1.3949(12)	1.24(2)	1.21(2)	2.439(1)	1.2778(15)	1.2206(15)	172.3(6)	125.55(12)	*(X)*
198	1.3951(11)	1.24(6)	1.20(6)	2.438(1)	1.2786(15)	1.2234(15)	174.0(6)	125.89(12)	*(X)*
223	1.3979(12)	1.22(6)	1.24(6)	2.450(1)	1.2757(16)	1.2258(15)	174.2 (6)	126.05(12)	*(X)*
248	1.3933(13)	1.26(3)	1.18(6)	2.430(1)	1.2680(18)	1.2147(18)	172.7(6)	126.00(15)	*(X)*
298	1.3940(14)	1.27(6)	1.18(3)	2.430(1)	1.263(2)	1.2107(19)	171.4(1)	126.47(16)	*(X)*
298	1.388(6)			2.435(4)	1.281(6)	1.200(6)		126.1(5)	[93]

The overall molecular structure, determined by spherical atom refinements of the X-ray data collected at seven temperatures, ranging from 123 K to room temperature, is unsurprising and the non-hydrogenous structure remains relatively invariant with temperature. Relevant structural parameters are given in Table 2.3. A representative structure of the asymmetric unit is shown in Figure 2.8(a)[124] with the corresponding packing diagram in Figure 2.8(b). The latter shows the orientation of the four molecules that are contained in the unit cell. It is notable that the packing segregates the more polar parts and less polar parts of the complex; the polar portions, consisting of the *N*-oxide and the hydrogen bound formic acid are mutually *anti* to each other across the sheet composed of less polar cages.

2.2.2 Hydrogen bond structure: urotropine-N-oxide·formic acid

Urotropine-*N*-oxide has four potential sites at which hydrogen bonding may occur: there is one electronegative oxygen atom and three tertiary amines which may act

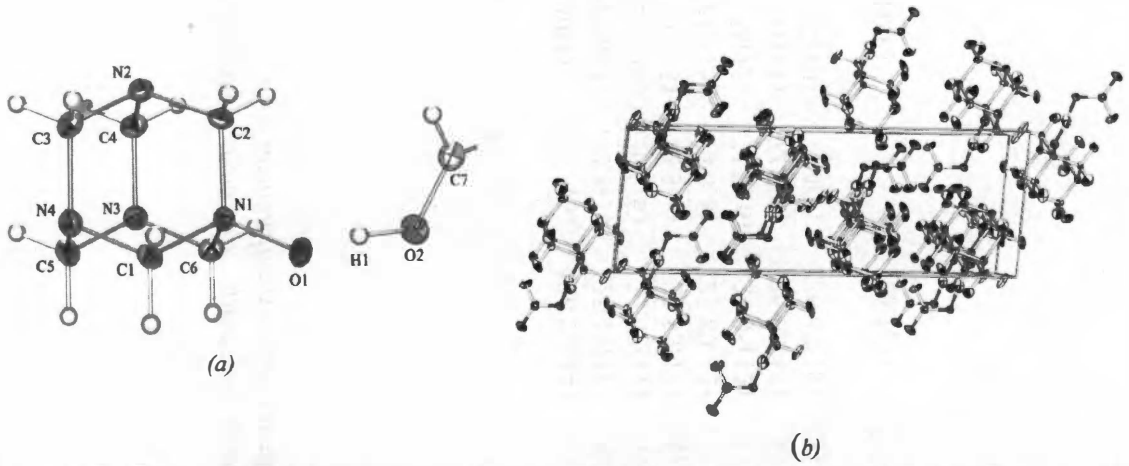


Figure 2.8. The molecular structure of urotropine-N-oxide·formic acid at 123K (a) and a packing diagram (b).[130]

as potential strong hydrogen bond acceptors. Examination of extended contacts in the unit cell using Mercury[35,125] revealed that the only substantial interaction was the short, strong hydrogen bond present between the urotropine-*N*-oxide and the formate residue.

The observed hydrogen bond in this case is to the *N*-oxide O atom, with a short oxygen- oxygen distance ranging from 2.4300(10) Å to 2.4469(10) Å based on the X-ray data and 2.428(7) Å in the neutron data at 123 K. This lies well within the standard definition a short very strong hydrogen bond,[29] which is defined as a hydrogen bond where the O…O lies in the range 2.2 – 2.5 Å.

In addition to the "very strong" hydrogen bond between the oxygen atom of the *N*-oxide, O1, and the oxygen atom, O2, of the formate segment, there are three other hydrogen bonds present in this system. Each of the three tertiary amines form hydrogen bonds to an adjacent molecules, which may be classified as a "weak" hydrogen bond,[29] with N…H bond distances ranging from 2.68 Å to 2.89 Å[35,125] However, it is notable that the van der Waals sum for N…H is 2.75 Å[126] and it may therefore be more appropriate to classify the N…H interaction as a hydrogen bridge.[29,56,84]

2.2.3 Nuclear structure of the hydrogen bond: urotropine-N-oxide·formic acid

The results of the neutron diffraction experiment at 123 K reveals the nuclear position of the H atom associated with the hydrogen bond. The proton is located at a distance of 1.221(7) Å from the oxygen atom of the *N*-oxide segment of the molecule and 1.211(7) Å from O2 of the formate segment, with an O1-H1-O2 angle of 173.3(6)°. Therefore, with in the errors associated with the experiment, this results in a short symmetric hydrogen bond.

2.2.4 Discussion: urotropine-N-oxide·formic acid

It has recently been shown that direct imaging of hydrogen density from X-ray diffraction experiments can be more reliable than parameters determined from refinements;[63,73] this is particularly true in the case of elongated or highly anisotropic electron density is observed in this system. In this case, X-ray data are not sufficiently robust to allow fully anisotropic H atom refinements. However, our multiple-temperature study, and the apparent invariance of the shape and position of the difference Fourier peak representing the electron density associated with H1, allows the conclusion that in this system the hydrogen atom strongly perturbed towards a position close to the centre of the O…O vector and its position appears invariant (within the accuracy of the X-ray data) as a function of temperature. This is a significant observation, particularly in light of several recent reports of migration of the H atom in such cases;[63,67,68,72,73] the nature of the hydrogen bond in urotropine-*N*-oxide·formic acid is robust towards such effects.

The distribution of electron density in the Fourier difference maps[127] in Figure 2.9 (calculated in the absence of H1 from the model) in the region of the short, strong hydrogen bond shows elongation of the density along the O1 – O2 vector, commonly observed in short, strong hydrogen bonds. As seen in the Fourier maps, the maximum in the electron density associated with the hydrogen bond is located approximately 1.16 Å from the formate segment of the molecule, representing a significant elongation of the O-H "covalent" bond, where the electron density is distributed between O and H over a length of ~ 1 Å. This is indicative of a centered proton which is frequently observed in short hydrogen bonded systems. However, this distribution is broad and full

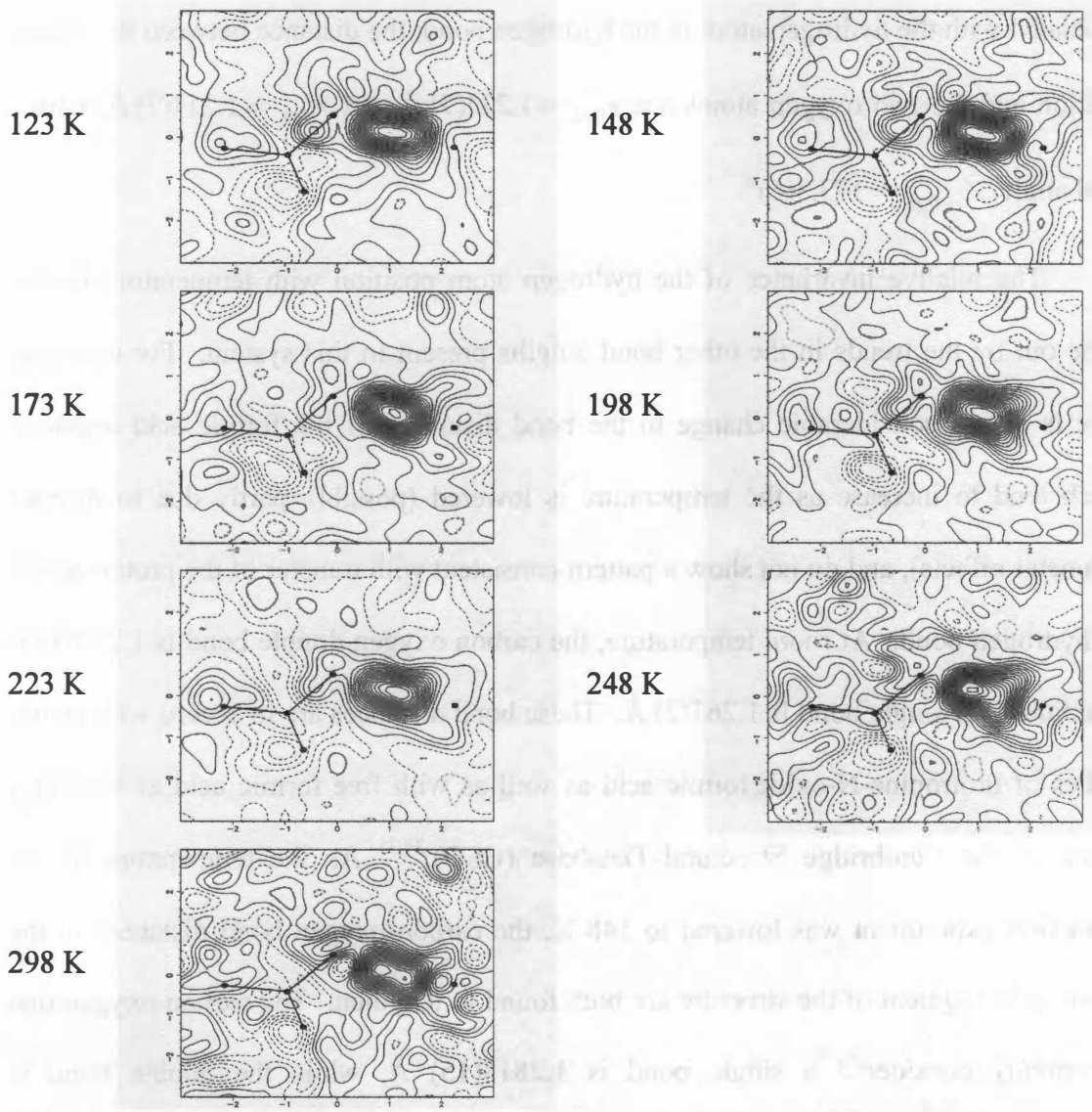


Figure 2.9. Fourier difference maps showing the electron density associated with the proton position of the formic acid OH in urotropine-N-oxide·formic acid.[94] *Contour levels are drawn at 0.03 eÅ*$^{-3}$.

quantification of the O-H distances in this system is complicated by the uncertainty introduced by the nature of the density representing this hydrogen atom.

Analysis of the neutron diffraction data at 123 K clarifies the position of proton associated with the hydrogen atom in the hydrogen bond; the distance between the proton position and the two oxygen atoms are $r_{H_1O_1} = 1.221(7)$ Å and $r_{H_1O_2} = 1.211(7)$ Å, with a bond angle $\angle_{O_1\hat{H}_1O_2} = 173.3(6)°$.

The relative invariance of the hydrogen atom position with temperature is also borne out by the trends in the other bond lengths present in this system. For example, there is also a considerable change in the bond distances of the formic acid segment, which tend to increase as the temperature is lowered (possibly partly due to thermal parameter effects), and do not show a pattern consistent with transfer of the proton across the hydrogen bond. At room temperature, the carbon oxygen double bond is 1.2107(19) Å and the C-O single bond is 1.263(2) Å. These bond distances are in accord with earlier studies of urotropine-N-oxide·formic acid as well as with free formic acid as seen in a search of the Cambridge Structural Database (CSD).[34,35] As the temperature of the diffraction experiment was lowered to 148 K, the carbon-oxygen bond distances in the formic acid segment of the structure are both found to lengthen. The carbon-oxygen that is formally considered a single bond is 1.2818(15) Å, while the double bond is 1.2252(15) Å. A comparison of the bond lengths in the formate segment of the molecule are shown in Figure 2.10. These distances are closely related to a formic acid fragment which is hydrogen bound to another species.[34,35]

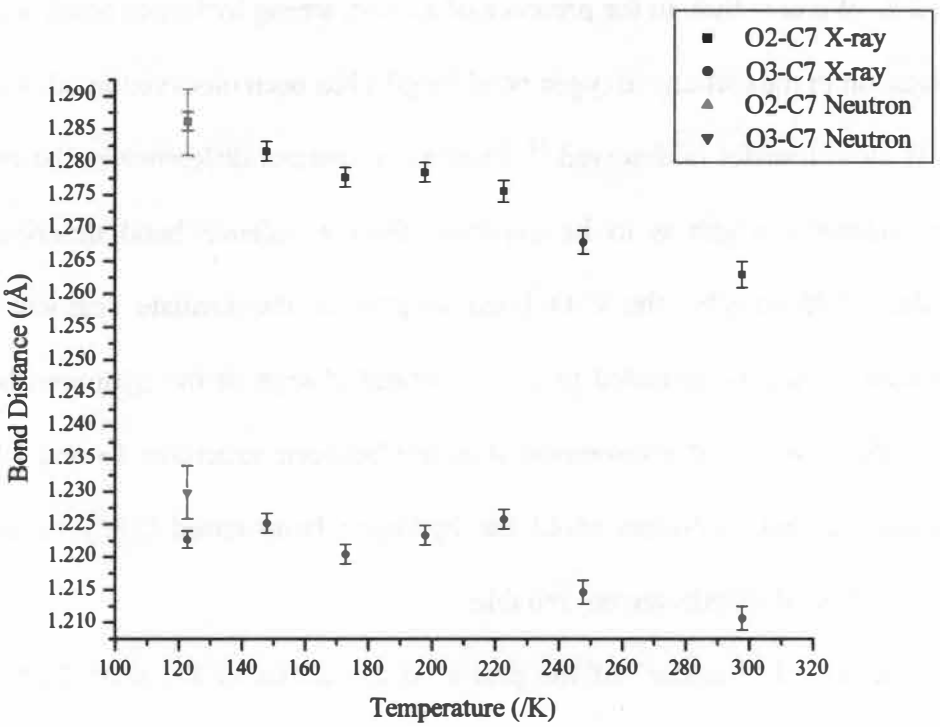


Figure 2.10. Comparison of the variation of the C-O and C=O bond lengths of the formate segment by neutron diffraction and variable temperature X-ray diffraction experiments for urotropine-N-oxide·formic acid.

At 123 K, the heavy atom positions and the bond lengths derived from the data show a strong correlation between the X-ray and neutron data, though there is not a strong correlation for the H atom. Given the experimental data, it may be assumed that the correlation of the heavy atom holds true at all temperatures. The carbon – oxygen bonds in the formate segment do not show any evidence of structures **1b** or **1c** shown in Figure 2.7. We note that, in the presence of a short, strong hydrogen bond, a similar lack of correlation in the carbon – oxygen bond lengths has been observed in other compounds where H atom transfer is observed.[24] There is no distinct difference in the two carbon–oxygen distances which is to be expected from a valence bond description of the molecule. Additionally, the C-O bond lengths in the formate segment vary with temperature, which is unrelated to any structural change in the hydrogen bond. This indicates the presence of a resonance structure between structures **1a** and **1d** in Figure 2.7, indicating that assertions about the hydrogen bond based solely on heavy atom positions and bond lengths are not reliable.

The partial "transfer" of the proton to the center of the short hydrogen bond, indicated by the difference Fourier maps, is supported by analysis of the N-O bond distance in the system. This is considerably longer than in free urotropine-*N*-oxide (1.363 Å) and slightly longer than previously known urotropine-*N*-oxide hydrogen-bonded systems (1.380-1.391 Å) as seen in a search of the CSD.[34,35] The formation of a significant bonding interaction with the partly transferred proton withdraws electron density from the N-O bond, weakening the strength of the bond and therefore increasing the bond length. The average bond distance for the N-O bond in hydroxylammonium cations, as seen in a search of the Cambridge Structural Database, is 1.417(2) Å, with a

range from 1.396-1.436 Å.[34,35] This bond length corresponds more directly to urotropine-*N*-oxide·formic acid than does the average bond length for a typical *N*-oxide system. Once again the relative invariance of this N-O distance with temperature supports the stability of the "partly-transferred" proton in this hydrogen bonding system.

For a comparative study of the bond lengths in the formic acid segment of the structure, single crystal X-ray diffraction data were collected for rubidium hydrogen formate at 173K using the data collection strategy as described in section 7.2. There is a considerable amount of hydrogen bonding present in the solid-state structure of this material where the hydrogen bonds exist between two formic acid segments, with an oxygen-oxygen distance of 2.4360(13) Å. In the crystal structure, rubidium atom is eight coordinate, with bond distances to the oxygen atoms of the formate ranging from 2.8853(13) Å to 3.1556(12) Å. The bond distances for the C-O single and double bonds were found to be 1.272(2) Å and 1.2269(19) Å, respectively. These distances are similar with those found at the same temperature in urotropine-*N*-oxide·formic acid which are 1.2778(15) Å and 1.2206(15) Å. As expected, the O-C-O angle in rubidium formate, 125.06(15)°, is only slightly smaller than that in urotropine-*N*-oxide·formic acid [125.55(12)°]. The lengthening of these bond distances is indicative of a stronger hydrogen bond present between formic acid and urotropine-*N*-oxide as is the migration of the electron density associated with the proton position as the temperature is lowered.

An anisotropic displacement parameter (ADP) may be defined as '*the second moment of atomic probability distribution function*'.[128] This essentially describes the average displacement of atoms in crystals from the mean atomic positions in the Bragg average. Figure 2.11 depicts the variation in U_{aniso} with temperature for the X-ray data as well as a

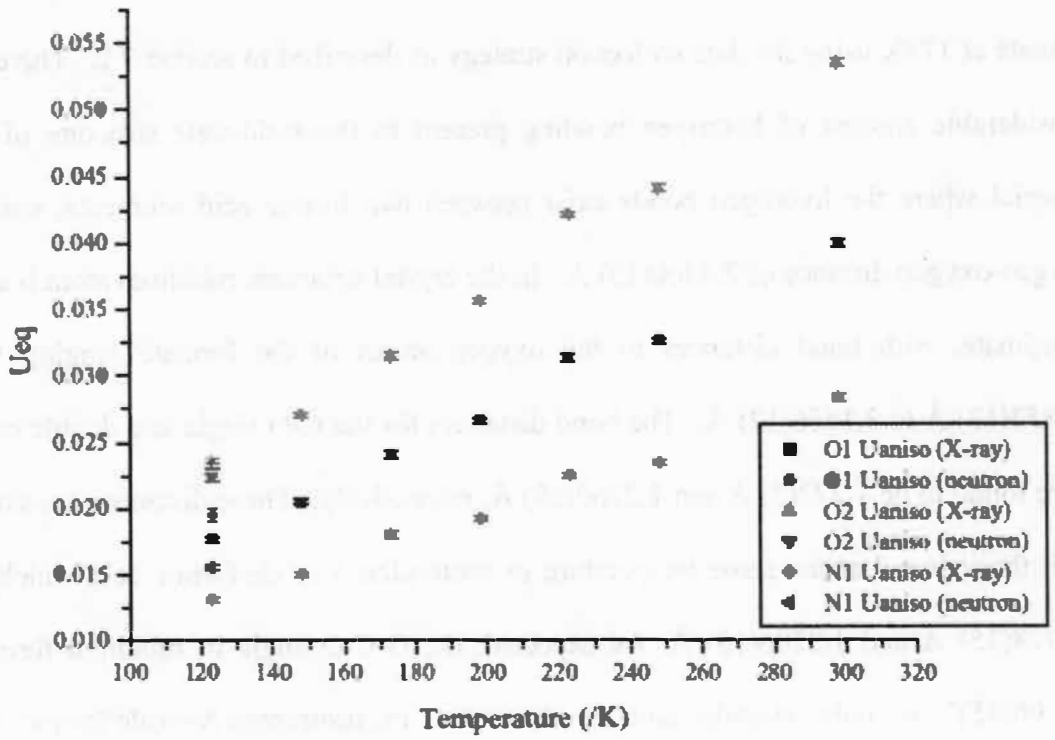


Figure 2.11. Comparison of the results from neutron (U_{aniso}) and X-ray (U_{iso}) data for the hydrogen bound H atom, H1, in urotropine-N-oxide·formic acid.

comparison of the neutron data, for the atoms which are most effected by the presence of the hydrogen bond, namely N1, O1 and O2. Upon comparison of the neutron and X-ray data collected at 123K, it is notable that there is very little difference in U_{aniso} for any of these atoms, the difference being approximately 0.001 $Å^2$. The major difference in the thermal parameters between the neutron and X-ray data is best shown in Figure 2.12 which represents H1, the hydrogen bonded H atom. Table 2.4 shows the anisotropic thermal parameter tensor components, U_{ij}^{X} and U_{ij}^{N} of H1 extracted from the refinement of the X-ray and neutron data, respectively, and it shows the difference in ADP's between the two sets of experiments. For a hydrogen atom, the valence electron density is also the core electron density, leading to the diminished correlation between the distribution of nuclear and electron density. From Figures 2.11 and 2.12 it is clear that the description of isotropic displacement parameters for the hydrogen atom from X-ray data is inadequate. Though results from the X-ray and neutron diffraction experiments showed very similar positional parameters for H1 in that position of maximum electron density from the X-ray data corresponds well to the position of the proton in the neutron data, the ADP's clearly differ. In the refinement of neutron diffraction data, the ADP's of the proton position associated with the hydrogen bond are consistent with the average displacement over the thermally populated normal coordinates and lattice modes, and in this respect the ADP's of the proton are not anomalous when compared to the other atomic ADP's in the crystal. Therefore, given the broad distribution of electron density associated with the hydrogen bond, the use of ADP's to refine the structural parameters of the electron density associated with the hydrogen bond is clearly not in accord with the

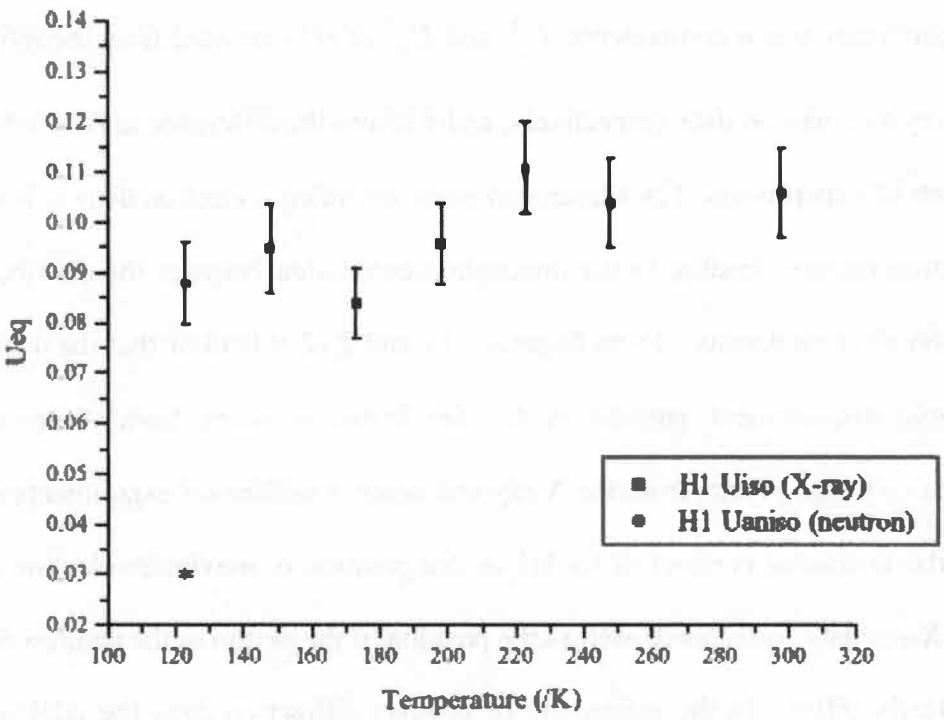


Figure 2.12. Comparison of the results from neutron (U_{aniso}) and X-ray (U_{iso}) data for the hydrogen bound H atom, H1, in urotropine-N-oxide·formic acid.

Table 2.4. Anisotropic displacement parameter tensors for H1 from neutron and X-ray diffraction data for urotropine-N-oxide·formic acid. [108] *The average U_{ansio} for the H atoms in the urotropine cage is 0.03404 Å^2 (neutron data) for urotrôpine-N-oxide·formic acid.*

U_{11}	U_{12}	U_{13}	U_{22}	U_{23}	U_{33}	U_{aniso}	
0.043(4)	0.0035(24)	0.0048(29)	0.0201(29)	0.0013(25)	0.028(4)	0.03032	*H1 Neutron*
0.151(22)	0.031(13)	0.051(14)	0.038(11)	0.018(8)	0.047(13)	0.08263	*H1 X-ray*

definition of the ADP. The neutron diffraction refinement of the O-H-O positions and ADP's effectively define the nuclear potential in which the four electrons associated with the hydrogen bond are confined. From inspection of the ADP's associated with the nuclear potential, it is clear that the motion of the atoms are smaller in magnitude than have been interpreted from the refined ADP's for the "H atom" associated with the hydrogen bond. It is therefore clear parameterization of structural parameters of the distribution of electron density using ADP's is not physically realistic within the structural definition of the ADP. Moreover, it is clear that a standard "spherical atom and ADP" model is inadequate to describe this distribution. However, we note that the Bragg scattering experiment is *a priori* an elastic experiment and contains no dynamical information about the system.

Given the physical ambiguity implied in using ADP's to define the structure of the distribution of electron density in a system in which there is a poor correlation between the nuclear and core electron density distributions, it is clear that direct imaging of electron density *via* a Fourier synthesis gives good qualitative information in this case.

The results of spherical atom refinements using anisotropic atomic displacement parameters to model the distribution of electron density in the bond are shown in Figure 2.13(a), together with an isotropic refinement of the electron density (Figure 2.13(b)) and the result of the neutron diffraction experiment (Figure 2.13(c)). Though the use of an anisotropic thermal parameter for a hydrogen atom from X-ray diffraction experiments is not a realistic model for the distribution of the electron density, it demonstrates the inherent lack of correlation between the nuclear position of an H atom and the electron density distribution in a hydrogen bond.

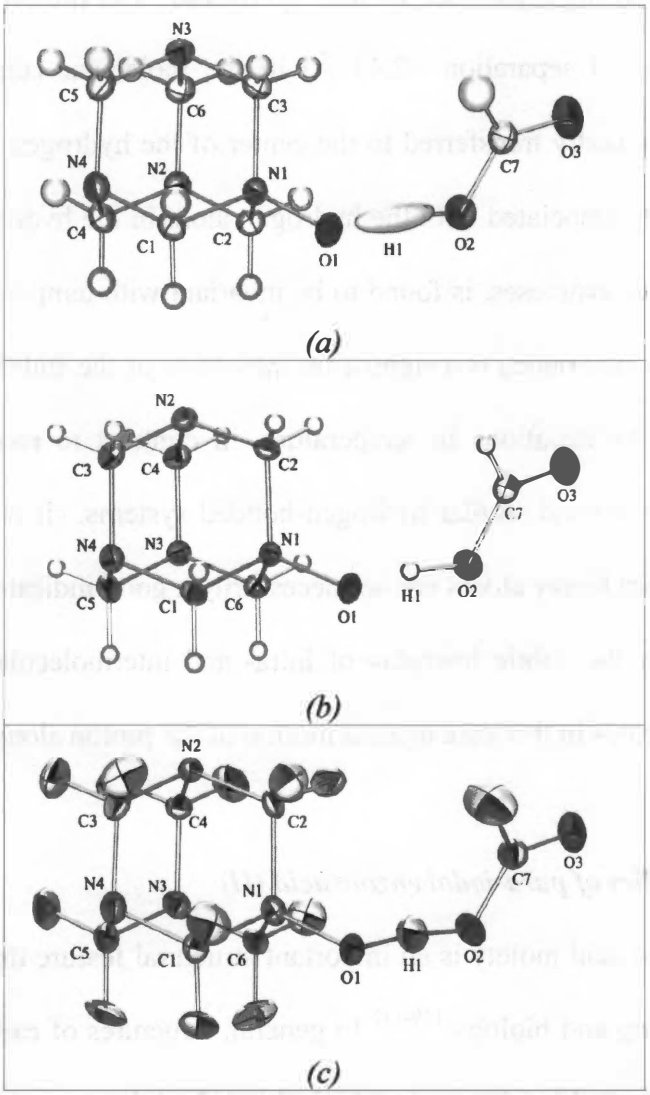


Figure 2.13. Comparison of X-ray and neutron data of urotropine-N-oxide·formic acid at 123K:7(a) X-ray data with anisotropic refinement of H1 using GSAS,[107] 7(b) X-ray data with isotropic refinement from Shelxtl,[71] (c) Neutron data with anisotropic refinement of all H atoms from GSAS.

2.2.5 Conclusions: urotropine-N-oxide·formic acid

The electron density associated with a short, strong hydrogen bond may be accurately modeled using difference Fourier syntheses. The proton in the short, strong hydrogen bond (O...O separation ~2.44 Å) in the molecular complex urotropine-*N*-oxide·formic acid is partly transferred to the center of the hydrogen bond. The position of maximum density associated with the hydrogen atom in the hydrogen bond, indicated by difference Fourier syntheses, is found to be invariant with temperature in the range of 123 to 298 K. This invariance is a significant indication of the stability of this hydrogen bond with respect to variations in temperature, in contrast to recent observations of proton migration in several similar hydrogen-bonded systems. It is clear that trends in bond lengths between heavy atoms are not necessarily a good indicator of hydrogen atom behavior, but rather the subtle interplay of intra- and intermolecular forces and lattice effects clearly mitigates in this case against motion of the proton along the bond.

2.3 Structural studies of para-iodobenzoic acid (II)

The carboxylic acid moiety is an important structural feature that occurs frequently in crystal engineering and biology.[129-132] In general, structures of carboxylic acids in the solid state are dominated by dimers in which the carbonyl oxygen and hydroxyl groups act as donors and acceptors, respectively.[130-134] The structure of a hydrogen bonded dimer is shown in Figure 2.14.

As also shown in Figure 2.14, the full, real space hydrogen bond scheme is often developed *via* a crystallographic center of inversion.[133,135-146] However, the presence of a carboxylic acid group does not always imply the presence of a dimeric structure[147] and

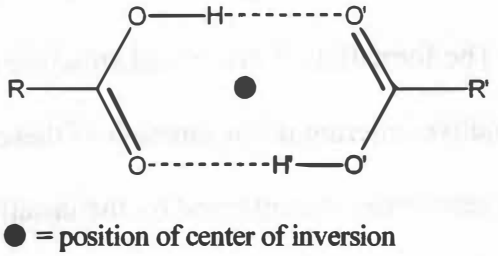


Figure 2.14. A schematic representation of a typical carboxylic acid dimer with the crystallographically generated atoms as X'.

two-dimensional networks and chains have also been observed in carboxylic acid containing systems. In systems where the dimeric structure is observed, the degenerate nature of the atoms involved in the hydrogen-bonded carboxylic acid dimer has attracted the interest of the theoretical community as a model for proton transfer.[66,131,148-156]

The 4-halo benzoic acids crystallize isostructurally in the monoclinic space group $P2_1/n$[157-160,134,161,162] and are dimeric in the solid state, a phenomenon that is also persistent in solution.[163] The structure of 4-iodobenzoic acid determined by powder diffraction was first reported in 1982,[161] and a subsequent single crystal diffraction experiment confirmed the molecular structure and lattice.[159] Here the structure of 4-iodobenzoic acid is investigated in order to characterize the intermolecular hydrogen bond and to investigate the other forces that determine the structure of this material, employing a series of X-ray diffraction measurements, solid state NMR and differential scanning calorimetry in addition to spherical atom refinements of the diffraction data.

4-iodobenzoic acid is of interest as the molecular structure indicates the presence of several identifiable forces existing in the lattice; the most obvious of these is the

hydrogen bonding interaction, but 'π-stacking', van der Waals, dispersion and multipole forces may all play a role. The formation of the crystal structure is dependent on several of these factors, and a qualitative ordering of the strength of these interactions is offered; moreover, the presence of these forces is confirmed by the unsatisfactory spherical atom refinement of the diffraction data at any temperature. Given the interest in the structural chemistry of the hydrogen atom, interests in the arrangement of the hydrogen atom positions in the presence of a range of other possible interactions are explored.

2.3.1 Temperature variation and structure of the lattice: para-iodobenzoic acid

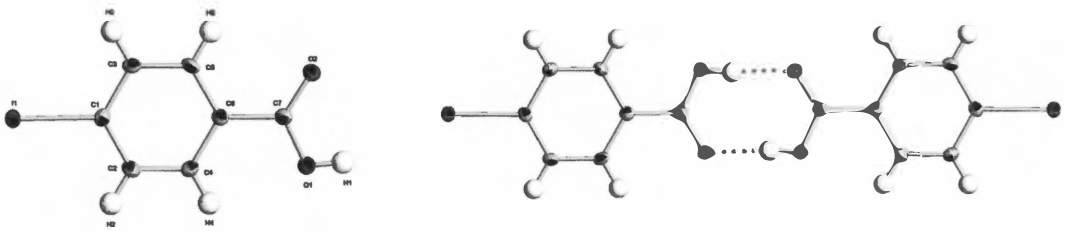
Diffraction data were collected at temperatures of 103, 123, 148, 173, 198, 248 and 298 K. from crystals of 4-iodobenzoic acid grown from slow evaporation of an acetone solution. Initial spherical atom refinements were unsurprising and confirmed the previously determined space group of $P2_1/n$ and the room temperature lattice parameters were found to be similar to the previously reported values.[159,161] The two sets of previously determined lattice constants are compiled in Table 2.5, together with the same constants determined in these experiments.

2.3.2 Molecular structure from spherical atom refinements: para-iodobenzoic acid

The gross molecular structure, determined from spherical atom refinements, is unsurprising with the non-hydrogenous structure remaining relatively invariant with temperature. A representative structure of the asymmetric unit is shown in Figure 2.15(a) together with the structure of the dimer evolved through the center of inversion. Figure 2.16 shows the unit cell for the lowest experimental temperature and Figure 2.17 shows

Table 2.5. Lattice parameters (reduced unit cell) for the collected data at variable temperature for para-iodobenzoic acid.

a / Å	b / Å	c / Å	β / °	T / K	reference
4.160	6.040	30.108	90.48	298	161
4.156	6.030	30.109	90.52	298	159
4.0567(12)	5.9409(17)	30.223(9)	91.019(4)	103	this work
4.0688(10)	5.9466(15)	30.253(8)	90.982(4)	123	this work
4.0778(11)	5.9724(17)	30.243(8)	90.893(4)	148	this work
4.0960(13)	5.9745(19)	30.157(10)	90.852(5)	173	this work
4.1049(6)	5.9933(9)	30.179(5)	90.878(2)	198	this work
4.1305(5)	6.0075(7)	30.143(3)	90.731(2)	248	this work
4.1527(19)	6.009(3)	30.037(3	90.623(7)	298	this work



(a) *(b)*

Figure 2.15. (a) The molecular structure of para-iodobenzoic acid, corresponding to the asymmetric unit in the crystal, together with (b) the structure of the dimer at 103 K.

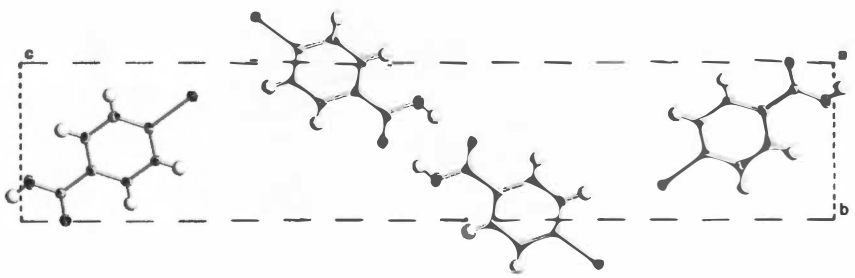


Figure 2.16. Packing diagram of para-iodobenzoic acid at 103K showing the orientation of the dimeric unit within the unit cell.

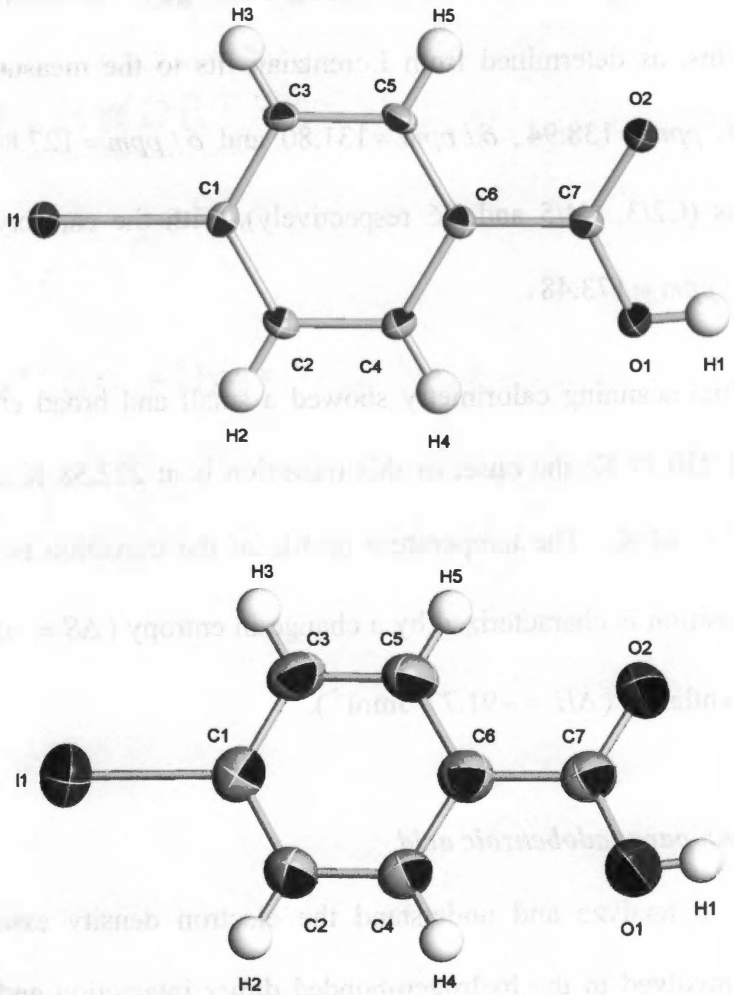


Figure 2.17. Representation of the asymmetric unit of para-iodobenzoic acid at 103K (top) and 298K (bottom).

the asymmetric unit at the highest and lowest temperatures of measurement. Salient bond molecular structural parameters are given in Table 2.6.

Solid state NMR spectra were consistent with the asymmetric unit, and are shown in Figure 2.18. These spectra also showed a slight change in the relaxation time for the ring carbon atoms, as determined from Lorentzian fits to the measured spectra. The resonances at $\delta / ppm = 138.94$, $\delta / ppm = 131.80$ and $\delta / ppm = 127.86$ are assigned to the ring carbons (C2/3, C4/5 and C6 respectively), with the carboxylate carbon, C7, resonating at $\delta / ppm = 173.48$.

Differential scanning calorimetry showed a small and broad endothermic event centered around 230.77 K; the onset of this transition is at 222.58 K and the transition incomplete by 233.44 K. The temperature profile of the transition is shown in Figure 2.19 and the transition is characterized by a change in entropy ($\Delta S = -0.393\ JK^{-1}mol^{-1}$) and a change in enthalpy ($\Delta H = -91.77\ Jmol^{-1}$).

2.3.3 Discussion: para-iodobenzoic acid

In order to analyze and understand the electron density associated with the hydrogen atom involved in the hydrogen-bonded dimer interaction and its temperature dependence, diffraction data collected at a variety of temperatures revealed the expected intramolecular structure which was not substantially changed. However, repeated attempts at structure solution from the 223K data set were unsuccessful. Data were re-collected at 223K several times, each time the reflections could not be indexed. When the data was indexed using a known unit cell from the 198 K data collection, the

Table 2.6. Selected intramolecular structural parameters at variable temperature for para-iodobenzoic acid.

T / K	r_{IC_1} / Å	$r_{C_1C_2}$ / Å	$r_{C_1C_3}$ / Å	$r_{C_2C_4}$ / Å	$r_{C_3C_5}$ / Å	$r_{C_4C_6}$ / Å	$r_{C_5C_6}$ / Å	$r_{C_6C_7}$ / Å
103	2.096(5)	1.389(7)	1.390(7)	1.378(7)	1.380(7)	1.396(7)	1.394(7)	1.485(7)
123	2.097(10)	1.390(14)	1.385(14)	1.376(15)	1.381(14)	1.399(14)	1.389(14)	1.487(14)
148	2.100(11)	1.385(14)	1.390(15)	1.379(16)	1.382(15)	1.404(15)	1.386(14)	1.488(15)
173	2.101(6)	1.373(9)	1.386(9)	1.381(10)	1.383(9)	1.395(9)	1.390(9)	1.487(9)
198	2.105(9)	1.375(12)	1.382(13)	1.388(13)	1.381(12)	1.395(13)	1.389(12)	1.485(13)
248	2.101(6)	1.370(9)	1.386(9)	1.382(9)	1.377(9)	1.391(9)	1.396(9)	1.487(9)
298	2.095(7)	1.363(10)	1.369(11)	1.381(11)	1.379(11)	1.380(11)	1.388(10)	1.486(11)

T / K	$r_{O_1C_7}$ / Å	$r_{O_2C_7}$ / Å	ϑ / O	ϕ / O	ω / O
103	1.300(7)	1.233(7)	123.0(5)	120.2(4)	120.0(5)
123	1.295(13)	1.240(13)	123.2(10)	120.5(9)	120.3(7)
148	1.284(13)	1.248(13)	122.7(10)	121.2(10)	119.9(8)
173	1.281(8)	1.242(8)	122.9(7)	120.4(6)	119.9(5)
198	1.282(11)	1.241(11)	122.9(9)	120.6(8)	119.9(6)
248	1.277(8)	1.241(8)	122.8(6)	120.6(6)	119.6(4)
298	1.268(10)	1.234(10)	122.6(8)	120.4(7)	119.9(5)

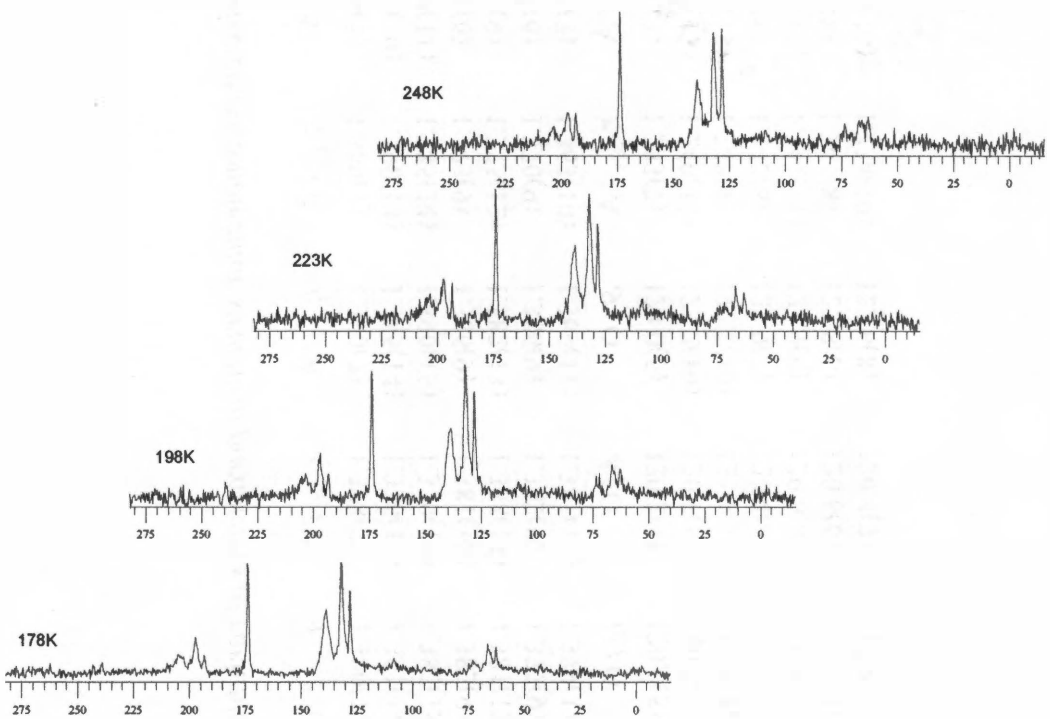


Figure 2.18. ^{13}C *CPMAS SSNMR variable temperature spectra for para-iodobenzoic acid.*

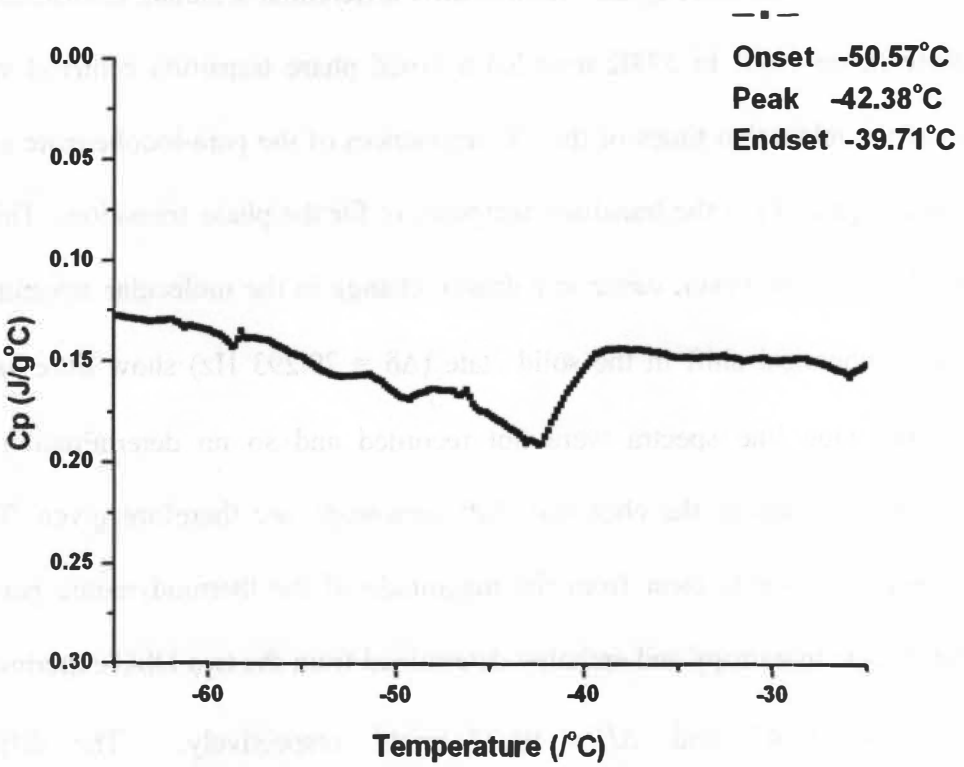


Figure 2.19. DSC data for para-iodobenzoic acid, with the temperature transition centered around 230-233K.

agreement in the reflections was poor. Of 800 reflections analyzed using Smart,[164] all 800 were indexed in *h* and *k*, but only 205 were indexed in *l*. The final structural solution from this attempt led to unreliable results with R-factors of greater than 35 % when using the atomic positions and thermal parameters from the 198 K data set. The putative molecular structure from this attempted refinement was unphysical with respect to geometry, bond lengths and angles. Additionally, differential scanning calorimetry in the temperature range 153K to 373K revealed a broad phase transition centered at 230K. Analysis of the relaxation times of the ^{13}C resonances of the para-iodobenzoic acid also showed a change in T_2 at the transition temperature for the phase transition. This phase transition does not, however, cause any drastic change in the molecular structure. The ^{13}C isotropic chemical shift in the solid state ($\Delta\delta$ = 29.293 Hz) show little variation, though static wide line spectra were not recorded and so no determination of the individual components of the chemical shift anisotropy are therefore given. That the phase change is minor is clear from the magnitude of the thermodynamic parameters where the change in entropy and enthalpy determined from the two DSC experiments are $\Delta S = -0.393$ $JK^{-1}mol^{-1}$ and $\Delta H = -91.77$ $Jmol^{-1}$ respectively. The differences observed in the two sets of data are due to the residual solvent present in the first run which was subsequently evaporated upon heating of the sample.

As is common in many carboxylic acids, the dimeric unit present in 4-iodobenzoic acid is generated by the presence of a center of inversion and this center of inversion lies in the plane of the carboxylate group. Figure 2.17 shows the two asymmetric units for the low and high temperature phases. Unsurprisingly, these dimeric units persist at all temperatures of measurement, with the only observable structural

difference between them being the hydrogen positions, *vide infra.* As such, the description of the crystal is best discussed using the dimer as the basic chemical unit present.

This dimeric unit is stacked in single stacks and a series of packing diagrams are presented in Figure 2.20 showing the arrangement of these dimers. Interestingly, the dimeric units are arranged in the maximum energy configuration with respect to the dipole moment present on each acid moiety, though the net dipole moment of the dimer is zero.

These one-dimensional lamellæ are bound through interactions between the iodine atoms. This interaction is strong and is the dominant structure-developing force in the crystal, after the hydrogen bond interaction. The interaction between iodine atoms occurs both between molecules in the layers as well as between iodine atoms of adjacent layers. The interlayer iodine-iodine contact distance ranges from 4.075 - 4.153 Å for the available temperature range of experimental data. The van der Waals radius for I is 1.98 Å,[165] which implies that there is a nonbonding contact between the iodine atoms. However, the iodine-iodine distance between adjacent layers ranges from 3.932 to 3.992 Å for the given temperature range, distances that are within the van der Waals radius sum for two iodine atoms.

The strength of the I – I interaction are most easily seen in the spherical atom refinements. The electron density at each I atom is highly distorted and cannot be adequately described by a spherical atom model, therefore the residual electron density surrounding the iodine atom ranges from -4.24 to 2.84 $eÅ^{-3}$ when an *empirical* absorption

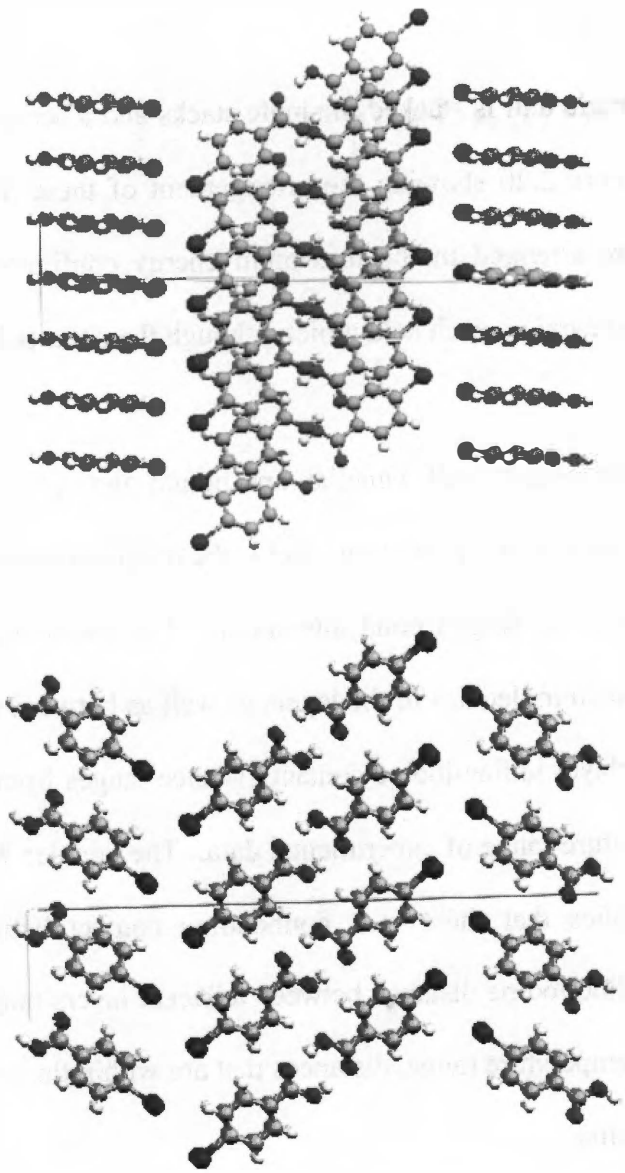


Figure 2.20. Packing diagrams of para-iodobenzoic acid from the 103K data set demonstrating the stacking of the dimeric units as well as the I – I interactions.

correction is applied for the 173 K data set.[93] When an *analytical* absorption correction was applied to a data set at the same temperature, the residual electron density ranges from -5.78 to 2.05 eÅ^{-3}.[93] Figure 2.21 shows a difference Fourier map[127] of the distribution of the residual electron density around the I atom from an empirical absorption correction at 103 K. The deformation of this electron density protrudes perpendicular to the plane of the asymmetric unit. This raises questions as to the driving force for the packing seen in the crystalline state. Though hydrogen bonding is an obvious driving force for the formation of the dimeric unit, the iodine-iodine contacts appear to be the interactions that drive the disposition of the lamellar structure. This type of halogen - halogen interaction is found to be quite common for 1,4-substituted benzene molecules, with the shortest reported contact distance for the I – I contact being 3.748 Å.[34,35]

In terms of the intramolecular structure of 4-iodobenzoic acid, all bond lengths and angles are well within the normal observed range.[34,35] The torsion angles described by O1-C7 and C6-C4 [6.6(8) °] and by O2-C7 and C6-C5 [6.8(8) °] are typical for benzoic acid derivatives. The oxygen-carbon-oxygen angle of the carboxylate unit has a value of 123.2(5)°, which is typical of carboxylic acid units. A search of the CSD demonstrates that the range for the O-C-O angle in 4-substituted benzoic acid molecules is 113.6° - 128.4°.[34,35]

The dimeric unit is held together by the presence of a strong hydrogen bond. The electron density associated with the H atom in this bond was located in Fourier difference maps, $\rho_{diff,1} = F_{Obs} - F_{Calc}$, with no placement of the H atom in the calculated model. Fourier maps at successive temperatures are shown in Figure 2.22. Table 2.7 shows

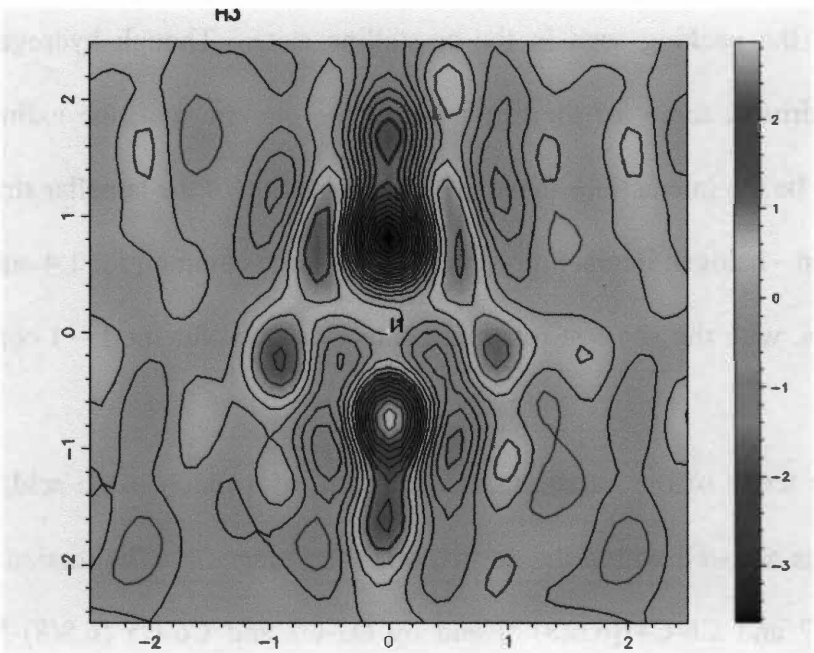


Figure 2.21. Fourier difference map of para-iodobenzoic acid showing the residual electron density around the iodine position at 103 K ranging from –3.64 to 2.87 $e^{-}/Å^{3}$.

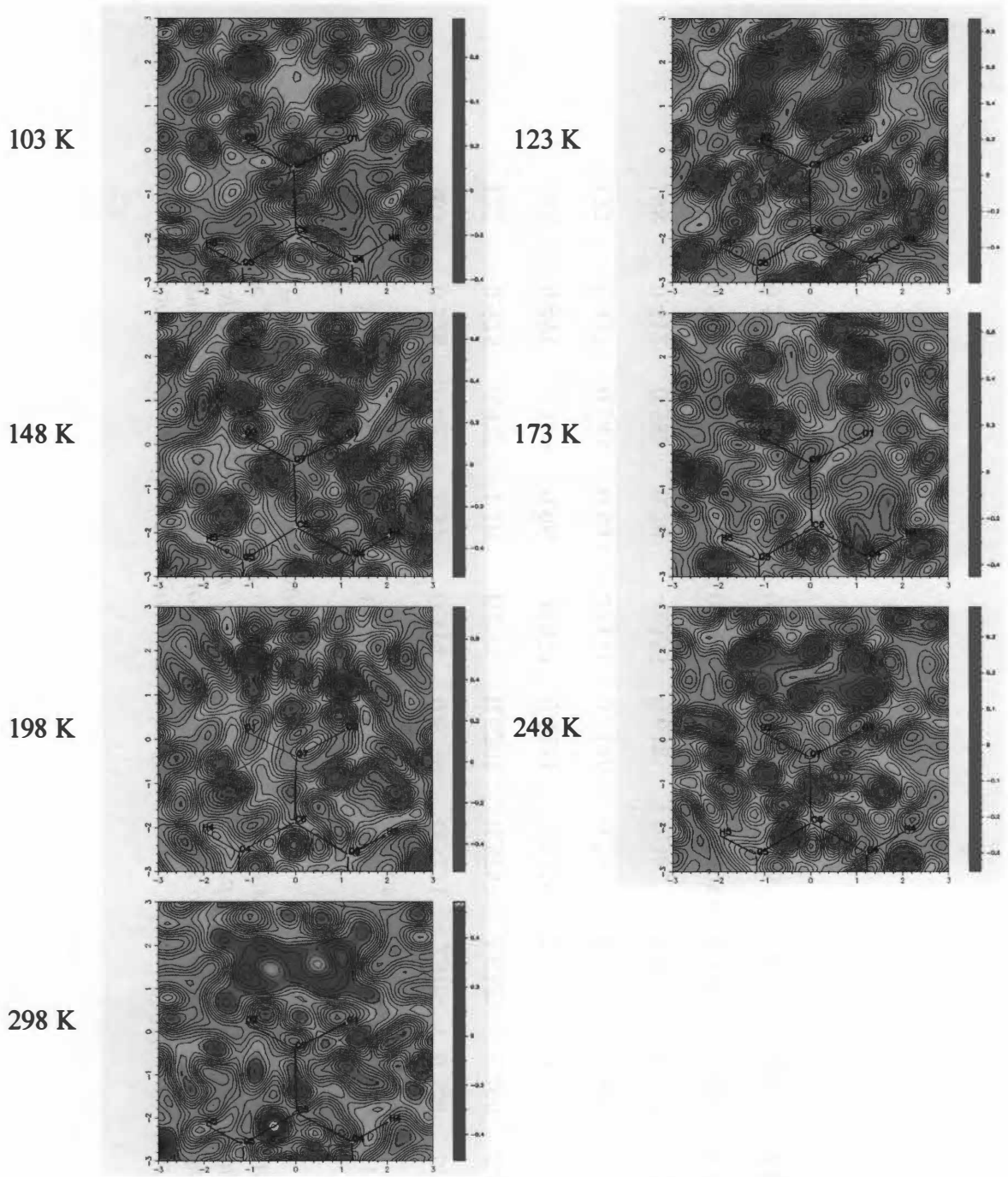


Figure 2.22. Fourier difference maps showing the carboxylate proton position in the dimeric unit from spherical atom refinements. Contour levels are drawn at 0.04 eÅ^{-3}.[127]

Table 2.7. Population of the major (A) configuration in the structure of para-iodobenzoic acid. The linear region is in the low temperature range, up to 198 K. The SOF, sight occupancy factor, refinements are less reliable for these split site H atoms than are the occupancies estimated from direct imaging from the Fourier maps.[39] *[X_A is the population of the major configuration as determined from examination of the difference Fourier maps. $K = (X_A)/(1-X_A)$. ITF is the isotropic thermal factor.]*

T [K]	$X_{A,F}$	$1-X_{A,F}$	$K_{H,F}$	ln $K_{H,F}$	$X_{A,SOF}$	$1-X_{A,SOF}$	$K_{H,SOF}$	ln $K_{H,SOF}$	ITF
103	0.578	0.422	1.37	0.314	0.6779	0.3221	2.105	0.744	0.029
123	0.525	0.475	1.10	0.099	0.6201	0.3799	1.6323	0.490	0.022
148	0.491	0.509	0.96	-0.037	0.6861	0.3139	2.1857	0.782	0.028
173	0.457	0.543	0.84	-0.171	0.6146	0.3854	1.5947	0.467	0.028
198	0.412	0.588	0.70	-0.355	0.638	0.362	1.7624	0.567	0.052
248	0.547	0.453	1.21	0.190	0.5502	0.4498	1.2232	0.201	0.037
298	0.503	0.497	1.01	0.012	0.633	0.376	1.6835	0.521	0.034

the site occupancy factors for each temperature for the distribution of electron density associated with the H atom position and the 3-center 4-electron (3c-4e) bond between dimers.

As seen in the difference Fourier maps in Figure 2.22, at 103K the electron density associated with the hydrogen bonded proton position (H1) is strongly associated with only one of the oxygen atoms in the carboxylic acid unit.[127] However, this correlation changes dramatically with temperature, in accord with previous studies in similar systems.[63] In the 173K data, for example, there appears to be a "split-site" disorder associated with the electron density in the hydrogen bond. This trend is followed with increasing temperature, but at room temperature the presence of thermal motion and disorder does not allow us to image adequately the distribution of the electron density associated with the hydrogen atom in the hydrogen bond.

It is reasonable to assume that the observed peaks in the Fourier maps are due to a disordered population over two possible H atom sites. A valence bond representation of the two possible forms **I** and **II**, shown in Figure 2.23, observed in the average structure illustrates the hydrogen bond split-site equilibrium. Moreover, it is assumed there is no order in the distribution of these valence bond representations from unit cell to unit cell and that therefore the distribution is statistically random. No evidence of ordering of the dimeric units with respect to **I** and **II** or any resulting superlattice was found in the diffraction data. It should be noted if the only discrimination between the system of valence bond isomers ordered over a superlattice and a randomly disordered situation were the location of the hydrogen atoms, then these X-ray diffraction experiments would

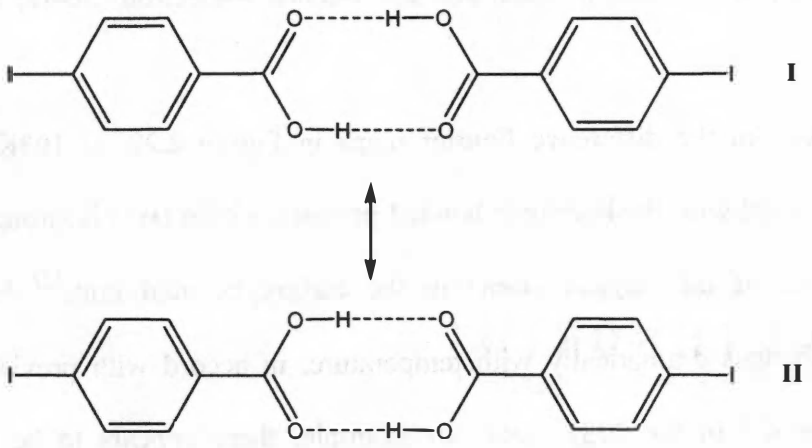


Figure 2.23. Valence bond representations of the split-site equilibrium in para-iodobenzoic.

be unlikely to reveal them, given the scattering power of the electron density associated with a hydrogen atom.

Taking a perfectly disordered system, as described above, as the model for the data, then an equilibrium constant, K_H, can be written as

$$K_H = \frac{X_A}{X_B} = \frac{X_A}{(1 - X_A)} \tag{2.1}$$

assuming a site occupancy over the disordered hydrogen atom sites such that

$$X_A + X_B = 1 \tag{2.2}$$

where X_i is the population of the i^{th} atom site.

Using the definition of K_H, it follows that

$$\ln K_H = \frac{-\Delta G}{RT} = \frac{-\Delta H}{RT} + \frac{\Delta S}{R} \text{ at any temperature } T. \quad (2.3)$$

where ΔG is the difference in Gibbs free energy for the two isomers with populations A and B. Table 2.10 contains the results of the population analyses derived from the integration of the Fourier map, with a data cutoff of $\frac{F_{obs}}{\sigma(F_{obs})} = 0$ and the site occupancy factors, SOF, from the spherical atom refinements of the data. A plot of ln $K_{H,(Fourier)}$ *vs.* inverse temperature for temperatures in the range 103-198 K is shown in Figure 2.24. From the slope of the linear fit to the data, $\frac{\Delta H}{R} = 135.43$, yielding a value for $\Delta H = 1.13$ kJmol^{-1} for the enthalpy difference between the configurations. This value compares favorably with other similar measurements *viz.* 0.50(4) kJ mol^{-1} for benzoic acid[70,71] and 1.64(9) kJmol^{-1} for p-chlorobenzoic acid[166,167] obtained previously from neutron diffraction data. Interestingly, in spite of the redistribution of proton occupancies between the two oxygen atoms in the COOH unit, there is no parallel trend evident in the C-O bond length differences; the simple **I/II** site model does not reproduce the bond lengths observed in this study. By inspecting the literature for carboxylic acid dimers and extracting the O-H, C-O and C=O bond lengths, it is apparent there is no correlation between these structural parameters; the accumulated data are shown in Figure 2.25.

The lack of correlation between these parameters implies that the simple **I/II** model is not supported by the data; if the **I/II** model were to apply, a bimodal distribution would be expected. Moreover, an average bond length determined by $r_{C\text{-}O}$ and $r_{C=O}$ and subsequently weighted to the hydrogen atom populations does not account for the observed variation of these carbon – oxygen bonds with temperature in this study.

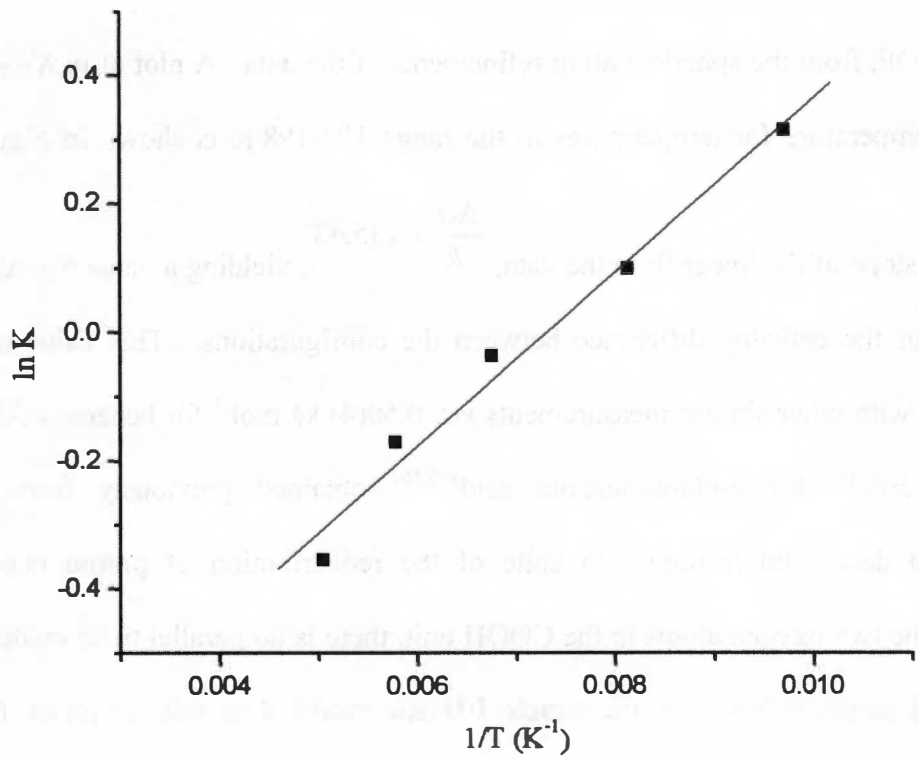


Figure 2.24. A plot of ln K_H vs inverse temperature for the split-site populations of the proton position in para-iodobenzoic acid, extracted from the integration of the Fourier map with a data cutoff of $F_{Obs}/\sigma(F) = 0$.

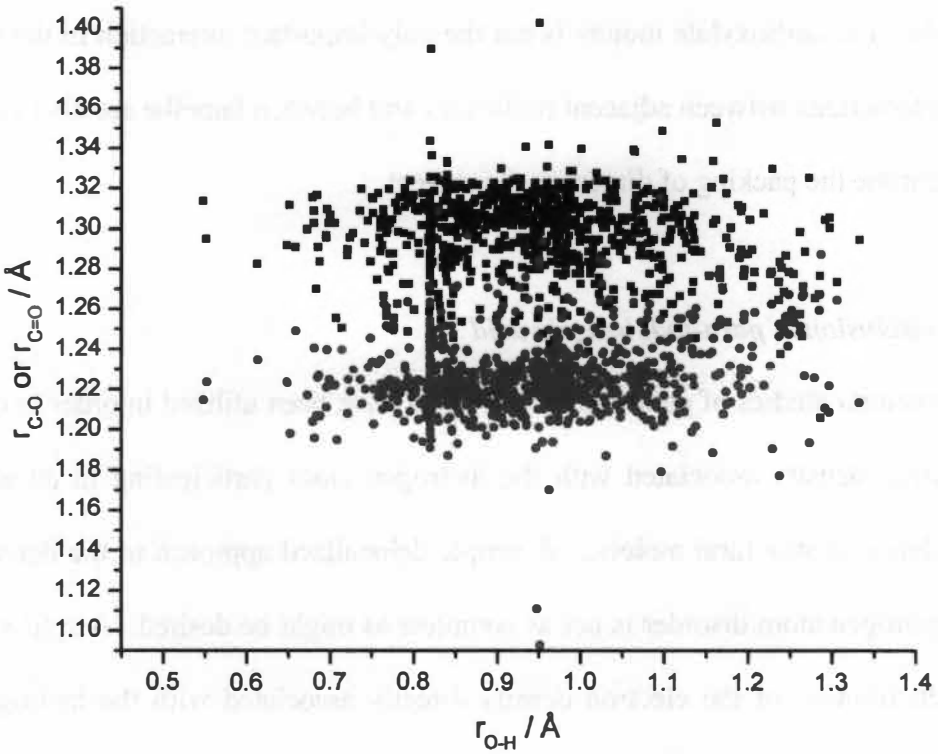


Figure 2.25: Comparison of the O-H vs. C-O and O-H vs. C=O (red) distances, r_{O-H} and r_{C-O} and $r_{C=O}$, extracted from the CCSD, showing no correlation between these structural parameters.

It is evident there is a complex relationship between the H atom distributions and the structural response of the [CO_2] unit which is not adequately described by the **I/II** model. Theoretical descriptions of hydrogen bonding show that the rearrangement of the total electron distribution in the system must be considered, not simply that local to the COOH unit. These fine details of the bonding picture are, however, inaccessible from this study. The carboxylate moiety is not the only important interaction in the system as the I-I interactions between adjacent molecules and between lamellæ are also very strong and determine the packing of dimers in the system.

2.3.4 Conclusions: para-iodobenzoic acid

Structural studies of para-iodobenzoic acid have been utilized in order to determine the electron density associated with the hydrogen atom participating in an apparently well-understood structural moiety,. A simple delocalized approach to the determination of the hydrogen atom disorder is not as complete as might be desired. A split-site model of the distribution of the electron density directly associated with the hydrogen atom, obtained from difference Fourier maps, yields values for the enthalpy differences between the two distinct molecular configurations in the lattice that is consistent with previous measurements. However, the structural consequences of this model for the carboxylate group in terms of a valence bond delocalized picture of the bonding are not fully borne out in the observed C...O bond lengths determined from spherical atom refinements of the data, suggesting further complexity.

2.4 Experimental

Urotropine-*N*-oxide·formic acid was synthesized by addition of an excess of hydrogen peroxide to an aqueous solution of urotropine. Single crystals suitable for X-ray or neutron diffraction experiments were either grown by slow evaporation of the reaction mixture or were recrystallized from concentrated aqueous solutions by passing a current of air over a droplet of the solution that was placed on a glass plate made hydrophobic by the application of a very small quantity of British nose oil.

4-iodobenzoic acid was purchased from Acros and was recrystallized from acetone. The material crystallizes as thin plates from the slow evaporation of an acetone solution (0.0534M).

Details of the data collection strategies may be found in Chapter 5. For urotropine-*N*-oxide·formic acid, variable temperature data collections which analyzed hydrogen bonding track section 5.2. Neutron diffraction data were collected on SCD at IPNS and the experimental details follow section 5.5. For para-iodobenzoic acid, hydrogen bonding data collections were performed as in section 5.2.

Details for the data collections strategies and refinements of the variable temperature hydrogen bond data collections are found in Tables 2.8 and 2.9 for Urotropine-*N*-oxide·formic acid and para-iodobenzoic acid, respectively. The respective table of lattice parameters is Table 2.10 for **I**.

Differential scanning calorimetry was used to determine the thermodynamics of any phase behavior of **II**, according to section 5.9 by Dr. M. Pyda.

CPMAS solid state NMR data were collected according to section 5.7, and solution NMR data were obtained according to section 5.8.

Table 2.8. Selected refinement parameters for the collected data on urotropine-N-oxide·formic acid.

Temperature (K)	123 (Neutron)	123 (X-ray)	148	173
θ range		2.10 to 28.34°	2.10 to 28.34°	2.11 to 28.31°
Index range for data collection	-13 <=h <= 13	-9 <= h <= 8	-9 <= h <= 8	-9 <= h <= 8
	-13 <= k <= 2	-8 <= k <= 9	-8 <= k <= 9	-8 <= k <= 8
	-31 <= l <= 38	-25 <= l <= 25	-25 <= l <= 25	-24 <= l <= 25
Reflections collected	3771	9144	9144	9107
Independent reflections	2144	2145 [R(int) = 0.0232]	2145 [R(int) = 0.0232]	2143 [R(int) = 0.0226]
Completeness to theta = 28.33°		97.1 %	97.1 %	97.1 %
Data / restraints / parameters	2144 / 0 /313	2145 / 0 / 131	2145 / 0 / 131	2143 / 0 / 131
S	1.02	1.037	1.037	1.045
Final R indices $[I>2s(I)]^X$ $[I>3s(I)]^N$	R1 = 0.151, wR2 = 0.092	R1 = 0.0349, wR2 = 0.0990	R1 = 0.0349, wR2 = 0.0990	R1 = 0.0359, wR2 = 0.0973
R indices (all data)	R1 = 0.221, wR2 = 0.095	R1 = 0.0393 wR2 = 0.1043	R1 = 0.0393 wR2 = 0.1043	R1 = 0.0414 wR2 = 0.1025

Table 2.8. continued

Temperature (K)	198	223	248	298
θ range	3.10 to 28.27°	2.10 to 28.34°	2.10 to 28.29°	2.10 to 28.79°
Index range for data collection	-9 <= h <= 8	-8 <= h <= 8	-8 <= h <= 8	-9 <= h <= 9
	-9 <= k <= 8	-9 <= k <= 9	-9 <= k <= 9	-9 <= k <= 9
	-25 <= l <= 25	-25 <= l <= 25	-25 <= l <= 25	-25 <= l <= 25
Reflections collected	8748	9329	9177	9415
Independent reflections	2144 [R(int) = 0.0216]	2176 [R(int) = 0.0279]	2168 [R(int) = 0.0216]	2195 [R(int) = 0.0252]
Completeness to theta = 28.33°	96.6 %	97.3 %	97.1 %	92.8 %
Data / restraints / parameters	2144 / 0 / 131	2176 / 0 / 131	2168 / 0 / 131	2195 / 0 / 131
S	1.043	1.014	1.025	1.017
Final R indices [I>2s(I)]	R1 = 0.0355, wR2 = 0.0992	R_1 = 0.0379, wR_2 = 0.1012	R_1 = 0.0398, wR_2 =0.1039	R_1 = 0.0409, wR_2 = 0.1056
R indices (all data)	R1 = 0.0386 wR2 = 0.1030	R_1 = 0.0490 wR_2 = 0.1120	R_1 = 0.0501 wR_2 = 0.1126	R_1 = 0.0555 wR_2 = 0.1153

Table 2.9. Selected refinement parameters for the collected data on para-iodobenzoic acid.

Temperature (K)	103	123	148	173
θ range (°)	2.70 to 28.33	1.35 to 28.28	2.69 to 28.20	2.70 to 28.24
Index range for data collection	-5 <= h <= 5	-5 <= h <= 5	-5 <= h <= 5	-5 <= h <= 5
	-7 <= k <= 7	-7 <= k <= 7	-7 <= k <= 7	-7 <= k <= 7
	-39 <= l <= 39	-39 <= l <= 40	-40 <= l <= 40	-39 <= l <= 39
Reflections collected	6519	6704	6783	7365
Independent reflections	1759 [R(int) = 0.0232]	1755 [R(int) = 0.0267]	1748 [R(int) = 0.0294]	1781 [R(int) = 0.0267]
Completeness to theta = 28.33o	96.30%	96.00%	95.70%	97.20%
Data / restraints / parameters	1759 / 0 / 93	1755 / 0 / 92	1748 / 0 / 92	1781 / 0 / 92
S	1.311	1.446	1.426	1.323
Final R indices [I>2s(I)]	R1 = 0.0335, wR2 = 0.0777	R1 = 0.0574, wR2 = 0.1492	R1 = 0.0613, wR2 = 0.1533	R1 = 0.0423, wR2 = 0.1011
R indices (all data)	R1 = 0.0366, wR2 = 0.0785	R1 = 0.0584, wR2 = 0.1495	R1 = 0.0627, wR2 = 0.1538	R1 = 0.0474, wR2 = 0.1025

Table 2.9. continued

Temperature (K)	198	248	298
θ range	1.35 to 28.25o	2.70 to 28.29o	1.36 to 28.24o
Index range for data collection	-5 <= h <= 5	-5 <= h <= 5	-5 <= h <= 5
	-7 <= k <= 7	-8 <= k <= 8	-7 <= k <= 8
	-39 <= l <= 39	-39 <= l <= 39	-39 <= l <= 39
Reflections collected	7325	7007	6917
Independent reflections	1775 [R(int) = 0.0291]	1789 [R(int) = 0.0283]	1785 [R(int) = 0.0312
Completeness to theta = 28.33 °	96.20%	95.90%	96.10%
Data / restraints / parameters	1775 / 0 / 92	1789 / 0 / 92	1785 / 0 / 92
S	1.319	1.358	1.308
Final R indices [I>2s(I)]	R1 = 0.0550, wR2 = 0.1275	R1 = 0.0417, wR2 = 0.1047	R1 = 0.0506, wR2 = 0.1234
R indices (all data)	R1 = 0.0607, wR2 = 0.1292	R1 = 0.0457, wR2 = 0.1059	R1 = 0.0589, wR2 = 0.1260

Table 2.10. Lattice parameters (reduced unit cell) for the collected data at variable temperature for urotropine-N-oxide·formic acid. The superscript in the reference column denoted X-ray (X) versus Neutron (N) data.

a / Å	*b* / Å	*c* / Å	β / o	T / K	reference
6.845	6.847	19.480	95.06	298	*92*
6.726(1)	6.732(1)	19.418(4)	95.391(16)	123	*this work* $^{(N)}$
6.774(2)	6.790(2)	19.472(7)	95.159(6)	123	*this work* $^{(X)}$
6.7679(19)	6.779(2)	19.487(6)	95.446(5)	148	*this work* $^{(X)}$
6.770(3)	6.799(3)	19.433(8)	95.297(7)	173	*this work* $^{(X)}$
6.787(2)	6.802(2)	19.532(7)	95.266(6)	198	*this work* $^{(X)}$
6.785(2)	6.8176(19)	19.473(6)	95.107(1)	223	*this work* $^{(X)}$
6.7989(5)	6.8226(4)	19.4639(13)	95.1020(10)	248	*this work* $^{(X)}$
6.8272(13)	6.8456(13)	19.484(4)	94.983(3)	298	*this work* $^{(X)}$

Chapter 3: Characterization of the electron density in the short, strong hydrogen bond in cobaltocenium 3,5 bis(trifluoromethyl)phenoxide 3,5-bis(trifluoromethyl)phenol

Crystalline samples of cobaltocenium 3,5 bis(trifluoromethyl)phenoxide 3,5 bis(trifluoromethyl)phenol were prepared by Dr. L.H. Doerrer and Ms. M.C. Buzzeo at Barnard College. Density Functional Theory calculations presented in part in this chapter were also done by Dr. L.H. Doerrer.

3.1 Introduction

Short, strong hydrogen bonds found between phenoxides and phenols are relatively rare.[168] In this chapter, a detailed experimental picture of the charge density in an example of such a system is presented, together with theoretical aspects of the system that complement this determination. As the system contains two basic elements, the phenol-phenolate anion and the cobaltocenium cation, both are treated independently with respect to their electronic structure.

There are a few phenol-phenoxide systems which are supported by a metal center[169-171] and others which are the counter anion of metallic complexes.[172] Most occur with a third species present to support the hydrogen bond such as in the 2,2'-biphenol supported structure, or in di-tert-butyl-(phenolato)-(pyrazine)gallium, phenol solvate which is shown in Figure 3.1.[172,173]

The molecular structure of cobaltocenium 3,5 bis(trifluoromethyl)phenoxide 3,5-bis(trifluoromethyl)phenol, **III**, was first reported in 2003[168] and consists of a hydrogen

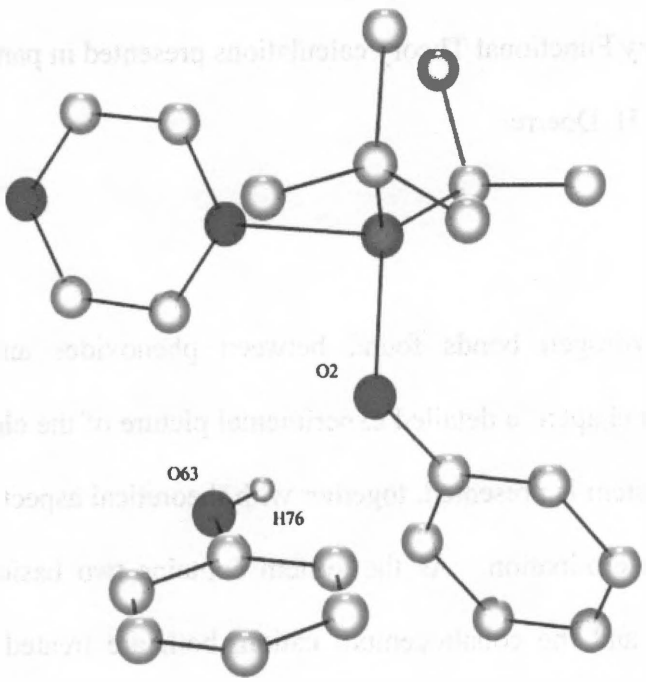


Figure 3.1. Example of a supported hydrogen bond between phenol and phenoxide moieties in di-tert-butyl-(phenolato)-(pyrazine)gallium, phenol solvate. The atoms involved in the hydrogen bond are labeled.

bonded phenol-phenoxide anion and a cobaltocenium cation. The hydrogen bonded segment of the structure is shown in Figure 3.2. These complexes satisfy the criteria for a short, strong hydrogen bond in that the distance along the O...O vector is less than 2.5 Å.[29] This assignment is supported by the fact that the bridging proton between the phenol-phenoxide moieties has a deshielded ^{1}H resonance in the range of 16-22 ppm, specifically 17.11 ppm in **III**. Moreover, the acidity constants for the XH and YH segments, which are identical in the case of **III**,[168] which is often observed in systems that contain a short, strong hydrogen bond.

Phenoxide-phenol systems are acid base pairs, in which the O...H distance in the hydrogen bond is found to decrease with increasing acidity of the hydrogen atom donor and increasing basicity of the acceptor atoms.[29] Acid-base hydrogen bonded species are exemplified by such systems as bifluorosulfate[174-177] and bisulfate[178-181]; in biology, acid-base pairs are an important structural motif in nucleotides[182-187], although they are often symmetric.

In the case of hydrogen bonded systems of the type [O-H...O]$^{-}$, in which the

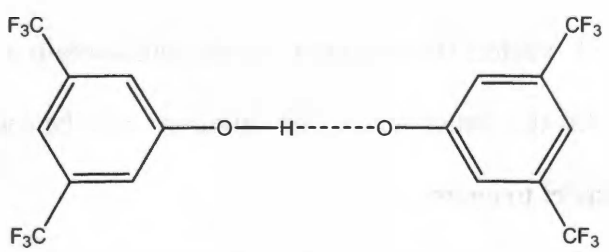


Figure 3.2. Representation of the asymmetric, short, strong hydrogen bond between 3,5-bis(trifluoromethyl)phenoxide and 3,5-bis(trifluormethyl)phenol.

O...H interaction can be defined as any type of non-bonded contact, there is a wide distribution for the distance of the interaction. A search of the CSD showed a range of 1.214(5) Å to 2.720(5) Å, with the mean distance being 1.933(5) Å.[34,35] The distribution of these distances versus the [O-H...O] angle (average angle, 153.4(3)°) is shown in Figure 3.3. The distribution of the number of structures with respect to distance and angles show that there are two maxima present, one sharp and one much broader, although there is a general and even distribution of occurrence over the ranges of distance and angle. A more general discussion of the hydrogen bond is found in section 2.1.

3.1.1 The distribution of scattering density in the hydrogen bond

A hydrogen bond has three atoms which contribute to the nuclear potential. The distribution of the electron density in such a potential is often strongly anisotropic in comparison to that displayed by a 2-centered-2-electron bond, especially in short, strong hydrogen bonds.[25]

If the defining metrical parameter is taken as the distance along the X...Y vector, then there are two general cases that describe the cross-section of the potential energy surface along the X...Y vector: the potential surface can contain a single minimum or a double minimum. In the latter case, the minima can be either symmetrical or asymmetrical with respect to energy.

Hydrogen-bonded systems of the type O-H...O^-, are often short, strong hydrogen bonds. When the O...O separation is in the range of very strong hydrogen bonds (<2.5 Å), the potential energy surface is often relatively flat due to the nearly symmetric hydrogen bond. In this case, the X-H covalent bond is elongated as compared to a non-

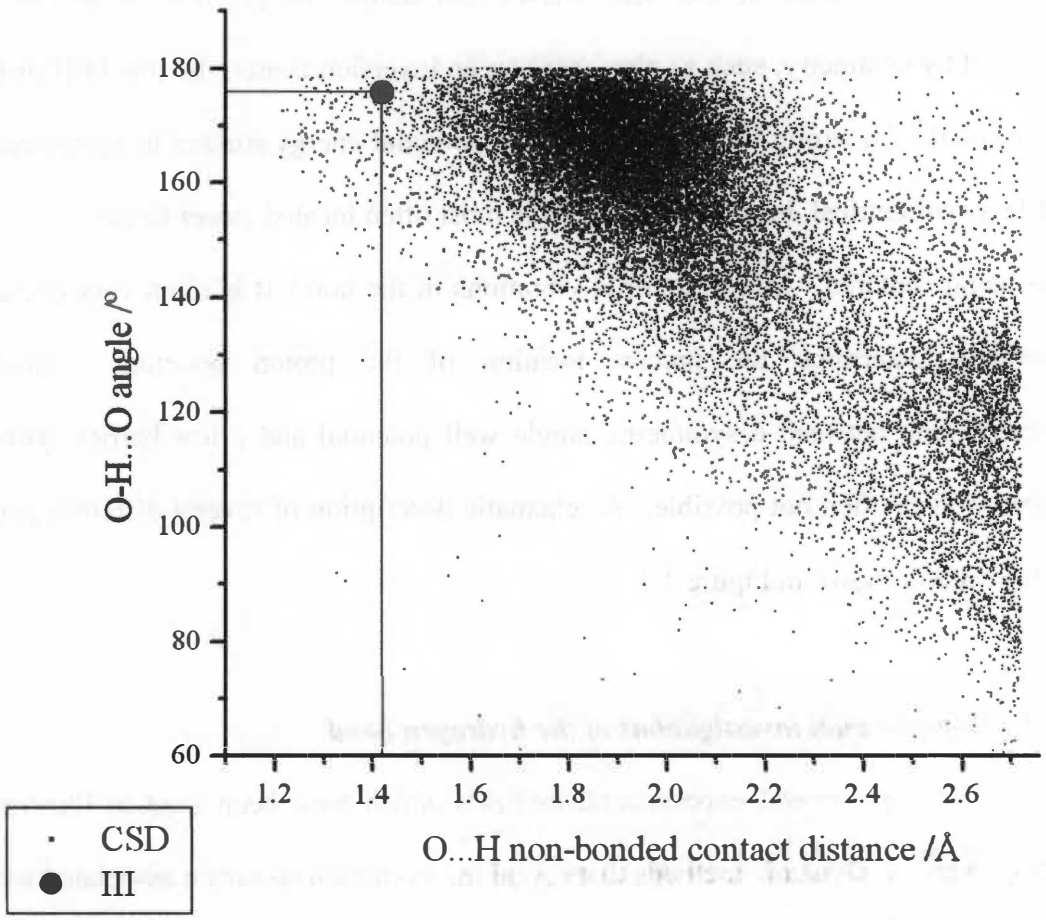


Figure 3.3. Distribution of the O...H non-bonded contact distances versus O-H...O angle in a search of the CSD.

hydrogen bonded system, and the H...Y ionic interaction is shortened. Neutron diffraction studies of systems that contain very strong hydrogen bonds are often interpreted in terms of a the potential energy curve that displays a broad and flat minimum and the proton then vibrates anharmonically in the well.[9] In the O-H...O short, strong hydrogen bond, it has been shown that unless the position of the proton is restricted by symmetry, such as placement on an inversion center, the two O-H distances are unequal.[9] In strong hydrogen bonds, the potential energy surface is more structured and less symmetrical, in which the proton is most often located closer to one atom, rather than being centered. Due to thermal vibrations in the bond, it is often very difficult to accurately determine the precise location of the proton position. Therefore, differentiating between a symmetric single well potential and a low-barrier symmetric double well is often not possible. A schematic description of several different potential energy well is shown in Figure 3.4.

3.1.2 Experimental investigations of the hydrogen bond

There are several experimental methods which have been used to illustrate the hydrogen bond. Dynamic methods that reveal the excitation spectrum associated with the hydrogen bond include inelastic neutron scattering experiments,[188,189] Raman and IR spectroscopy[190-197] and ^{1}H NMR.[79,198-202] Inelastic neutron scattering experiments measure all of the vibrational and rotational transitions in a molecule. Raman and IR spectroscopy measure the vibrational transitions in a molecule. In IR spectroscopy, the presence of a hydrogen bond results in the X-H stretching frequencies being lowered in comparison with the free X-H frequency.[203] There is often a concomitant increase in the

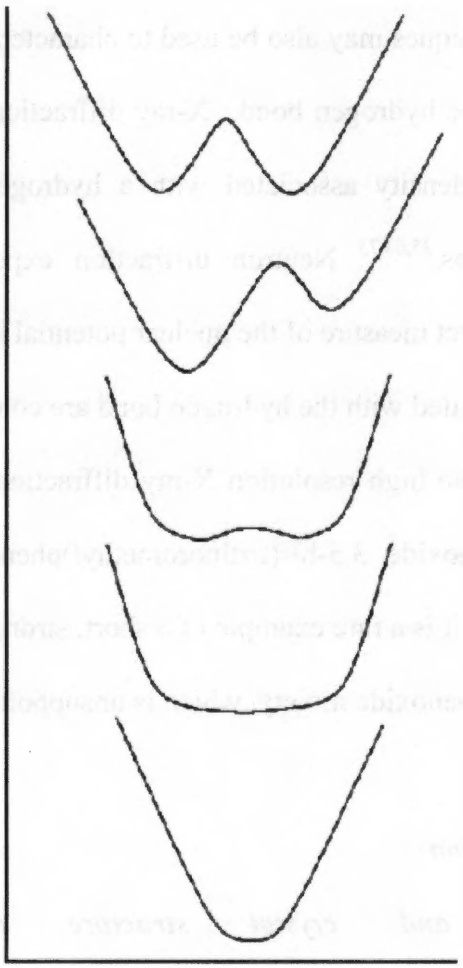


Figure 3.4. Schematic diagram of several different types of potential wells found in hydrogen bonds. From the top: symmetric double well; asymmetric double well; low-barrier symmetric double well; symmetric double well with nearly no barrier; symmetric single well with a centered proton position.

intensity and the band width. The chemical shift measured via NMR spectroscopy also yields an indirect measure of the electron density at the proton.[203] In addition, theoretical methods have been used to calculate both the ground state structure as well as the excited state.[190,204-208]

Diffraction techniques may also be used to characterize the distribution of nuclear or electron density in the hydrogen bond. X-ray diffraction experiments can be used to visualize the electron density associated with a hydrogen bond through the use of difference Fourier maps.[25,63,73] Neutron diffraction experiments reveal the nuclear positions, yielding a direct measure of the nuclear potential in the Bragg average in which the four electrons associated with the hydrogen bond are confined.[63,65,66,68,69]

In this chapter the high resolution X-ray diffraction study of cobaltocenium 3,5 bis(trifluoromethyl)phenoxide 3,5-bis(trifluoromethyl)phenol (**III**), is reported. This material is of interest as it is a rare example of a short, strong, asymmetric hydrogen bond between a phenol and phenoxide moiety, which is unsupported by any other species.

3.2 Results and discussion

3.2.1 Molecular and crystal structure of cobaltocenium 3,5 bis(trifluoromethyl)phenoxide 3,5-bis(trifluoromethyl)phenol

The molecular structure of cobaltocenium 3,5 bis(trifluoromethyl)phenoxide 3,5-bis(trifluoromethyl)phenol[168,209] is shown in Figure 3.5. In **III**, the cobalt is coordinated in an η^5 manner to the cyclopentadienyl ligands (Cp). The average C_{Cp}-Co bond distance in **III** is 2.048(12) Å, as compared with the mean distance in a search of the CSD being 2.022(2) Å.[34,35] The two Cp rings are nearly eclipsed, being offset by only 1.41°.

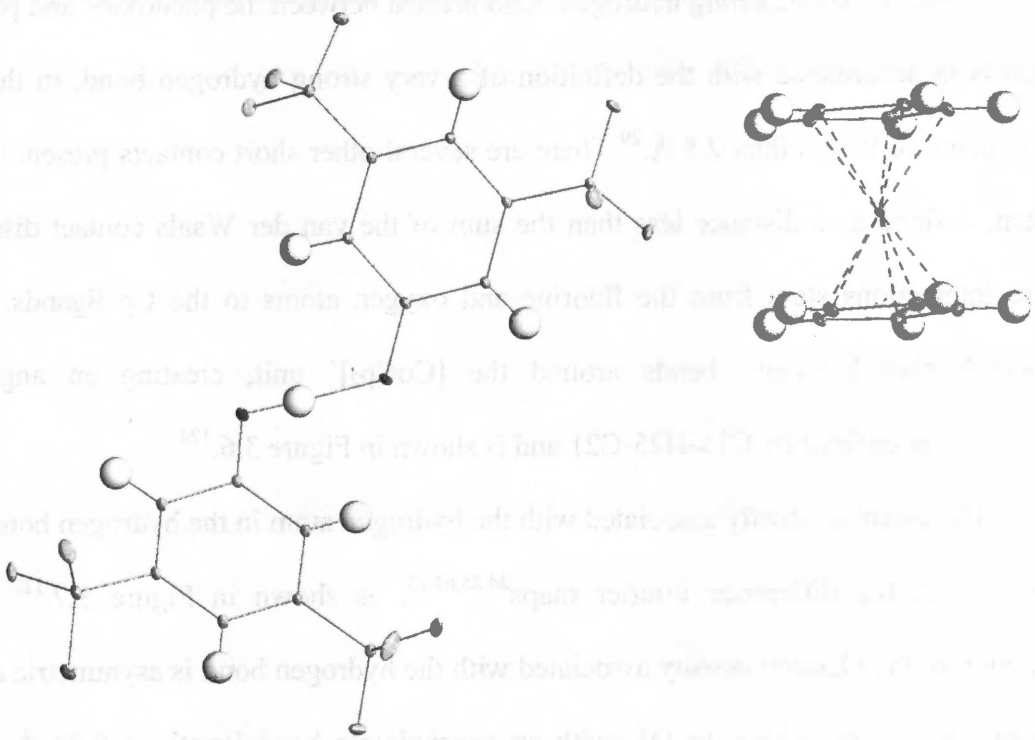


Figure 3.5. Molecular structure of cobaltocenium 3,5 bis(trifluoromethyl)phenoxide 3,5-bis(trifluoromethyl)phenol, III, from a SHELXTL refinement of the data collected at 16 K.

Geometry optimized density functional theory calculations on the $CoCp_2^+$ segment are excellent agreement with the experimental results in that the two cyclopentadienyl ligands are offset from a perfect eclipsed geometry by 1.41°; however, the calculated bond length from C_{Cp} to cobalt is slightly shorter than observed experimentally, that distance being approximately 2.017 Å.

There is a short, strong hydrogen bond present between the phenoxide and phenol, which is in accordance with the definition of a very strong hydrogen bond, in that the O…O distance is less than 2.5 Å.[29] There are several other short contacts present in this system, defined as a distance less than the sum of the van der Waals contact distance. These interactions stem from the fluorine and oxygen atoms to the Cp ligands. The phenoxide-phenol moiety bends around the $[CoCp_2]^+$ unit, creating an angle of 149.54(5)°, as defined by C15-H25-C21 and is shown in Figure 3.6.[124]

The electron density associated with the hydrogen atom in the hydrogen bond was located from the difference Fourier maps[24,25,63,73], as shown in Figure 3.7.[127] The maximum of the electron density associated with the hydrogen bond is asymmetric and is located significantly closer to O1, with an approximate bond length of 0.98 Å. The location of the maximum of the electron density associated with the hydrogen atom was a starting point for both the spherical and aspherical atom refinements. Full positional and isotropic thermal parameter of this H atom in SHELXTL resulted in an O1-H25 distance of 0.9790 Å and an O2…H25 distance of 1.4824 Å. These bond distances were held constant for all aspherical atom analyses.

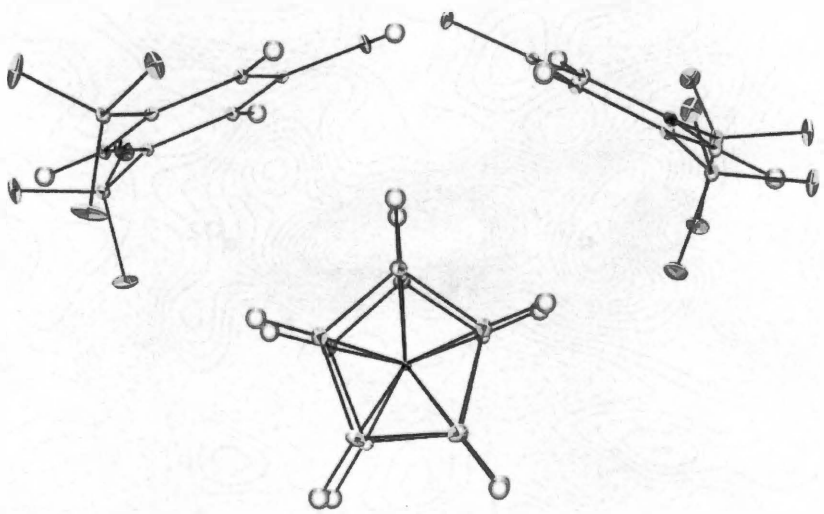


Figure 3.6. ORTEP diagram of III demonstrating the bend of the phenol-phenoxide moiety around the $CoCp_2$ segment.

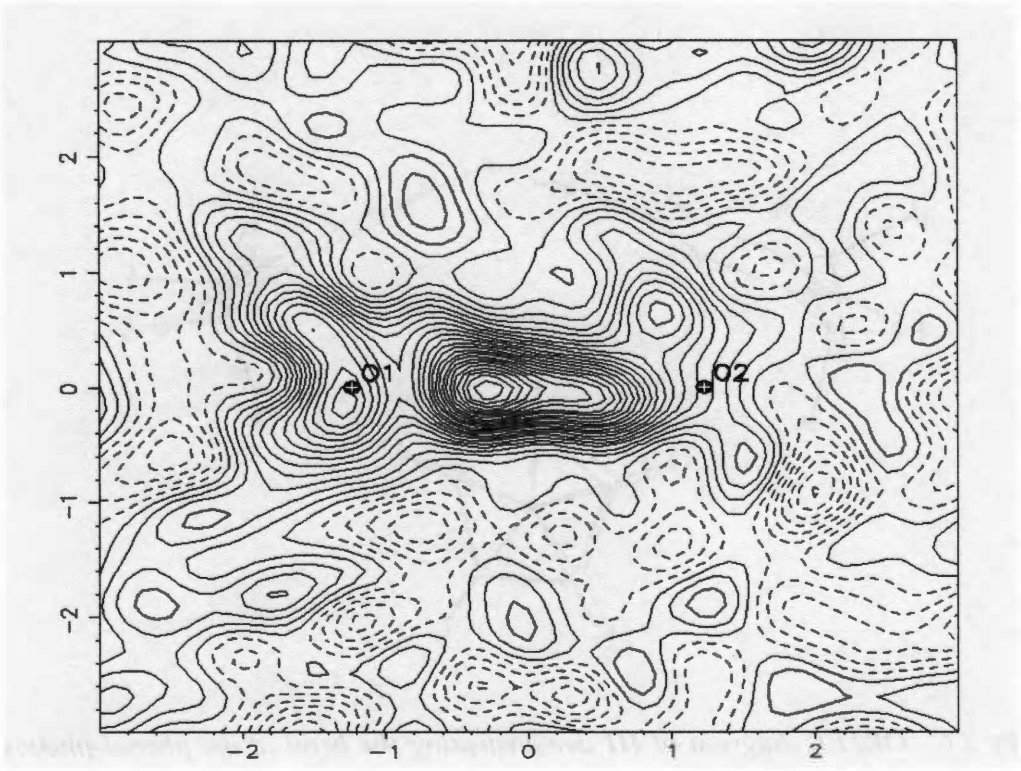


Figure 3.7. Difference Fourier map showing the electron density associated with the hydrogen bond in III. Contour levels are drawn at 0.03 eÅ^{-3}.

3.2.2 Discussion of the hydrogen bonded anion

Apart from the obvious covalent fragments present, the only structural motif of note in the anion is the short, strong hydrogen bond between the phenol and phenoxide moieties. In **III**, the measure of the O…O vector at 16 K is 2.459(3) Å. A search of the CSD showed the average O-H distance for phenoxide-phenol hydrogen bond interactions is 1.235 Å with an O-H-O angle of 163.417°.[34,35] The hydrogen bond distances and angles in **III** are within the range of values for phenol systems given in the CSD.[34,35]

Charge density analysis was performed to provide a more accurate model of the total electron density in the system.[22] The electron density at the bond critical point along the O1-H25 vector is 1.550(50) eÅ^{-3} and along the H25…O2 vector is 0.675(35) eÅ^{-3}. The values of the electron density along the O1-H25 and O2…H25 vectors are typical of the presence of a covalent and an ionic interaction, respectively, in strong hydrogen bonds. There is a (3,-1) bond critical point (bcp) located along each of these vectors, which indicates the presence of a bond, despite the disparity between the two values. The bond critical points are located 0.7949 Å from O1 in the O1-H25 bond, and 1.0028 Å from O2 in the O2…H25 bond. In both cases, the bond critical point is located closer to the hydrogen atom than the oxygen atoms.

Where the O1-H25 and O2…H25 bonds differ significantly is in the values for the Laplacian. Figure 3.8 is a representation of the Laplacian along the O-H…O vector. The value of $\nabla^2\rho$ at the bond critical point of the O1…H25 bond is -3.397(407) eÅ^{-5} and 2.913(62) eÅ^{-5} at the bond critical point of O2…H25.[22] A positive value of the Laplacian is typical of ionic bonds, whereas the negative value is indicative of covalent bonds. The maximum of the electron density along the hydrogen bond in **III** is not

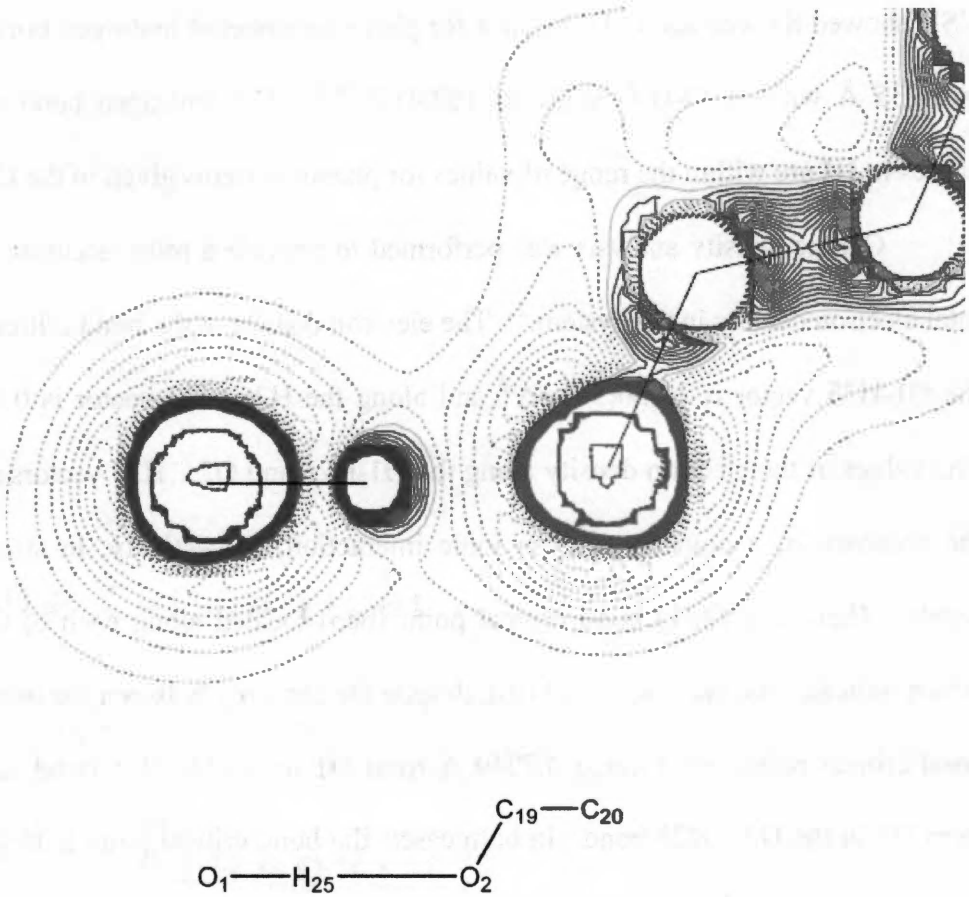


Figure 3.8. The Laplacian along the O-H-O bond in cobaltocenium 3,5-bis(trifluoromethyl)phenoxide 3,5-bis(trifluoromethyl)phenol (III). Contours levels are drawn at 2 eÅ^{-5}. Positive values are represented by solid blue lines, negative values by dotted red lines and the zero level contour is a green solid line.

centered and leads to more typical values observed for the Laplacian in other known examples of non-symmetric hydrogen bonded systems.

These topological properties extracted from charge density studies reveal a better understanding of the chemistry of **III**. As is expected, the short, strong hydrogen bond along the O1…O2 vector consists of an ionic and a covalent part. The O1-H25 bond is covalent, in which the charge density analysis reveals that the amount of density located at the bond critical point is approximately 2.5 times greater than that found in the ionic portion of the bond (H25…O2). The Laplacian shows a positive value at the bond critical point along the H25…O2 vector, which is indicative of a closed-shell interaction, whereas the Laplacian at the bond critical point in the covalent O-H bond is negative. All of these values are typical of asymmetric hydrogen bonds; however, in the case of short, strong, symmetric hydrogen bonds, there is often a significant amount of covalent character to both of the O-H bonds.

Both single point and geometry optimized DFT calculations were performed on **III** by Dr. L.H. Doerrer at Barnard College. Further calculations were performed as linear transit studies in order to map the potential well in which the hydrogen atom moves along the O…O vector and in the O…H…O angle. The first study systematically moved the H atom stepwise along the O…O vector, with the O…H…O angle of 176.4° as shown by the X-ray diffraction studies, calculating the energy at each point, to determine the location of the H atom along the hydrogen bond in the minimum energy configuration, with all other atoms in the system being held constant. The second and third studies kept the O-H distance fixed at 0.98 Å and 1.20 Å while varying the H…O angle. The results of the linear transit studies are shown in Figure 3.9, which show a broad-barrier single

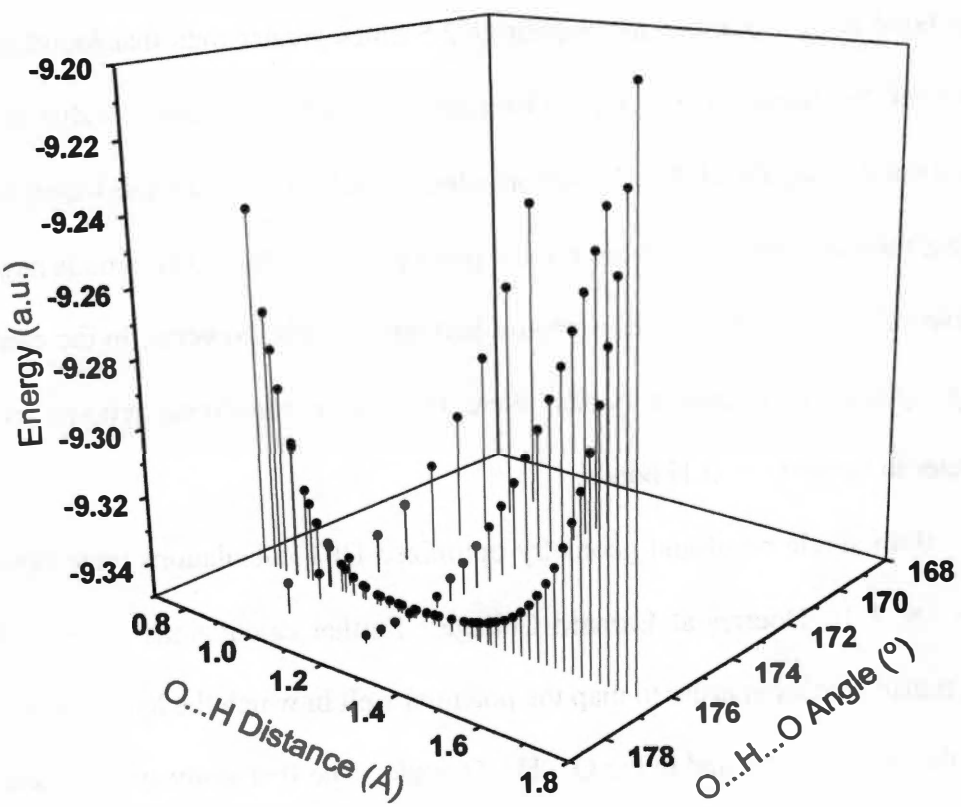


Figure 3.9. Results of linear transit studies with DFT calculations on III.

well potential with a low angular dependence. These linear transit studies were performed solely on the phenol-phenoxide segment of the molecule, with no allowance for any interaction of influence by the cobaltocenium cation. As is shown in Figure 3.6, the cobaltocenium cation clearly has an effect on the structure of the phenol-phenoxide moiety. Further density functional theory studies which include this interaction may help improve the correlation between the experimental results of an asymmetric hydrogen bond and the theoretical results.

Plane-wave density functional theory calculations have been used to accurately reproduce crystalline lattices.[65,167,210,211] Periodic density functional theory calculations may help improve the correlation between the experimental and theoretical results in this cobaltocenium complex with respect to the hydrogen bonded structure.

Deformation density analysis allows for a further visual description of the hydrogen bond. The total electron density is subtracted from a core of a reference molecule with no predisposed understanding of the position or thermal parameters. The result is a visual description of the bonding density in the hydrogen bond. A deformation density map in the O…O plane of the hydrogen bond is shown in Figure 3.10.[22]

3.2.3 Discussion of the electronic structure of the heavy atom moieties

Figure 3.11 shows the Laplacian and the deformation density maps for one of the cyclopentadienyl (Cp) ligands. These maps show an even distribution of density throughout the rings, as is expected based on the delocalization of density present in these aromatic ligands. The average electron density in each bond of the cyclopentadienyl ligand is 2.037(14) $eÅ^{-3}$. The average value of the Laplacian at each bond critical point

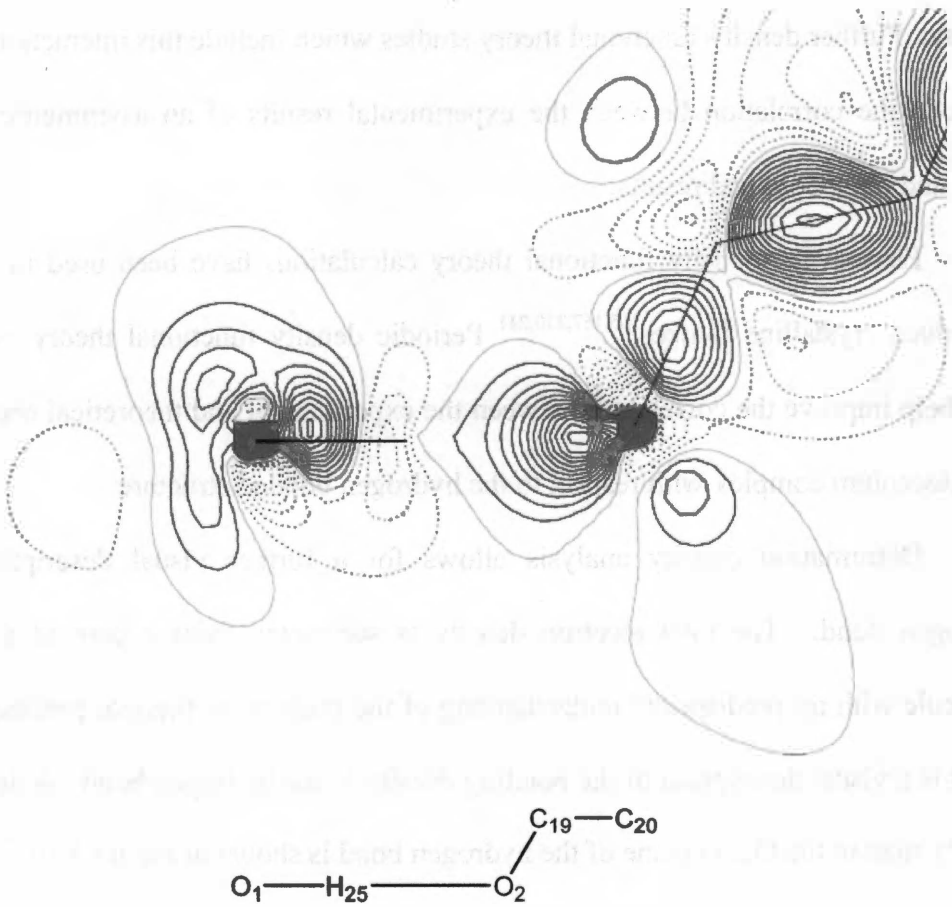


Figure 3.10. Deformation density map of the O-H...O vector. Contour levels are drawn at 0.05 eÅ^{-3}. Positive values are represented by solid blue lines, negative values by dotted red lines and the zero level contour is a green solid line.

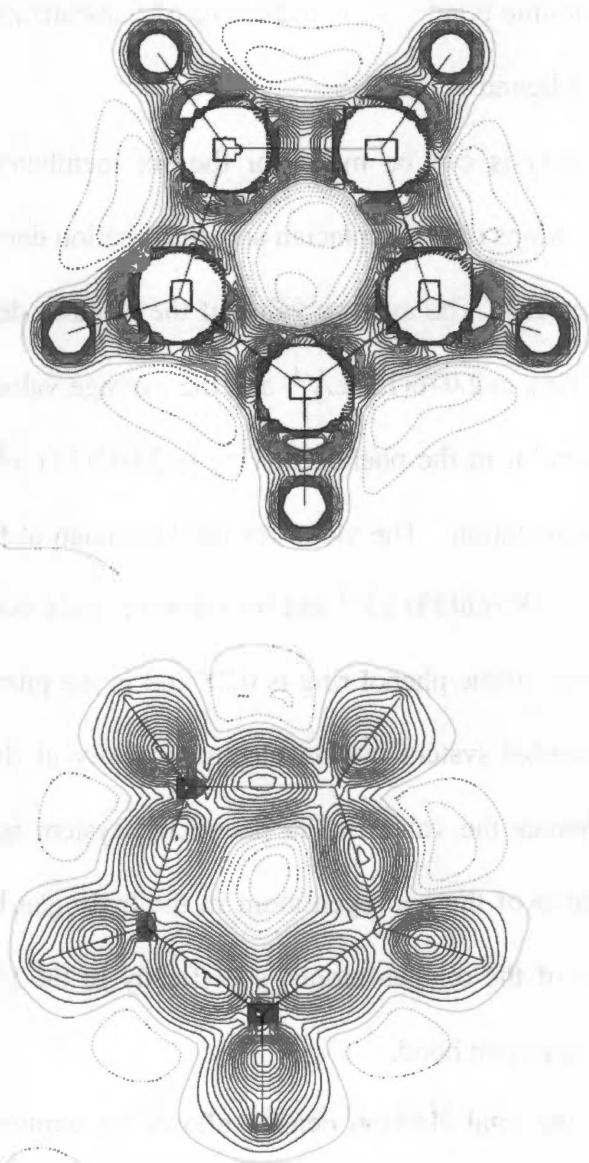
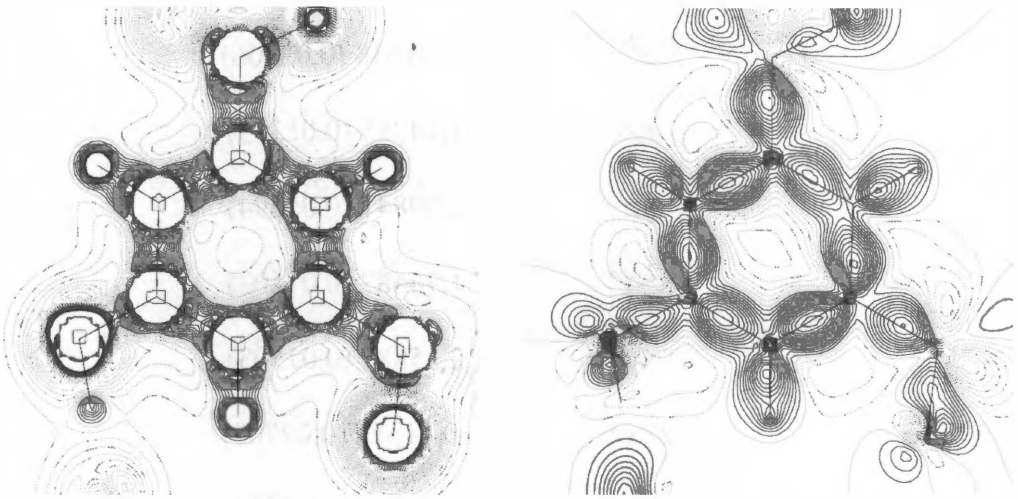


Figure3.11. Laplacian (top) and deformation density (bottom) maps of the Cp ring comprised of C1-C5. Contour levels are drawn at 2 eÅ^{-5} in the Laplacian and at 0.05 eÅ^{-3} in the deformation density map. Positive values are represented by solid blue lines, negative values by dotted red lines and the zero level contour is a green solid line.

in the Cp ring is -17.314(45) eÅ^{-5}. The average value for the ellipticity in the cyclopentadienyl ligands is 0.13, which is greater than the value for a single bond, yet less than that of a double bond[21,212], is indicative of delocalization of electron density in the cyclopentadienyl ligand.

A similar analysis can be made for the six membered rings; the phenol and phenoxide systems. Maps of the Laplacian and deformation density of the phenol system are shown in Figure 3.12. The average value of the electron density at the bond critical point in the phenol ring is 2.076(13) eÅ^{-3}, and the average value for the electron density at the bond critical point in the phenoxide ring is 2.049(12) eÅ^{-3}, which are equivalent within the standard deviation. The value for the Laplacian at the bond critical point of the phenol system is -18.766(33) eÅ^{-5} and for the phenoxide system is -18.018(32) eÅ^{-5}. The average ellipticity in the phenol ring is 0.28 and in the phenoxide ring is 0.27. The C-O bond of the phenol system has an electron density at the bond critical point of 2.228(15) eÅ^{-3}, whereas the value in the phenoxide system is 2.260(16) eÅ^{-3}. These densities are indicative of the hydrogen atom in the hydrogen bond being more closely associated with one of the oxygen atoms, specifically in the phenol molecule, and not being a symmetric hydrogen bond.

Analysis of the total electron density allows for explicit interpretation of the d orbital population. The central cobalt atom has a total d orbital population of 7.29088 electrons. The population of the *d*-orbitals as well as the mixing terms are analyzed in Table 3.1. The populations of *d*-orbitals are derived from a least squares analysis of the coefficients of the multipole populations,[213]and there have been several previous studies analyzing the populations of d orbitals in inorganic and [21,214-216]organometallic



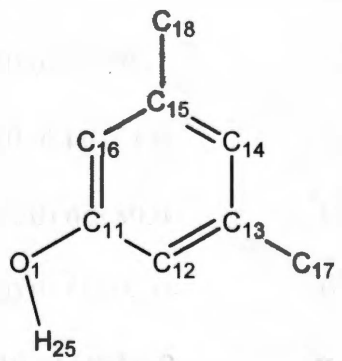


Figure 3.12. The Laplacian (left) in the plane of phenol system in III. Contour levels are drawn at 2 eÅ^{-5}. Deformation density map (right) of the phenol system. Contour levels are drawn at 0.05 eÅ^{-3}. Positive values are represented by solid blue lines, negative values by dotted red lines and the zero level contour is a green solid line.

*Table 3.1. d-orbital population summary for **III**.*

Orbital	Population
z^2	-0.01638 (0.02366)
xz	1.14265 (0.01713)
yz	2.09841 (0.01694)
x^2-y^2	1.74487 (0.01502)
xy	2.35881 (0.01503)
z^2/xz	-0.41377 (0.02707)
z^2/yz	-0.50068 (0.02419)
z^2/x^2-y^2	-1.29315 (0.02045)
z^2/xy	-0.13794 (0.01810)
xz/yz	-0.08756 (0.01971)
xz/x^2-y^2	-0.30825 (0.02096)
xz/xy	0.60703 (0.01956)
yz/x^2-y^2	-0.09232 (0.01965)
yz/xy	-0.00755 (0.02074)
x^2-y^2/xy	-0.23973 (0.01800)
total	7.32836

complexes. The assumption is made that the overlap between metal and ligand orbitals is very small and that the *d*-orbitals may be described by single Slater-type orbitals. Using charge density analysis, the total electron density in a molecular is described by

$$\rho_{atom} = P_{core}\rho_{core}(r) + P_{valence}\kappa^3 \rho_{valence}(\kappa r) + \sum_{l=0}^{l_{max}} \kappa'^3 R_l(\kappa' r) \sum_{m=0}^{l} P_{lm\pm} d_{lm\pm}(\vartheta, \varphi) \tag{3.1}$$

as described in detail in section 1.10.1. In transition metals, the *d*-orbital density is described by the second and third terms of equation (3.1).

$$\rho_{atom} = P_{valence}\kappa^3 \rho_{valence}(\kappa r) + \sum_{l=0}^{l_{max}} \kappa'^3 R_l(\kappa' r) \sum_{m=0}^{l} P_{lm\pm} d_{lm\pm}(\vartheta, \varphi) \tag{3.2}$$

The *d*-orbital occupancies, as products of individual pairs of d functions *viz* $d_i^1 d_j^1$ where both $i = j$ and $i \neq j$ are allowed, are expanded in terms of the real, density spherical harmonics. As the real density in the system must be independent of the description used, the description in terms of populations and hydrogenic *d* functions, the atomic description, and the description in terms of real, density spherical harmonics and refinement populations must also be equal. Given that any product of spherical harmonics can be expanded as a suitably weighted linear combination of other spherical harmonics, the two descriptions are simply connected by an effective transformation between the two 'representations', the transformation matrix being the weights of the linear combinations that describe the conversion between the two descriptions. Thus,

$$\mathbf{P_i} = \mathbf{M^{-1}} \mathbf{P_{lm\pm}} \tag{3.3}$$

where $\mathbf{P}_{lm\pm}$ is a vector containing the coefficients of the fifteen spherical harmonic functions generated by the products of the *d*-orbitals, $\mathbf{P}_i$ is fifteen element vector of the *d*-orbital population coefficients, and $\mathbf{M}^{-1}$ is the inverse of the matrix, **M**, which is defined by the *d*-orbital populations and their mixing terms, for *l=0, 2* or *4*, which are specific to a given point group.

Density functional theory calculations were performed on the $CoCp_2^+$ segment of the structure, both as single point and geometry optimized calculations. The molecular orbital diagram corresponding to these calculations is shown in Figure 3.13. The d orbital populations from these calculations are slightly higher than those obtained from the charge density studies. The total d orbital populations are 7.9185 and 7.9188, for the single point and geometry optimized calculations, respectively.

3.3 Conclusions

High resolution X-ray diffraction experiments were performed on cobaltocenium 3,5-bis(trifluoromethyl)phenoxide 3,5-bis(trifluoromethyl)phenol. The results showed an asymmetric, short, strong hydrogen bond between the phenol and phenoxide segments of the molecular structure. The maximum of the electron density in the hydrogen bond was located in a difference Fourier map as being approximately 0.98 Å from O1. Charge density analysis provided a complete description of the electron density both in the hydrogen bond as well as the rest of the molecular structure, in which the position of the maximum of the electron density in the hydrogen bond was refined to have an O1-H25 bond distance of 0.9790 Å and an O…H distance of 1.4824 Å.

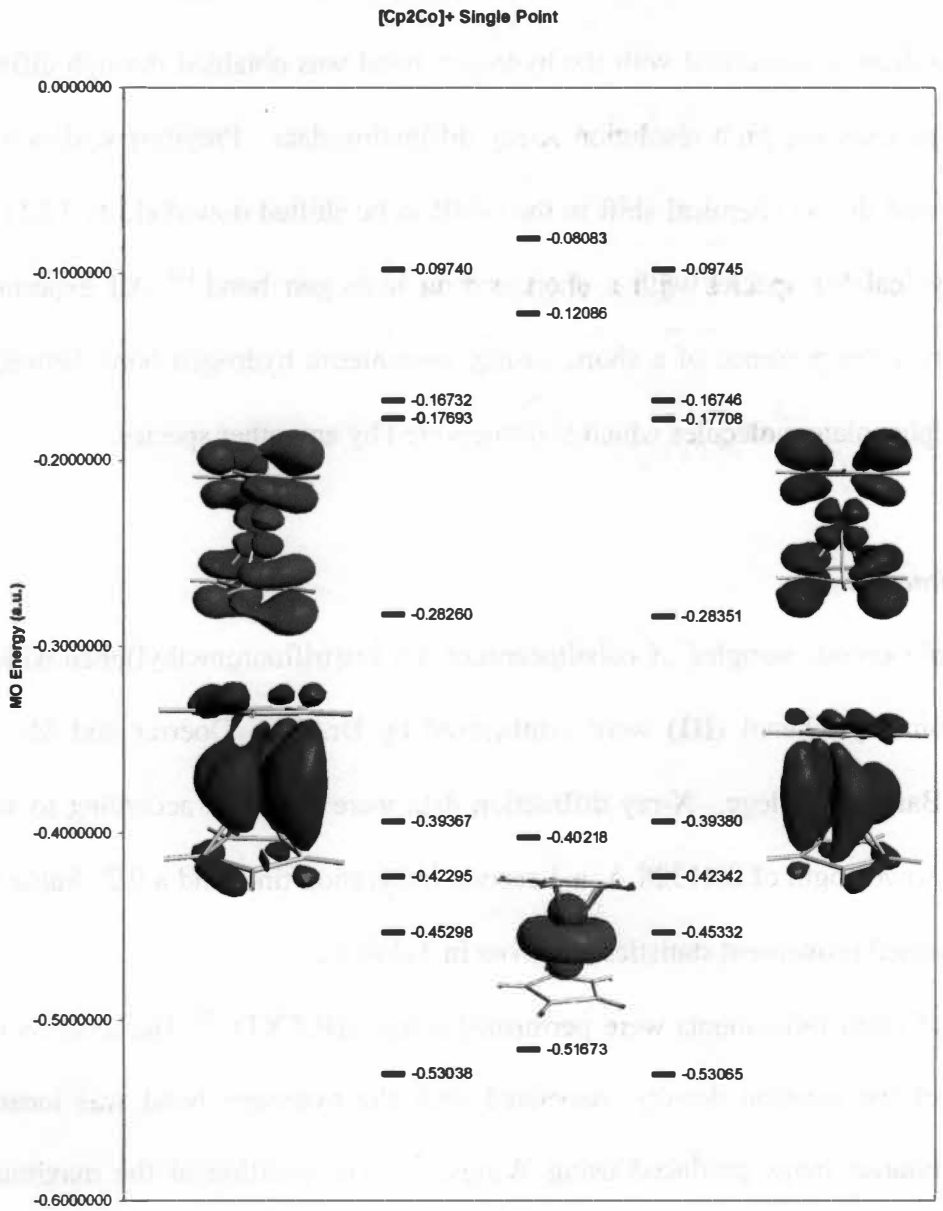


Figure 3.13. Molecular orbital diagram of the $CoCp_2^+$ based on single point density functional theory calculations.

On the basis of the simplest definition of a short, strong hydrogen bond[29], the phenolate-phenol moiety in III, clearly fits the criteria. The distance along the O...O vector is less than 2.5 Å and each O-H distance is less than 1.5 Å. Direct visualization of the electron density associated with the hydrogen bond was obtained through difference Fourier maps from the high resolution X-ray diffraction data. Previous studies on this system showed the ^{1}H chemical shift in the NMR to be shifted downfield to 17.11 ppm, which is typical for species with a short, strong hydrogen bond.[168] All experimental results support the presence of a short, strong, asymmetric hydrogen bond between the phenol and phenolate molecules which is unsupported by any other species.

3.4 Experimental

Single crystal samples of cobaltocenium 3,5 bis(trifluoromethyl)phenoxide 3,5-bis(trifluoromethyl)phenol (**III**) were synthesized by Dr. L.H. Doerrer and Ms. M.C. Buzzeo at Barnard College. X-ray diffraction data were collected according to section 7.4, with a wavelength of 0.41328 Å, a 1 second integration time and a 0.2° frame width for **III**. Selected refinement statistics are given in Table 3.2.

Spherical atom refinements were performed using SHLEXTL.[93] The location of the maximum of the electron density associated with the hydrogen bond was located in difference Fourier maps produced using Wingx.[127] The position of the maximum of electron density was used as a starting point for the spherical atom refinements, in which the positional parameters of the H atom were refined freely as well as the isotropic thermal parameter. The position and thermal parameter of the hydrogen atom was then held constant throughout the aspherical atom refinement. Aspherical atom refinements

Table 3.2. Selected refinement statistics for III.

Unit cell	a = 8.2263(16) b = 35.610(7) β = 102.58(3) c = 8.7012(17)
z	4
Space Group	$P\,2_1/n$
Absoption coefficient (μ)	0.425 mm^{-1}
Reflections	-18 <=h <= 18 -91 <=k <= 91 -21 <=l <= 21
Reflections	102396
Parameters	1151
R(F)	0.0351
wR(F)	0.0473
GOF	1.1916

were performed using XDLSM, part of the XD suite of programs.[22] The cobalt atom and the cyclopentadienyl carbon atoms, C1-C10, were refined with a hexadecapole expansion. All other carbon atoms, oxygen and fluorine atoms were refined with an octupole expansion. Most hydrogen atoms were refined with a monopole, H25 was refined with a z-directed dipole. κ and κ'were refined for all non-hydrogen atoms. The progress and stability of the refinement was checked by analysis of the residual electron density using XDFFT as well as analysis of the difference means squares displacement amplitude using Hirshfield's rigid body analysis.[217]

Chapter 4: The experimental and theoretical electronic structure of 1,2,3,4,5,6,7,8-octahydro-2a,4a,6a,8a-tetraaza-cyclopenta[fg]acenaphthylene and its derivatives

Crystalline samples of 1,2,3,4,5,6,7,8,8*c*-Octahydro-1*H*-4*a*,6*a*,8*a*-triaza-2*a*-azoniacyclopent[*fg*]acenaphthylene bromide, **[IVH]$^+$**, 1,2,3,4,5,6,7,8,8*c*-octahydro-6*a*,8*a*-diaza-2*a*,4*a*,-diazoniacyclopent[*fg*]acenaphthylene **[IV]$^{2+}$** and 1,2,3,4,5,6,7,8-octahydro-2a,4a,6a,8a-tetraaza-cyclopenta[fg]acenaphthylene, **(IV)**, were prepared by Mr. A.J. Colvin or Mr. B.C. Harrison. Density Functional Theory calculations and photoelectron spectroscopy measurements were performed by Mr. R.C. Lonsdale and Professor J.C. Green, respectively, at the University of Oxford.

4.1 Introduction

Electron-rich alkenes have found use in several areas of materials chemistry as reducing agents in the formation of organic metals and organic-based magnetic materials.[218-224] A sub-class of electron-rich alkenes contains the tetrazaalkenes, which possess the general framework shown in Figure 4.1.

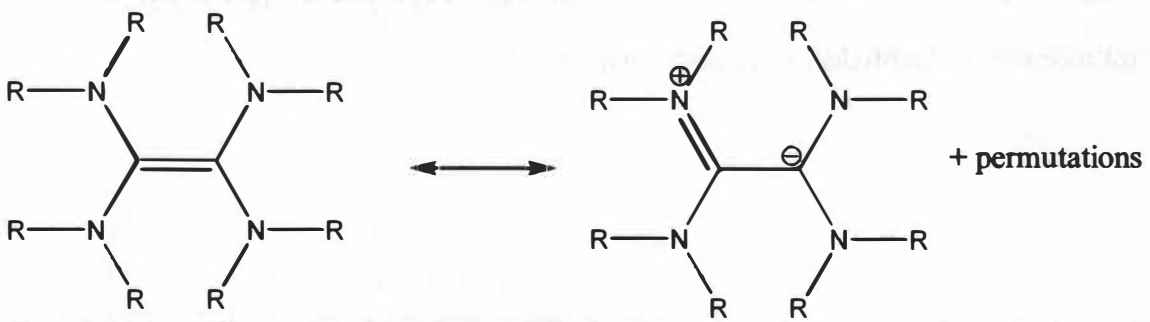


Figure 4.1. The general tetrazaamine framework and one of the simple, polar contributions to the ground state

The electronic structure of compounds that possess this frame work is dominated by the π-donation into the C=C bond, with polar resonance contributions to the ground state structure expected on a qualitative, valence bond basis. Since the first synthesis of this type of functionality, the electron-rich nature has been noted.[225-231]

The simplest and most widely used tetraazaalkene is *tetrakis*(dimethylamino)ethylene (TDAE) (R = Me in Figure 4.1).[231] The structures of TDAE[231] and $[TDAE]^{2+}$ [230,232] are known and are shown schematically in Figure 4.2. In the neutral species, the N_2CCN_2 framework is almost planar, whereas, in the dication, the two $(Me_2N)C$ moieties are staggered. A projection down the central C…C vector of these two species is shown in Figure 4.3, which depicts the difference in torsion angles between TDAE and $TDAE^{2+}$. [124] The torsion angles described by N-C and C-N for these species are 28.02° and 75.78°, for TDAE and $TDAE^{2+}$, respectively.

The electron-rich nature of TDAE has been confirmed by early photoelectron spectroscopic measurements,[233] which show the first ionization energy of TDAE at 5.95 eV. The ease of ionization is also reflected in the chemical reactivity of the system; TDAE is a highly reactive material that has been used in organic chemistry extensively.[228,229,234-241] Indeed it has been termed 'organic zinc',[239] due to its reducing power in solution but belying the involvement of both ion size and ionization energy in the reductive chemistry displayed. The reducing power of TDAE is also shown in the reaction of TDAE with C_{60}, which gives rise to the salt $[TDAE][C_{60}]$, which displays ferromagnetism at low temperature and thus constitutes a rare example of an organic ferromagnet.[242-249]

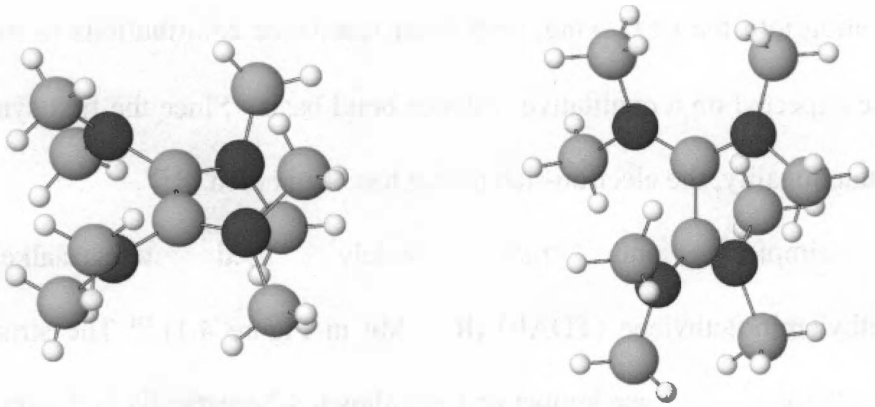


Figure 4.2. Schematic representations of the molecular structure of TDAE (left) and $[TDAE]^{2+}$ (right).

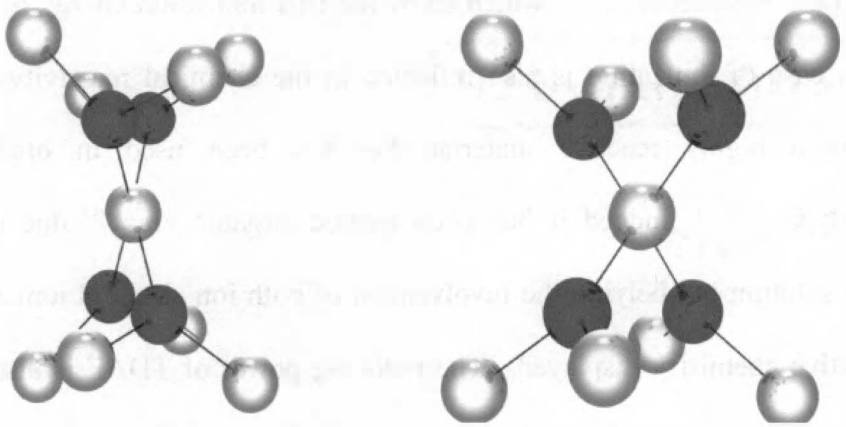


Figure 4.3. Projections down the C-C vector of TDAE (left) and $TDAE^{2+}$ (right) demonstrating the difference in torsion angles in the two species.

The tetrazaalkene framework is also of interest due to the formal relationship with the *N*-heterocyclic or Arduengo-Wanzlick carbenes, shown schematically in Figure 4.4, the equilibrium being termed the Wanzlick equilibrium.[52,250-253] The equilibrium shown in Figure 4.4 has been extensively investigated by Lemal,[250-252,254] Denk[234] and Alder,[255-259] amongst others; the equilibrium position has been found to lie extensively to the left hand side as written from crossover experiments using closely similar tetraazaamines, though the exchange has been found to be easily catalyzed by electrophiles. Indeed, the reaction of tetraazaamines with transition metal complexes was one of the early methods of synthesis for *N*-heterocyclic carbene-transition metal complexes.[260-270]

The work presented in this chapter details the compete distribution of electron density in **IV**, and compares the molecular structure of **IV** to two of its derivatives, $[\mathbf{IV}]^{2+}$ and $[\mathbf{IVH}]^{+}$, the chemistry of which is shown in scheme 4.1. Given the unusual *pseudo*-planar nature of the N_4C_2 core, *vide infra*, complete characterization of the bonding situation in **IV** is investigated in both the ground state electron distribution

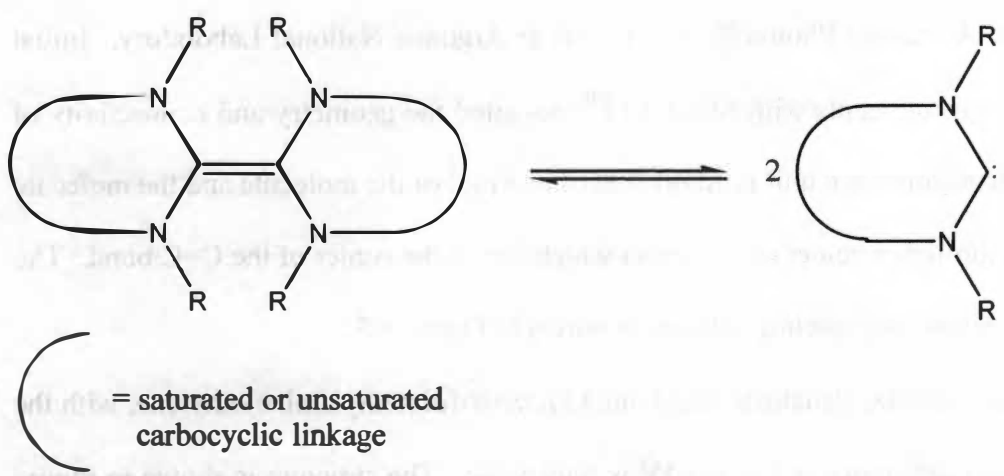
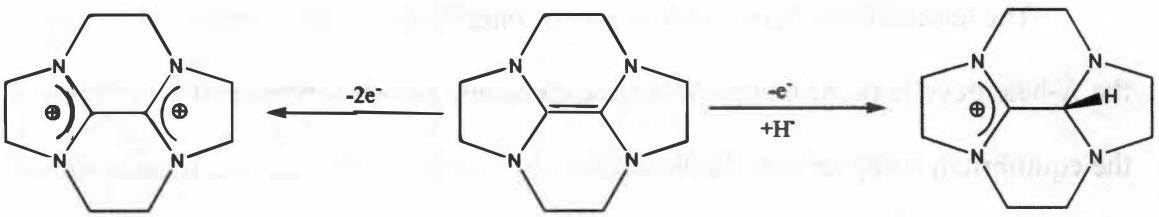


Figure 4.4. The Wanzlick equilibrium



Scheme 4.1. Chemistry of IV.

experimentally using X-ray scattering to define the autocorrelation function of the electron density in the crystal, which was then modeled using a charge density approach, augmented by theoretical calculations using density functional theory on the observed molecular structure. In order to gain information on the electronic energies, photoelectron spectroscopy measurements of the ionization energies of **IV** were undertaken in order to correlate the calculated with the experimental energies.

4.2 Results

4.2.1 Molecular and crystal structure of IV

X-ray diffraction data were collected on the in-house Bruker diffractometer as well as at the Advanced Photon Source (APS) at Argonne National Laboratory. Initial spherical atom refinements with SHELXTL[93] revealed the geometry and connectivity of **IV**. In **IV**, the asymmetric unit is comprised of one half of the molecule and the molecule is completed through a center of inversion which lies at the center of the C=C bond. The molecular structure and labeling scheme is shown in Figure 4.5.

IV has a similar structural backbone to *tetrakis*(dimethylamine)ethylene, with the major structural difference being that **IV** is polycyclic. The structure is shown in Figure 4.5. However, the two species are electronically very different. **IV** is an atypical

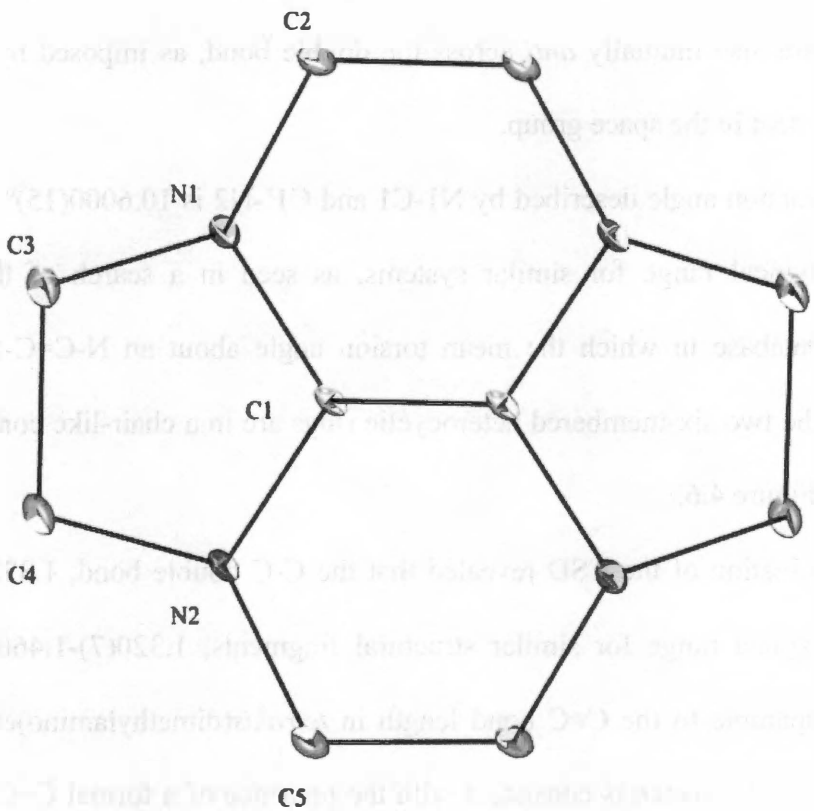


Figure 4.5. Molecular structure of IV, with the asymmetric unit labeled. Thermal ellipsoids are drawn at the 50% probability level and all hydrogen atoms have been omitted for clarity.

tetraazaalkene in that it is polycyclic; however, it is typical in the sense that it is very electron-rich and contains the N_4C_2 core. The molecular structure is unsurprising and contains two imidazolinyl rings in mutually *anti* envelope conformations, fused with an octahydro-pyrazino[2,3-b]pyrazine nucleus. The C_4N_2 rings of the last residue are in the standard conformation for general cyclohexenyl ring systems and imply that the lone pairs on N are also mutually *anti* across the double bond, as imposed by the center of inversion present in the space group.

The torsion angle described by N1-C1 and C1'-N2 is 10.6000(15)°, which is well within the typical range for similar systems, as seen in a search of the Cambridge Structural Database in which the mean torsion angle about an N-C=C-N fragment is 8.716 [34,35] The two six-membered heterocyclic rings are in a chair-like conformation and is shown in Figure 4.6.

Examination of the CSD revealed that the C-C double bond, 1.332(2) Å is well within the typical range for similar structural fragments, 1.320(7)-1.460(7) Å, and is directly comparable to the C=C bond length in *tetrakis*(dimethylamino)ethylene, 1.350 Å.[34,35] This bond distance is consistent with the presence of a formal C=C double bond,

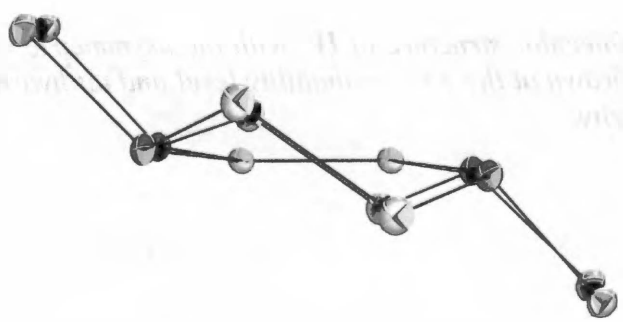


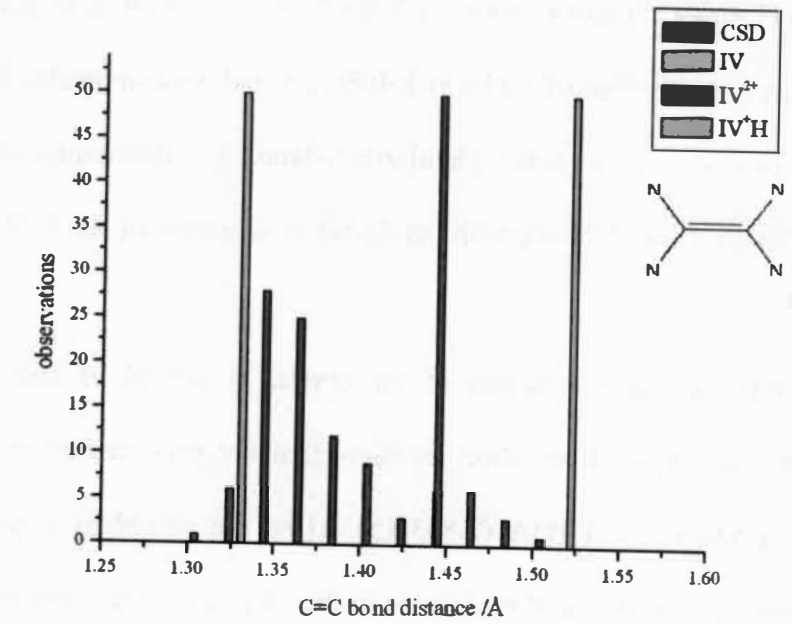
Figure 4.6. Side view of IV, showing the chair-like conformation of the six membered rings.

with no evidence of conjugation as would be indicated by a longer bond length. The N-C bond lengths (1.4096(15) and 1.4104(15) Å for N1-C1 and N2-C1, respectively) are also well within the normal range of 1.334(5)-1.408(5) Å and are comparable to the C-N bond length of 1.418 Å in *tetrakis*(dimethylamino)ethylene. The distribution of C=C and C-N bond distances in a NC=CN segment, as found in a search of the CSD, are shown in Figure 4.7.[34,35]

The intermolecular structure of the crystal is devoid of any strong contacts between molecules apart from short contacts that are present between C2 and H3A [2.872(19) Å) and C3 and H3A (2.853(15) Å] of the neighboring molecule. These contacts create *zig-zag* sheets of molecules in the *ab* plane. There are no other apparent intermolecular contacts present with the intermolecular distance between layers being greater than 4 Å, which is evident in the packing diagram shown in Figure 4.8.

4.2.2 Molecular and crystal structure of [IV]$^{2+}$

Compared to **IV**, the molecular structure of $C_{10}H_{16}N_4^{2+}$ is relatively planar and retains the same connectivity. The molecular structure is shown in two orientations in Figure 4.9. The torsion angle about the C...C vector in the N_4C_2 unit is 0.22(5)°, as compared to 10.6000(15)° in **IV**, and there are other clear and significant differences between **IV** and **[IV]$^{2+}$**. The presence of the double bond in **IV** leads to the strain on the molecule; conversely, the lack of a double bond in the dication reduces the amount of strain on the molecular structure, which is evident from the values for the torsion angle. However, a search of the CSD shows that for a NC=CN segment, the range of observed



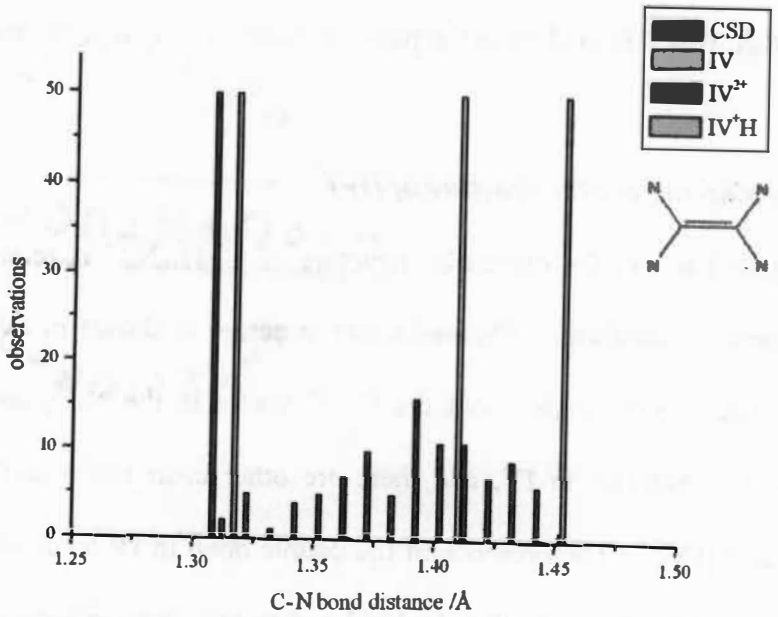


Figure 4.7. Distribution of bond distances in a search of the CSD on a NC=CN fragment.

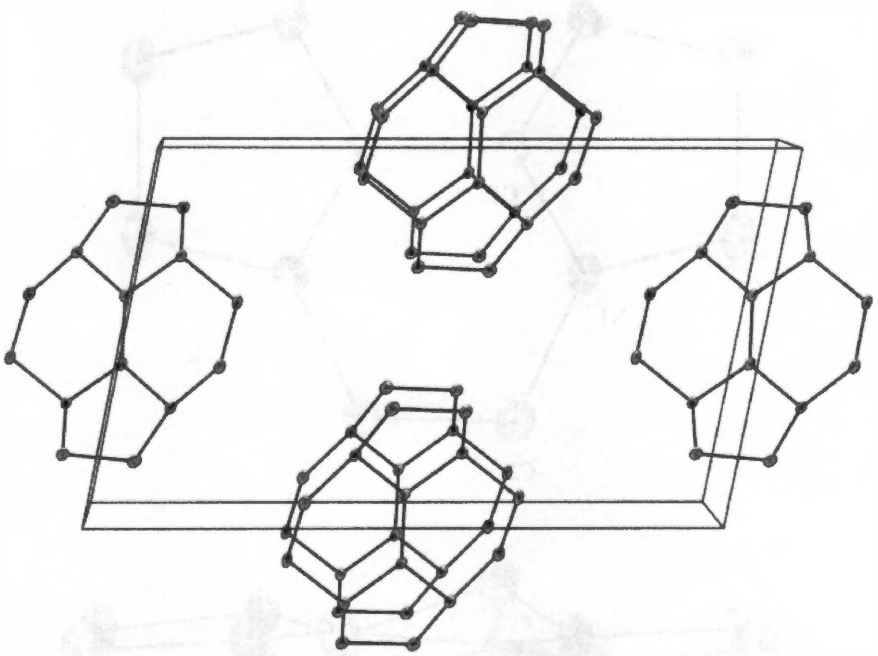


Figure 4.8. Packing diagram of (IV)

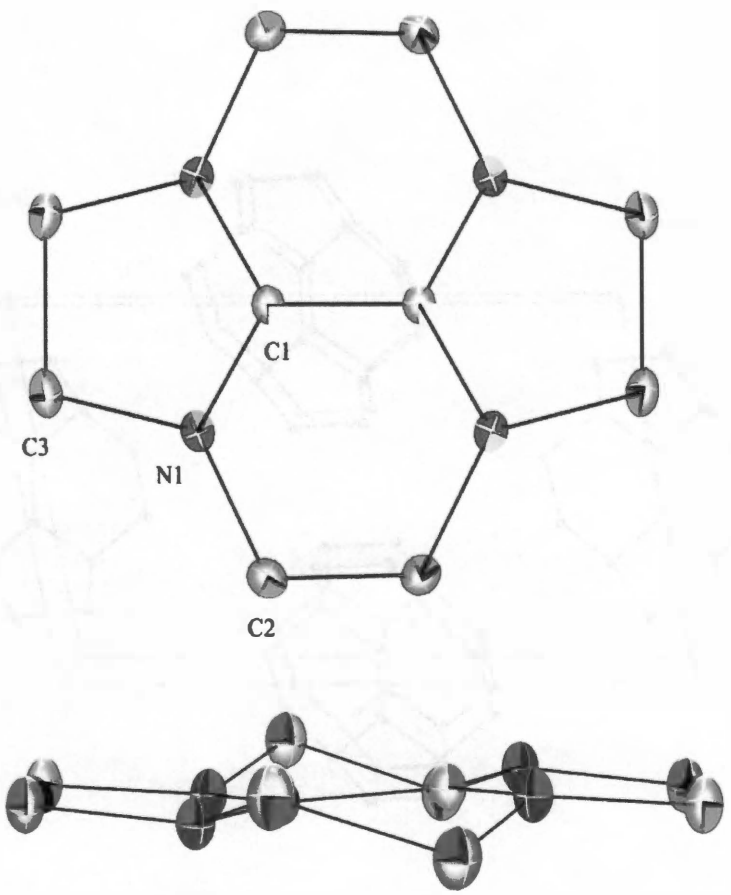


*Figure 4.9. ORTEP diagram of the dication, **[IV]**$^{2+}$, and a side view of the molecule. Hydrogen atoms have been omitted for clarity, thermal ellipsoids are drawn at the 50 % probability level and the asymmetric unit is labeled.*

values for the torsion angle is zero to 180°, with the mean torsion angle being approximately 2.004°, of which both of these structures fall in this range.[34,35] The distribution of N-C-N angles and NC=CN torsion angles is shown in Figure 4.10 with a comparison of the values observed in **IV**, $[\mathbf{IV}]^{2+}$ and $[\mathbf{IVH}]^{+}$.

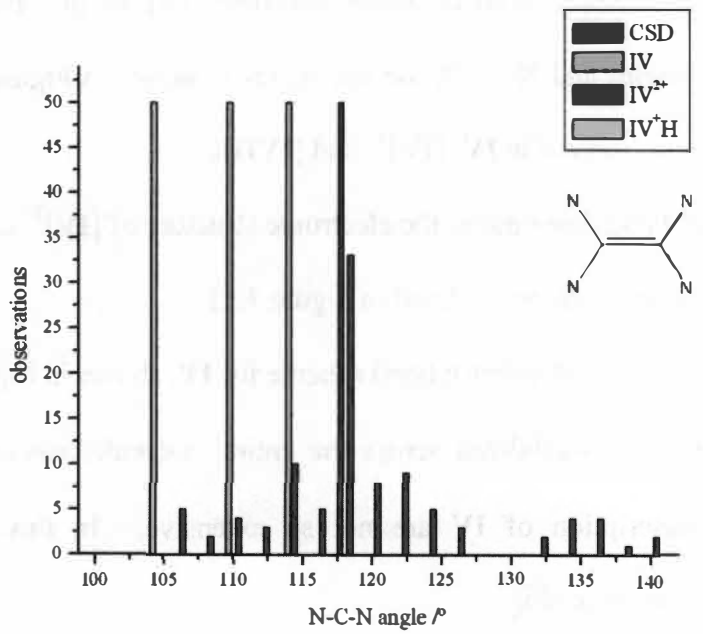
Under a valence bond description, the electronic structure of $[\mathbf{IV}]^{2+}$ can be written with several resonance contributions, outlined in Figure 4.11

In comparison to a similar valence bond scheme for **IV**, shown in Figure 4.12, the resonance contributions are π-stabilized across the entire molecule, whereas the polar contributions in the description of **IV** are not so extensive. In this respect, the comparative planarity is unsurprising.

4.2.3 Molecular and crystal structure of [IVH]⁺

The molecular structure of $[\mathbf{IVH}]^{+}$ is shown in Figure 4.13 and is very different to both **IV** and $[\mathbf{IV}]^{2+}$ molecular structures in the C-C back bone. The torsion angle described by the central N-C and C-N bonds is 31.9 (2)°. The side of the structure that is described by the protonated central carbon atom is bent out of the plane of the rest of the molecule by 98.16(8)° as described by the angle C2-C1 and the centroid (Ct01) between atoms C5 and C6, as shown in Figure 4.14.

Removal of the formal double bond from the central C...C vector lengthens the bond distance in $[\mathbf{IV}]^{2+}$ to 1.4427(18) Å compared to 1.3332(14) Å in **IV** and is further lengthened in $[\mathbf{IVH}]^{+}$ to 1.516(3) Å. In **IV**, the average C1-N bond distance is 1.411(10) Å, whereas the distance in the dication, $[\mathbf{IV}]^{2+}$, in slightly shorter at 1.3074(8) Å. In



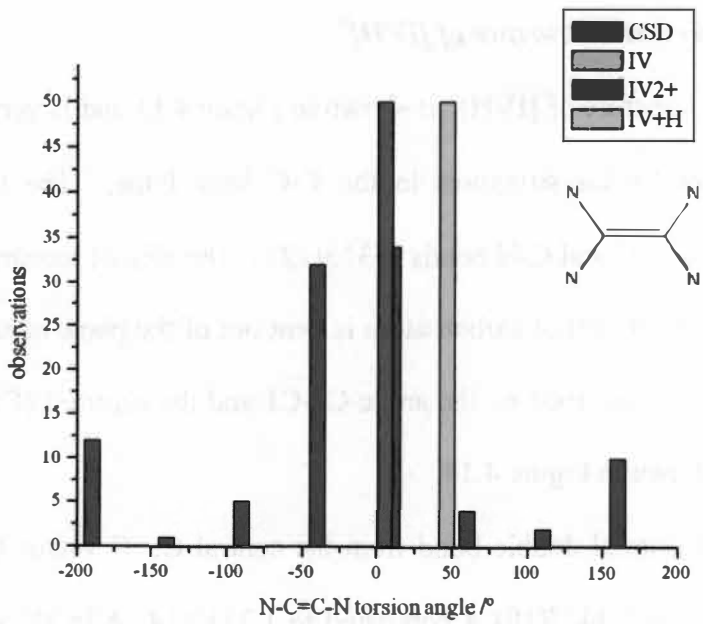


Figure 4.10. Distribution of angles and torsions angles in a NC=CN segment from a search of the CSD.

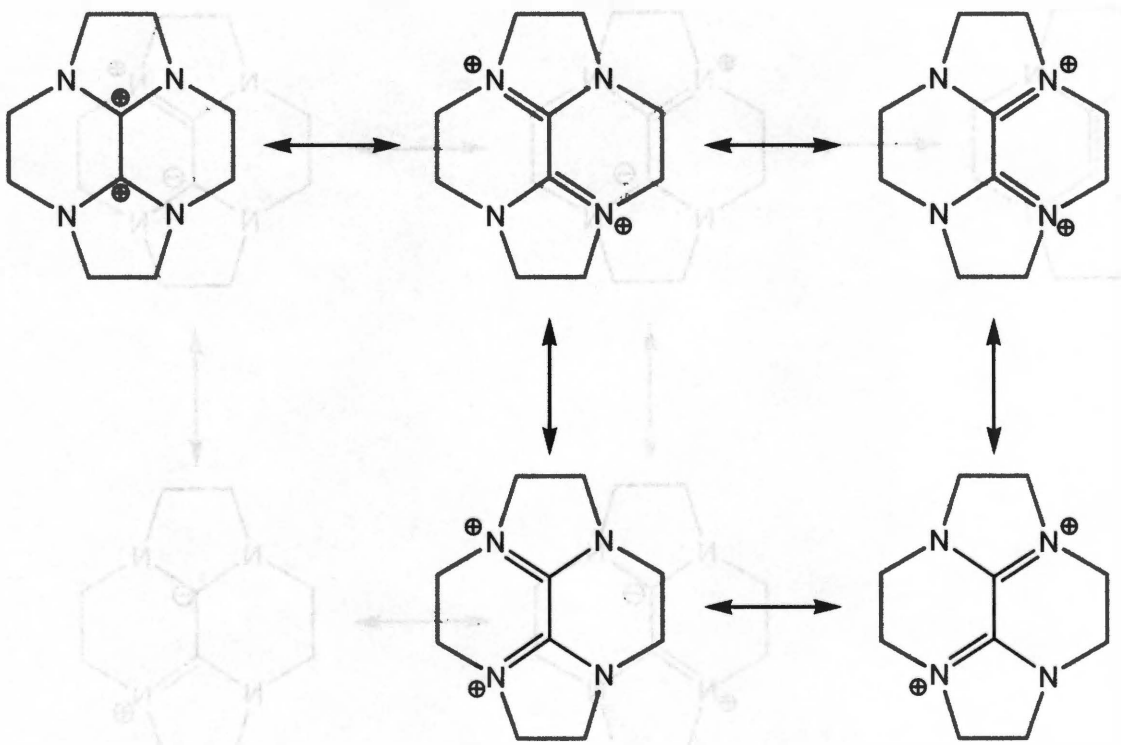


Figure 4.11. Valence bond description of $[IV]^{2+}$.

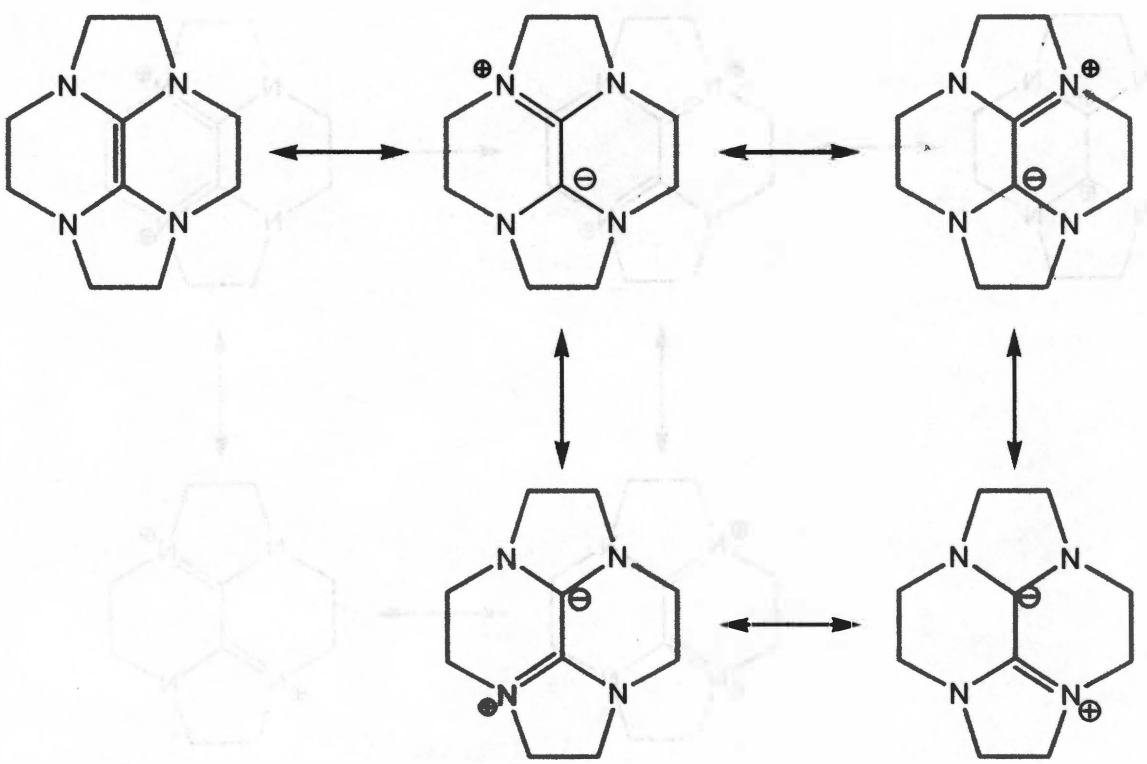


Figure 4.12. Valence bond description of IV.

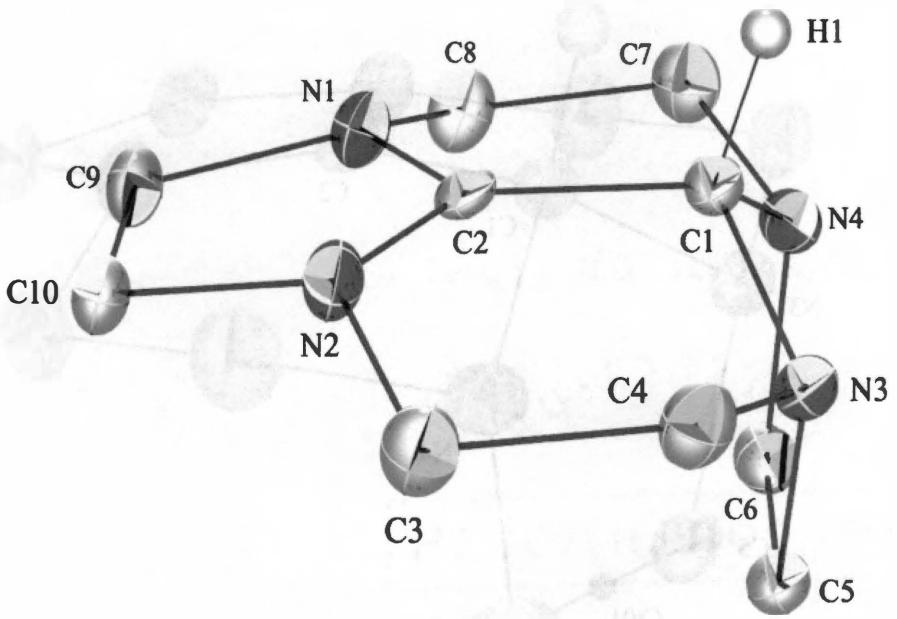


Figure 4.13. ORTEP diagram of ***[IVH]***$^{+}$. *Most hydrogen atoms have been omitted for clarity. Thermal parameters are drawn at the 50 % probability level.*

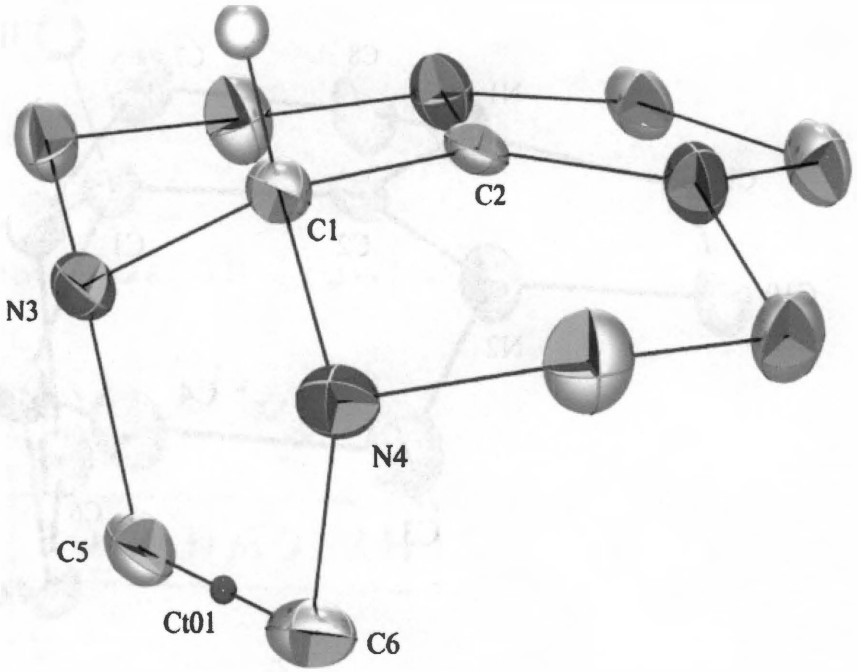


Figure 4.14. Description of the 98.16(8)° bend in ***[IVH]***$^{+}$*, which is defined by C2-C1-Ct01.*

$[\mathbf{IVH}]^+$, this bond distance for the protonated carbon, C1, is 1.450(2) Å, but for the non-protonated carbon, the average distance is 1.315(2) Å, showing similarities to $\mathbf{IV}^{2+}$.

As in **IV**, there are no hydrogen bonds present in $[\mathbf{IV}]^{2+}$ or $[\mathbf{IVH}]^+$. However, there are several short contacts, defined by van der Waals interactions, present in each of these structures. In $[\mathbf{IV}]^{2+}$, there is a contact between each iodide ion and the central C^+ atoms, with a distance of approximately 3.629 Å and this interaction may be seen in Figure 4.15. In $[\mathbf{IVH}]^+$, there are several contacts between the bromide ion and the non-protonated side of the molecule, as is depicted in Figure 4.16. The distance of these interactions ranges from approximately 2.972 Å to 3.544 Å.

The distribution of electron density in $[\mathbf{IV}]^{2+}$ and $[\mathbf{IVH}]^+$ is very different to that in **IV**. In $\mathbf{IV}^{2+}$, the double bond at the central carbon atoms has been removed, alleviating the severe strain on the molecular structure of **IV**. This allows the molecule to adopt a more planar configuration and results in a drastic change in the bond lengths and angles in the structure. In $[\mathbf{IVH}]^+$, the protonation of one of the central carbon atoms again drastically changes the molecular structure of the system. On the side of the molecule where the protonation occurs, the five-membered ring bends to a 98.16(8)° angle, causing changes in the overall molecular geometry. This angle is defined by C2, C1 and the centroid (ct01) of C5 and C6, which has been described in Figure 4.14. Based solely on the argument of bond lengths, it would appear as though both $[\mathbf{IV}]^{2+}$ and $[\mathbf{IVH}]^+$ contain only a single bond along the central C...C vector. However, as is seen in the charge density analysis of **IV**, *vide infra*, the determination of bond order based on the single metrical parameter of the bond length is an inadequate and perhaps naïve interpretation in systems of this type.

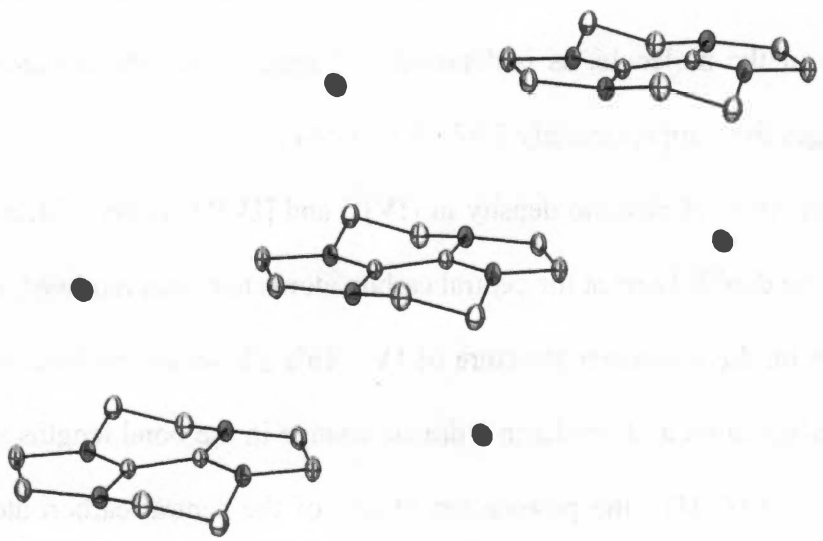


Figure 4.15. Diagram of $[IV]^{2+}$*, which shows the non-bonded contacts between the iodine atoms and the heterocyclic structure.*

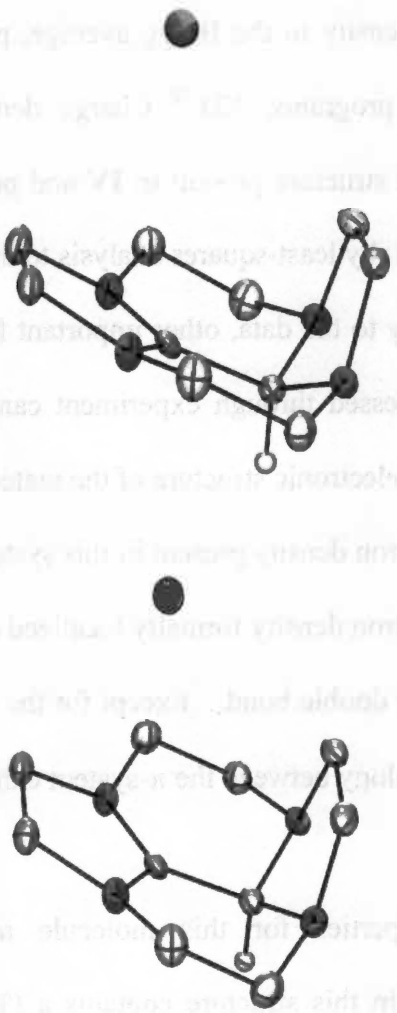


Figure 4.16. Diagram of [IVH]$^+$, showing the possible non-bonded contacts present in the structure.

4.3 Description of the experimentally determined electron density in IV

A more comprehensive understanding of the total distribution of electron density in **IV** is aided by high resolution X-ray diffraction experiments and charge density analysis of the scattering density in the Bragg average, performed using the aspherical atom refinement suite of programs, XD.[22] Charge density analyses yields in-depth information about the bond structure present in **IV** and provides an analytical model of the density that is the best fit by least-squares analysis to the measured density. From the best-fit model of the density to the data, other important features of the electron density that cannot be directly accessed through experiment can be generated calculationally, giving deep insight into the electronic structure of the material.

Analysis of the electron density present in this system shows a significant amount of delocalization of the electron density formally localized on the four nitrogen atoms and the two carbon atoms of the double bond. Except for the electron count and the nuclear charges, there is a direct analogy between the π-system exhibited in **IV** and other systems such as B_2F_4.

Selected bond properties for this molecule are presented in Table 4.1. Unsurprisingly, each bond in this structure contains a (3,-1) bond critical point. The presence of a center of inversion in the space group and the location of the asymmetric unit within the unit cell constrains the bond critical point to lie at the center of the C-C double bond. However, this is not the case in the remaining bonds. In the C1-N bonds, the bond critical point is displaced towards the nitrogen atoms. Analysis of the individual charge on each atom shows the unique nitrogen atoms, N1 and N2, possess a formal charge of -0.034 and -0.037 net to the isolated atom model respectively, whereas C1 has a

Table 4.1. Selected bond properties for IV based on aspherical atom refinements.

Bond	ρ /eÅ^{-3}	$\nabla^2\rho$ /eÅ^{-5}	bcp	R_{ij} /Å	d_1 /Å	d_2 /Å	ε
C1-C1	2.507(22)	-27.276(38)	(3,-1)	1.3382	0.6691	0.6691	0.55
C1-N1	1.950(35)	-14.411(103)	(3,-1)	1.4062	0.7845	0.6218	0.29
C1-N2	2.027(26)	-16.437(79)	(3,-1)	1.4060	0.7796	0.6264	0.21
N1-C2	1.752(16)	-12.955(48)	(3,-1)	1.4661	0.8337	0.6324	0.10
N1-C3	1.729(17)	-12.891(54)	(3,-1)	1.4792	0.8603	0.6190	0.10
N2-C4	1.721(18)	-12.052(55)	(3,-1)	1.4876	0.8621	0.6255	0.12
N2-C5	1.751(18)	-12.320(54)	(3,-1)	1.4690	0.8289	0.6401	0.07

formal charge of -0.013 in the same manner. In the remaining N-C bonds, not adjacent to the double bond, the location of the bond critical point is displaced towards the carbon atoms which, in the case of these bonds, are the more negative atoms in the bond with an average charge of approximately -0.629, net with respect to the isolated atom model of the system. It is notable from these charge density results that the location of the bond critical point is displaced toward the more electronegative atom.

The amount of electron density at each bond critical point is also given in Table 4.1, which shows a significant difference in the amount of electron density in the N-C bonds adjacent to the double bonded carbon atoms as compared to further removed C-N bonds.

Deformation density maps allow for visualization of the bonding density in this system. The deformation density map of **IV** in the N1-C1-C1' plane is shown in Figure 4.17. There is an accumulation of electron density in the carbon-carbon double bond as compared to the adjacent carbon-nitrogen bonds, which is evident in this figure.

The delocalization of the electron density is also emphasized by the values for ellipticity, or ε. As seen in Table 4.1, the value for ε in the carbon-carbon double bond is 0.55, which is similar to previous reported values for double bonds.[21,212] However, the ellipticity values for C1-N1 and C1-N2 are 0.29 and 0.21, respectively. These values are significantly greater than for the adjacent carbon-nitrogen bonds, for which the ellipticity ranges from 0.07 to 0.12, which are characteristic values for single bonded species.[21,212] Consequently, the ellipticity values for C1-N1 and C1-N2 in this system demonstrate a significant amount of delocalization of the electron density from the lone pairs of electrons on nitrogen distributed over the π bond.

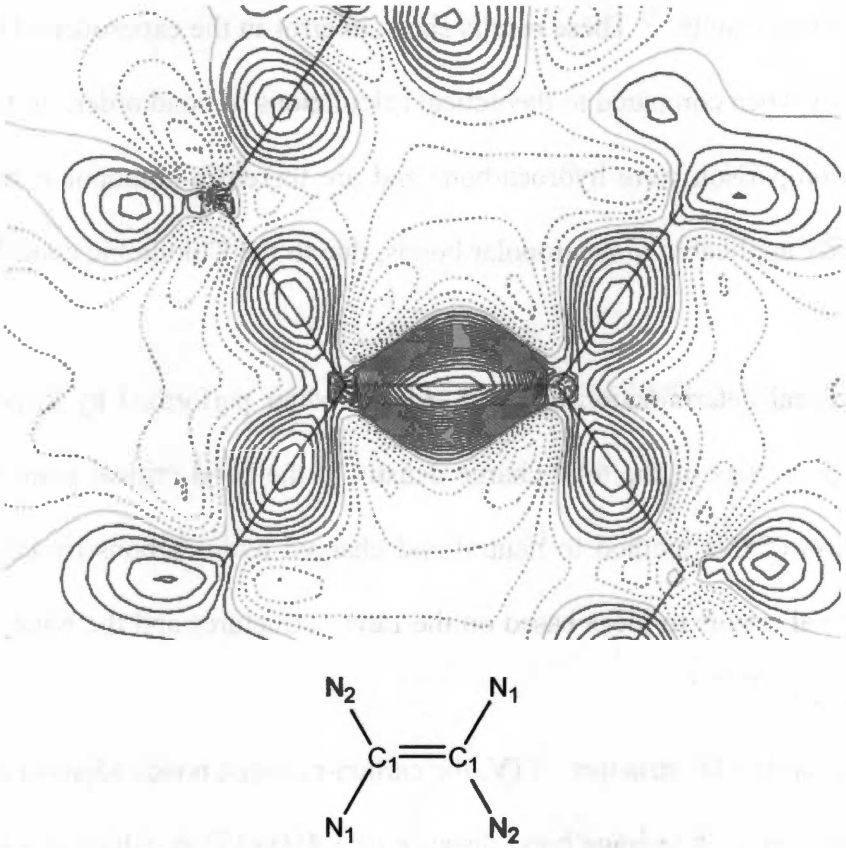


Figure 4.17. Deformation density map in the N-C-N plane. Contours are drawn at 0.05 e Å^{-3}. Positive values are represented by solid blue lines, negative values by dotted red lines and the zero level contour is a green solid line.

It is common practice in the assignment of bond type to use bond lengths as the determining metrical parameter. However, as shown by the ellipticity values, bond lengths are not always the best indicator of bond order. In 1951, Coulson provided a detailed analysis of the correlation of bond order versus bond length from both theoretical and experimental results.[271] These results show an error in the experimental bond lengths of only 0.02 Å when compared to theoretical calculations of bond order. In this work, the systems of comparison were hydrocarbons and are therefore homopolar; the method is not necessarily applicable to heteropolar bonds, due to the Coloumbic contribution to the bond energy.

A general determination of bond order is better performed by inspection of the topological properties of the total charge density at the bond critical point.[23,272] Indeed, the application of this method to neutral and charged hydrocarbons by Bader provides almost identical results to ideas based on the Lewis structures and the bond order - bond length correlation.[271-274]

In the molecular structure of **IV**, the carbon-nitrogen bonds adjacent to the central C-C backbone, have an average bond distance of 1.4100(15) Å, which is well within the range of typical single C-N bonds as seen in a search of the fragment $C_3C\text{-}NC_2$ (1.362 – 1.719 Å) with the mean distance being 1.493(1) Å. Although the C-N bond distances in **IV** correspond to a single bond based purely on length, a significant amount of π-character is present due to delocalization over the p orbitals on nitrogen as is evident by the ellipticity.

The Laplacian, $\nabla^2\rho$, is also used as an indicator of the type of bond present in a molecular system. A negative value for the Laplacian is typical for covalently bonded species and is directly related to the bond character. A map of the Laplacian for **IV** is shown in Figure 4.18. Noticeably, the concentration of density in the double bond is significantly more than that of the adjacent bonds. The value for the Laplacian at the bond critical point in the C-C double bond is -27.276(38) $eÅ^{-5}$ as compared to the values for C1-N1 and C1-N2, which are -14.411(103) $eÅ^{-5}$ and -16.437(79) $eÅ^{-5}$, respectively. The C-N and C-C single bonds in **IV** have values for the Laplacian that range from approximately -9.8 $eÅ^{-5}$ to -12.9 $eÅ^{-5}$.

Of the four possible types of critical points, a (3,+1) critical point is found at the center of a ring of atoms or at the center of a cage. There are two (3,+1) critical points that were located in **IV**. One is found at the center of the five membered ring composed of C1, N1, C3, C4 and N2 and the other is at the center of the six membered ring comprised of C1, N2, C5, C1', N1' and C4'. These (3,+1) critical points are displaced off the center of the rings being in closer proximity to C1.

4.4 Calculation of the electron densities in IV, $[IV]^{2+}$ and $[IVH]^{+}$

Geometry optimized DFT calculations were performed on **IV**, $[\mathbf{IV}]^{2+}$ and $[\mathbf{IVH}]^{+}$ by Professor J.C. Green's group at the University of Oxford. Table 4.2 lists selected bond lengths and angles for comparison between the geometry optimized calculated structure and the experimental structure for **IV**. The most pronounced difference between these two structures is the C-C double bond length. In the experimental structure, the C1-C1' bond distance is 1.3332(4) Å, whereas in the calculated structure,

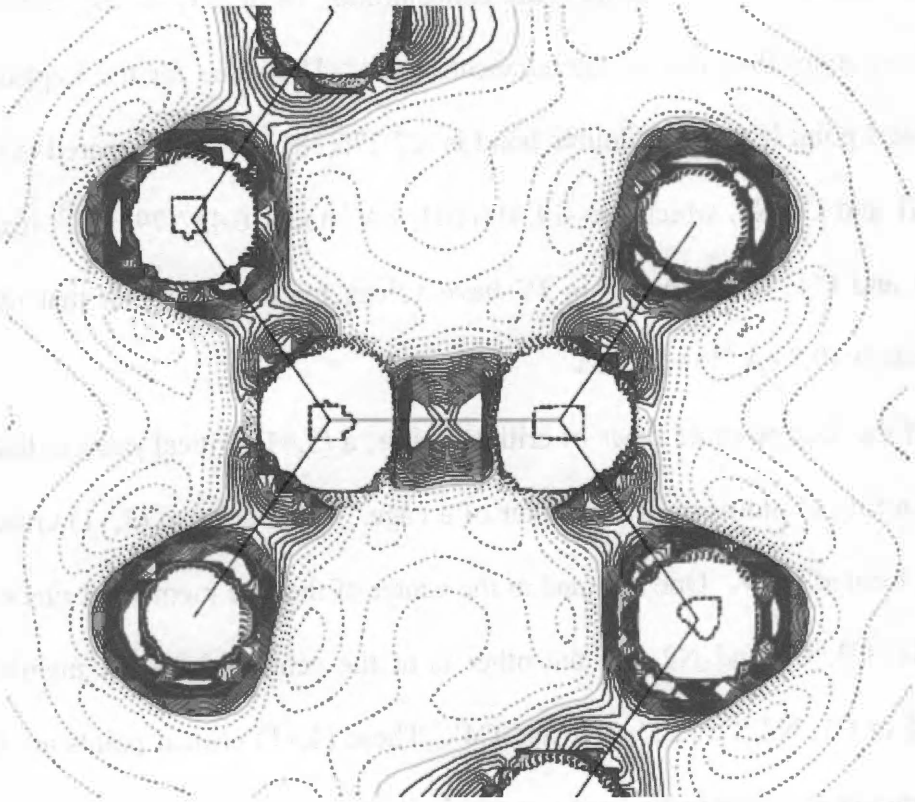


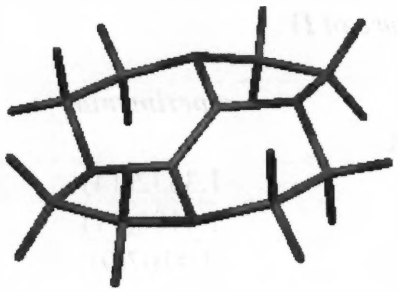
Figure 4.18. Laplacian in the N-C-N plane. Contours are drawn at 2 e $Å^{-5}$. Positive values are represented by solid blue lines, negative values by dotted red lines and the zero level contour is a green solid line.

Table 4.2 Selected geometric parameters for the experimental and calculated structure of IV.

	experimental	***calculated***
Bonds /Å		
C1-C1'	1.3332(14)	1.341
C1-N1	1.4106(11)	1.411
C1-N2	1.4107(9)	1.408
Angles /°		
N1-C1-N2	109.89(6)	110.3
C1-N1-C3	103.42(6)	103.0
N1-C1-C1'	124.70(8)	124.5
N2-C1-C1'	124.69(9)	124.2
C2-N1-C1	110.55(6)	111.0
C5-N2-C1	109.92(6)	110.8

this distance is lengthened to 1.341 Å. The remaining bonds and angles in the molecular structure of **IV** are relatively similar between the experimental values and the geometry optimized calculated structure.

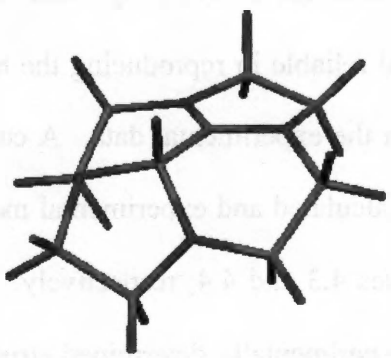
The optimized geometries of **IV**, $[\mathbf{IV}]^{2+}$ and $[\mathbf{IVH}]^{+}$ are shown in Figure 4.19. These calculations proved reliable in reproducing the molecular structure and geometric parameters obtained from the experimental data. A comparison of selected geometrical parameters between the calculated and experimental molecular structures for $[\mathbf{IV}]^{2+}$ and $[\mathbf{IVH}]^{+}$ are given in Tables 4.3 and 4.4, respectively. In $[\mathbf{IV}]^{2+}$, the most pronounced difference between the experimentally determined structure and the calculated model is less than 0.001 Å, clearly demonstrating a reliable interpretation of the molecular structure based on the density functional theory calculations. However, in the case of $[\mathbf{IVH}]^{+}$, there are striking differences between the two molecular structures. The most pronounced difference is found in the bond length of the central C-C bond. This



IV



IV^{2+}



$IV^{+}H$

Figure 4.19. Geometry optimized molecular structure of IV, $[IV]^{2+}$ and $[IVH]^{+}$ from Density Functional Theory calculations.

*Table 4.3. Comparison of selected geometric parameters of the experimental and calculated molecular structure of $[IV]^{2+}$. *Indicates the average distance or angle in the calculations.*

	experimental	*calculated*
Bonds /Å		
C1-C1'	1.4427(18)	1.445
C1-N1	1.3074(8)	1.315*
Angles /°		
N1-C1-N1	117.48(9)	117.3*
N1-C1-C1'	121.26(5)	121.4*

*Table 4.4. Comparison of selected geometric parameters of the experimental and calculated molecular structure of $[IVH]^{+}$. *Indicates the average distance or angle in the calculations.*

	experimental	*calculated*
Bonds /Å		
C1-C2	1.516(3)	1.470
C1-N3	1.450(2)	1.482
C1-N4	1.450(2)	1.445
C2-N1	1.314(2)	1.318
C2-N2	1.315(2)	1.309
Angles /°		
N3-C1-N4	103.64(16)	108.9
N1-C2-N2	113.35(19)	114.0
C1-C2-N2	123.13(16)	123.0*
C2-C1-N3	110.09(15)	111.7*

experimentally determined bond length is 1.516(3) Å, whereas the calculated structure shows a significantly shorter bond distance of 1.470 Å. However, the difference in the C-C bond lengths is not reflected in the subsequent bonds and angles in the calculated structure, which is reasonably reproduced from the geometry optimized density functional theory calculations.

4.5 Experimental measurement of the ionization of energies of IV

He I and He II photoelectron spectra for the neutral alkene are displayed in Figures 4.20 and 4.21 with a comparison of the experimental and calculated vertical ionization energies in Table 4.5. Assignment of the bands is also given in the Table 4.5. The adiabatic ionization energy was calculated as 5.625eV (cf. 5.3eV). The first band, A, is assigned to ionization of orbital 38, which is the highest occupied molecular orbital (HOMO), of which a diagram is shown in Figure 4.22. The intensity pattern of bands B-E suggests assignment of B and C to ionizations of orbitals 37 and 36 respectively, D to ionization of orbital 35 and E to the ionization of orbital 34, which is a π-orbital. Calculated ionization energies are in good agreement with the experimental values. Even though the geometric structure of **IV** is drastically different than TDAE, in that it is heterocyclic, there is a striking resemblance in the ionization energies. Strain on the molecular structure of **IV** is perhaps compensated for in the ionization when the molecule 'flattens out', increasing the orbital overlap, and thus resulting in an ionization energy that is very similar to TDAE.

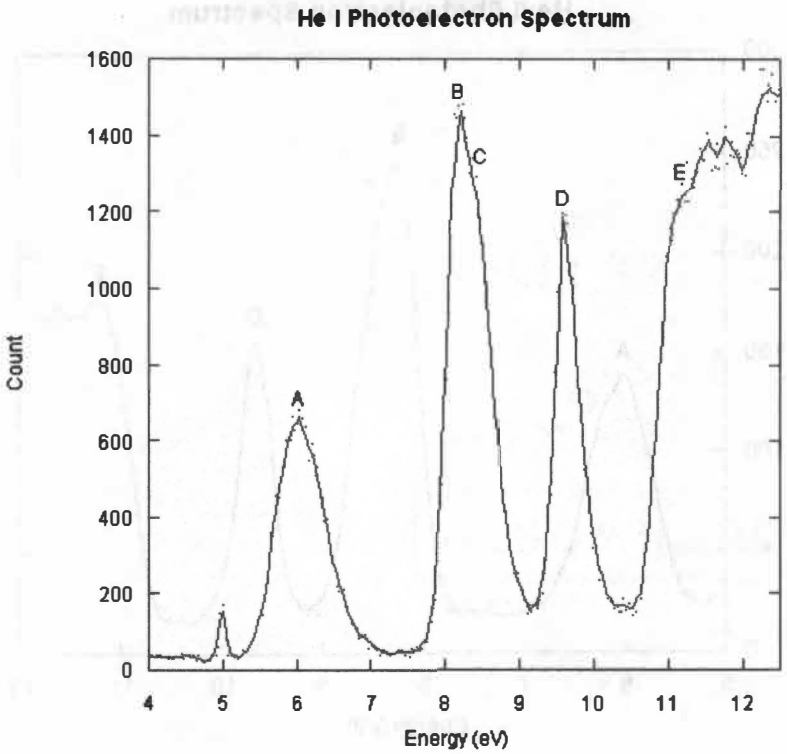


Figure 4.20. He I photoelectron spectrum of IV.

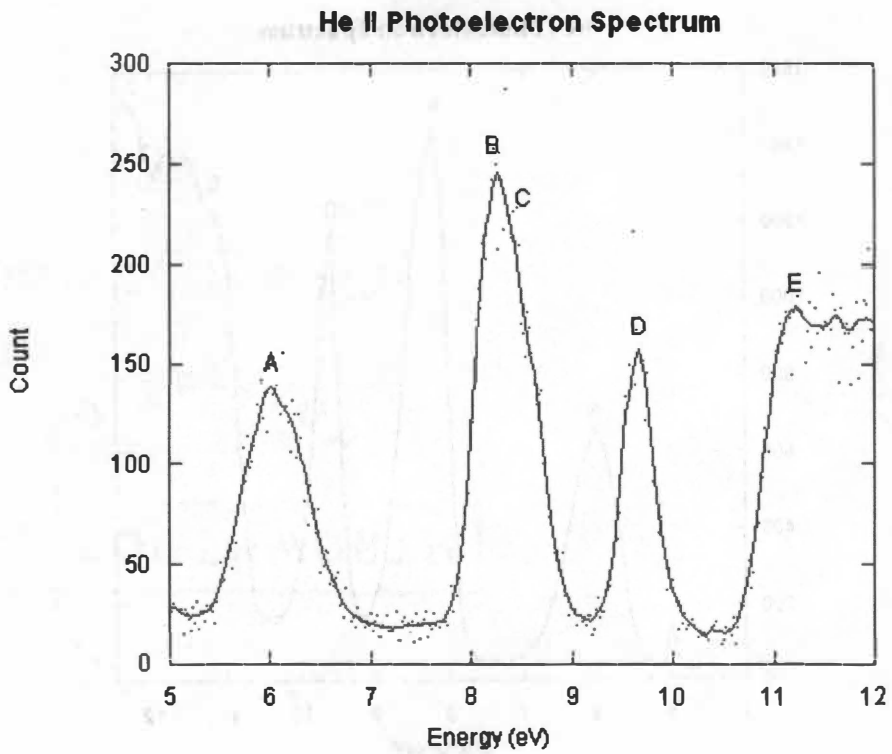


Figure 4.21. He II photoelectron spectrum of IV.

Table 4.5. Ionization energies for IV.

Orbital	*Orbital energy (/eV)*	*Ionization energy (calculated) (/eV)*	*Ionization energy (experimental) (/eV)*	*Photoelectron spectrum assignment*
39 *(LUMO)*	0.112			
38 *(HOMO)*	-3.013	6.142	6.031	A
37	-4.939	7.875	8.204	B
36	-5.088	8.239	8.553	C
35	-6.255	9.189	9.590	D
34	-7.806	10.749	11.330	E

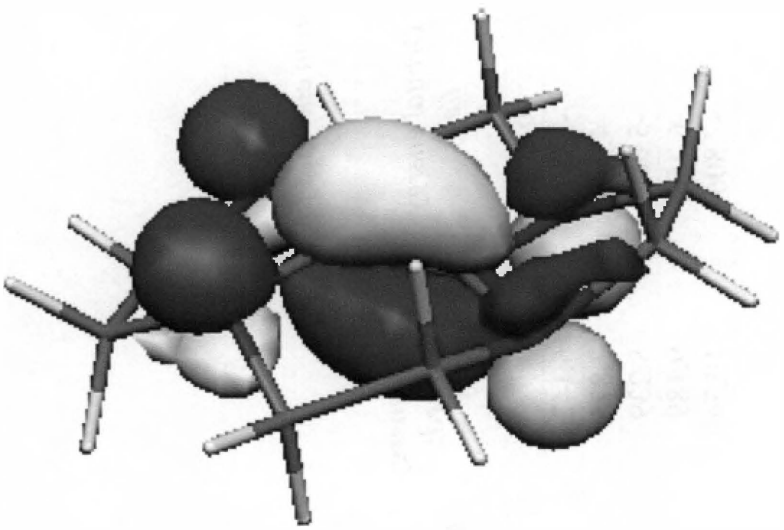


Figure 4.22. Highest occupied molecular orbital of IV from density functional theory calculations.

4.6 Conclusions

The total electron density in 1,2,3,4,5,6,7,8-octahydro-2a,4a,6a,8a-tetraaza-cyclopenta[fg]acenaphthylene was determined by high resolution X-ray diffraction. The results of these experiments show a significant amount of delocalization of the electron density in the π bond over the p orbitals on nitrogen. The delocalization is evident by analysis of the results of aspherical atom refinements as seen in the values for the electron density at the bond critical point and the ellipticity. The dication derivative of 1,2,3,4,5,6,7,8-Octahydro-2a,4a,6a,8a-tetraaza-cyclopenta[fg]acenaphthylene shows a relatively flat molecular geometry, whereas the protonated monocation is bent at an angle of 98.16(8)° at the protonated carbon. Analysis of these three molecular structures shows drastic changes in molecular geometry with the removal of the formal double bond character by protonation of the molecule.

4.7 Experimental

Samples of **IV**, $\mathbf{IV}^{2+}$ and $[\mathbf{IVH}]^{+}$ were prepared by either Mr. A.J. Colvin or Mr. B.C. Harrison.

Experimental charge density data for **IV** were collected according to section 5.4. Selected refinement statistics for **IV** are given in Table 4.6. X-ray diffraction experiments for $\mathbf{IV}^{2+}$ and $[\mathbf{IVH}]^{+}$ were collected in accordance with sections 5.3 and 5.1, respectively. Selected refinement statistics for $\mathbf{IV}^{2+}$ and $[\mathbf{IVH}]^{+}$ are given in Table 4.7.

Geometry optimized DFT calculations were preformed at the ICL at Oxford University using ADF by Professor J.C. Green and Mr. R. Lonsdale.[275-277] The generalized gradient approximation (non-local) using the local density approximation of

*Table 4.6. Selected refinement statistics for **IV**.*

Unit cell	a = 7.3861(15) b = 4.8808(10) β = 102.11(3) c = 13.042(3)
z	2
Space Group	$P\,2_1/n$
Absoption coefficient (μ)	0.057 mm^{-1}
Reflections	-14 <=h <= 14 -10 <=k <= 10 -27 <=l <= 27
Reflections	2536
Parameters	146
R(F)	0.0358
wR(F)	0.0254
GOF	2.2465

Table 4.7. Selected refinement statistics for $[IV]^{2+}$ and $[IVH]^{+}$.

	IV^{2+}	$IV^{+}H$
Temperature	173 K	173 K
Unit cell	a = 13.437(2) b = 8.9005(11) β = 115.141(4) c = 6.1153(8)	a = 7.763(3) b = 8.653(3) β = 99.407(6) c = 16.255(6)
Z	2	4
Cell setting	Monoclinic	Monoclinic
Space group	*C* 2/*m*	*P* $2_1/c$
Theta range	2.84 <= θ <= 51.16	2.54 <= θ <= 26.05
Index range for data collection	-28 <= h <= 29	-9 <= h <= 9
	-18 <= k <= 19	-10 <= k <= 10
	-13 <= l <= 13	-20 <= l <= 19
Reflections collected	17139	9255
Independent reflections	3618 [R(int) = 0.0332]	2129 [R(int) = 0.0413]
Completeness to theta	95.4 %	99.7 %
Data/restraints/parameters	3351 / 0 / 41	2129 /0 / 140
Extinction coefficient	0.0166(8) $'F_c^* = kF_c[1+0.001 \times F_c^2\lambda^3/\sin(2\theta)]^{-1/4}$	
Absorption coefficient	4.732 mm^{-1}	3.789 mm^{-1}
S	1.147	1.069
Final R indices [I>2s(I)]	R1 = 0.0237, wR^2 = 0.0579	R1 = 0.0273, wR^2 = 0.0769
R indices (all data)	R1 = 0.0261 wR^2 = 0.0605	R1 = 0.0291 wR^2 = 0.0779

Vosko, Wilk and Nusair[278] was employed together with non-local exchange correction by Beck[279] and non-local exchange correlation corrections by Perdew. [280] TZP basis sets were used with triple-ζ accuracy Slater orbitals and a single polarization function added to the atoms.

Photoelectron spectra of **IV** were obtained at the ICL at Oxford University by Professor J.C. Green using a PES Laboratories Ltd. model 0078 spectrometer with a helium discharge lamp capable of producing both He I and He II spectra. The spectrometer was interfaced with an Atari processor which enabled the acquisition of the spectra by repeated scans. The sample was held between 368 K and 371 K and was calibrated using He, Xe and N2.

Vertical ionization energies were calculated using the optimized structure for the molecule and carrying out single-point spin-unrestricted calculations on the mono-cation in the ground state and various excited states found by creating holes in the top occupied orbitals of the molecule.

Chapter 5 Experimental Section

5.1. X-ray diffraction of non-hydrogen bonded systems

Single crystal X-ray diffraction data were collected using a Bruker AXS Smart 1000 Diffractometer equipped with a CCD area detector and graphite monochromatized Mo source (Mo K_α, 0.71073 Å), with a crystal–to–detector distance of 5.0 cm. For low temperature data collections, a Nicolet LT-2 cooling device was used, in which the crystals were coated in paratone oil and mounted on a cryoloop. For room temperature data collections, the crystals were mounted to the end of a glass fiber using epoxy. 2424 frames of data were collected, resulting in more than a hemisphere of data, using frame widths of 0.3° with a 20 second integration time.[164] A multi-scan absorption correction was made using SADABS.[281] The structures were solved by direct methods (SHELXTL),[93] refined by the full matrix least-squares method and completed by a series of difference Fourier syntheses. All non-hydrogen atoms were refined anisotropically, with hydrogen atoms being introduced at idealized positions and refined using a riding model. Weighted R-factors, wR^2, and all goodness–of–fit values are based on F^2.

5.2. X-ray diffraction of hydrogen bonded systems

Single crystal X-ray diffraction data were collected using a Bruker AXS Smart 1000 Diffractometer equipped with a CCD area detector and graphite monochromatized Mo source (Mo K_α, 0.71073 Å), with a crystal–to–detector distance of 5.0 cm. For low temperature data collections, a Nicolet LT-2 cooling device was used, in which the crystals were coated in paratone oil and mounted on a cryoloop. For room temperature

data collections, the crystals were mounted to the end of a glass fiber using epoxy. 2424 frames of data were collected, resulting in more than a hemisphere of data, using frame widths of 0.3° with a 40 second integration time.[164] A multi-scan absorption correction was made using SADABS.[281] The structure was solved by direct methods (SHELXTL),[93] refined by the full matrix least squares method and completed by a series of difference Fourier syntheses. All non-hydrogen atoms were refined anisotropically, with most hydrogen atoms being introduced at idealized positions and refined using a riding model. Hydrogen atoms involved in the hydrogen bond were located in difference Fourier maps[127] with unconstrained refinement of position and isotropic thermal parameters. Weighted R-factors, wR^2, and all goodness–of–fit values are based on F^2.

5.3. Charge density studies using the in-house X-ray diffractometer

Single crystal X-ray diffraction data were collected using a Bruker AXS Smart 1000 Diffractometer equipped with a CCD area detector and graphite monochromatized Mo source (Mo K_α, 0.71073 Å), with a crystal–to–detector distance of 5.0 cm. Low temperature data collections were completed using a Nicolet LT-2 cooling device, in which the crystals were coated in paratone oil and mounted on a cryoloop. A full shell of data was collected in three data set covering an angular range of approximately $5° < 2\theta < 120°$. The data were collected using a frame with of ~0.3° and an exposure time ranging from 15 to 45 seconds per frame.[164] Data reduction and spherical atom analyses were carried out using Saint[282] and the General Structure Analysis System (GSAS).[283] A multi-scan absorption correction was made using SADABS.[281] The spherical atom structures were solved by direct methods (SHELXTL),[93] refined by the full matrix least

squares method and completed by a series of difference Fourier syntheses. All non-hydrogen atoms were refined anisotropically, with hydrogen atoms being introduced at idealized positions and refined using a riding model. Data were input into XD[22] using the instructions file (*name.ins*) and reflections file (*name.hkl*) generated using SHELXTL.[93] The input files were converted to XD format using XDINI. Least-squares refinements were carried out using XDLSM in the following manner: The aspherical atom refinement was initiated by refining the scale factors and the positional and anisotropic thermal parameters. This was followed by refinement of the monopoles for all atoms in the structure. Stepwise, the $\ell = 1, 2, 3$ and in some cases the $\ell = 4$ multipoles were refined for all nonhydrogen atoms. The difference mean-square-displacement amplitude was checked in accordance with Hirshfield's rigid body analysis throughout the refinement to check the validity of the refinement.[217,284] The refinements were completed with the refinement of κ and κ' for nonhydrogen atoms. Residual electron density maps were generated and analyzed to just the progress of the refinement using XDFFT. Analysis of the dipole moment as well as generation of electron density, gradient of ρ, the Laplacian and deformation density maps were generated using XDPROP.

5.4. Charge density studies using synchrotron radiation

Single crystal X-ray diffraction data were collected at the Advanced Photon Source (APS) at Argonne National Laboratory using Sector 15, ChemMatCARS (15-ID-B). Double diamond (111) reflections were used to obtain a monchromated wavelength of 0.48595 Å or 0.41328 Å radiation from the synchrotron source and higher order harmonics were eliminated with mirrors. Data were collected at a temperature of 16 K

using a Pinkerton-type cooling devise.[285] Micron sized single crystals were glued to the end of a quartz fiber and inserted into a bronze pin. The pins were mounted on the goiniometer of a Bruker Huber 4-circle diffractometer equipped with a 4 chip mosaic CCD area detector. Between 3600 and1800 frames of data were collected, resulting in more than a sphere of data, using frame widths of either 0.2° or 0.1° with a 1 second integration time. The crystal–to–detector distance was 6.26 cm or 6.475 cm.

Data reduction and spherical atom analyses were carried out using Saint[282] and the General Structure Analysis System (GSAS).[283] A multi-scan absorption correction was made using SADABS.[281] The spherical atom structures were solved by direct methods (SHELXTL),[93] refined by the full matrix least-squares method and completed by a series of difference Fourier syntheses. All non-hydrogen atoms were refined anisotropically, with hydrogen atoms being introduced at idealized positions and refined using a riding model. Data were input into XD[22] using the instructions file (*name.ins*) and reflections file (*name.hkl*) generated using SHELXTL.[93] The input files were converted to XD format using XDINI. Least squares refinements were carried out using XDLSM in the following manner: The aspherical atom refinement was initiated by refining the scale factors and the positional and anisotropic thermal parameters. This was followed by refinement of the monopoles for all atoms in the structure. Stepwise, the $\ell = 1, 2, 3$ and in some cases the $\ell = 4$ multipoles were refined for all nonhydrogen atoms. The difference mean-square-displacement amplitude was checked in accordance with Hirshfield's rigid body analysis throughout the refinement to check the validity of the refinement.[217,284] The refinements were completed with the refinement of κ and κ' for nonhydrogen atoms. Residual electron density maps were generated and analyzed to just the progress of the

refinement using XDFFT. Analysis of the dipole moment as well as generation of electron density, gradient of ρ, the Laplacian and deformation density maps were generated using XDPROP.

ChemMatCARS Sector 15 is principally supported by the National Science Foundation/Department of Energy under grant number CHE0087817 and by the Illinois Board of Higher Education. The Advanced Photon Source is supported by the U.S. Department of Energy, Basic Energy Sciences, Office of Science, under Contract No. W-31-109-Eng-38.

5.5. Neutron diffraction

Neutron diffraction data were obtained at the Intense Pulsed Neutron Source (IPNS) at Argonne National Laboratory using the time-of-flight Laue single crystal diffractometer (SCD).[286,287] At the IPNS, pulses of protons are accelerated into a heavy-element target 30 times a second to produce pulses of neutrons by the spallation process. Because of the pulsed nature of the source, neutron wavelengths are determined by time-of-flight based on the de Broglie equation

$$\lambda = \frac{hm}{tl},$$

where h is Planck's constant, m is the neutron mass, and t is the time-of-flight for a flight path l, so that the entire thermal spectrum of neutrons can be used. With position-sensitive area detectors and a range of neutron wavelengths, a solid volume of reciprocal space is sampled with each stationary orientation of the sample and the detectors. The SCD has two ^{6}Li-glass scintillation position-sensitive area detectors, each with active

areas of 15 x 15 cm^2 and a spatial resolution of < 1.5 mm. One of the detectors is centered at a scattering angle of 75° and a crystal-to-detector distance of 23 cm, and the second detector is at 120° and 18 cm. Details of the data collection and analysis procedures have been published previously.[286,287]

A crystal of urotropine-*N*-oxide·formic acid with approximate dimensions of 1.8 x 1.3 x 0.6 mm^3 was molded into an aluminum foil "sandwich" and was glued to the end of a standard aluminum pin with epoxy adhesive. The sample was placed on the DISPLEX® cold stage in the SCD, cooled to 260 K in a helium atmosphere, and then cooled to 123 K under vacuum.

For each setting of the diffractometer angles, data were stored in three-dimensional histogram form with coordinates *x,y,t* corresponding to horizontal and vertical detector positions and the time-of-flight, respectively. Data were analyzed using the ISAW software package[286] in addition to other local IPNS SCD programs. For intensity data collection, runs of 6 hours per histogram were initiated, arranged at χ and φ values suitable to cover at least one unique quadrant of reciprocal space. With this counting time, 17 histograms were completed during the 5 days available for the experiment. The recorded histograms were indexed and integrated using individual orientation matrices for each histogram, to allow for any misalignment of the sample. The intensities were corrected for wavelength dependence of the incident spectrum and sample absorption (μ (cm^{-1}) = 4.205).

Bragg reflections were integrated about their predicted location and were corrected for the Lorentz factor, the incident spectrum and the detector efficiency. A wavelength-dependent spherical absorption correction was applied using cross sections

from Sears[288] for the nonhydrogen atoms and from Howard et al.[289] for the hydrogen atoms. Symmetry-related reflections were not averaged since different extinction factors are applicable to reflections measured at different wavelengths. The GSAS software package was used for structural analysis.[283] The atomic positions of the X-ray diffraction structure were used as a starting point in the refinement. All atoms including hydrogen atoms were refined with anisotropic thermal parameters.

Work done at Argonne was supported by the U.S. Department of Energy, BES-Materials Science, under contract W-31-109-Eng-38.

5.6. Density Functional Theory

DFT calculations for chapter 3 were performed at Barnard College using ADF, the Amsterdam Density Functional program.[275-277] DFT calculations for chapter 4 were performed at the ICL at Oxford University using ADF, the Amsterdam Density Functional program.[275-277] Data in the form of *name.cif* or *name.pdb* files were input into MOLDEN.[290] For crystallographic information obtained from X-ray diffraction data, the hydrogen bond lengths were adjusted to the values determined by neutron diffraction. MOLDEN was used to create an input file for ADF.

5.7. Solid state nuclear magnetic resonance experiments

CPMAS solid state NMR data were collected at a frequency of 100.550 MHz using a Varian INOVA 400 NMR spectrometer. The 90° pulse of proton resonance was 4 μs, the contact time was 5 ms and a MAS rate 6.555 KHz was used. 400 transients

were collected with a relaxation delay of 3s and an acquisition time of 45ms. A liquid nitrogen cooling system was utilized for variable temperature experiments.

5.8. Solution nuclear magnetic resonance experiments

Solution NMR data were obtained using a Varian Mercury 300MHz spectrometer, at which field the resonant frequency of ^{13}C is 75.454 MHz, with the ^{1}H frequency being 300.088 MHz, from solutions of the recrystallized material in d_6-DMSO. Chemical shifts were referenced to tetramethylsilane *via* residual ^{1}H residues in the solvent or the ^{13}C shift of the solvent.

5.9 Differential Scanning Calorimetry

Differential scanning calorimetry was used to determine the thermodynamics of any phase behavior, using a Mettler Toledo DSC 820 with a temperature range of –120°C to 100°C and a heating/cooling rate of 10°C / minute. DSC measurements were made by Dr. Marek Pyda at the University of Tennessee. The samples were prepared in aluminum pans. For the measurement of heat capacity, the basic lines of the empty pan and sapphire reference were measured and compared to the heat flow measurements of the sample. The heat capacity of the sample was measured in two runs.

WORKS CITED

(1) Ziman, J. M. *Principles of the Theory of Solids*; 2 ed.; Cambridge University Press: New York, 1995.

(2) Sands, D. E. *Vectors and Tensors in Crystallography*; Dover Publications: Mineola, N. Y., 2002.

(3) Warren, B. E. *X-ray Diffraction* Mineola, N. Y., 1990.

(4) Sands, D. E. *Introduction to Crystallography*; Dover Publications: Mineola, N.Y., 1993.

(5) Guinier, A. *X-ray diffraction in crystals, imperfect crystals, and amorphous bodies*; Dover Publications, Inc.: New York, 1994.

(6) Nave, C. R. http://hyperphysics.phy-astr.gsu.edu/hbase/quantum/xrayc.html

(7) West, a. R. *Solid State Chemistry and Its Applications*; John Wiley & Sons, Ltd.: New York, 1998.

(8) Stout, G. H.; Jensen, L. H. *X-ray structure determination: A practical guide*; Macmillan Publishing Co., Inc: New York, 1968.

(9) Wilson, C. C. *Single Crystal Neutron Diffraction from Molecular Materials*; World Scientific Publishing: River Edge, N. J., 2000; Vol. 2.

(10) Bragg, W. L. *Proc. Roy. Soc. London, (A)*, "The Structure of Crystals as Indicated by their Diffraction of X-Rays", **1913**, *89*, 248-277.

(11) Bragg, W. H. *Proc. Roy. Soc. London, (A)*, "The Reflection of X-Rays by Crystals", **1913**, *89*, 246-248.

(12) Ramachandran, G. N.; Srinivasan, R. *Fourier methods in crystallography*; Wiley - Interscience: New York, 1970.

(13) Sivia, D. S.; David, W. I. F. *Journal of Physics and Chemistry of Solids*, "A Bayesian approach to phase extension", **2001**, *62*, 2119-2127.

(14) Coulson, C. A. *Valence*; Oxford University Press: Oxford, 1961.

(15) DeMarco, J. J.; Weiss, R. J. *Phys. Rev.*,, **1965**, *A137*, 1896.

(16) Dawson, B. *Proc. R. Soc. Lond. Series A*,, **1967**, *298*, 264.

(17) Kurki-Suonio, K. *Acta Cryst*, "On the information about deformations of the atoms in X-ray diffraction data", **1968**, *A24*, 379.

(18) Stewart, R. F. *J. Chem. Phys.*, "Generalized X-ray scattering factors", **1969**, *51*, 4569-4577.

(19) Coppens, P.; Guru Row, T. N.; Leung, P.; Stevens, E. D.; Becker, P. J. *Acta Cryst*, "Net atomic charges and molecular dipole moments from spherical-atom X-ray refinements, and the relationship between atomic charge and shape", **1979**, *A35*, 63-72.

(20) Hansen, N. K.; Coppens, P. *Acta Cryst*, "Testing aspherical atom refinements on small-molecule data sets", **1978**, *A34*, 909-921.

(21) Coppens, P. *X-Ray Charge Densities and Chemical Bonding*, 1997.

(22) Koritsanszky, T.; Howard, S. T.; Richter, T.; Macchi, P.; Volkov, A.; Gatti, C.; Farrugia, L. J.; Mallinson, P. R.; Su, Z.; Hansen, N. K.; *XD. A Computer Program Package for Multipole Refinement and Analysis of Charge Densities from X-ray Diffraction Data*, Berlin, 2003

(23) Bader, R. F. W. *Atoms in Molecules: A Quantum Theory*; Oxford University Press: New York, 1995; Vol. 22.

(24) Nygren, C. L.; Wilson, C. C.; Turner, J. F. C. *J. Phys. Chem. A*, "On the solid state structure of para-iodobenzoic acid", **2005**, *109*, 2586-2593.

(25) Nygren, C. L.; Wilson, C. C.; Turner, J. F. C. *Journal of Physical Chemistry A*, "Electron and Nuclear Positions in the Short Hydrogen Bond in Urotropine-N-oxide.Formic Acid", **2005**, *109*, 1911-1919.

(26) Pauling, L. *J. Am. Chem. Soc.*, "The structure and entropy of ice ad of other crystals with some randomness of atomic arrangement", **1935**, *57*, 2680-2684.

(27) Latimer, W. M.; Rodebush, W. H. *J. Am. Chem. Soc.*, "Polarity and Ionization from the standpoint of the lewis theory of valence", **1920**, *42*, 1419-1444.

(28) Werner, v. A. *Liegbigs Annalen der Chemie*, "Ueber Haupt- und Nebenvalenzen und die Constitution der Ammoniumverbindungen", **1902**, *322*, 261-297.

(29) Desiraju, G. R.; Steiner, T. *The Weak Hydrogen Bond*; Oxford University Press: New York, 2001; Vol. 9.

(30) Pimentel, G. C.; McClellan, A. L. *The Hydrogen Bond*; Reinhold Publishing Corporation: New York, 1960.

(31) Wang, C.-C.; YTang, T.-H.; Wu, L.-C.; Wang, Y. *Acta Cryst*, "Topological analysis and bond characterization of 1,3,5,7-tetra-*tert*-butyl-*s*-indacene: a weak C_{sp3}-H...H-C_{sp3}-type dihydrogen interaction", **2004**, *A60*, 488-493.

(32) Huheey, J. E. *Inorganic Chemistry: Principles of structure and reactivity*; 2nd ed.; Harper & Row: New York, 1978.

(33) Larson, J. W.; McMahon, T. B. *Journal of the American Chemical Society*, "Gas-phase bifluoride ion. An ion cyclotron resonance determination of the

hydrogen bond energy in fluoride ion (FHF-) from gas-phase fluoride transfer equilibrium measurements", **1982**, *104*, 5848-5849.

(34) Allen, F. H.; Motherwell, W. D. S. *Acta Cryst.*, "Applications of the Cambridge Structural Database in organic chemistry and crystal chemistry", **2002**, *B58*, 407-422.

(35) Bruno, I. J.; Cole, J. C.; Edgington, P. R.; Kessler, M.; Macrae, C. F.; McCabe, P.; Pearson, J.; Taylor, R. *Acta Cryst*, "New Software for searching the Cambridge Structural Database and visualizing crystal structures", **2002**, *B58*, 389-397.

(36) Steiner, T.; Saenger, W. *J. Am. Chem. Soc.*, "Role of C-H...O hydrogen bonds in the coordination of water molecules. Analysis of neutron diffraction data", **1993**, *115*, 4540-4547.

(37) Bader, R. F. W. *Accounts of Chemical Research*, "Atoms in molecules", **1985**, *18*, 9-15.

(38) Alkorta, I.; Elguero, J. *Chemical Society Reviews*, "Non-conventional hydrogen bonds", **1998**, *27*, 163-170.

(39) Flensburg, C.; Larsen, S.; Stewart, R. F. *Journal of Physical Chemistry*, "Experimental charge density study of methylammonium hydrogen succinate monohydrate. A salt with a very short O-H-O hydrogen bond", **1995**, *99*, 10130-10141.

(40) Madsen, D.; Flensburg, C.; Larsen, S. *Journal of Physical Chemistry A*, "Properties of the Experimental Crystal Charge Density of Methylammonium Hydrogen Maleate. A Salt with a Very Short Intramolecular O-H-O Hydrogen Bond", **1998**, *102*, 2177-2188.

(41) Steiner, T. *Angewandte Chemie, International Edition*, "Reviews: The hydrogen bond in the solid state", **2002**, *41*, 48-76.

(42) Schowen, K. B.; Limbach, H. H.; Denisov, G. S.; Schowen, R. L. *Biochimica et Biophysica Acta*, "Hydrogen bonds and proton transfer in general-catalytic transition-state stabilization in enzyme catalysis", **2000**, *1458*, 43-62.

(43) Cleland, W. W. *Archives of Biochemistry and Biophysics*, "Low-barrier hydrogen bonds and enzymic catalysis", **2000**, *382*, 1-5.

(44) Perrin, C. L.; Nielson, J. B. *Annu. Rev. Phys. Chem.*, ""Strong" hydrogen bonds in chemistry and biology", **1997**, *48*, 511-544.

(45) Urquidi, J.; Benmore, C. J.; Egelstaff, P. A.; Guthrie, M.; McLain, S. E.; Tulk, C. A.; Klug, D. D.; Turner, J. F. C. *Mol. Phys.*, "A structural comparison of supercooled water
and intermediate density amorphous ices", **2004**, Submitted.

(46) George, W. O.; Jones, B. F.; Lewis, R. H. *Philosophical Transactions of the Royal Society of London, Series A: Mathematical, Physical and Engineering Sciences*, "Water and its homologues: A comparison of hydrogen-bonding phenomena", **2001**, *359*, 1611-1629.

(47) Soper, A. K.; Ricci, M. A. *Phys. Rev. Lett.*, "Structures of High-Density and Low-Density Water", **2000**, *84*, 2881-2884.

(48) Soper, A. K. *Chem. Phys.*, "The radial distribution functions of water and ice from 220 to 673 K and at pressures up to 400 MPa", **2000**, *258*, 121-137.

(49) Soper, A. K. *Physica B (Amsterdam)*, "Probing the structure of water around biological molecules: concepts, constructs and consequences", **2000**, *276-278*, 12-16.

(50) Soper, A. K. *J. Phys.: Condens. Matter*, "Bridge over troubled water: the apparent discrepancy between simulated and experimental non-ambient water structure", **1996**, *8*, 9263-9267.

(51) Tromp, R. H.; Postorino, P.; Neilson, G. W.; Ricci, G. W.; Ricci, M. A.; Soper, A. K. *J. Chem. Phys.*, "Neutron diffraction studies of H_2O/D_2O at supercritical temperatures. A direct determination of $g_{HH}(r)$, $g_{OH}(r)$, and $g_{OO}(r)$", **1994**, *101*, 6210-6215.

(52) Ricci, M. A.; Nardone, M.; Ricci, F. P.; Andreani, C.; Soper, A. K. *J. Chem. Phys.*, "Microscopic structure of low temperature liquid ammonia: A neutron diffraction experiment", **1995**, *102*, 7650-7655.

(53) McLain, S. E.; Benmore, C. J.; Siewenie, J. E.; Urquidi, J.; Turner, J. F. C. *Angewandte Chemie, International Edition*, "The structure of liquid hydrogen fluoride", **2004**, Accepted.

(54) Pfleiderer, T.; Waldner, I.; Bertagnolli, H.; Todheide, K.; Fischer, H. E. *J. Chem. Phys.*, "The structure of liquid and supercritical deuterium fluoride from neutron scattering using high-pressure techniques", **2000**, *113*, 3690-3696.

(55) Deraman, M.; Dore, J. C.; Powles, J. G.; Holloway, J. H.; Chieux, P. *Mol. Phys.*, "Structural studies of liquid hydrogen fluoride by neutron diffraction. I. Liquid deuterium fluoride at 293 K", **1985**, *55*, 1351-1367.

(56) Desiraju, G. R. *Accounts of Chemical Research*, "Hydrogen Bridges in Crystal Engineering: Interactions without Borders", **2002**, *35*, 565-573.

(57) Desiraju, G. R. *Dalton*, "Hydrogen bonds and other intermolecular interactions in organometallic crystals", **2000**, 3745-3751.

(58) Holman, K. T.; Pivovar, A. M.; Swift, J. A.; Ward, M. D. *Accounts of Chemical Research*, "Metric Engineering of Soft Molecular Host Frameworks", **2001**, *34*, 107-118.

(59) Nangia, A.; Desiraju, G. R. *Acta Crystallographica, Section A: Foundations of Crystallography*, "Supramolecular structures - reason and imagination", **1998**, *A54*, 934-944.

(60) Subramanian, S.; Zaworotko, M. J. *Coordination Chemistry Reviews*, "Exploitation of the hydrogen bond: recent developments in the context of crystal engineering", **1994**, *137*, 357-401.

(61) Aakeroy, C. B.; Seddon, K. R. *Chemical Society Reviews*, "The hydrogen bond and crystal engineering", **1993**, *22*, 397-407.

(62) Wozniak, K.; Mallinson, P. R.; Smith, G. T.; Wilson, C. C.; Grech, E. *Journal of Physical Organic Chemistry*, "Role of C-H.cntdot...O hydrogen bonds in the ionic complexes of 1,8-bis(dimethylamino)naphthalene", **2003**, *16*, 764-771.

(63) Wilson, C. C.; Goeta, A. E. *Angewandte Chemie, International Edition*, "Towards designing proton-transfer systems - Direct imaging of proton disorder in a hydrogen-bonded carboxylic acid dimer by variable-temperature x-ray diffraction", **2004**, *43*, 2095-2099.

(64) Mallinson, P. R.; Smith, G. T.; Wilson, C. C.; Grech, E.; Wozniak, K. *Journal of the American Chemical Society*, "From Weak Interactions to Covalent Bonds: A Continuum in the Complexes of 1,8-Bis(dimethylamino)naphthalene", **2003**, *125*, 4259-4270.

(65) Wilson, C. C.; Morrison, C. A. *Chemical Physics Letters*, "Structural and theoretical investigations of short hydrogen bonds: neutron diffraction and plane-wave DFT calculations of urea-phosphoric acid", **2002**, *362*, 85-89.

(66) Wilson, C. C. *New Journal of Chemistry*, "Interesting proton behaviour in molecular structures. Variable temperature neutron diffraction and ab initio study of acetylsalicylic acid: characterising librational motions and comparing protons in different hydrogen bonding potentials", **2002**, *26*, 1733-1739.

(67) Wilson, C. C.; Shankland, K.; Shankland, N. *Zeitschrift fuer Kristallographie*, "Single-crystal neutron diffraction of urea-phosphoric acid: evidence for H-atom migration in a short hydrogen bond between 150 K and 350 K", **2001**, *216*, 303-306.

(68) Wilson, C. C. *Acta Crystallographica, Section B: Structural Science*, "Migration of the proton in the strong O-H...O hydrogen bond in urea-phosphoric acid (1/1)", **2001**, *B57*, 435-439.

(69) Wilson, C. C. *Chemical Physics Letters*, "Hydrogen atoms in acetylsalicylic acid (Aspirin): the librating methyl group and probing the potential well in the hydrogen-bonded dimer", **2001**, *335*, 57-63.

(70) Wilson, C. C.; Shankland, N.; Florence, A. J. *Chemical Physics Letters*, "Direct determination of the temperature dependence of proton transfer in the benzoic acid dimer by single crystal neutron diffraction", **1996**, *253*, 103-107.

(71) Wilson, C. C.; Shankland, N.; Florence, A. J. *Journal of the Chemical Society, Faraday Transactions*, "A single-crystal neutron diffraction study of the temperature dependence of hydrogen-atom disorder in benzoic acid dimers", **1996**, *92*, 5051-5057.

(72) Steiner, T.; Majerz, I.; Wilson, C. C. *Angewandte Chemie, International Edition*, "First O-H-N hydrogen bond with a centered proton obtained by thermally induced proton migration", **2001**, *40*, 2651-2654.

(73) Parkin, A.; Harte, S. M.; Goeta, A. E.; Wilson, C. C. *New Journal of Chemistry*, "Imaging proton migration from X-rays and neutrons", **2004**, *28*, 718-721.

(74) Kollman, P. A.; Allen, L. C. *Chemical Reviews (Washington, DC, United States)*, "Theory of the hydrogen bond", **1972**, *72*, 283-303.

(75) Harris, D. C.; Bertolucci, M. D. *Symetry and Spectroscopy: An Introduction to Vibrational and Electronic Spectroscopy*; Dover Publications: Mineola, N. Y., 1989.

(76) Legon, A. C. *Accounts of Chemical Research*, "Directional character, strength, and nature of the hydrogen bond in gas phase dimers", **1987**, *20*, 39-46.

(77) Legon, A. C.; Millen, D. J. *Chemical Society Reviews*, "Angular geometries and other properties of hydrogen-bonded dimers: a simple electrostatic interpretation of the success of the electron-pair model", **1987**, *16*, 467-498.

(78) Hobza, P.; Zahradnik, R. *Chem. Rev. (Washington, D. C.)*, "Intermolecular interactions between medium-sized systems. Nonempirical and empirical calculations of interaction energies: successes and failures", **1988**, *88*, 871-897.

(79) Brunner, E.; Sternberg, U. *Progress in Nuclear Magnetic Resonance Spectroscopy*, "Solid-state NMR investigations on the nature of hydrogen bonds", **1998**, *32*, 21-57.

(80) Braga, D.; Maini, L.; de Sanctis, G.; Rubini, K.; Grepioni, F.; Chierotti, M. R.; Gobetto, R. *Chem. Eur. J.*, "Mechanochemical preparation of hydrogen-bonded adducts between the diamine 1,4-diazabicyclo[2.2.2]octane and dicarboxylic acids of variable chain length:: An X-ray diffraction and solid-state NMR study", **2003**, *9*, 5538-5548.

(81) Howes, A. P.; Smith, M. E.; Dupree, R.; Jenkins, R.; Crout, D. H. G. *Chemical Communications (Cambridge, United Kingdom)*, "Influence of low-barrier hydrogen bonds on solid state 17O NMR spectra of labelled phthalate species", **2001**, 1448-1449.

(82) Coulson, C. A.; Thomas, M. W. *Acta Cryst*, "The effect of molecular vibrations on apparent bond lengthes", **1971**, *B27*, 1354-1359.

(83) Robertson, K. N.; Knop, O.; Cameron, T. S. *Canadian Journal of Chemistry*, "C-H...H-C interaction in organometallic tetraphenylborates: another look at dihydrogen bonds", **2003**, *81*, 727-743.

(84) Steiner, T.; Desiraju, G. R. *Chem. Comm.*, "Distinction between the weak hydrogen bond and the van der Waals interaction", **1998**, 891-892.

(85) Bader, R. F. W. *NATO ASI Series, Series C: Mathematical and Physical Sciences*, "The physics of an atom in a molecule", **1993**, *406*, 313-349.

(86) Bader, R. F. W. *Chemical Reviews (Washington, DC, United States)*, "A quantum theory of molecular structure and its applications", **1991**, *91*, 893-928.

(87) Bader, R. F. W. *Mol. Phys., Chem., Biol.*, "The physical basis of the Lewis electron pair model", **1989**, *3*, 73-92.

(88) Nguyen-Dang, T. T.; Bader, R. F. W. *Physica A: Statistical Mechanics and Its Applications (Amsterdam, Netherlands)*, "A theory of molecular structure", **1982**, *114A*, 68-73.

(89) Bader, R. F. W. http://www.chemistry.mcmaster.ca/faculty/bader/aim/

(90) Dye, J. L. *Inorganic Chemistry*, "Electrides: From 1D Heisenberg Chains to 2D Pseudo-Metals", **1997**, *36*, 3816-3826.

(91) Wagner, M. J.; Dye, J. L. *Annual Review of Materials Science*, "Alkalides, electrides and expanded metals", **1993**, *23*, 223-253.

(92) Dye, J. L. *Science (Washington, DC, United States)*, "Electrides: ionic salts with electrons as the anions", **1990**, *247*, 663-668.

(93) Sheldrick, G. M.; *SHELXL97, SHELXS97, SHELXTL*, Gottingen, Germany, 1997

(94) Dickinson, R. G.; Raymond, A. L. *Journal of the American Chemical Society*, "The crystal structure of hexamethylenetetramine", **1923**, *45*, 22-29.

(95) Gonell, H. W.; Mark, H. *Z. physik. Chem.*, "X-ray determination of the structural formula of hexamethylenetetramine", **1923**, *107*, 181-218.

(96) Shaffer, P. A., Jr. *Journal of the American Chemical Society*, "Anisotropic oscillations in the hexamethylenetetramine crystal", **1947**, *69*, 1557-1561.

(97) Andresen, A. F. *Acta Cryst.*, "Investigation of hexamethylenetetramine by neutron diffraction", **1957**, *10*, 107-110.

(98) Becka, L. N.; Cruickshank, D. W. J. *Proc. Roy. Soc. (London)*, "The crystal structure of hexamethylenetetramine. II. The lattice vibrations of a simple molecular crystals", **1963**, *273*, 455-465.

(99) Becka, L. N.; Cruickshank, D. W. J. *Proc. Roy. Soc. (London)*, "The crystal structure of hexamethylenetetramine. I. X-ray studies at 298, 100, and 34 K", **1963**, *273*, 435-454.

(100) Duckworth, J. A. K.; Willis, B. T. M.; Pawley, G. S. *Acta Crystallographica, Section A: Crystal Physics, Diffraction, Theoretical and General Crystallography*, "Joint refinement of neutron and x-ray diffraction data", **1969**, *25*, 482-484.

(101) Willis, B. T. M.; Howard, J. A. K. *Acta Crystallographica, Section A: Crystal Physics, Diffraction, Theoretical and General Crystallography*, "Do the ellipsoids of thermal vibration mean anything. Analysis of neutron diffraction measurements on hexamethylenetetramine", **1975**, *A31*, 514-520.

(102) Parini, E. V.; Tsirel'son, V. G.; Ozerov, R. P. *Kristallografiya*, "A model for a multipole anharmonic pseudo-atom in a precise x-ray structure analysis", **1985**, *30*, 857-866.

(103) Chekhlov, A. N.; Ionov, S. P. *Kristallografiya*, "Experimental atomic charges in hexamethylenetetramine", **1982**, *27*, 506-510.

(104) Grochowski, J.; Serda, P.; Wilson, K. S.; Dauter, Z. *Journal of Applied Crystallography*, "Refinement of hexamethylenetetramine based on diffractometer and imaging-plate data", **1994**, *27*, 722-726.

(105) Kampermann, S. P.; Sabine, T. M.; Craven, B. M.; McMullan, R. K. *Acta Crystallographica, Section A: Foundations of Crystallography*, "Hexamethylenetetramine: extinction and thermal vibrations from neutron diffraction at six temperatures", **1995**, *A51*, 489-497.

(106) Spackman, M. A.; Byrom, P. G. *Acta Crystallographica, Section B: Structural Science*, "Retrieval of structure-factor phases in non-centrosymmetric space groups. Model studies using multipole refinements", **1997**, *B53*, 553-564.

(107) Terpstra, M.; Craven, B. M.; Stewart, R. F. *Acta Crystallographica, Section A: Foundations of Crystallography*, "Hexamethylenetetramine at 298 K: New refinements", **1993**, *A49*, 685-692.

(108) Resing, H. A. *Molecular Crystals and Liquid Crystals*, "NMR relaxation in adamantane and hexamethylenetetramine: diffusion and rotation", **1969**, *9*, 101-132.

(109) Burgi, H. B.; Capelli, S. C.; Birkedal, H. *Acta Crystallographica, Section A: Foundations of Crystallography*, "Anharmonicity in anisotropic displacement parameters", **2000**, *A56*, 425-435.

(110) Mak, T. C. W.; Ladd, M. F. C.; Povey, D. C. *Journal of the Chemical Society, Perkin Transactions 2: Physical Organic Chemistry (1972-1999)*, "Molecular and crystal structure of hexamethylenetetramine oxide", **1979**, 593-595.

(111) Yu, P.-Y.; Mak, T. C. W. *Acta Crystallographica, Section B: Structural Crystallography and Crystal Chemistry*, "Preparation and x-ray analysis of a 1:1 adduct of hexamethylenetetramine oxide and thiourea", **1978**, *B34*, 3053-3056.

(112) Trotter, J.; Mak, T. C. W. *Acta Crystallographica, Section B: Structural Crystallography and Crystal Chemistry*, "Preparation and x-ray analysis of a 1:1 adduct of hexamethylenetetramine oxide and hydroquinone", **1979**, *B35*, 2367-2369.

(113) Mak, T. C. W.; Lam, Y.-S. *Acta Crystallographica, Section B: Structural Crystallography and Crystal Chemistry*, "The Crystal and Molecular Structure of a 1:1 Aduct of Hexamethylenetetramine Oxide and Formic Acid", **1978**, *B34*, 1915-1918.

(114) Lam, Y.-S.; Mak, T. C. W. *Acta Crystallographica, Section B: Structural Crystallography and Crystal Chemistry*, "The crystal and molecular structure of a 1:1 adduct of hexamethylenetetramine oxide and formic acid", **1978**, *B34*, 1915-1918.

(115) Lam, Y.-S.; Mak, T. C. W. *Australian Journal of Chemistry*, "Preparation and characterization of hexamethylenetetramine N-oxide and some acid adducts", **1978**, *31*, 1249-1253.

(116) Chesnut, D. B.; Savin, A. *J. Am. Chem. Soc.*, "The Electron Localization Function (ELF) Description of the PO Bond in Phosphine Oxide", **1999**, *121*, 2335-2336.

(117) Chesnut, D. B. *J. Am. Chem. Soc.*, "An Ab Initio Nuclear Magnetic Resonance and Atoms-in-Molecules Study of the PO Bond in Phosphine Oxides", **1998**, *120*, 10504-10510.

(118) Cunningham, T. P.; Cooper, D. L.; Gerratt, J.; Karadakov, P. B.; Raimondi, M. *J. Chem. Soc., Faraday Trans.*, "Chemical bonding in oxofluorides of hypercoordinate sulfur", **1997**, *93*, 2247-2254.

(119) Cunningham, T. P.; Cooper, D. L.; Gerratt, J.; Karadakov, P. B.; Raimondi, M. *Int. J. Quantum Chem.*, "Chemical bonding in oxohalides of hypercoordinate nitrogen and phosphorus", **1996**, *60*, 393-400.

(120) Rai, U. S.; Symons, M. C. R. *J. Chem. Soc., Faraday Trans.*, "EPR data do not support the P:O representation for trialkyl phosphates and phosphine oxides or sulfides", **1994**, *90*, 2649-2652.

(121) Gilheany, D. G. *Chem. Rev. (Washington, D. C.)*, "Ylides, phosphoniumNo d Orbitals but Walsh Diagrams and Maybe Banana Bonds: Chemical Bonding in Phosphines, Phosphine Oxides, and Phosphonium Ylides", **1994**, *94*, 1339-1374.

(122) Magnusson, E. *J. Am. Chem. Soc.*, "The role of d functions in correlated wave functions: main group molecules", **1993**, *115*, 1051-1061.

(123) Reed, A. E.; Schleyer, P. v. R. *J. Am. Chem. Soc.*, "Chemical bonding in hypervalent molecules. The dominance of ionic bonding and negative hyperconjugation over d-orbital participation", **1990**, *112*, 1434-1445.

(124) Fenn, T. D.; Ringe, D.; Petsko, G. A. *Journal of Applied Crystallography*, "POVScript+: A program for model and data visualization using persistence of vision ray-tracing", **2003**, *36*, 944-947.

(125) Taylor, R.; Macrae, C. F. *Acta Cryst*, "Rules governing the crystal packing of mono- and di-alcohols", **2001**, *B57*, 815-817.

(126) Bondi, A. *Journal of Physical Chemistry*, "van der Waals Volumes and Radii", **1964**, *68*, 441-451.

(127) Farrugia, L. J. *J. Appl. Cryst.*, "WinGX", **1999**, *32*, 837-838.

(128) Dunitz, J. D.; Schomaker, V.; Trueblood, K. N. *Journal of Physical Chemistry*, "Interpretation of atomic displacement parameters from diffraction studies of crystals", **1988**, *92*, 856-867.

(129) Sekiya, R.; Nishikiori, S.-I. *Chemistry--A European Journal*, "Design and structural extension of a supramolecular inclusion-compound host made by the formation of dimers of isonicotinic acid and thiocyanato coordinating bridges", **2002**, *8*, 4803-4810.

(130) Smith, G.; White, J. M. *Australian Journal of Chemistry*, "Molecular cocrystals of carboxylic acids: the preparation of the 1:1 proton-transfer compounds of creatinine with a series of aromatic acids and the crystal structure of that with pyrazine-2,3-dicarboxylic acid", **2001**, *54*, 97-100.

(131) Foces-Foces, C.; Echevarria, A.; Jagerovic, N.; Alkorta, I.; Elguero, J.; Langer, U.; Klein, O.; Minguet-Bonvehi, M.; Limbach, H.-H. *Journal of the American Chemical Society*, "A Solid-State NMR, x-ray Diffraction, and ab Initio Computational Study of Hydrogen-Bond Structure and Dynamics of Pyrazole-4-Carboxylic Acid Chains", **2001**, *123*, 7898-7906.

(132) Ashton, P. R.; Fyfe, M. C. T.; Hickingbottom, S. K.; Menzer, S.; Stoddart, J. F.; White, A. J. P.; Williams, D. J. *Chemistry--A European Journal*, "Molecular meccano. 34. Combining different hydrogen-bonding motifs to self-assemble interwoven superstructures", **1998**, *4*, 577-589.

(133) Papadakis, M. M.; Martins, S. P.; Thompson, H. W.; Lalancette, R. A. *Acta Crystallographica, Section C: Crystal Structure Communications*, "(+-)-12-Oxotricyclo[6.2.2.01,6]dodecane-10-carboxylic acid: hydrogen bonding in a tricyclic d-keto acid", **2002**, *C58*, o321-o322.

(134) Colapietro, M.; Domenicano, A.; Pela Ceccarini, G. *Acta Crystallographica, Section B: Structural Crystallography and Crystal Chemistry*, "Structural studies of benzene derivatives. V. The crystal and molecular structure of p-fluorobenzoic acid", **1979**, *B35*, 890-894.

(135) Luner, P. E.; Patel, A. D.; Swenson, D. C. *Acta Crystallographica, Section C: Crystal Structure Communications*, "(+-)-Tartaric acid", **2002**, *C58*, o333-o335.

(136) Gilardi, R.; Butcher, R. J.; Bashir-Hashemi, A. *Acta Crystallographica, Section E: Structure Reports Online*, "4,7-Dichlorotricyclo[3.1.1.03,6]heptane-2-carboxylic acid", **2002**, *E58*, o860-o861.

(137) Crispini, A.; Neve, F. *Acta Crystallographica, Section C: Crystal Structure Communications*, "2,6-Diphenylpyridine-4-carboxylic acid", **2002**, *C58*, o34-o35.

(138) Hokelek, T.; Patir, S.; Ergun, Y.; Okay, G. *Acta Crystallographica, Section C: Crystal Structure Communications*, "4-Methylcarbazole-3-carboxylic acid", **2001**, *C57*, 414-416.

(139) Degen, A.; Bolte, M. *Acta Crystallographica, Section C: Crystal Structure Communications*, "2-(p-toluoyl)benzoic acid", **1999**, *C55*, 1306-1308.

(140) Fitzgerald, L. J.; Gerkin, R. E. *Acta Crystallographica, Section C: Crystal Structure Communications*, "Phenanthrene-4-carboxylic acid and 1,2-dihydrophenanthrene-4-carboxylic acid", **1998**, *C54*, 966-969.

(141) Dobson, A. J.; Gerkin, R. E. *Acta Crystallographica, Section C: Crystal Structure Communications*, "Biphenyl-2-carboxylic acid: a layered structure", **1998**, *C54*, 795-798.

(142) Fitzgerald, L. J.; Gerkin, R. E. *Acta Crystallographica, Section C: Crystal Structure Communications*, "Anthracene-9-carboxylic acid", **1997**, *C53*, 71-73.

(143) Fitzgerald, L. J.; Gerkin, R. E. *Acta Crystallographica, Section C: Crystal Structure Communications*, "Anthracene-1-carboxylic acid", **1997**, *C53*, 1080-1082.

(144) Fitzgerald, L. J.; Gerkin, R. E. *Acta Crystallographica, Section C: Crystal Structure Communications*, "Phenanthrene-9-carboxylic acid", **1997**, *C53*, 1265-1267.

(145) Ferguson, G.; Gallagher, J. F.; McAlees, A. J. *Acta Crystallographica, Section C: Crystal Structure Communications*, "Ligands for application in coordination chemistry: three dicarboxylic acids", **1995**, *C51*, 454-458.

(146) Thompson, H. W.; Lalancette, R. A.; Vanderhoff, P. A. *Acta Crystallographica, Section C: Crystal Structure Communications*, "9-Oxobicyclo[3.3.1]nonane-1-carboxylic acid: structure and hydrogen-bonding pattern", **1992**, *C48*, 66-70.

(147) Butcher, R. J.; Bashir-Hashemi, A.; Gilardi, R. D. *Journal of Chemical Crystallography*, "Network hydrogen bonding: the crystal and molecular structure of 1,3,5,7-cubanetetracarboxylic acid dihydrate", **1997**, *27*, 99-107.

(148) Basilevsky, M. V.; Vener, M. V. *Russian Chemical Reviews*, "Theoretical investigations of proton and hydrogen atom transfer in the condensed phase", **2003**, *72*, 1-33.

(149) Maurin, J. K.; Czarnocki, Z.; Wojtasiewicz, K.; Maleszewska, E.; Magdziak, K.; Paluchowska, B. *Journal of Molecular Structure*, "Crystallographic and ab initio theoretical studies of (2R,3R)-1-methyl-5-oxo-2-phenyltetrahydro-1H-pyrrole-3-

carboxylic acid. The comparison of chiral (I) and racemic (II) structure", **2002**, *610*, 33-40.

(150) Gavezzotti, A. *Journal of Molecular Structure*, "Modeling hydrogen bonded crystals", **2002**, *615*, 5-12.

(151) Fillaux, F.; Limage, M. H.; Romain, F. *Chemical Physics*, "Quantum proton transfer and interconversion in the benzoic acid crystal: vibrational spectra, mechanism and theory", **2002**, *276*, 181-210.

(152) Latanowicz, L.; Reynhardt, E. C. *Chemical Physics Letters*, "Quantum mechanical and classical dynamics of double proton transfer in the hydrogen bond", **2001**, *341*, 561-567.

(153) Fillaux, F. *International Reviews in Physical Chemistry*, "Hydrogen bonding and quantum dynamics in the solid state", **2000**, *19*, 553-564.

(154) Grabowski, S. J.; Krygowski, T. M. *Chemical Physics Letters*, "The proton transfer path for C:O...H-O systems modeled from crystal structure data", **1999**, *305*, 247-250.

(155) Loerting, T.; Liedl, K. R. *Journal of the American Chemical Society*, "Toward Elimination of Discrepancies between Theory and Experiment: Double Proton Transfer in Dimers of Carboxylic Acids", **1998**, *120*, 12595-12600.

(156) Horsewill, A. J.; Brougham, D. F.; Jenkinson, R. I.; McGloin, C. J.; Trommsdorff, H. P.; Johnson, M. R. *Berichte der Bunsen-Gesellschaft*, "The quantum dynamics of proton transfer in the hydrogen bond", **1998**, *102*, 317-324.

(157) Toussaint, J. *Acta Cryst.*, "The structure of p-chlorobenzoic acid", **1951**, *4*, 71-72.

(158) Pollock, J. M.; Woodward, I. *Acta Cryst.*, "The unit-cell dimensions of p-chlorobenzoic acid", **1954**, *7*, 605.

(159) Baughman, R. G.; Nelson, J. E. *Acta Crystallographica, Section C: Crystal Structure Communications*, "The structure of p-iodobenzoic acid, $C_7H_5IO_2$", **1984**, *C40*, 204-206.

(160) Miller, R. S.; Paul, I. C.; Curtin, D. Y. *Journal of the American Chemical Society*, "Reactions of molecular crystals with gases. II. X-ray structure of crystalline 4-chlorobenzoic acid and the anisotropy of its reaction with ammonia gas", **1974**, *96*, 6334-6339.

(161) Takaki, Y.; Kurisu, A.; Nakata, K. *Bulletin of the Chemical Society of Japan*, "The crystal structure of p-iodobenzoic acid investigated by x-ray powder diffraction", **1982**, *55*, 319-320.

(162) Ohkura, K.; Kashino, S.; Haisa, M. *Bulletin of the Chemical Society of Japan*, "Crystal and molecular structure of p-bromobenzoic acid", **1972**, *45*, 2651-2652.

(163) Hanrahan, E. S.; Bruce, B. D. *Spectrochimica Acta, Part A: Molecular and Biomolecular Spectroscopy*, "Dimerization of p-substituted benzoic acids", **1967**, *23*, 2497-2503.

(164) Bruker; *Smart (Version 5.044)*, Madison, Wisconson, 1997

(165) Winter, M. http://www.webelements.com/

(166) C. C. Wilson; A. J. Florence; X. Xu; N. Shankland *New J. Chem.*,, **2003**, submitted.

(167) Wilson, C. C.; Thomas, L. H.; Morrison, C. A. *Chemical Physics Letters*, "A symmetric hydrogen bond revisited: potassium hydrogen maleate by variable

temperature, variable pressure neutron diffraction and plane-wave DFT methods", **2003**, *381*, 102-108.

(168) Buzzeo, M. C.; Zakharov, L. N.; Rheingold, A. L.; Doerrer, L. H. *Journal of Molecular Structure*, "Short, strong hydrogen bond between an aryloxide and phenol in aprotic media", **2003**, *657*, 19-24.

(169) Braga, D.; Sabatino, P.; Di Bungo, C.; Leoni, P.; Pasquali, M., "Oxidative addition of O-H bond to a metal center: synthesis and crystal structure of *trans*-(PhO)(H)Pd(PCy_3)$_2$·PhOH", **1987**.

(170) Othman, A. H.; Goh, S.-C.; Fun, H.-K.; Sivakumar, K. *Acta Cryst*, "Hydrogen bis[(8-quinolinol-*N*)(8-quinolinolate-*N*,*O*)(triphenylphosphine-*P*)silver(I)] acetate monohydrate", **1996**, *C52*, 2760-2763.

(171) Klein, H.-F.; Dal, A.; Jung, T.; Ulrich, F.; Haupt, H.-J. *European Journal of Inorganic Chemistry*, "Intermediates and side-reactions in teh synthesis of molecular diphenolatonickel compounds containing trimethylphosphine ligands", **1998**, 2027-2032.

(172) Hou, Z.; Koizumi, T.-a.; Fujita, A.; Yamazaki, H.; Wakatsuki, Y. *J. Am. Chem. Soc.*, "The binuclear irridium(II) hydride complex [(C_5Me_5)Ir(μ-H)]$_2$: A novel base for reversible derotonation of acidic organic compounds and a unique catalyst for C-C bond cleavage of aromatic 1,2-diols and Micheal additions", **2001**, *123*, 5812-5813.

(173) van Poppel, L. H.; Bott, S. G.; Barron, A. R. *Polyhedron*, "Molecular structures of Ga(tBu)2(OPh)(pyz).PhOH and [(tBu)2Ga(H2O)(m-OH)Ga(tBu)2]2(m-OC6H4O).4(2-Mepy): intra- and inter-molecular hydrogen bonding to gallium aryloxides", **2002**, *21*, 1877-1882.

(174) Belin, C.; Charbonnel, M.; Potier, J. *Journal of the Chemical Society, Chemical Communications*, "X-ray crystal structure of cesium hydrogen bis(monofluorosulfate) with a very short hydrogen bond", **1981**, 1036-1037.

(175) Belin, C.; Roziere, J.; Potier, J. *Acta Crystallographica, Section B: Structural Crystallography and Crystal Chemistry*, "The structure of 2,2'-bipyridinium bis(fluorosulfate)", **1981**, *B37*, 1306-1309.

(176) O'Sullivan, K.; Thompson, R. C.; Trotter, J. *Journal of the Chemical Society [Section] A: Inorganic, Physical, Theoretical*, "Crystal structure of ammonium fluorosulfate", **1970**, 1814-1817.

(177) Kvick, A.; Jonsson, P. G.; Olovsson, I. *Inorganic Chemistry*, "Hydrogen-bond studies. XXXVI. Crystal structure of the 1:1 addition of acetic acid with fluorosulfuric acid", **1969**, *8*, 2775-2780.

(178) Varma, V.; Rangavittal, N.; Rao, C. N. R. *Journal of Solid State Chemistry*, "A study of superionic cesium bisulfate and cesium lithium bisulfate (Cs1-xLixHSO4) by vibrational spectroscopy and x-ray diffraction", **1993**, *106*, 164-173.

(179) Brown, I. D. *Acta Crystallographica, Section B: Structural Crystallography and Crystal Chemistry*, "Prediction of the stereochemistry of polysulfate and hydrogen sulfate ions", **1973**, *29*, 1979-1983.

(180) Kolthoff, I. M.; Chantooni, M. K., Jr. *Journal of the American Chemical Society*, "Complexation in acetonitrile of tetramethylguanidinium (BH+) sulfate with bisulfate, BHSO4-, and BH+ ions", **1969**, *91*, 2875-2883.

(181) Kolthoff, I. M.; Chantooni, M. K., Jr. *Journal of the American Chemical Society*, "Heteroconjugation of the sulfate and bisulfate ions in acetonitrile with uncharged hydrogen bond donors", **1969**, *91*, 25-31.

(182) Nishizawa, S.; Teramae, N.; Yoshimoto, K. In *Jpn. Kokai Tokkyo Koho*; (Tokyo Instrument Mfg. Co., Ltd., Japan).: Jp, 2004; p 19 pp.

(183) Gu, J.; Wang, J.; Leszczynski, J. *Journal of Physical Chemistry B*, "Hydrogen Bonding in 5-Bromouracil-Adenine-5-Bromouracil-Adenine (T+AT+A) Tetrads", **2004**, *108*, 9277-9286.

(184) Matsuda, S.; Henry, A. A.; Schultz, P. G.; Romesberg, F. E. *Journal of the American Chemical Society*, "The Effect of Minor-Groove Hydrogen-Bond Acceptors and Donors on the Stability and Replication of Four Unnatural Base Pairs", **2003**, *125*, 6134-6139.

(185) Cheng, A. C.; Chen, W. W.; Fuhrmann, C. N.; Frankel, A. D. *Journal of Molecular Biology*, "Recognition of Nucleic Acid Bases and Base-pairs by Hydrogen Bonding to Amino Acid Side-chains", **2003**, *327*, 781-796.

(186) Dingley, A. J.; Grzesiek, S. *Journal of the American Chemical Society*, "Direct Observation of Hydrogen Bonds in Nucleic Acid Base Pairs by Internucleotide 2JNN Couplings", **1998**, *120*, 8293-8297.

(187) Tarui, M.; Nomoto, N.; Hasegawa, Y.; Minoura, K.; Doi, M.; Ishida, T. *Chemical & Pharmaceutical Bulletin*, "Thermodynamic effect of complementary hydrogen bond base pairing on aromatic stacking interaction in the guanine-X-Trp complex (X = adenine, guanine, cytosine, thymine)", **1996**, *44*, 1998-2002.

(188) Belot, J. A.; Clark, J.; Cowan, J. A.; Harbison, G. S.; Kolesnikov, A. I.; Kye, Y.-S.; Schultz, A. J.; Silvernail, C.; Zhao, X. *Journal of Physical Chemistry B*, "The Shortest Symmetrical O-H.cntdot..O Hydrogen Bond Has a Low-Barrier Double-Well Potential", **2004**, *108*, 6922-6926.

(189) Mortimer, R. G. *Physical Chemistry*; 2nd ed.; Hartcourt Science and Technology Company: New York, 2000.

(190) Bienko, A. J.; Latajka, Z.; Sawka-Dobrowolska, W.; Sobczyk, L.; Ozeryanskii, V. A.; Pozharskii, A. F.; Grech, E.; Nowicka-Scheibe, J. *Journal of Chemical Physics*, "Low barrier hydrogen bond in protonated proton sponge. X-ray diffraction, infrared, and theoretical ab initio and density functional theory studies", **2003**, *119*, 4313-4319.

(191) Ebata, T.; Fujii, A.; Mikami, N. *International Reviews in Physical Chemistry*, "Vibrational spectroscopy of small-sized hydrogen-bonded clusters and their ions", **1998**, *17*, 331-361.

(192) Poliakoff, M.; Howdle, S. M.; Kazarian, S. G. *Angewandte Chemie, International Edition in English*, "Vibrational spectroscopy in supercritical fluids: from analysis and hydrogen bonding to polymers and synthesis", **1995**, *34*, 1275-1295.

(193) Hudson, B. S. *Proceedings of SPIE-The International Society for Optical Engineering*, "Resonance Raman studies of hydrogen bonded solutions: Quantitative comparisons of experiment with ab initio calculations", **1995**, *2370*, 152-160.

(194) Tomkinson, J. *Spectrochimica Acta, Part A: Molecular and Biomolecular Spectroscopy*, "The vibrations of hydrogen bonds", **1992**, *48A*, 329-348.

(195) Bureiko, S. F.; Denisov, G. S. *Journal of Molecular Structure*, "Spectroscopic study of hydrogen exchange processes and structure of intermediate complexes with intermolecular hydrogen bonds", **2004**, *700*, 49-53.

(196) Flakus, H. T. *Polish Journal of Chemistry*, "Investigation of polarized infrared spectra of the hydrogen bond in molecular crystals. New spectral effects in the vibrational spectroscopy of hydrogen bonded systems", **2003**, *77*, 489-517.

(197) Bratos, S.; Leicknam, J. C.; Gallot, G.; Ratajczak, H. *Understanding Chemical Reactivity*, "Infra-red spectra of hydrogen bonded systems: theory and experiment", **2002**, *23*, 5-30.

(198) Garcia-Viloca, M.; Gelabert, R.; Gonzalez-Lafont, A.; Moreno, M.; Lluch, J. M. *Journal of the American Chemical Society*, "Temperature Dependence of Proton NMR Chemical Shift As a Criterion To Identify Low-Barrier Hydrogen Bonds", **1998**, *120*, 10203-10209.

(199) Harris, R. K. *Solid State Sci.*, "NMR crystallography. The use of chemical shifts", **2004**, *6*, 1025-1037.

(200) Mildvan, A. S.; Massiah, M. A.; Harris, T. K.; Marks, G. T.; Harrison, D. H. T.; Viragh, C.; Reddy, P. M.; Kovach, I. M. *Journal of Molecular Structure*, "Short, strong hydrogen bonds on enzymes: NMR and mechanistic studies", **2002**, *615*, 163-175.

(201) Harris, T. K.; Zhao, Q.; Mildvan, A. S. *Journal of Molecular Structure*, "NMR studies of strong hydrogen bonds in enzymes and in a model compound", **2000**, *552*, 97-109.

(202) Wei, Y.; McDermott, A. E. *ACS Symposium Series*, "Effects of hydrogen bonding on 1H chemical shifts", **1999**, *732*, 177-193.

(203) Jeffrey, G. A. *An introduction to hydrogen bonding*; Oxford Univeristy Press: New York, 1997.

(204) Ventura, K. M.; Greene, S. N.; Halkides, C. J.; Messina, M. *Structural Chemistry*, "A mixed quantum-classical approach for computing effects of intramolecular motion on the low-barrier hydrogen bond", **2001**, *12*, 23-31.

(205) Gilli, P.; Bertolasi, V.; Pretto, L.; Lycka, A.; Gilli, G. *Journal of the American Chemical Society*, "The Nature of Solid-State N-H.cntdot...O/O-H.cntdot...N Tautomeric Competition in Resonant Systems. Intramolecular Proton Transfer in Low-Barrier Hydrogen Bonds Formed by the ...O:C-C:N-NH... .dblarw. ...HO-C:C-N:N... Ketohydrazone-Azoenol System. A Variable-Temperature X-ray Crystallographic and DFT Computational Study", **2002**, *124*, 13554-13567.

(206) Mariam, Y. H.; Chantranupong, L.; Niles, J. *Theochem*, "Computational studies of intramolecular hydrogen-bonding interactions and proton transfer in the tautomers of 1,4-dihydroxy-5,8-naphthoquinone imine: a model for 5-iminodaunomycin", **1999**, *487*, 127-144.

(207) Zhang, Q.; Bell, R.; Truong, T. N. *Journal of Physical Chemistry*, "Ab Initio and Density Functional Theory Studies of Proton Transfer Reactions in Multiple Hydrogen Bond Systems", **1995**, *99*, 592-599.

(208) Ayala, P. Y.; Schlegel, H. B. *J. Chem. Phys.*, "A combined method for determining reaction paths, minima, and transition state geometries", **1997**, *107*, 375-384.

(209) Buzzeo, M. C.; Iqbal, A. H.; Long, C. M.; Millar, D.; Patel, S.; Pellow, M. A.; Saddoughi, S. A.; Smenton, A. L.; Turner, J. F. C.; Wadhawan, J. D.; Compton, R. G.; Golen, J. A.; Rheingold, A. L.; Doerrer, L. H. *Inorganic Chemistry*, "Homoleptic

Cobalt and Copper Phenolate A2[M(OAr)4] Compounds: The Effect of Phenoxide Fluorination", **2004**, *43*, 7709-7725.

(210) Wilson, C. C.; Thomas, L. H.; Morrison, C. A. *Chemical Physics Letters*, "A symmetric hydrogen bond revisited: potassium hydrogen maleate by variable temperature, variable pressure neutron diffraction and plane-wave DFT methods [Chem. Phys. Lett. 381 (2003) 102]. Reply", **2004**, *399*, 292-293.

(211) Morrison, C. A.; Siddick, M. M. *Chemistry--A European Journal*, "Determining the strengths of hydrogen bonds in solid-state ammonia and urea: Insight from periodic DFT calculations", **2003**, *9*, 628-634.

(212) Koritsanszky, T.; Buschmann, J.; Luger, P. *Journal of Physical Chemistry*, "Topological Analysis of Experimental Electron Densities. 1. The Different C-C Bonds in Bullvalene", **1996**, *100*, 10547-10553.

(213) Holladay, A.; Leung, P.; Coppens, P. *Acta Cryst*, "Generalized relations between d-orbital occupancies of transition-metal atoms and electron-density multipole population parameters from X-ray diffraction data", **1983**, *A39*, 377-387.

(214) Coppens, P.; Iversen, B.; Larsen, F. K. *Coordination Chemistry Reviews*, "The use of synchrotron radiation in X-ray charge density analysis of coordination complexes", **2005**, *249*, 179-195.

(215) Coppens, P.; Koritsanszky, T.; Becker, P. *Chemica Scripta*, "Transition metal complexes: what can we learn by combining experimental spin and charge densities?", **1986**, *26*, 463-467.

(216) Coppens, P. *Coordination Chemistry*, "Experimental charge density distribution in metal-metal and metal-ligand bonds", **1981**, *21*, 53-63.

(217) Hirshfeld, F. L. *Acta Crystallographica, Section A: Foundations of Crystallography*, "Can X-ray data distinguish bonding effects from vibrational smearing?", **1976**, *32*, 239-244.

(218) Kobayashi, H.; Cui, H.; Kobayashi, A. *Chemical Reviews (Washington, DC, United States)*, "Organic Metals and Superconductors Based on BETS (BETS = Bis(ethylenedithio)tetraselenafulvalene)", **2004**, *104*, 5265-5288.

(219) Miller, J. S. *Inorganic Chemistry*, "Organometallic- and Organic-Based Magnets: New Chemistry and New Materials for the New Millennium", **2000**, *39*, 4392-4408.

(220) Amabilino, D. B.; Cirujeda, J.; Veciana, J. *Philosophical Transactions of the Royal Society of London, Series A: Mathematical, Physical and Engineering Sciences*, "Crystal architectures of organic molecular-based magnets", **1999**, *357*, 2873-2891.

(221) Lahti, P. M. *Magnetic Properties of Organic Materials*, "An integrated approach to organic-based molecular magnetic materials", **1999**, 661-701.

(222) Nakatsuji, S. i.; Anzai, H. *Journal of Materials Chemistry*, "Recent progress in the development of organomagnetic materials based on neutral nitroxide radicals and charge transfer complexes derived from nitroxide radicals", **1997**, *7*, 2161-2174.

(223) Lahti, P. M. *ACS Symposium Series*, "Design of organic-based materials with controlled magnetic properties", **1996**, *644*, 218-235.

(224) Lahti, P. M. *Trends in Organic Chemistry*, "Studying interelectronic exchange interactions in organic compounds: A molecular approach", **1992**, *3*, 179-191.

(225) Lemal, D. M.; Kawano, K. I. *Journal of the American Chemical Society*, "Stepwise electron abstraction from tetraaminoethylene", **1962**, *84*, 1761-1762.

(226) Wanzlick, H. W.; Kleiner, H. J. *Angewandte Chemie*, "Nucleophilic carbene chemistry. Preparation of 2,2'bis(1,3-diphenylimidazolidine)", **1961**, *73*, 493.

(227) Wanzlick, H. W.; Schikora, E. *Chemische Berichte*, "A nucleophilic carbene", **1961**, *94*, 2389-2393.

(228) Hocker, J.; Giesecke, H.; Merten, R. *Angewandte Chemie*, "On the reactivity of electron-rich olefins. 7. Synthesis of phenol aldehydes from electron-rich olefins", **1976**, *88*, 151-152.

(229) Bock, H.; Hierholzer, B. *Angewandte Chemie*, "Electron transfer and ion pair formation. Part 6. ENDOR spectroscopy in water: reductions and oxidations of organic compounds", **1988**, *100*, 1127-1129.

(230) Bock, H.; Ruppert, K.; Merzweiler, K.; Fenske, D.; Goesmann, H. *Angewandte Chemie*, "Structures of distorted p systems. 2. Tetrakis(dimethylamino)ethene dication, [(Me2N)2C+]2 carbenium ions connected with a twisted carbon-carbon single bond", **1989**, *101*, 1715-1717.

(231) Bock, H.; Borrmann, H.; Havlas, Z.; Oberhammer, H.; Ruppert, K.; Simon, A. *Angew. Chemie., Int. Ed.*, "Tetrakis(dimethylamino)ethene: An extremely Electron-Rich Molecule with Unusual Structure both in the Crystal and in the Gas Phase", **1991**, *30*, 1678-1681.

(232) Bruckmann, J.; Krueger, C.; Borrmann, H.; Simon, A.; Bock, H. *Zeitschrift für Kristallographie*, "Structure of teterakis(dimethylamino)ethene (TDAE) at low temperatures", **1995**, *210*, 521-524.

(233) Cetinkaya, B.; King, G. H.; Krishnamurthy, S. S.; Lappert, M. F.; Pedley, J. B. *Journal of the Chemical Society [Section] D: Chemical Communications*, "Photoelectron spectra of electron-rich olefins and an isostructural boron compound. Olefins of exceptionally low first ionization potential", **1971**, 1370-1371.

(234) Denk, M.; Green, J. C.; Metzler, N.; Wagner, M. *Journal of the Chemical Society, Dalton Transactions: Inorganic Chemistry (1972-1999)*, "Electronic structure of a stable silylene: photoelectron spectra and theoretical calculations of Si(NRCHCHNR), Si(NRCH2CH2NR) and SiH2(NRCHCHNR)", **1994**, 2405-2410.

(235) Kuroboshi, M.; Waki, Y.; Tanaka, H. *Synlett*, "Tetrakis(dimethylamino)ethylene (TDAE)-Pd promoted reductive homo-coupling of aryl halides", **2002**, 637-639.

(236) Dolbier, W. R.; Medebielle, M.; Ait-Mohand, S. *Tetrahedron Letters*, "Single electron transfer approaches to the practical synthesis of aromatic and heterocyclic-CF2H derivatives", **2001**, *42*, 4811-4814.

(237) Burkholder, C. R.; Dolbier, W. R.; Medebielle, M. *Journal of Fluorine Chemistry*, "Synthesis and reactivity of halogeno-difluoromethyl aromatics and heterocycles. Application to the synthesis of gem-difluorinated bioactive compounds", **2001**, *109*, 39-48.

(238) Kuroboshi, M.; Goto, K.; Mochizuki, M.; Tanaka, H. *Synlett*, "Tetrakis(dimethylamino)ethylene (TDAE) as a potent electron source for Cr-mediated allylation of aldehydes and ketones", **1999**, 1930-1932.

(239) Burkholder, C.; Dolbier, W. R., Jr.; Medebielle, M. *Tetrahedron Letters*, "Reaction of 2-(bromodifluoromethyl)benzoxazole with tetrakis(dimethylamino)ethylene

(TDAE) in the presence of aldehydes. A convenient synthesis of 2-(difluoromethyl)benzoxazole alcohols", **1997**, *38*, 821-824.

(240) Burkholder, C.; Dolbier, W. R., Jr.; Medebielle, M. *Journal of Organic Chemistry*, "Tetrakis(dimethylamino)ethylene as a useful reductant of some bromodifluoromethyl heterocycles. Application to the synthesis of new gem-difluorinated heteroarylated compounds", **1998**, *63*, 5385-5394.

(241) Burkholder, C.; Dolbier, W. R., Jr.; Medebielle, M.; Ndedi, A. *Tetrahedron Letters*, "Tetrakis(dimethylamino)ethylene as a useful reductant of some chlorodifluoromethylated ketones. A new approach for the synthesis of a,a-difluoro ketone derivatives", **1998**, *39*, 8853-8856.

(242) Kambe, T.; Nogami, Y.; Oshima, K. *Physical Review B: Condensed Matter and Materials Physics*, "Annealing effects on the magnetic and structural properties of single-crystal TDAE-C60", **2000**, *61*, R862-R865.

(243) Narymbetov, B.; Kobayashi, H.; Tokumoto, M.; Omerzu, A.; Mihailovic, D. *Chemical Communications (Cambridge)*, "Low temperature structural analysis of a TDAE.cntdot.C60 crystal", **1999**, 1511-1512.

(244) Blinc, R.; Arcon, D.; Cevc, P.; Mihailovic, D.; Omerzu, A. *Applied Magnetic Resonance*, "Magnetic resonance of the weak organic magnet TDAE-C-60", **1996**, *11*, 203-228.

(245) Blinc, R.; Pokhodnia, K.; Cevc, P.; Arcon, D.; Omerzu, A.; Mihailovic, D.; Venturini, P.; Golic, L.; Trontelj, Z.; et al. *Physical Review Letters*, "Antiferromagnetic correlations and weak ferromagnetism in a TDAE+-C60- single crystal", **1996**, *76*, 523-526.

(246) Konarev, D. V.; Drichko, N. V.; Graja, A. *Journal de Chimie Physique et de Physico-Chimie Biologique*, "Optical absorption spectra of chemically generated C60 and C70 anions", **1998**, *95*, 2143-2156.

(247) Konarev, D. V.; Drichko, N. V.; Semkin, V. N.; Graja, A. *Synthetic Metals*, "Spectral studies of chemically generated C60n- and C70n- anions; n = 1, 2 and 3", **1999**, *103*, 2384-2385.

(248) Sato, T.; Yamabe, T.; Tanaka, K. *Physical Review B: Condensed Matter*, "Magnetic ordering in fullerene charge-transfer complexes", **1997**, *56*, 307-314.

(249) Colvin, A. J.; Dolgos, M. R.; Turner, J. F. C., "unpublished results", **2005**.

(250) Liu, Y.; Lindner, P. E.; Lemal, D. M. *Journal of the American Chemical Society*, "Thermodynamics of a Diaminocarbene-Tetraaminoethylene Equilibrium", **1999**, *121*, 10626-10627.

(251) Liu, Y.; Lemal, D. M. *Tetrahedron Letters*, "Concerning the "Wanzlick equilibrium"", **2000**, *41*, 599-602.

(252) Lemal, D. M.; Lovald, R. A.; Kawano, K. I. *Journal of the American Chemical Society*, "Tetraaminoethylenes. The question of dissociation", **1964**, *86*, 2518-2519.

(253) Denk, M. K.; Hatano, K.; Ma, M. *Tetrahedron Letters*, "Nucleophilic carbenes and the Wanzlick equilibrium: a reinvestigation", **1999**, *40*, 2057-2060.

(254) Winberg, H. E.; Carnahan, J. E.; Coffman, D. C.; Brown, M. *Journal of the American Chemical Society*, "Tetraaminoethylenes", **1965**, *87*, 2055-2056.

(255) Alder, R. W.; Allen, P. R.; Williams, S. J. *Journal of the Chemical Society, Chemical Communications*, "Stable carbenes as strong bases", **1995**, 1267-1268.

(256) Alder, R. W.; Allen, P. R.; Murray, M.; Orpen, A. G. *Angewandte Chemie, International Edition in English*, "Bis(diisopropylamino)carbene", **1996**, *35*, 1121-1123.

(257) Alder, R. W.; Blake, M. E. *Chemical Communications (Cambridge)*, "Bis(N-piperidyl)carbene and its slow dimerization to tetrakis(N-piperidyl)ethene", **1997**, 1513-1514.

(258) Alder, R. W.; Blake, M. E. *Chemical Communications (Cambridge)*, "Bis(N-piperidyl)carbene and its slow dimerization to tetrakis(N-piperidyl)ethene. [Erratum to document cited in CA127:262414]", **1998**, 441.

(259) Alder, R. W.; Blake, M. E.; Oliva, J. M. *Journal of Physical Chemistry A*, "Diaminocarbenes; Calculation of Barriers to Rotation about Ccarbene-N Bonds, Barriers to Dimerization, Proton Affinities, and 13C NMR Shifts", **1999**, *103*, 11200-11211.

(260) Cardin, D. J.; Doyle, M. J.; Lappert, M. F. *Journal of the Chemical Society, Chemical Communications*, "Rhodium(I)-catalyzed dismutation of electron-rich olefins. Rhodium(I) carbene complexes as intermediates", **1972**, 927-928.

(261) Cetinkaya, B.; Dixneuf, P.; Lappert, M. F. *Journal of the Chemical Society, Chemical Communications*, "General synthesis of transition metal carbene complexes. Chromium(0), iron(0), iridium(I), nickel(II), palladium(II), platinum(II), and gold(I) mono- and oligocarbene species from electron-rich olefins", **1973**, 206.

(262) Cetinkaya, B.; Dixneuf, P.; Lappert, M. F. *Journal of the Chemical Society, Dalton Transactions: Inorganic Chemistry (1972-1999)*, "Carbene complexes. VIII. Chromium(0), iron(0), rhodium(I), iridium(I), nickel(II), palladium(II), platinum(II), and gold(I) mono- and oligocarbene species from electron-rich olefins", **1974**, 1827-1833.

(263) Lappert, M. F.; Pye, P. L. *Journal of the Chemical Society, Dalton Transactions: Inorganic Chemistry (1972-1999)*, "Carbene complexes. Part 10. Electron-rich olefin-based mono-, bis-, and tris-carbene-tungsten(0) complexes and some derived six- and seven-coordinate mono- and bis-carbene-dihalogenotungsten(II) and related molybdenum(II) species", **1977**, 1283-1291.

(264) Lappert, M. F.; Pye, P. L. *Journal of the Less-Common Metals*, "Carbene and related complexes of molybdenum derived from electron-rich olefins", **1977**, *54*, 191-207.

(265) Lappert, M. F.; Pye, P. L. *Journal of the Chemical Society, Dalton Transactions: Inorganic Chemistry (1972-1999)*, "Carbene complexes. Part 12. Electron-rich olefin-derived neutral mono- and bis-(carbene) complexes of low-oxidation-state manganese, iron, cobalt, nickel, and ruthenium", **1977**, 2172-2180.

(266) Lappert, M. F.; Pye, P. L.; McLaughlin, G. M. *Journal of the Chemical Society, Dalton Transactions: Inorganic Chemistry (1972-1999)*, "Carbene complexes. Part 9. Electron-rich olefin-derived carbene-molybdenum(0) and amidinium molybdate(0) complexes, and the crystal and molecular structure of cis-tetracarbonylbis(1,3-dimethylimidazolidin-2-ylidene)molybdenum(0)", **1977**, 1272-1282.

(267) Carty, A. J.; Taylor, N. J.; Smith, W. F.; Lappert, M. F.; Pye, P. L. *Journal of the Chemical Society, Chemical Communications*, "Carbon-carbon bond-making by trapping of a nucleophilic carbene (from an electron-rich olefin) by a s-p-acetylido(hexacarbonyl)di-iron complex; x-ray crystal and molecular structure", **1978**, 1017-1019.

(268) Hitchcock, P. B.; Lappert, M. F.; Pye, P. L.; Thomas, S. *Journal of the Chemical Society, Dalton Transactions: Inorganic Chemistry (1972-1999)*, "Carbene complexes. 16. Synthesis of NN'N"N"'-tetraaryl-substituted electron-rich olefin-derived carbeneruthenium(II) complexes containing an ortho-metalated-N-arylcarbene ligand; crystal structures of RuClR(PEt3)2 and Ru(CO)ClR(PEt3)2 (R = 1,3-bis(4-tolyl)imidazolidin-2-ylidene-C2C2')", **1979**, 1929-1942.

(269) Hitchcock, P. B.; Lappert, M. F.; Terreros, P. *Journal of Organometallic Chemistry*, "Homoleptic tris(organochelate)iridium(III) complexes by spontaneous ortho-metalation of election-rich olefin-derived N,N'-diarylcarbene ligands and the x-ray structures of tris(ortho-metalated-carbene)iridium(III) complexes", **1982**, *239*, C26-C30.

(270) Doyle, M. J.; Lappert, M. F.; Pye, P. L.; Terreros, P. *Journal of the Chemical Society, Dalton Transactions: Inorganic Chemistry (1972-1999)*, "Carbene complexes. Part 18. Synthetic routes to electron-rich olefin-derived monocarbenerhodium(I) neutral and cationic complexes and their chemical and physical properties", **1984**, 2355-2364.

(271) Coulson, C. A. *Proc. R. Soc. Lond. Series A*, "Bond lengths in conjugated molecules: the present position", **1951**, *207*, 91-100.

(272) Bader, R. F. W.; Tang, T.-H.; Tal, Y.; Biegler-Konig, F. *J. Am. Chem. Soc.*, "Properties of atoms and bonds in hydrocarbon molecules", **1982**, *104*, 946-952.

(273) Bader, R. F. W.; Tang, T.-H.; Tal, Y.; Biegler-Konig, F. *J. Am. Chem. Soc.*, "Molecular structure and its change: Hydrocarbons", **1982**, *104*, 940-945.

(274) Knop, O.; Boyd, R. J.; Choi, S. C. *J. Am. Chem. Soc.*, "S-S bond lengths,or can abond length be estimated from a single parameter/", **1988**, *110*, 7299-7301.

(275) Baerends, E. J.; al., e.; *Amsterdam Denisty Functional*, Amsterdam, 2004

(276) Fonseca Guerra, C.; al., e. *Theoretical Chemistry Accounts*,, **1998**, *99*, 391.

(277) te Velde, G.; al., e. *Journal of Computational Chemistry*, "Chemistry with ADF", **2001**, *22*, 931-967.

(278) Vosko, S. H.; Wilk, L.; Nusair, M. *Canadian Journal of Physics*,, **1980**, *58*, 1200-1211.

(279) Beck, A. D. *Physics Reviews A.*,, **1988**, *38*, 3098-3100.

(280) Perdew, J. P. *Physics Reviews B.*,, **1986**, *33*, 8822-8824.

(281) Sheldrick, G. M.; *SADABS*, Gottingen, Germany, 1996

(282) Bruker; *Saint (Version 5.01)*, Madison, Wisconson, 1997

(283) Larson, A. C.; von Dreele, R. B.; *GSAS: General Structure Analysis System*, Los Alamos, NM. USA, 2000

(284) Schomaker, V.; Trueblood, K. N. *Acta Crystallographica, Section B: Structural Science*, "On the rigid body motion of molecules in crystals", **1968**, *24*, 63-77.

(285) Hardie, M. J.; Kirschbaum, K.; Martin, A.; Pinkerton, A. A. *Journal of Applied Crystallography*, "An open flow helium cryostat for single crystal X=ray diffraction experiments", **1998**, *31*, 815-817.

(286) Schultz, A. J.; Carlin, R. L. *Acta Crystallographica, Section B: Structural Science*, "Single-crystal pulsed neutron diffraction structure of the antiferromagnet K2[FeCl5(H2O)] with and without applied pressure", **1995**, *B51*, 43-47.

(287) Schultz, A. J.; Srinivasan, K.; Teller, R. G.; Williams, J. M.; Lukehart, C. M. *Journal of the American Chemical Society*, "Single-crystal, time-of-flight, neutron-diffraction structure of hydrogen cis-diacetyltetracarbonylrhenate, [cis-(OC)4Re(CH3CO)2]H: a metallaacetylacetone molecule", **1984**, *106*, 999-1003.

(288) Sears, V. F. *Methods of Experimental Physics*; Academic Press:, 1986; Vol. 23.

(289) Howard, J. A. K.; Johnson, O.; Schultz, A. J.; Stringer, A. M. *Journal of Applied Crystallography*, "Determination of the neutron absorption cross section for hydrogen as a function of wavelength with a pulsed neutron source", **1987**, *20*, 120-122.

(290) Schaftenaar, G.; Noordik, J. H. *J. Comput.-Aided Mol. Design*, "Molden: a pre- and post-processing program
for molecular and electronic structures", **2000**, *14*, 123-134.

APPENDIX

Nygren, C. L.; Wilson, C. C.; Turner, J. F. C. *Journal of Physical Chemistry A*, "On the Solid State Structure of 4-Iodobenzoic Acid", **2005**, *109*, 2586-2593.

Nygren, C. L.; Wilson, C. C.; Turner, J. F. C. *Journal of Physical Chemistry A*, "Electron and Nuclear Positions in the Short Hydrogen Bond in Urotropine-N-oxide.Formic Acid", **2005**, *109*, 1911-1919.

Manson, J. L.; Lancaster, T.; Chapon, L. C.; Blundell, S. J.; Schlueter, J. A.; Brooks, M. L.; Pratt, F. L.; Nygren, C. L.; Qualls, J. S. *Inorganic Chemistry*, "Cu(HCO2)2(pym) (pym = pyrimidine): Low-Dimensional Magnetic Behavior and Long-Range Ordering in a Quantum-Spin Lattice", **2005**, *44*, 989-995.

Nygren, C. L.; Bragg, M. E. T.; Turner, J. F. C. *Acta Crystallographica, Section C: Crystal Structure Communications*, "trans-Dichloro-cis-bis(3,6-dimethylcarbazolyl)-cis-bis(tetrahydrofuran)zirconium(IV) benzene sesquisolvate", **2004**, *C60*, m4-m6.

Nygren, C.; Chen, T.; Zhong, S.; Kaczmarek, C.; Turner, J. F. C.; Baker, D. C. *Acta Crystallographica, Section C: Crystal Structure Communications*, "A pair of epimeric 13-hydroxy-2,3,6,7-tetramethoxy-8b,11,12,12a,13,13a-hexahydro-9H-9a-azacyclopenta[b]triphenylene-10-ones", **2004**, *C60*, o208-o210.

Nygren, C. L.; Bragg, M. E. T.; Turner, J. F. C. *Acta Crystallographica, Section C: Crystal Structure Communications*, "Tetrakis(tetrahydrofuran-kO)lithium mer-tris(carbazolyl-kN)-trans-dichloro(tetrahydrofuran-kO)zirconate", **2004**, *C60*, m94-m96.

Masuda, T.; Chakoumakos, B. C.; Nygren, C. L.; Imai, S.; Uchinokura, K. *Journal of Solid State Chemistry*, "A novel germanate, Cu2Fe2Ge4O13, with a four tetrahedra oligomer", **2003**, *176*, 175-179.

Nygren, C. L.; Bragg, M. E. T.; Turner, J. F. C. *Acta Crystallographica, Section C: Crystal Structure Communications*, "(Tetrahydrofuran)potassium mer-trans-tris(carbazolyl)dichloro(tetrahydrofuran)zirconate", **2003**, *C59*, m275-m276.

On the Solid State Structure of 4-Iodobenzoic Acid

Cara L. Nygren,[†] Chick C. Wilson,[‡] and John F. C. Turner*[,§]

Department of Chemistry, University of Tennessee, Knoxville, Tennessee 37996-1600, Department of Chemistry, University of Glasgow, Glasgow, G12 8QQ United Kingdom, and Neutron Sciences Consortium and Department of Chemistry, University of Tennessee, Knoxville, Tennessee 37996-1600

Received: June 28, 2004; In Final Form: November 11, 2004

The solid-state structure of 4-iodobenzoic acid has been confirmed by variable temperature X-ray diffraction, variable temperature solid-state NMR and differential scanning calorimetry. 4-iodobenzoic acid crystallizes in the space group $P2_1/n$, and dimerizes in the solid state about a center of inversion. Using extensive X-ray crystallographic data collections, the placement of the carboxylate H atoms from the residual electron density in difference Fourier maps was determined. The position of the electron density associated with the proton is found to vary with temperature in that the population of the disordered sites changes with varying temperature. Determination of the crystal structure between the temperatures of 248 and 198 K was not possible due to a phase transition, an endothermic event occurring at 230.77 K. The phase transition is also indicated by a change in the relaxation time of the ring carbon atoms in the solid-state NMR data. Though the dominating force in the dimeric unit in the solid state is the presence of strong hydrogen bonds, there are also van der Waals forces present between the iodine atoms. In the layered structure, the iodine−iodine distance is within the van der Waals contact radii, an interaction which causes a deformation in the electron density of the iodine atoms.

I. Introduction

The carboxylic acid moiety is an important structural feature that occurs frequently in crystal engineering and biology.[1−4] In general, structures of carboxylic acids in the solid state are dominated by dimers in which the carbonyl oxygen and hydroxyl groups act as donors and acceptors.[2,5−35] The structure of this hydrogen-bonded dimer is shown in Figure 1.

As also shown in Figure 1, the full, real space hydrogen bond scheme is often developed via a crystallographic center of inversion.[5−16] However, the presence of a carboxylic acid group does not always imply the presence of a dimeric structure[36] and two-dimensional networks and chains have also been observed. In systems where the dimeric structure is observed, the degenerate nature of the atoms involved in the hydrogen-bonded carboxylic acid dimer has attracted the interest of the theoretical community as a model for proton transfer.[3,37−46]

The 4-halo benzoic acids crystallize isostructurally in the monoclinic space group $P2_1/n$[29,31−35,47,48] and are dimeric in the solid state, a phenomenon that is also persistent in solution.[49] The structure of 4-iodobenzoic acid has been known since 1982, when the powder diffraction pattern was first reported.[31] A single crystal diffraction experiment two years later also substantially confirmed the molecular structure and lattice.[29] In this paper, we examine the structure of 4-iodobenzoic acid to characterize the intermolecular hydrogen bond and to investigate the other forces that determine the structure of this material, employing a series of X-ray diffraction measurements, solid-state NMR, and differential scanning calorimetry in addition to spherical atom refinements of the diffraction data.

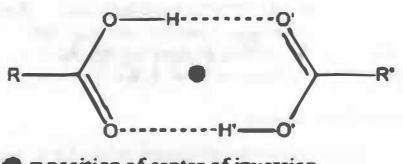


Figure 1. Schematic representation of a typical carboxylic acid dimer with the crystallographically generated atoms as X'.

4-Iodobenzoic acid is of interest as the molecular structure ensures that there are several possible identifiable forces that may exist in the lattice: the most obvious of these is the hydrogen-bonding interaction, but "π-stacking", van der Waals, dispersion, and multipole forces may all play a role. As we shall show, the structure that is evolved on crystallization is dependent on several of these factors, and we offer a qualitative ordering of the strength of these interactions; moreover, the presence of these forces is confirmed by the unsatisfactory spherical atom refinement of the diffraction data at any temperature. Given our interest in the structural chemistry of the hydrogen atom, we were interested in the arrangement of the hydrogen atom positions in the presence of a range of other possible interactions.

It is well accepted that the most common diffraction technique for the location of H atoms in a hydrogen bond is neutron diffraction. However, an important distinction must be made, in that a neutron diffraction experiment simply describes the nuclear density in the hydrogen bond and the distribution of electron density in a molecular system is only measurable by X-ray diffraction experiments. In many heavy atom systems, the nuclear and electron densities are strongly correlated; however, the density in a hydrogen bond is not correlated in the same manner.[50] The distribution of density in a 3-centered−4-electron bond such as the hydrogen bond is often diffuse and

† Department of Chemistry, University of Tennessee.
‡ University of Glasgow.
§ Neutron Sciences Consortium and Department of Chemistry, University of Tennessee.

10.1021/jp047189b CCC: $30.25 © 2005 American Chemical Society
Published on Web 02/25/2005

TABLE 1: Selected Refinement Parameters for the Collected Data

T (K)	103	123	148	173
θ range (deg)	2.70–28.33	1.35–28.28	2.69–28.20	2.70–28.24
index range for data collection	$-5 \le h \le 5$ $-7 \le k \le 7$ $-39 \le l \le 39$	$-5 \le h \le 5$ $-7 \le k \le 7$ $-39 \le l \le 40$	$-5 \le h \le 5$ $-7 \le k \le 7$ $-40 \le l \le 40$	$-5 \le h \le 5$ $-7 \le k \le 7$ $-39 \le l \le 39$
no. of reflns collected	6519	6704	6783	7365
no. of ind reflns	1759 [R(int) = 0.0232]	1755 [R(int) = 0.0267]	1748 [R(int) = 0.0294]	1781 [R(int) = 0.0267]
completeness to θ = 28.33°	96.30%	96.00%	95.70%	97.20%
data/restraints/parameters	1759/0/93	1755/0/92	1748/0/92	1781/0/92
S	1.311	1.446	1.426	1.323
final R indices [$I > 2\sigma(I)$]	$R1$ = 0.0335, $wR2$ = 0.0777	$R1$ = 0.0574, $wR2$ = 0.1492	$R1$ = 0.0613, $wR2$ = 0.1533	$R1$ = 0.0423, $wR2$ = 0.1011
R indices (all data)	$R1$ = 0.0366, $wR2$ = 0.0785	$R1$ = 0.0584, $wR2$ = 0.1495	$R1$ = 0.0627, $wR2$ = 0.1538	$R1$ = 0.0474, $wR2$ = 0.1025
T (K)	198	248	298	
θ range (deg)	1.35–28.25	2.70–28.29	1.36–28.24	
index range for data collection	$-5 \le h \le 5$ $-7 \le k \le 7$ $-39 \le l \le 39$	$-5 \le h \le 5$ $-8 \le k \le 8$ $-39 \le l \le 39$	$-5 \le h \le 5$ $-7 \le k \le 8$ $-39 \le l \le 39$	
no. of reflns collected	7325	7007	6917	
no. of ind reflns	1775 [R(int) = 0.0291]	1789 [R(int) = 0.0283]	1785 [R(int) = 0.0312	
completeness to θ = 28.33°	96.20%	95.90%	96.10%	
data/restraints/parameters	1775/0/92	1789/0/92	1785/0/92	
S	1.319	1.358	1.308	
final R indices [$I > 2\sigma(I)$]	$R1$ = 0.0550, $wR2$ = 0.1275	$R1$ = 0.0417, $wR2$ = 0.1047	$R1$ = 0.0506, $wR2$ = 0.1234	
R indices (all data)	$R1$ = 0.0607, $wR2$ = 0.1292	$R1$ = 0.0457, $wR2$ = 0.1059	$R1$ = 0.0589, $wR2$ = 0.1260	

anisotropic in nature; however, the nuclear density is generally not diffuse in a 3c–4e bond. Therefore, the only way to clearly demonstrate the distribution of electron density in a bond is through a series of extensive X-ray diffraction experiments.

II. Experimental Section

4-Iodobenzoic acid was purchased from Acros and was recrystallized from acetone. The material crystallizes as thin plates from the slow evaporation of an acetone solution (0.0534 M). For the temperature range 103–198 K, the crystals were mounted in a loop in Paratone oil. For temperatures of 223 K to room temperature, the crystals were mounted with epoxy on a glass fiber. Single-crystal X-ray diffraction data were collected using a Bruker AXS Smart 1000 diffractometer equipped with a CCD area detector and graphite monochromatized Mo source (Mo Kα, 0.71073 Å) and a Nicolet LT-2 cooling system. The crystal-to-detector distance was 5.0 cm. The parameters of each data collection are collated in Table 1.

More than a hemisphere of data were collected over the angular range of $2.70 < 2\theta < 28.33$ (103 K).[51] Frame widths of 0.3° were used for the data collection of 6519 reflections, counting 40 s per frame. Data reduction and spherical atom analyses were carried out using the Bruker program Saint[52] and the General Structure Analysis System (GSAS).[53] The unit cell dimensions were refined on the basis of 5544 reflections. A multiscan absorption correction was made using SADABS.[54] The data collection for 173 and 298 K was repeated and an analytical absorption correction[55] was used to ensure the results of the preceding experiments were valid, considering the habit of the crystal as well as the presence of iodine in the molecular structure. The results from these experiments showed little change in the hydrogen bond motif or in the residual electron density distributed around the iodine.

Systematic absences were consistent with the space group $P2_1/n$. A total of 6159 reflections were collected, and merging of equivalent reflections gave 1759 unique reflections (R_{int} = 2.32%), with 1622 classed as observed ($|F_{io}| > 4\sigma_F$). The structure was solved by direct methods (SHELXTL),[56] refined by the full matrix least-squares method, and completed by a series of difference Fourier syntheses. All non-hydrogen atoms were refined anisotropically, with the aromatic hydrogen atoms being introduced at idealized positions and refined using a riding model. Weighted R-factors, wR^2, and all goodness-of-fit values are based on F^2.

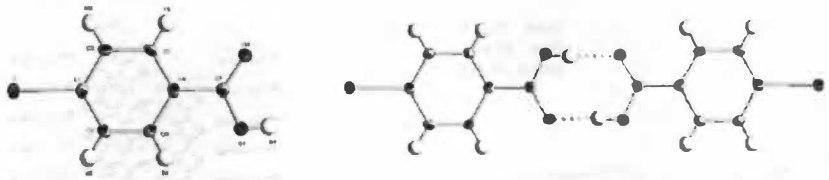
Differential scanning calorimetry was used to determine the thermodynamics of any phase behavior, using a Mettler Toledo DSC 820 with a temperature range of −120 to +100 °C and a heating/cooling rate of 10 °C/min. The samples were prepared in aluminum pans. For the measurement of heat capacity, the basic lines of the empty pan and sapphire reference were measured and compared to the heat flow measurements of the sample. The heat capacity of the sample was measured in two runs.

CPMAS solid-state NMR data were collected at a frequency of 100.550 MHz using a Varian INOVA 400 NMR spectrometer. The 90° pulse of proton resonance was 4 μs, the contact time was 5 ms and a MAS rate 6.555 kHz was used. A total of 400 transients were collected with a relaxation delay of 3 s and an acquisition time of 45 ms.

Solution NMR data were obtained using a Varian Mercury 300 MHz spectrometer, at which field the resonant frequency of ^{13}C is 75.454 MHz, with the ^{1}H frequency being 300.088 MHz, from solutions of the recrystallized material in DMSO-d_6. Chemical shifts were referenced to tetramethylsilane via residual ^{1}H residues in the solvent or the ^{13}C shift of the solvent.

III. Results

A. Temperature Variation and Structure of the Lattice. Diffraction data were collected from crystalline specimens of 4-iodobenzoic acid, grown from evaporation of an acetone solution, at temperatures of 103, 123, 148, 173, 198, 248, and 298 K. Initial spherical atom refinements were unsurprising and confirmed the previously determined space group of $P2_1/n$, and the room temperature lattice parameters were found to be similar



(a) (b)

Figure 2. (a) Molecular structure of 4-iodobenzoic acid, corresponding to the asymmetric unit in the crystal, together with (b) the structure of the dimmer at 103K.



Figure 3. Packing diagram at 103 K showing the dimeric unit within the unit cell.

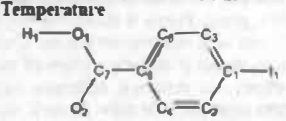
to the previously reported values.[29,31] The two sets of previously determined lattice constants are compiled in Table 2, together with the same constants determined in these experiments.

TABLE 2: Lattice Parameters (Reduced Unit Cell) for the Collected Data at Variable Temperature

a (Å)	b (Å)	c (Å)	β (deg)	T (K)	ref
4.160	6.040	30.108	90.48	298	31
4.156	6.030	30.109	90.52	298	29
4.0567(12)	5.9409(17)	30.223(9)	91.019(4)	103	this work
4.0688(10)	5.9466(15)	30.253(8)	90.982(4)	123	this work
4.0778(11)	5.9724(17)	30.243(8)	90.893(4)	148	this work
4.0960(13)	5.9745(19)	30.157(10)	90.852(5)	173	this work
4.1049(6)	5.9933(9)	30.179(5)	90.878(2)	198	this work
4.1305(5)	6.0075(7)	30.143(3)	90.731(2)	248	this work
4.1527(19)	6.009(3)	30.037(3	90.623(7)	298	this work

B. Molecular Structure from Spherical Atom Refinements. The gross molecular structure, determined from spherical atom refinements, is unsurprising with the non-hydrogenous structure remaining relatively invariant with temperature. A representative structure of the asymmetric unit is shown in Figure 2a together with the structure of the dimer evolved through the center of inversion. Figure 3 shows the unit cell for the lowest experimental temperature, and Figure 4 shows the asymmetric unit at the highest and lowest temperatures of measurement. Salient bond molecular structural parameters are given in Table 3, together with the labeling scheme.

TABLE 3: Selected Intramolecular Structural Parameters at Variable Temperature



T (K)	$r_{O_2C_7}$ (Å)	$r_{O_2C_8}$ (Å)
103	1.300(7)	1.233(7)
123	1.295(13)	1.240(13)
148	1.284(13)	1.248(13)
173	1.281(8)	1.242(8)
198	1.282(11)	1.241(11)
248	1.277(8)	1.241(8)
298	1.268(10)	1.234(10)

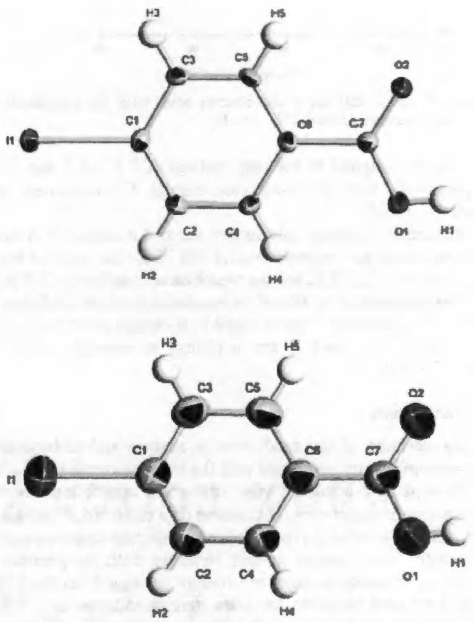


Figure 4. Representation of the asymmetric unit at 103 K (top) and 298 K (bottom).

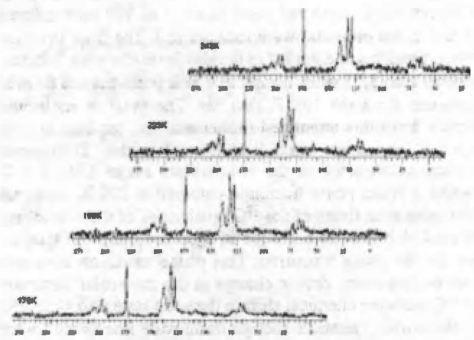


Figure 5. ^{13}C CPMAS SSNMR variable temperature spectra.

Solid-state NMR spectra were consistent with the asymmetric unit and are shown in Figure 5. These spectra also showed a slight change in the relaxation time for the ring carbon atoms, as determined from Lorentzian fits to the measured spectra. The resonances at δ/ppm = 138.94, δ/ppm = 131.80 and δ/ppm =

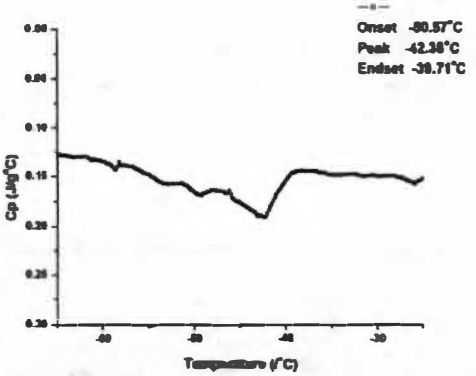


Figure 6. DSC data for 4-iodobenzoic acid, with the temperature transition centered around 230−233 K.

127.86 are assigned to the ring carbons (C2/3, C4/5 and C6 respectively), with the carboxylate carbon, C7, resonating at δ/ppm = 173.48.

Differential scanning calorimetry showed a small and broad endothermic event centered around 230.77 K; the onset of this transition is at 222.58 K and the transition is complete by 233.44 K. The temperature profile of the transition is shown in Figure 6 and the transition is characterized by a change in entropy (ΔS = −0.393 J K^{-1} mol^{-1}) and a change in enthalpy (ΔH = −91.77 J mol^{-1}).

IV. Discussion

The intention of this study was to analyze and understand the electron density associated with the hydrogen atom involved in the hydrogen-bonded dimer interaction and follow these changes with temperature. Diffraction data collected at variable temperature revealed the expected intramolecular structure with apparently little change in this structure with temperature. However, repeated attempts at structure solution from the 223 K data set were unsuccessful. Data were re-collected at 223 K several times, each time the reflections could not be indexed. When the data were indexed using a known unit cell from the 198 K data collection, the agreement in the reflections was poor. Of 800 reflections analyzed using Smart,[31] all 800 were indexed in h and k, but only 205 were indexed in l. The final structure solution from this attempt led to unreliable results with R-factors of greater than 35% when using the atomic positions and thermal parameters from the 198 K data set. The putative molecular structure from this attempted refinement was unphysical with respect to geometry, bond lengths, and angles. Differential scanning calorimetry in the temperature range 153−373 K revealed a broad phase transition centered at 230 K. Analysis of the relaxation times of the ^{13}C resonances of the 4-iodobenzoic acid also showed a change in T_2 at the transition temperature for the phase transition. This phase transition does not, however, cause any drastic change in the molecular structure. The ^{13}C isotropic chemical shift in the solid state ($\Delta\delta$ = 29.293 Hz) show little variation, though static wide line spectra were not recorded and so no determination of the individual components of the chemical shift anisotropy are therefore given.

That the phase change is minor is clear from the magnitude of the thermodynamic parameters. The change in entropy and enthalpy determined from the two DSC experiments are ΔS = −0.393 J K^{-1} mol^{-1} and ΔH = −91.77 J mol^{-1}, respectively. The differences observed in the two sets of data are due to the residual solvent present in the first run that was subsequently evaporated upon heating of the sample.

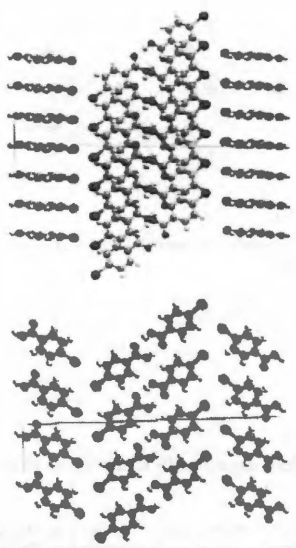


Figure 7. Packing diagrams from the 103 K data set demonstrating the stacking of the dimeric units as well as the I−I interactions.

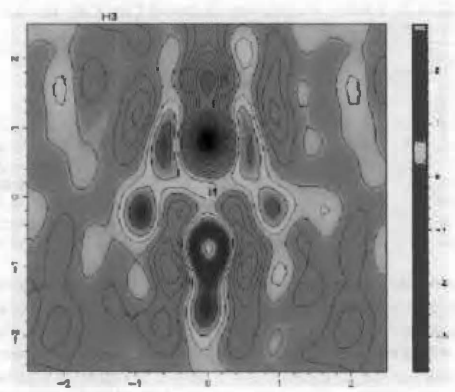


Figure 8. Fourier difference map showing the residual electron density around the iodine position at 103 K ranging from −3.64 to +2.87 e$^-$/Å^3.

In common with many carboxylic acids, the dimeric unit present in 4-iodobenzoic acid is generated by the presence of a center of inversion and this center of inversion lies in the plane of the carboxylate group. Figure 4 shows the two asymmetric units for the low and high temperature phases. Unsurprisingly, these dimeric units persist at all temperatures of measurement, with the only observable structural difference between them being the hydrogen positions, vide infra. As such, the description of the crystal is best discussed using the dimer as the basic chemical unit present.

This dimeric unit is stacked in single stacks and a series of packing diagrams are presented in Figure 7, showing the arrangement of the dimers. Interestingly, the dimeric units are arranged in the maximum energy configuration with respect to the dipole moment present on each acid moiety, though the net dipole moment of the dimer is clearly zero.

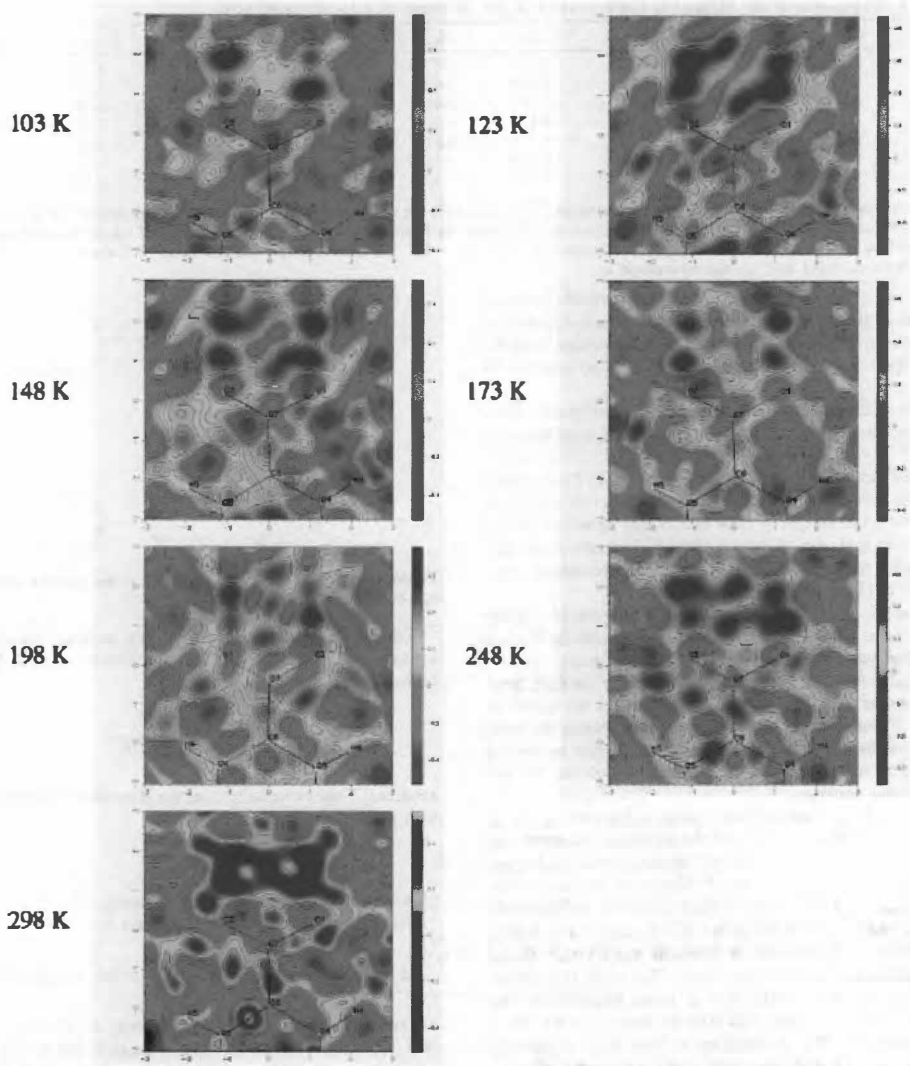


Figure 9. Fourier difference maps showing the carboxylate proton position in the dimeric unit from the spherical atom refinement.[60] Contour levels are drawn at 0.04 e Å^{-3}.

These one-dimensional lamellæ are bound through interactions between the iodine atoms. This interaction is strong and is the dominant structure-developing force in the crystal, after the hydrogen bond interaction. The interaction between iodine atoms occurs both between molecules in the layers and between iodine atoms of adjacent layers. The interlayer iodine−iodine contact distance ranges from 4.075 to 4.153 Å for the available temperature range of experimental data. The van der Waals radius for I is 1.98 Å,[57] which implies that there is a nonbonding contact between the iodine atoms. However, the iodine−iodine distance between adjacent layers ranges from 3.932 to 3.992 Å for the given temperature range, distances that are within the van der Waals radius sum for two iodine atoms.

The strength of the I−I interaction is seen in the spherical atom refinements carried out; the electron density at each I atom is highly distorted and cannot be adequately described by a spherical atom model. The residual electron density surrounding the iodine atom ranges from −4.24 to +2.84 e Å^{-3} when an empirical absorption correction was applied for the 173 K data set.[54] When an analytical absorption correction was applied to a data set at the same temperature, the residual electron density ranges from −5.78 to +2.05 e Å^{-3}.[56] Figure 8 shows a difference Fourier map of the distribution of the residual electron density around the I atom following an empirical absorption correction at 103 K. The deformation of this electron density protrudes perpendicular to the plane of the asymmetric unit. This raises questions as to the driving force for the packing. Though hydrogen bonding is an obvious driving force for the formation of the dimeric unit, the iodine−iodine contacts appear to be the interactions that drive the disposition of the lamellar

TABLE 4: Population of the Major (A) Configuration in the Structure of 4-Iodobenzoic Acid

T (K)	$X_{A,F}$	$1 - X_{A,F}$	$K_{H,F}$	$\ln K_{H,F}$	$X_{A,SOF}$	$1 - X_{A,SOF}$	$K_{H,SOF}$	$\ln K_{H,SOF}$	ITF
103	0.578	0.422	1.37	0.314	0.6779	0.3221	2.105	0.744	0.029
123	0.525	0.475	1.10	0.099	0.6201	0.3799	1.6323	0.490	0.022
148	0.491	0.509	0.96	−0.037	0.6861	0.3139	2.1857	0.782	0.028
173	0.457	0.543	0.84	−0.171	0.6146	0.3854	1.5947	0.467	0.028
198	0.412	0.588	0.70	−0.355	0.638	0.362	1.7624	0.567	0.052
248[b]	*0.547*	*0.453*	*1.21*	*0.190*	*0.5502*	*0.4498*	*1.2232*	*0.201*	*0.037*
298[b]	*0.503*	*0.497*	*1.01*	*0.012*	*0.633*	*0.376*	*1.6835*	*0.521*	*0.034*

[a] The linear region is in the low-temperature range, up to 198 K. The SOF, site occupancy factor, refinements are less reliable for these split site H atoms than are the occupancies estimated from direct imaging from the Fourier maps.[61] [X_A is the population of the major configuration as determined from examination of the difference Fourier maps. $K = (X_A)/(1 - X_A)$. ITF is the isotropic thermal factor.] [b] These data above the phase transition were excluded from the thermodynamic fit.

structure. In a search of the Cambridge Structural Database (CSD), this type of halogen−halogen interaction is found to be quite common for 1,4-substituted benzene molecules, with the shortest reported contact distance for the I−I contact being 3.748 Å.[58,59]

In terms of the intramolecular structure of 4-iodobenzoic acid, all bond lengths and angles are well within the normal observed range.[58,59] The torsion angles described by O1−C7 and C6−C4 [6.6(8)°] and by O2−C7 and C6−C5 [6.8(8)°] are typical for benzoic acid derivatives. The oxygen−carbon−oxygen angle of the carboxylate unit has a value of 123.2(5)°, which is typical of carboxylic acid units. A search of the CSD demonstrates that the range for the O−C−O angle in 4-substituted benzoic acid molecules is 113.6−128.4°.[58,59]

The dimeric unit is held together by the presence of a strong hydrogen bond. The electron density associated with the H atom in this bond was located in Fourier difference maps, $\rho_{diff} = F_{obs} - F_{calc}$, with no placement of the H atom in the calculated model. Fourier maps at successive temperatures are shown in Figure 9. Table 4 shows the site occupancy factors for each temperature for the distribution of electron density associated with the H atom position and the 3-center−4-electron (3c−4e) bond between dimers.

As seen in the difference Fourier maps in Figure 9, at 103 K the electron density associated with the hydrogen-bonded proton position (H1) is strongly associated with only one of the oxygen atoms in the carboxylic acid unit.[60] However, this correlation changes dramatically with temperature, in accord with previous studies in similar systems.[61] In the 173 K data, for example, there appears to be a "split-site" disorder associated with the electron density in the hydrogen bond. This trend is followed with increasing temperature, but at room temperature, the presence of thermal motion and disorder does not allow us to image adequately the distribution of the electron density associated with the hydrogen atom in the hydrogen bond.

It is reasonable to assume that the observed peaks in the Fourier maps are due to a disordered population over two possible H atom sites. A valence bond representation of the two possible forms I and II observed in the average structure is shown in Figure 10, illustrating the hydrogen bond split-site equilibrium. Moreover, it is assumed that there is no order in the distribution of these valence bond representations from unit cell to unit cell and that therefore the distribution is statistically random. No evidence of any ordering of the dimeric units with respect to I and II or any resulting superlattice was found in the diffraction data; we note that if the only discrimination between a system of valence bond isomers ordered over a superlattice and a randomly disordered situation were the location of the hydrogen atoms, then these X-ray diffraction experiments would be unlikely to reveal them, given the scattering power of the electron density associated with a hydrogen atom.

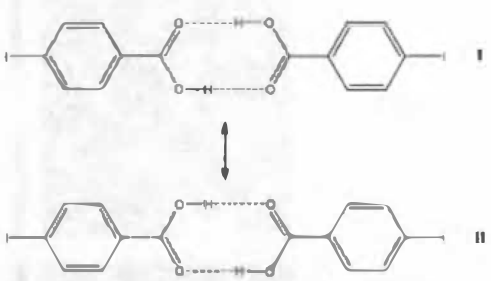


Figure 10. Valence bond representations of the split-site equilibrium in 4-iodobenzoic acid.

Taking a perfectly disordered system, as described above, as the model for the data, then an equilibrium constant, K_H, can be written as

$$K_H = \frac{X_A}{X_B} = \frac{X_A}{(1 - X_A)}$$

assuming a site occupancy over the disordered hydrogen atom sites such that

$$X_A + X_B = 1$$

where X_i is the population of the ith atom site.

Using the definition of K_H, it follows that

$$\ln K_H = \frac{-\Delta G}{RT} = \frac{-\Delta H}{RT} + \frac{\Delta S}{R} \qquad \text{at any temperature } T$$

ΔG is the difference in Gibbs free energy for the two isomers with populations A and B. Table 4 contains the results of the population analyses derived from the integration of the Fourier map, with a data cutoff of $F_{obs}/\sigma(F_{obs}) = 0$ and the site occupancy factors, SOF, from the spherical atom refinements of the data. A plot of $\ln K_{H(Fourier)}$ vs inverse temperature for temperatures in the range 103−198 K is shown in Figure 11. From the slope of the linear fit to the data, $\Delta H/R = 135.43$, yielding a value for ΔH of 1.13 kJ mol^{-1} for the enthalpy difference between the configurations. This value compares favorably with other similar measurements, viz. 0.50(4) kJ mol^{-1} for benzoic acid[62,63] and 1.64(9) kJ mol^{-1} for *p*-chlorobenzoic acid[64] obtained previously from neutron diffraction data.

Interestingly, despite the clearly strong trend in the redistribution of proton occupancies between the two oxygen atoms in the COOH unit, there is no parallel trend evident in the C−O bond length differences; the simple I:II site model does not reproduce the bond lengths observed in this study. Indeed, inspection of the CSD for carboxylic acid dimers and extracting the O−H, C−O, and C=O bond lengths reveals that there is

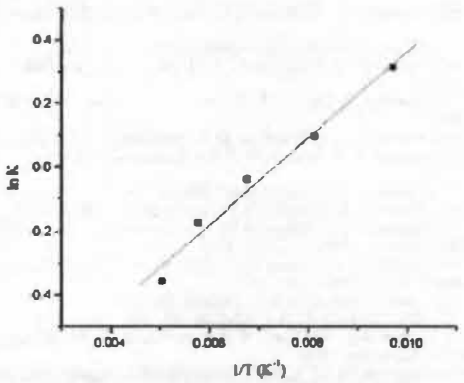


Figure 11. Plot of ln K_{eq} vs inverse temperature for the split-site populations, extracted from the integration of the Fourier map with a data cutoff of $F_{obs}/\sigma(F) = 0$. As $\Delta H'/R = 135.44$, $\Delta H = 1.126$ kJ mol^{-1} for the enthalpy difference between the sites.

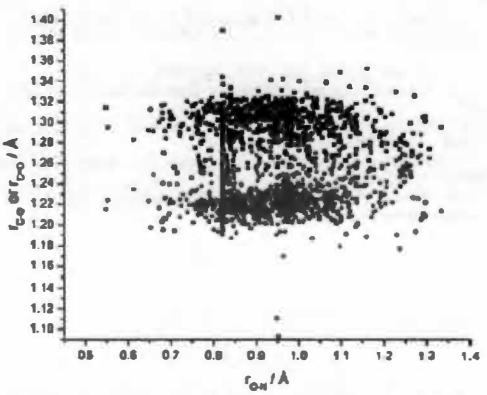


Figure 12. Comparison of the O−H vs C−O and O−H vs C=O (red) distances, r_{O-H}, r_{C-O}, and $r_{C=O}$, extracted from the CCSD, showing no correlation between these structural parameters.

no correlation between these structural parameters; the accumulated data are shown in Figure 12.

The lack of correlation between these parameters implies that the simple I/II model is not supported by the data; if the I/II model were to apply, a bimodal distribution would be expected. Moreover, an average bond length determined by r_{C-O} and $r_{C=O}$ and weighted to the hydrogen atom populations does not account for the observed variation of these carbon−oxygen bonds with temperature in this study.

Clearly, there is complex relationship between the H atom distributions and the structural response of the [CO_2] unit which is not adequately described by the I/II model. We note that theoretical descriptions of hydrogen bonding show that the rearrangement of the total electron distribution in the system must be considered, not simply that local to the COOH unit. These fine details of the bonding picture are, however, inaccessible from this study. It is also clear that the carboxylate moiety is not the only important interaction in the system. The I−I interactions between adjacent molecules and between lamellae are also very strong and determine the packing of dimers in the system.

V. Conclusions

This study, by determining the electron density associated with the hydrogen atom participating in an apparently well-understood structural moiety, has shown that a simple delocalized approach to the determination of the hydrogen atom disorder is not as complete as might be desired. A split-site model of the distribution of the electron density directly associated with the hydrogen atom, obtained from difference Fourier maps yield values for the enthalpy differences between the two distinct molecular configurations in the lattice that are consistent with previous measurements. However, the structural consequences of this model for the carboxylate group in terms of a valence bond delocalized picture of the bonding are not fully borne out in the observed C···O bond lengths determined from spherical atom refinements of the data, suggesting further complexity. The application of theoretical calculations to this and similar systems, as well as charge density analysis, are in progress.

Acknowledgment. J.F.C.T. acknowledges the financial support of the University of Tennessee, through provision of start-up funds, and the Petroleum Research Fund, administered through the American Chemical Society (PRF-37341-G4). C.C.W. acknowledges this work was funded in part by EPSRC under grant number GR/R04690.

Supporting Information Available: Variable temperature X-ray diffraction data are available free of charge via the Internet at http://pubs.acs.org

References and Notes

(1) Sakiya, R.; Nishikawa, S.-I. *Chem.−Eur. J.* **2002**, *8*, 4803−4810.
(2) Smith, G.; White, J. M. *Aust. J. Chem.* **2001**, *54*, 97−100.
(3) Perez-Perez, C.; Echevarria, A.; Jagerovic, N.; Alkorta, I.; Elguero, J.; Langer, U.; Klein, O.; Minguet-Bonvehi, M.; Limbach, H.-H. *J. Am. Chem. Soc.* **2001**, *123*, 7898−7906.
(4) Achim, P. R.; Fyfe, M. C. T.; Hickingbottom, S. K.; Mansour, S.; Stoddart, J. F.; White, A. J. P.; Williams, D. J. *Chem.−Eur. J.* **1998**, *4*, 577−589.
(5) Papadakis, M. M.; Marcos, S. P.; Thompson, H. W., Lalancette, R. A. *Acta Crystallogr., Sect. C: Cryst. Struct. Commun.* **2002**, *C58*, o321−o322.
(6) Lamar, P. E.; Patel, A. D.; Swenson, D. C. *Acta Crystallogr., Sect. C: Cryst. Struct. Commun.* **2002**, *C58*, o333−o335.
(7) Galardi, R.; Butcher, R. J.; Bashir-Hashemi, A. *Acta Crystallogr., Sect. E: Struct. Rep. Online* **2002**, *E58*, o860−o861.
(8) Crispini, A.; Neve, F. *Acta Crystallogr., Sect. C: Cryst. Struct. Commun.* **2002**, *C58*, o34−o35.
(9) Hokelek, T.; Pazir, S.; Ergun, Y.; Oktay, G. *Acta Crystallogr., Sect. C: Cryst. Struct. Commun.* **2001**, *C57*, 414−416.
(10) Degen, A.; Bolte, M. *Acta Crystallogr., Sect. C: Cryst. Struct. Commun.* **1999**, *C55*, 1306−1308.
(11) Fitzgerald, L. J.; Gerkin, R. E. *Acta Crystallogr., Sect. C: Cryst. Struct. Commun.* **1998**, *C54*, 966−969.
(12) Dobson, A. J.; Gerkin, R. E. *Acta Crystallogr., Sect. C: Cryst. Struct. Commun.* **1998**, *C54*, 795−798.
(13) Fitzgerald, L. J.; Gerkin, R. E. *Acta Crystallogr., Sect. C: Cryst. Struct. Commun.* **1997**, *C53*, 1080−1082.
(14) Fitzgerald, L. J.; Gerkin, R. E. *Acta Crystallogr., Sect. C: Cryst. Struct. Commun.* **1997**, *C53*, 1265−1267.
(15) Ferguson, G.; Gallagher, J. F.; McAlees, A. J. *Acta Crystallogr., Sect. C: Cryst. Struct. Commun.* **1996**, *C51*, 454−458.
(16) Thompson, H. W.; Lalancette, R. A.; Vanderhoff, P. A. *Acta Crystallogr., Sect. C: Cryst. Struct. Commun.* **1992**, *C48*, 66−70.
(17) Kumar, V. S. S.; Nangia, A.; Katz, A. K.; Carrell, H. L. *Cryst. Growth Des.* **2002**, *2*, 313−318.
(18) Thallapally, V. R.; Nangia, M.; Boese, R. *J. Am. Chem. Soc.* **2000**, *122*, 9227−9236.
(19) Kariuki, B. M.; Bauer, C. L.; Harris, K. D. M.; Tedesco, S. J. *Angew. Chem., Int. Ed.* **2000**, *39*, 4485−4488.
(20) Marsh, S. B.; Valerio, E. J. *J. Chem. Crystallogr.* **1998**, *28*, 203−207.

(21) Fitzgerald, L. J.; Gerkin, R. E. *Acta Crystallogr., Sect. C: Cryst. Struct. Commun.* **1997**, *C53*, 71−73.
(22) Blackburn, A. C.; Dobson, A. J.; Gerkin, R. E. *Acta Crystallogr., Sect. C: Cryst. Struct. Commun.* **1996**, *C52*, 907−910.
(23) Blackburn, A. C.; Dobson, A. J.; Gerkin, R. E. *Acta Crystallogr., Sect. C: Cryst. Struct. Commun.* **1996**, *C52*, 1482−1486.
(24) Blackburn, A. C.; Dobson, A. J.; Gerkin, R. E. *Acta Crystallogr., Sect. C: Cryst. Struct. Commun.* **1996**, *C52*, 1486-1488.
(25) Blackburn, A. C.; Dobson, A. J.; Gerkin, R. E. *Acta Crystallogr., Sect. C: Cryst. Struct. Commun.* **1996**, *C52*, 2320−2323.
(26) Blackburn, A. C.; Dobson, A. J.; Gerkin, R. E. *Acta Crystallogr., Sect. C: Cryst. Struct. Commun.* **1996**, *C52*, 2638−2641.
(27) Smith, G.; Lynch, D. E.; Bynel, K. A.; Kennard, C. H. L. *Aust. J. Chem.* **1996**, *48*, 1133−1149.
(28) Smith, G.; Lynch, D. E.; Bynel, K. A.; Kennard, C. H. L. *Acta Crystallogr., Sect. C: Cryst. Struct. Commun.* **1995**, *C51*, 2629−2633.
(29) Broughton, R. G.; Nelson, J. E. *Acta Crystallogr., Sect. C: Cryst. Struct. Commun.* **1984**, *C40*, 204−206.
(30) Lynch, D. E.; Smith, G.; Bynel, K. A.; Kennard, C. H. L. *Aust. J. Chem.* **1991**, *44*, 1017−1022.
(31) Takaki, Y.; Kurisu, A.; Nakata, K. *Bull. Chem. Soc. Jpn.* **1982**, *55*, 319−320.
(32) Ohkura, K.; Kashino, S.; Haisa, M. *Bull. Chem. Soc. Jpn.* **1972**, *45*, 2651−2652.
(33) Miller, R. S. *Organic gas−solid reactions and the single crystal X-ray structure of 4-chlorobenzoic acid*. Ph.D. Thesis. University Illinois, Urbana, IL, USA. FIELD URL, 1973; p 216.
(34) Miller, R. S.; Paul, I. C.; Curtin, D. Y. *J. Am. Chem. Soc.* **1974**, *96*, 6334−6339.
(35) Colapietro, M.; Domenicano, A.; Pela Ceccarini, G. *Acta Crystallogr., Sect. B: Struct. Crystallogr. Cryst. Chem.* **1979**, *B35*, 890−894.
(36) Butcher, R. J.; Bashir-Hashemi, A.; Gilardi, R. D. *J. Chem. Crystallogr.* **1997**, *27*, 99−107.
(37) Bazilevsky, M. V.; Venus, M. V. *Russ. Chem. Rev.* **2003**, *72*, 1−33.
(38) Wilson, C. C. *New J. Chem.* **2002**, *26*, 1733−1739.
(39) Maurin, J. K.; Czarnocki, Z.; Wojtasiewicz, K.; Maleszewska, E.; Magdziak, K.; Paluchowska, B. *J. Mol. Struct.* **2002**, *610*, 33−40.
(40) Gavezzotti, A. *J. Mol. Struct.* **2002**, *615*, 5−12.
(41) Fillaux, F.; Lunage, M. H.; Romain, F. *Chem. Phys.* **2002**, *276*, 181−210.
(42) Latanowicz, L.; Reynhardt, E. C. *Chem. Phys. Lett.* **2001**, *341*, 561−567.
(43) Fillaux, F. *Int. Rev. Phys. Chem.* **2000**, *19*, 553−564.
(44) Grabowski, S. J.; Krygowski, T. M. *Chem. Phys. Lett.* **1999**, *305*, 247−250.
(45) Loerting, T.; Liedl, K. R. *J. Am. Chem. Soc.* **1998**, *120*, 12595−12600.
(46) Horsewill, A. J.; Brougham, D. F.; Jenkinson, R. I., McGloin, C. J.; Trommsdorff, H. P.; Johnson, M. R. *Ber. Bunsen-Ges.* **1998**, *102*, 317−324.
(47) Toussaint, J. *Acta Crystallogr.* **1951**, *4*, 71−72.
(48) Pollock, J. M.; Woodward, I. *Acta Crystallogr.* **1964**, *7*, 605.
(49) Hamrahan, E. S.; Bruce, B. D. *Spectrochim. Acta, Part A: Mol. Biomol. Spectrosc.* **1967**, *23*, 2497−2503.
(50) Nyguen, C. L.; Wilson, C. C.; Schultz, A. J.; Piccoli, P. M. B.; Turner, J. F. C. *J. Phys. Chem.*, in press.
(51) *Smart*; Bruker AXS, Inc.: Madison, WI, 1997.
(52) *Saint*; Bruker AXS, Inc: Madison, WI, 1997.
(53) Larson, A. C.; Von Dreele, R. B. Report LAUR 86-748; Los Alamos National Laboratory, 2000.
(54) Sheldrick, G. M. *SADABS*; University of Gottingen: Gottingen, Germany, 1996.
(55) *XPREP*; Bruker AXS, Inc: Madison, WI, 1997.
(56) Sheldrick, G. M. *SHELXTL*; University of Gottingen: Gottingen, Germany, 1997.
(57) Winter, M. http://www.webelements.com/.
(58) Allen, F. H.; Motherwell, W. D. S. *Acta Crystallogr.* **2002**, *B58*, 407−422.
(59) Bruno, I. J.; Cole, J. C.; Edgington, P. R.; Kessler, M.; Macrae, C. F., McCabe, P.; Pearson, J.; Taylor, R. *Acta Crystallogr.* **2002**, *B58*, 389−397.
(60) Farrugia, L. J. *J. Appl. Crystallogr.* **1999**, *32*, 837−838.
(61) Wilson, C. C.; Goeta, A. E. *Angew. Chem., Int. Ed.* **2004**, *43*, 2095−2099.
(62) Wilson, C. C.; Shankland, N.; Florence, A. J. *J. Chem. Soc., Faraday Trans.* **1996**, *92*, 5051−5057.
(63) Wilson, C. C.; Shankland, N.; Florence, A. J. *Chem. Phys. Lett.* **1996**, *253*, 103−107.
(64) Wilson, C. C.; Florence, A. J.; Xu, X.; Shankland, N. *New J. Chem.*, submitted for publication.

Electron and Nuclear Positions in the Short Hydrogen Bond in Urotropine-*N*-oxide·Formic Acid

Cara L. Nygren,[†] Chick C. Wilson,[‡] and John F. C. Turner*[,†,||]

Department of Chemistry and Neutron Sciences Consortium, University of Tennessee, Knoxville, Tennessee 37996-1600, and Department of Chemistry, University of Glasgow, Glasgow, G12 8QQ, U.K.

Received: June 28, 2004; In Final Form: November 9, 2004

The crystal structure of urotropine-*N*-oxide·formic acid, as determined from multiple temperature single-crystal X-ray diffraction experiments in the range 123−295 K and from neutron diffraction at 123 K, is reported. There is a strong hydrogen bonding interaction between the OH of formic acid and the *N*-oxide of urotropine, with the oxygen−oxygen distance ranging from 2.4300(10) to 2.4469(10) Å. The electron density of the hydrogen atom associated with this interaction was located in the Fourier difference maps of the spherical atom refinement after all heavy atom positions were determined. The maximum of the electron density associated with the hydrogen bond is located approximately 1.16 Å from the formate segment, though the distribution of electron density is very broad. The electron density associated with the H atom is thus shown by these accurate X-ray diffraction experiments to be approximately centered at all temperatures studied. This was conclusively confirmed by single-crystal neutron diffraction data obtained at 123 K, from which statistically equivalent O−H distances of 1.221(7) and 1.211(7) Å were obtained.

1. Introduction

Hydrogen bonding is a common interaction in many areas of structural chemistry.[1−4] In chemically simple systems, such as the hydrides of the first-row elements, it is responsible for the strongly associated nature of water,[5−11] ammonia,[12] and hydrogen fluoride,[13−15] as well as the excellent solvent properties of these fluids. The physical and chemical properties of more complex systems are also due to the presence of the hydrogen bond; highly complex examples occur in structural biology, where the generation and maintenance of protein secondary and tertiary structure is dependent on this interaction.[2−4,8] Protein−protein interactions,[4] enzymatic catalysis,[2,3] and the structural chemistry of DNA are yet more complex examples.

The presence of a hydrogen bond is relatively simple to predict in the solid state. The presence of two electronegative atoms, usually N, O, or F, one of which is bound to at least one hydrogen, normally ensures that a hydrogen bond will exist, assuming that there is no structural motif that prevents bond formation. The ease of formation and the predictability of the presence of hydrogen bonds have led to the exploitation of this interaction in the intelligent design of crystal structures—the field of crystal engineering.[16−21]

Apart from the importance and flexibility of the hydrogen bond as an important interaction in the solid state, it is also of theoretical interest in the study of proton transfer in several systems: notably, carboxylic acid dimers have been investigated theoretically and experimentally toward this end.[22−31] It has been demonstrated, through both variable temperature X-ray and neutron diffraction experiments, that in some molecular systems the hydrogen atom migrates to the center of the X−H−Y bond as the temperature of the experiment is raised.[28,29,32,33] It is notable that proton migration may occur in both homonuclear (X−H−X) and heteronuclear (X−H−Y) systems. In this area, one of us (C.C.W.) has played a role in the application of neutron and X-ray diffraction at variable temperature to this type of problem; neutron diffraction has generally played an important role in the determination of nuclear positions for low-*Z* atom problems. A combination of neutron and X-ray diffraction permits a complete characterization of all scattering density present—the nuclear and electron densities associated with the H atom.

For many chemical systems, the determination of structure is based on the assumptions of the existence of atoms within the molecules; in this sense, a molecule may be defined as a bound ensemble of atoms and is therefore an extra hierarchical layer over and above the structure of the atom in the description of matter. Though this assumption is widespread in chemistry, a comprehensive definition of the atom within this hierarchical structure that is quantum mechanically satisfactory has only been derived in the past 25 years or so, predominantly due to the work of Bader.[34−39] More succinctly,[40] *[t]he molecular structure hypothesis—that a molecule is a collection of atoms linked by a network of bonds—was forged in the crucible of nineteenth century experimental chemistry. It has continued to serve as the principal means of ordering and classifying the observations of chemistry.*

An issue arises when considering the structure of a crystalline material that derives from the bipartite nature of the atom itself: it is not possible, by a single experimental method, to determine the structure of an atom or any ensemble of atoms; one may determine the electron density *or* the nuclear density, but not both, using the same radiation source. If the nuclear position of the atom and the electron density associated with the atom are very strongly correlated, then it is certainly reasonable to assert that either the distribution of the nuclear positions or the distribution of total electron density is a good

† Department of Chemistry, University of Tennessee.
‡ University of Glasgow.
|| Neutron Sciences Consortium, University of Tennessee.

10.1021/jp047187r CCC: $30.25 © 2005 American Chemical Society
Published on Web 02/10/2005

measure of the position of any atom within the system. We also note that, for the vast majority of atoms, the total electron density is dominated by the core electron density.

There are at least two areas where this last generality is not true in molecular systems: the electrides[41-43] and those systems that contain the hydrogen bond. In the latter case, the valence density of hydrogen is also the "core" density and in the hydrogen bond the delocalized nature of the electron density ensures that the normally strong correlation between the distribution of nuclear density and the distribution of electron density breaks down. Consequentially, the "atomic" definition of a hydrogen bond is more problematic.

In this report, we detail extensive X-ray diffraction studies at variable temperature, as well as a neutron diffraction study, of urotropine-*N*-oxide·formic acid. By using both radiation sources, we thereby define all the scattering density in the Bragg average associated with the hydrogen bond. We note that the neutron diffraction data are not essential or even necessary in an a priori sense to define the electron density distribution in the hydrogen bond, but as we shall show, the inclusion of information about the distribution of nuclear density is instructive. Moreover, we explore the possible methods of visualization of the electron density associated with the hydrogen bond and show that direct, Fourier imaging is a useful method that is complementary to other, more usual methods of refinement.[44] We also explore the chemical ramification of our results in an "atomistic", chemical sense and show that such a description of the hydrogen bond is not particularly illuminating.

Urotropine is a molecular system that has had an important role in crystallography, due in part to the similarity of this molecule to adamantane.[45-58] Whereas adamantane is of great interest as an archetype for plasticity, urotropine is brittle,[59] despite the apparent similarity between the molecular structures. Urotropine crystallizes in the cubic space group $I\bar{4}3m$, with one nitrogen atom and one carbon atom in the asymmetric unit, and is structurally related to adamantane. Due to the high tetrahedral symmetry of the molecule, there is only one set of unique bond lengths for urotropine and the C−N bond length is 1.4715(14) Å. The simplicity of the asymmetric unit and the lattice has ensured that urotropine has been investigated as a model for lattice dynamics,[53] molecular vibrations in the solid state,[47,49,50,52,53,56,60] and multipole refinements.[53,57,58] among other areas. Urotropine-*N*-oxide is a potentially polybasic, polar molecule, and its adducts are interesting systems for the investigation of hydrogen bonding. The molecule has two potential sites at which hydrogen bonding may occur—the tertiary nitrogen centers and the *N*-oxide O atom—offering the potential for the "engineering" of intermolecular interactions with appropriate adducts.

The molecular structure of urotropine-*N*-oxide, shown in Figure 1, has previously been investigated by single-crystal X-ray diffraction.[51] It is notable that the N−O bond length is particularly short at 1.3951(12) Å, where the normal range for the N−O distance in hydroxylammonium cations is 1.396−1.436 Å.[62,63] It is a neutral molecule, though there is a formal charge separation between nitrogen and oxygen. The structure of several adducts of urotropine-*N*-oxide have also been reported;[64-68] we note that the molecular and crystal structure of **1** was first determined by Mak in 1978, from data accumulated at room temperature.[67,68]

There is a potential coupling between the distribution of electron density associated with the hydrogen position and the structure of the formic acid residue in urotropine-*N*-oxide·formic acid, and in a valence bond, atomistic description, this correlation automatically is present. This possibility was alluded to by Mak in 1978 in an inverted manner by asserting that, due to the asymmetry in the C−O and C=O bond lengths, there was no formal proton transfer, though the quality of his data collected at that time precluded a detailed analysis of the structural behavior of the hydrogen atom. Correlation of the bond lengths in the formic acid residue to the structure of the electron density, and therefore the proton position, can occur in this material as full H atom transfer to the N−O bond should result in the formation of a delocalized formate ion. Retention of $O_{formate}$−H bond order should make the delocalization less likely in the formate ion. Possible equilibria of this type are shown in Figure 2.

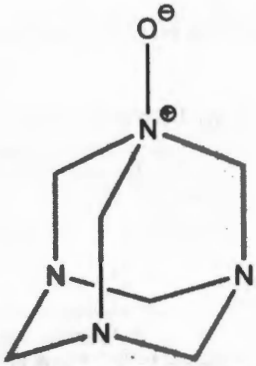


Figure 1. Molecular structure of urotropine-*N*-oxide.

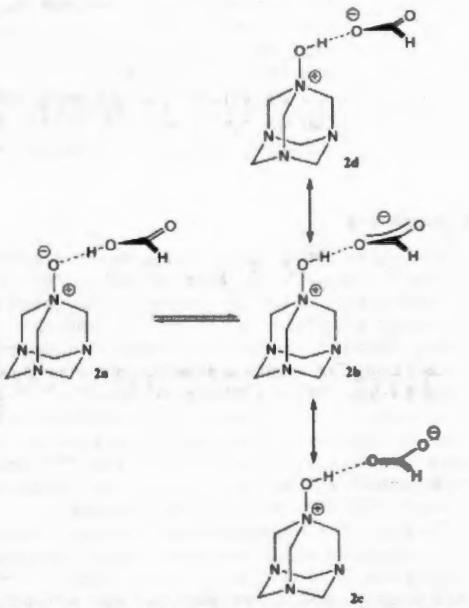


Figure 2. Potential equilibria involving both proton and electron redistribution.

Using a valence bond formalism, in principle, the *N*-oxide·formic acid adduct **2a** can equilibrate with **2b**, the hydroxylammonium formate salt where the formate ion is fully delocalized and therefore possesses equal C−O bond lengths, or

TABLE 1: Selected Refinement Parameters for the Collected Data

temp (K)	123 (neutron)	123 (X-ray)	148	173	198	223	248	298
θ range (deg)		2.10−28.34	2.10−28.34	2.11−28.31	3.10−28.27	2.10−28.34	2.10−28.29	2.10−28.79
index range for	$-13 \le h \le 13$	$-9 \le h \le 8$	$-9 \le h \le 8$	$-9 \le h \le 8$	$-9 \le h \le 8$	$-8 \le h \le 8$	$-8 \le h \le 8$	$-9 \le h \le 9$
data collection	$-13 \le k \le 2$	$-8 \le k \le 9$	$-8 \le k \le 9$	$-8 \le k \le 8$	$-9 \le k \le 8$	$-9 \le k \le 9$	$-9 \le k \le 9$	$-9 \le k \le 9$
	$-31 \le l \le 38$	$-25 \le l \le 25$	$-25 \le l \le 25$	$-24 \le l \le 25$	$-25 \le l \le 25$	$-25 \le l \le 25$	$-25 \le l \le 25$	$-25 \le l \le 25$
refins collected	3771	9144	9144	9107	8748	9329	9177	9415
independent refins [R(int)]	2144	2145 [0.0232]	2145 [0.0232]	2143 [0.0226]	2144 [0.0216]	2176 [0.0279]	2168 [0.0216]	2195 [0.0252]
completeness to $\theta = 28.35°$ (%)		97.1	97.1	97.1	96.6	97.3	97.1	92.8
data/restraints/params	2144/0/313	2145/0/131	2145/0/131	2143/0/131	2144/0/131	2176/0/131	2168/0/131	2195/0/131
S	1.02	1.037	1.037	1.045	1.043	1.014	1.025	1.017
final R indices	R1 = 0.151[a]	R1 = 0.0349[a]	R1 = 0.0349[a]	R1 = 0.0359[a]	R1 = 0.0355[b]	R1 = 0.0379[b]	R1 = 0.0398[b]	R1 = 0.0409[b]
	wR^2 = 0.092[a]	wR^2 = 0.0990[a]	wR^2 = 0.0990[a]	wR^2 = 0.0973[a]	wR^2 = 0.0992[b]	wR^2 = 0.1012[b]	wR^2 = 0.1039[b]	wR^2 = 0.1056[b]
R indices (all data)	R1 = 0.221	R1 = 0.0393	R1 = 0.0393	R1 = 0.0414	R1 = 0.0386	R1 = 0.0490	R1 = 0.0501	R1 = 0.0555
	wR^2 = 0.095	wR^2 = 0.1043	wR^2 = 0.1043	wR^2 = 0.1025	wR^2 = 0.1030	wR^2 = 0.1120	wR^2 = 0.1126	wR^2 = 0.1153

[a] $[I > 2\sigma(I)]^X$, $[I > 3\sigma(I)]^N$. [b] $[I > 2\sigma(I)]$.

with 2c/2d, the hydroxylammonium formate salts where the bond lengths in the formate ion are not resonance delocalized.

We note that the resonance structures illustrated in Figure 2 as intermediates only have formal meaning within a valence bond description and that the description of many main group and organic molecules is inadequate when the description is based on a hybridizational or valence bond approach.[69−76] By using a method of analysis which expressly uses a delocalized description of the electron density, we hope to shed light on the precise nature of the hydrogen bonding network in **1**.

2. Experimental Section

Urotropine-*N*-oxide·formic acid was synthesized by addition of an excess of hydrogen peroxide to an aqueous solution of urotropine. Single crystals suitable for X-ray or neutron diffraction experiments were either grown by slow evaporation of the reaction mixture or recrystallized from concentrated aqueous solutions by passing a current of air over a droplet of the solution that was placed on a glass plate made hydrophobic by the application of a very small quantity of sebaceous oil.

X-ray Diffraction Experiments. For the temperature range 123−198 K, suitable crystalline specimens were mounted in Paratone oil, while for temperatures of 223 K to room temperature the crystals were mounted with epoxy on a glass fiber. Single-crystal X-ray diffraction data were collected using a Bruker AXS Smart 1000 Diffractometer equipped with a CCD area detector and graphite monochromatized Mo source (Mo Kα, 0.710 73 Å) and a Nicolet LT-2 cooling device, with a crystal-to-detector distance of 5.0 cm. Diffraction data were collected from crystalline specimens of urotropine-*N*-oxide·formic acid at temperatures of 123, 148, 173, 198, 223, 248, and 298 K; the parameters of each data collection are collated in Table 1.

Refinement of X-ray Data. More than a hemisphere of data were collected over the angular range of 2.10−28.34° in θ (123 K).[77] Frame widths of 0.3° were used for the data collection of 9144 reflections, counting 40 s per frame. Data reduction and spherical atom analyses were carried out using the Bruker program Saint[78] and the General Structure Analysis System (GSAS).[79] The unit cell dimensions were refined on the basis of 7531 reflections. A multiscan absorption correction was made using SADABS.[80] Systematic absences were consistent with the space group $P2_1/n$. A total of 8163 reflections were collected, and merging of equivalent reflections gave 2145 unique reflections (R_{int} = 2.32%), with 2004 classed as observed ($|F_o| > 4\sigma_F$). The structure was solved by direct methods (SHELXTL),[44] refined by the full matrix least-squares method and completed by a series of difference Fourier syntheses. All non-hydrogen atoms were refined anisotropically, with most of the hydrogen atoms being introduced at idealized positions and refined using a riding model. The electron density associated with H1, the hydrogen bonded H atom, was located in the Fourier difference map and its positional parameters refined. Thermal parameter refinements for the hydrogen bonded H atom were performed using SHELXTL[44] for isotropic refinements and GSAS[79] for anisotropic refinements. Weighted R-factors, wR^2, and all goodness-of-fit values are based on F^2.

Neutron Diffraction Experiments. Neutron diffraction data were obtained at the Intense Pulsed Neutron Source (IPNS) at Argonne National Laboratory using the time-of-flight Laue single-crystal diffractometer (SCD).[81,82] At the IPNS, pulses of protons are accelerated into a heavy-element target 30 times per second to produce pulses of neutrons by the spallation process. Because of the pulsed nature of the source, neutron wavelengths are determined by time of flight based on the de Broglie equation

$$\lambda = \frac{hm}{tl}$$

where h is Planck's constant, m is the neutron mass, and t is the time of flight for a flight path l, so that the entire thermal spectrum of neutrons can be used. With position-sensitive area detectors and a range of neutron wavelengths, a solid volume of reciprocal space is sampled with each stationary orientation of the sample and the detectors. The SCD has two ^{6}Li-glass scintillation position-sensitive area detectors, each with active areas of 15 × 15 cm^2 and a spatial resolution of < 1.5 mm. One of the detectors is centered at a scattering angle of 75° and a crystal-to-detector distance of 23 cm, and the second detector is at 120° and 18 cm. Details of the data collection and analysis procedures have been published previously.[81,82]

A crystal of urotropine-*N*-oxide·formic acid with approximate dimensions of 1.8 × 1.3 × 0.6 mm^3 was molded into an aluminum foil "sandwich" and was glued to the end of a standard aluminum pin with epoxy adhesive. The sample was placed on the DISPLEX cold stage in the SCD, cooled to 260 K in a helium atmosphere, and then cooled to 123 K under vacuum.

For each setting of the diffractometer angles, data were stored in three-dimensional histogram form with coordinates x,y,t corresponding to horizontal and vertical detector positions and the time of flight, respectively. Data were analyzed using the ISAW software package[83] in addition to other local IPNS SCD programs. For intensity data collection, runs of 6 h per histogram were initiated, arranged at χ and φ values suitable to cover at

TABLE 2: Lattice Parameters (Reduced Unit Cell) for the Collected Data at Variable Temperature[a]

a/Å	b/Å	c/Å	β/deg	T/K	ref
6.845	6.847	19.480	95.06	298	67
6.726(1)	6.732(1)	19.418(4)	95.391(16)	123	this work(N)
6.774(2)	6.790(2)	19.472(7)	95.159(6)	123	this work(X)
6.7679(19)	6.779(2)	19.487(6)	95.446(5)	148	this work(X)
6.770(3)	6.799(3)	19.433(8)	95.297(7)	173	this work(X)
6.787(2)	6.802(2)	19.532(7)	95.266(6)	198	this work(X)
6.785(2)	6.8176(19)	19.473(6)	95.107(1)	223	this work(X)
6.7989(5)	6.8226(4)	19.4639(13)	95.1020(10)	248	this work(X)
6.8272(13)	6.8456(13)	19.484(4)	94.983(3)	298	this work(X)

[a] The superscripts in the reference column denote X-ray (X) versus neutron (N) data.

TABLE 3: Intermolecular Structural Parameters at Variable Temperature from Spherical Atom Refinement[a]

T/K	$r_{O1O1'}$/Å	$r_{O1H1'}$/Å	$r_{O2H1'}$/Å	$r_{O1O3'}$/Å	$r_{O2C1'}$/Å	$r_{O2C1'}$/Å	$\angle_{O1H1O3'}$/deg	$\angle_{O2C1O3'}$/deg	
123	1.3727(33)	1.221(7)	1.211(7)	2.428(6)	1.286(5)	1.230(4)	173.3(6)	126.28(34)	(N)
123	1.3984(11)	1.24(4)	1.19(7)	2.435(1)	1.2862(14)	1.2228(13)	173.1(5)	125.17(10)	(X)
148	1.3956(11)	1.25(3)	1.21(3)	2.443(1)	1.2818(15)	1.2252(15)	170.0(6)	125.62(11)	(X)
173	1.3949(12)	1.24(2)	1.21(2)	2.439(1)	1.2778(15)	1.2206(15)	172.3(6)	125.55(12)	(X)
198	1.3951(11)	1.24(6)	1.20(6)	2.438(1)	1.2786(15)	1.2234(15)	174.0(6)	125.89(12)	(X)
223	1.3979(12)	1.22(6)	1.24(6)	2.450(1)	1.2757(16)	1.2258(15)	174.2 (6)	126.05(12)	(X)
248	1.3933(13)	1.26(3)	1.18(6)	2.430(1)	1.2680(18)	1.2147(18)	172.7(6)	126.00(15)	(X)
298	1.3940(14)	1.27(6)	1.18(3)	2.430(1)	1.263(2)	1.2107(19)	171.4(1)	126.47(16)	(X)
298	1.388(6)			2.435(4)	1.281(6)	1.200(6)		126.1(5)	67

[a] Neutron data are represented by "(N)" and X-ray data by "(X)".

least one unique quadrant of reciprocal space. With this counting time, 17 histograms were completed during the 5 days available for the experiment. The recorded histograms were indexed and integrated using individual orientation matrices for each histogram, to allow for any misalignment of the sample. The intensities were corrected for wavelength dependence of the incident spectrum and sample absorption (μ (cm^{-1}) = 4.205).

Refinement of Neutron Data. Bragg reflections were integrated about their predicted location and were corrected for the Lorentz factor, the incident spectrum, and the detector efficiency. A wavelength-dependent spherical absorption correction was applied using cross sections from Sears[84] for the non-hydrogen atoms and from Howard et al.[85] for the hydrogen atoms. Symmetry-related reflections were not averaged since different extinction factors are applicable to reflections measured at different wavelengths. The GSAS software package was used for structural analysis.[79] The atomic positions of the X-ray diffraction structure were used as a starting point in the refinement. All atoms including hydrogen atoms were refined with anisotropic thermal parameters. The refinement used 313 variables and converged to $R_w(F^2) = 0.092$ and $R(F^2) = 0.151$. Data collection and refinement parameters are summarized in Table 1. A compilation of the lattice parameters for both the neutron data and the variable temperature X-ray data are found in Table 2.

3. Results

Molecular and Crystal Structure. The symmetry of free urotropine-*N*-oxide is C_{3v}, and therefore the carbon−nitrogen bond lengths are no longer equivalent. The carbon−nitrogen bond lengths adjacent to the *N*-oxide portion are considerably lengthened compared to the carbon−nitrogen bond distances which are further removed from the charge-separated segment of the molecule.[62,63,67] The three nitrogen−carbon bond distances (for the nitrogen atom of the *N*-oxide portion) are elongated to an average distance of 1.5411(18) and 1.5249(13) Å for the room temperature and 123 K X-ray diffraction study, respectively. The remaining nitrogen−carbon bond distances are similar to those of free urotropine-*N*-oxide [1.441(2) and 1.473(2) Å, 298 K; 1.4480(14) and 1.4783(14) Å, 123 K].[61,68] Based on the neutron diffraction data, the carbon−oxygen bond distances in the formate segment of the molecule are 1.286(5) and 1.230(4) Å for the C7−O2 and C7−O3 bonds, respectively, and these distances are compiled in Table 3. These distances coincide with the results extracted from the X-ray diffraction experiment at 123 K, 1.2862(14) and 1.2228(13) Å, respectively. The C−N bond distances in the cage correspond well with the distances obtained in the X-ray diffraction experiment, differing by less than 0.001 Å.

The gross molecular structure, determined by spherical atom refinements of the X-ray data, is unsurprising and the non-hydrogenous structure remains relatively invariant with temperature. Relevant structural parameters are given in Table 3. A representative structure of the asymmetric unit is shown in Figure 3a, with the corresponding packing diagram in Figure 3b. The latter shows the orientation of the four molecules that are contained in the unit cell. It is notable that the packing segregates the more polar parts and less polar parts of the complex; the polar portions, consisting of the *N*-oxide and the hydrogen bound formic acid, are mutually anti to each other across the sheet composed of less polar cages.

Hydrogen Bond Structure. Urotropine-*N*-oxide has four potential sites at which hydrogen bonding may occur: there is one electronegative oxygen atom and three tertiary amines which may act as potential strong hydrogen bond acceptors. Examination of extended contacts in the unit cell using Mercury[62,86] revealed that the only substantial interaction was the short, strong hydrogen bond present between the urotropine-*N*-oxide and the formate residue. The observed hydrogen bond in this case is to the *N*-oxide O atom, with a short oxygen−oxygen distance ranging from 2.4300(10) Å to 2.4469(10) Å based on the X-ray data and 2.428(7) Å in the neutron data at 123 K. This lies well within the standard definition for a short very strong hydrogen bond,[87] which is defined as one where the O···O lies in the range 2.2−2.5 Å.

In addition to the "very strong" hydrogen bond between the oxygen atom of the *N*-oxide, O1, and the oxygen atom, O2, of the formate segment, there are three other hydrogen bonds

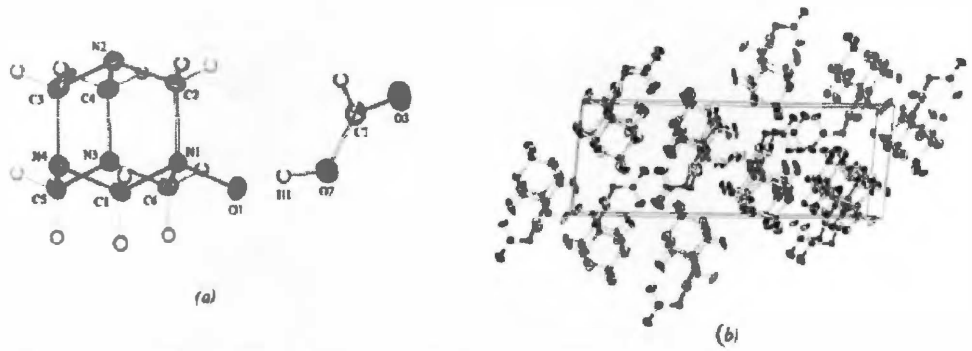


Figure 3. Molecular structure of urotropine-*N*-oxide·formic acid at 123 K (a) and packing diagram (b).[93]

present in this system. Each of the three tertiary amines forms a hydrogen bond to an adjacent molecule, which may be classified as a "weak" hydrogen bond,[87] with N···H bond distances ranging from 2.68 to 2.89 Å.[62,86] However, it is notable that the van der Waals sum for N···H is 2.75 Å,[88] and it may therefore be more appropriate to classify the N···H interaction as a hydrogen bridge.[16,87,89]

Nuclear Structure of the Hydrogen Bond. The results of the neutron diffraction experiment at 123 K reveal the nuclear position of the H atom associated with the hydrogen bond. The proton is located 1.221(7) Å from the oxygen atom of the *N*-oxide segment of the molecule and 1.211(7) Å from O2 of the formate segment, with an O1−H1−O2 angle of 173.3(6)°. Therefore, within the errors associated with the experiment, this results in a short symmetric hydrogen bond.

Discussion

It has recently been shown that direct imaging of hydrogen density from X-ray diffraction experiments can be more reliable than parameters determined from refinements;[33,90] this is particularly true in the case of elongated or highly anisotropic density as observed in this system. However, our multiple temperature study, and the apparent invariance of the shape and position of the difference Fourier peak representing the electron density associated with H1, allows us to conclude that in this system the hydrogen atom is strongly perturbed toward a position close to the center of the O···O vector and its position appears invariant (within the accuracy of the X-ray data) as a function of temperature. This is a significant observation, particularly in light of several recent reports of migration of the H atom in such cases;[28,29,32,33] the nature of the hydrogen bond in urotropine-*N*-oxide·formic acid is robust toward such effects.

The distribution of electron density in the Fourier difference maps in Figure 4 (calculated in the absence of H1 from the model) in the region of the short, strong hydrogen bond shows elongation of the density along the O1−O2 vector, commonly observed in short, strong hydrogen bonds. As seen in the Fourier maps, the maximum in the electron density associated with the hydrogen bond is located approximately 1.16 Å from the formate segment of the molecule, representing a significant elongation of the O−H "covalent" bond, where the electron density is distributed between O and H over a length of ~1 Å, and is indicative of a centered proton which is frequently observed in short hydrogen bonded systems. However, this distribution is broad and full quantification of the O−H distances in this system is complicated by the uncertainty introduced by the nature of the density representing this hydrogen atom.

Analysis of the neutron diffraction data at 123 K revealed the position of the proton associated with the hydrogen atom in the hydrogen bond: the distances between the proton position and the two oxygen atoms are $r_{H1O1} = 1.221(7)$ Å and $r_{H_1O_2} = 1.211(7)$ Å, with a bond angle $\angle_{O_1H_1O_2} = 173.3(6)°$.

The relative invariance of the hydrogen atom position with temperature is also borne out by the trends in the other bond lengths in the system. For example, there is also a considerable change in the bond distances of the formic acid segment, which tend to increase as the temperature is lowered (possibly partly due to thermal parameter effects) and do not show a pattern consistent with transfer of the proton across the hydrogen bond. At room temperature, the carbon−oxygen double bond is 1.2107(19) Å and the C−O single bond is 1.263(2) Å. These bond distances are in accord with earlier studies of urotropine-*N*-oxide·formic acid as well as with studies of free formic acid as seen in a search of the Cambridge Structural Database (CSD).[62,63] As the temperature of the diffraction experiment was lowered to 148 K, the carbon−oxygen bond distances in the formic acid segment of the structure were both found to lengthen. The carbon−oxygen that is formally considered a single bond is 1.2818(15) Å, while the double bond is 1.2252-(15) Å, and a comparison of the bond lengths in the formate segment of the molecule are shown in Figure 5. These distances are closely related to a formic acid fragment which is hydrogen bound to another species.[62,63]

At 123 K, the heavy atom positions and the bond lengths derived from the data show a strong correlation between the X-ray and neutron data. However, there is not a strong correlation for the H atom. Given the experimental data, it may be assumed that the correlation of the heavy atom holds true at all temperatures. The carbon−oxygen bonds in the formate segment do not show any evidence of structures 2b or 2c shown in Figure 2. We note that, in the presence of a short, strong hydrogen bond, a similar lack of correlation in the carbon−oxygen bond lengths has been observed in other compounds where H atom transfer is observed.[91] There is no distinct difference in the two carbon−oxygen distances, which is to be expected from a valence bond description of the molecule. Also, the C−O bond lengths in the formate segment vary with temperature, which is unrelated to any structural change in the hydrogen bond. This indicates a resonance structure between 2a and 2d in Figure 2. Therefore, one cannot make assertions about the hydrogen bond based solely on heavy atom positions and bond lengths.

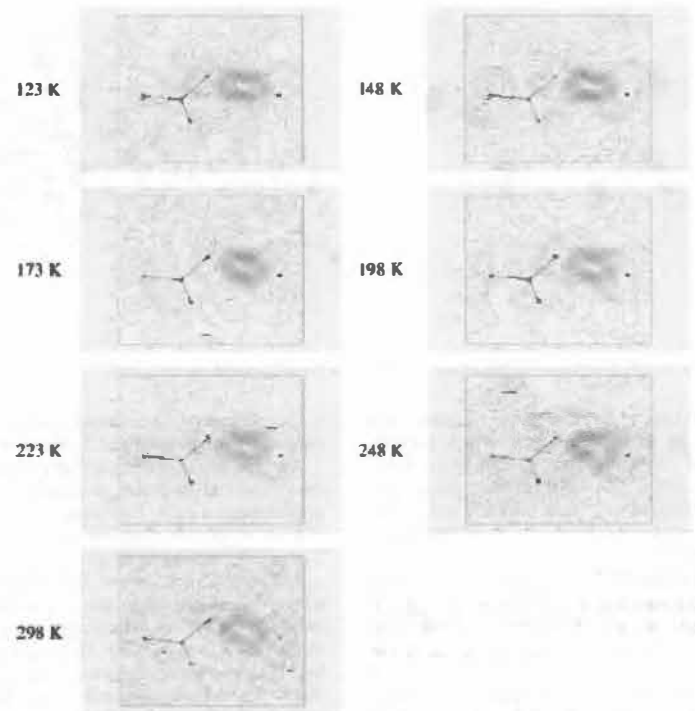


Figure 4. Fourier difference maps showing the electron density associated with the proton position of the formic acid OH.[84] Contour levels are drawn at 0.03 e Å^{-3}.

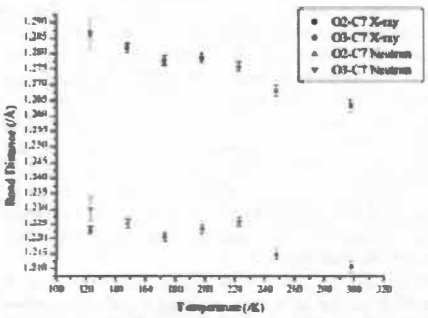


Figure 5. Comparison of the variation of C−O and C=O bond lengths of the formate segment by neutron diffraction and variable temperature X-ray diffraction experiments.

The partial "transfer" of the proton to the center of the short hydrogen bond, indicated by the difference Fourier maps, is supported by analysis of the N−O bond distance in the system. This is considerably longer than in free urotropine-*N*-oxide (1.363 Å) and slightly longer than previously known urotropine-*N*-oxide hydrogen bonded systems (1.380−1.391 Å) as seen in a search of the CSD.[62,63] The formation of a significant bonding interaction with the partly transferred proton withdraws electron density from the N−O bond, weakening the strength of the bond and therefore increasing the bond length. The average bond distance for the N−O bond in hydroxylammonium cations, as seen in a search of the Cambridge Structural Database, is 1.417-(2) Å, with a range from 1.396 to 1.436 Å.[62,63] This bond length corresponds more directly to urotropine-*N*-oxide-formic acid than does the average bond length for a typical *N*-oxide system. Once again the relative invariance of this N−O distance with temperature supports the stability of the "partly transferred" proton in this hydrogen bonding system.

For a comparative study of the bond lengths in the formic acid segment of the structure, single-crystal X-ray diffraction data were collected for rubidium hydrogen formate at 173 K using the data collection strategy as described above for urotropine-*N*-oxide-formic acid. There is a considerable amount of hydrogen bonding present in the solid-state structure of this material. The hydrogen bonds exist between two formic acid segments, with an oxygen−oxygen distance of 2.4360(13) Å. In the crystal structure, rubidium is 8-coordinate, with bond distances to the oxygen atoms of the formate ranging from 2.8853(13) to 3.1556(12) Å. The bond distances for the C−O single and double bonds were found to be 1.272(2) and 1.2269-(19) Å, respectively. These distances are similar to those found at the same temperature in urotropine-*N*-oxide-formic acid, 1.2778(15) and 1.2206(15) Å. Accordingly, the O−C−O angle in rubidium formate, 125.06(15)°, is only slightly smaller than that in urotropine-*N*-oxide-formic acid [125.55(12)°]. The lengthened bond distances demonstrate the strengthening of the hydrogen bond present between formic acid and urotropine-*N*-oxide as well as the migration of the electron density associated with the proton position as the temperature is lowered.

An anisotropic displacement parameter (ADP) may be defined as "the second moment of atomic probability distribution function".[92] This, in essence, describes the average displacement of atoms in crystals from the mean atomic positions in the Bragg

TABLE 4: Anisotropic Displacement Parameter Tensors for H1 from Neutron and X-ray Diffraction Data[79] a

U_{11}	U_{12}	U_{13}	U_{22}	U_{23}	U_{33}	U_{iso}	
0.043(4)	0.0035(24)	0.0048(29)	0.0201(29)	0.0013(25)	0.028(4)	0.03032	H1 neutron
0.151(22)	0.031(13)	0.051(14)	0.038(11)	0.018(8)	0.047(13)	0.08263	H1 X-ray

[a] The average U_{iso} for the H atoms in the urotropine cage is 0.03404 Å^2 (neutron data).

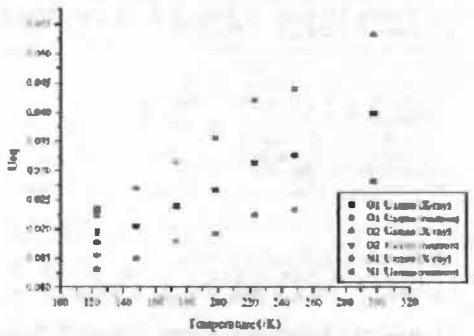


Figure 6. Comparison of U_{iso} between neutron and X-ray data for the atoms most directly affected by the hydrogen bond (N1, O1, O2).

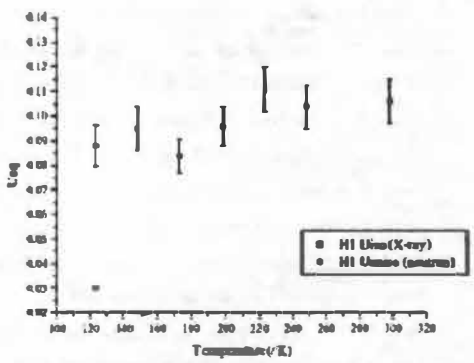


Figure 7. Comparison of results from neutron (U_{iso}) and X-ray (U_{iso}) data for the hydrogen bonded H atom, H1.

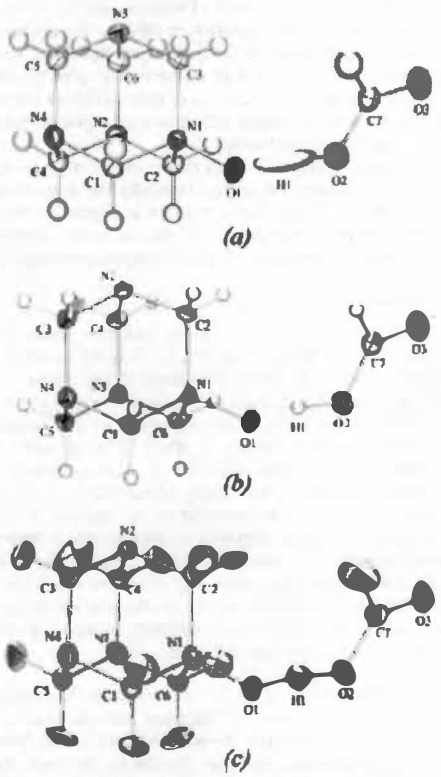


Figure 8. Comparison of X-ray and neutron data at 123 K. (a) X-ray data with anisotropic refinement of H1 using GSAS;[79] (b) X-ray data with isotropic refinement from SHELXTL;[44] (c) neutron data with anisotropic refinement of all H atoms from GSAS. Thermal ellipsoids are drawn at the 50% probability level using POV-Ray.[93]

average. Figure 7 depicts the variation in U_{eq} with temperature for the X-ray data, as well as a comparison of the neutron data, for the atoms that are most affected by the presence of the hydrogen bond, namely N1, O1, and O2. In comparing the neutron and X-ray data at 123 K, it is notable that there is very little difference in U_{eq} for any of these atoms, the difference being approximately 0.001 Å^2. The major difference in the thermal parameters between the neutron and X-ray data is best shown in Figure 7, which represents H1, the hydrogen bonded H atom. Table 4 shows the anisotropic thermal parameter tensor components, U_{ij}^X and U_{ij}^N, of H1 extracted from the refinement of the X-ray and neutron data, respectively, and it shows the difference in ADPs (U_{eq} for X-ray data, U_{iso} for neutron data) between the two sets of experiments. For a hydrogen atom, the valence electron density is also the core electron density, which leads to the diminished correlation between the distributions of nuclear and electron densities. From Figures 5 and 6 it is clear that the description of isotropic displacement parameters for the hydrogen atom from X-ray data is inadequate. Though results from the X-ray and neutron diffraction experiments showed very similar positional parameters for H1 in that the position of maximum electron density from the X-ray data corresponds well to the position of the proton in the neutron data, the ADPs clearly differ. In the refinement of neutron diffraction data, the ADPs of the proton position associated with the hydrogen bond are consistent with the average displacement over the thermally populated normal coordinates and lattice modes, and in this respect the ADPs of the proton are not anomalous when compared to the other atomic ADPs in the crystal. Therefore, given the broad distribution of electron density associated with the hydrogen bond, the use of ADPs to refine the structural parameters of the electron density associated with the hydrogen bond is clearly not in accord with the definition of the ADP. The neutron diffraction refinement of the O−H−O positions and ADPs effectively define the nuclear potential in which the four electrons associated with the hydrogen bond are confined. From inspection of the ADPs associated with the nuclear potential, it is clear that the motions of the atoms are smaller in magnitude than have been interpreted from the refined ADPs for the "H atom" associated with the hydrogen bond. It is therefore clear that parametrization of structural parameters of the distribution of electron density using ADPs is not physically

realistic within the structural definition of the ADP. Moreover, it is clear that a standard "spherical atom and ADP" model is inadequate to describe this distribution. However, we note that the Bragg scattering experiment is a priori an elastic experiment and contains no dynamic information about the system.

Given the physical ambiguity implied in using ADPs to define the structure of the distribution of electron density in a system in which there is a poor correlation between the nuclear and core electron density distributions, it is clear that direct imaging of electron density via a Fourier synthesis gives good qualitative information in this case. We note that more advanced aspherical methods are available which will allow a more precise quantitative description in these cases.

The results of spherical atom refinements using anisotropic atomic displacement parameters to model the distribution of electron density in the bond are shown in Figure 8a, together with an isotropic refinement of the electron density (Figure 8b) and the result of the neutron diffraction experiment (Figure 8c).

Conclusion

The proton in the short, strong hydrogen bond (O···O separation ~2.44 Å) in the molecular complex urotropine-*N*-oxide-formic acid is partly transferred to the center of the hydrogen bond. The position of maximum density associated with the hydrogen atom in the hydrogen bond, indicated by difference Fourier syntheses, is found to be invariant with temperature in the range 123−298 K. This invariance is a significant indication of the stability of this hydrogen bond with respect to variations in temperature, in contrast to recent observations of proton migration in several similar hydrogen bonded systems. It is clear that trends in bond lengths between heavy atoms is not necessarily a good indicator of hydrogen atom behavior. The subtle interplay of intra- and intermolecular forces and lattice effects clearly mitigates in this case against motion of the proton along the bond.

Acknowledgment. J.F.C.T. acknowledges the financial support of the University of Tennessee, through provision of startup funds and through the establishment of the Neutron Sciences Consortium, and the Petroleum Research Fund, administered through the American Chemical Society (PRF-37341-G4). C.C.W. acknowledges this work was funded in part by EPSRC under Grant GR/R04690. The authors thank Arthur J. Shultz for discretionary beam time on SCD and experimental help. This work has benefited from the use of the Intense Pulsed Neutron Source at Argonne National Laboratory, which is funded by the U.S. Department of Energy, BES-Materials Science, under Contract W-31-109-Eng-38.

Supporting Information Available: Variable temperature X-ray diffraction data. This information is available free of charge via the Internet at http://pubs.acs.org.

References and Notes

(1) Steiner, T. *Angew. Chem., Int. Ed.* **2002**, *41*, 48−76.
(2) Schowen, K. B.; Limbach, H. H.; Denisov, G. S.; Schowen, R. L. *Biochim. Biophys. Acta* **2000**, *1458*, 43−62.
(3) Cleland, W. W. *Arch. Biochem. Biophys.* **2000**, *382*, 1−5.
(4) Perrin, C. L.; Nielson, J. B. *Annu. Rev. Phys. Chem.* **1997**, *48*, 511−544.
(5) Urquidi, J.; Benmore, C. J.; Egelstaff, P. A.; Guthrie, M.; McLain, S. E.; Tulk, C. A.; Klug, D. D.; Turner, J. F. C. *Mol. Phys.* **2004**, *102*, 2007−2014.
(6) George, W. O.; Jones, B. F.; Lewis, R. H. *Philos. Trans. R. Soc. London, Ser. A: Math., Phys. Eng. Sci.* **2001**, *359*, 1611−1629.
(7) Soper, A. K. *Chem. Phys.* **2000**, *258*, 121−137.
(8) Soper, A. K. *Physica B (Amsterdam)* **2000**, *276*−*278*, 12−16.
(9) Soper, A. K.; Ricci, M. A. *Phys. Rev. Lett.* **2000**, *84*, 2881−2884.
(10) Soper, A. K. *J. Phys.: Condens. Matter* **1996**, *8*, 9263−9267.
(11) Tromp, R. H.; Postorino, P.; Neilson, G. W.; Ricci, G. W.; Ricci, M. A.; Soper, A. K. *J. Chem. Phys.* **1994**, *101*, 6210−6215.
(12) Ricci, M. A.; Nardone, M.; Ricci, F. P.; Andreani, C.; Soper, A. K. *J. Chem. Phys.* **1995**, *102*, 7650−7655.
(13) McLain, S. E.; Benmore, C. J.; Siewenie, J. E.; Urquidi, J.; Turner, J. F. C. *Angew. Chem., Int. Ed.* **2004**, *43*, 1952−1955.
(14) Pfleiderer, T.; Waldner, I.; Bertagnolli, H.; Todheide, K.; Fischer, H. E. *J. Chem. Phys.* **2000**, *113*, 3690−3696.
(15) Dawnson, M.; Dore, J. C.; Powles, J. G.; Holloway, J. H.; Chieux, P. *Mol. Phys.* **1986**, *55*, 1351−1367.
(16) Desiraju, G. R. *Acc. Chem. Res.* **2002**, *35*, 565−573.
(17) Desiraju, G. R. *Dalton* **2000**, 3745−3751.
(18) Holman, K. T.; Pivovar, A. M.; Swift, J. A.; Ward, M. D. *Acc. Chem. Res.* **2001**, *34*, 107−118.
(19) Nangia, A.; Desiraju, G. R. *Acta Crystallogr., Sect. A: Found. Crystallogr.* **1998**, *A54*, 934−944.
(20) Subramanian, S.; Zaworotko, M. J. *Coord. Chem. Rev.* **1994**, *137*, 357−401.
(21) Ashcroy, C. B.; Seddon, K. R. *Chem. Soc. Rev.* **1993**, *22*, 397−407.
(22) Wozniak, K.; Mallinson, P. R.; Smith, G. T.; Wilson, C. C.; Grech, E. *J. Phys. Org. Chem.* **2003**, *16*, 764−771.
(23) Wilson, C. C.; Goeta, A. E. *Angew. Chem., Int. Ed.* **2004**, *43*, 2095−2099.
(24) Mallinson, P. R.; Smith, G. T.; Wilson, C. C.; Grech, E.; Wozniak, K. *J. Am. Chem. Soc.* **2003**, *125*, 4259−4270.
(25) Wilson, C. C.; Morrison, C. A. *Chem. Phys. Lett.* **2002**, *362*, 85−89.
(26) Wilson, C. C. *New J. Chem.* **2002**, *26*, 1733−1739.
(27) Wilson, C. C. *Chem. Phys. Lett.* **2001**, *335*, 57−63.
(28) Wilson, C. C. *Acta Crystallogr., Sect. B: Struct. Sci.* **2001**, *B57*, 435−439.
(29) Wilson, C. C.; Shankland, K.; Shankland, N. *Z. Kristallogr.* **2001**, *216*, 303−306.
(30) Wilson, C. C., Shankland, N.; Florence, A. J. *Chem. Phys. Lett.* **1996**, *253*, 103−107.
(31) Wilson, C. C.; Shankland, N.; Florence, A. J. *J. Chem. Soc., Faraday Trans.* **1996**, *92*, 5051−5057.
(32) Sumner, T.; Majerz, I.; Wilson, C. C. *Angew. Chem., Int. Ed.* **2001**, *40*, 2651−2654.
(33) Parkin, A.; Harte, S. M.; Goeta, A. E.; Wilson, C. C. *New J. Chem.* **2004**, *28*, 718−721.
(34) Bader, R. F. W. *Atoms Molecules: A Quantum Theory*; Oxford University Press: Oxford, UK, 1994.
(35) Bader, R. F. W. *NATO ASI Ser., Ser. B: Phys.* **1995**, *337*, 237−272.
(36) Bader, R. F. W. *NATO ASI Ser., Ser. C: Math. Phys. Sci.* **1993**, *406*, 313−349.
(37) Bader, R. F. W. *Chem. Rev. (Washington, D.C.)* **1991**, *91*, 893−928.
(38) Bader, R. F. W. *Acc. Chem. Res.* **1985**, *18*, 9−15.
(39) Nguyen-Dang, T. T.; Bader, R. F. W. *Physica A: Stat. Mech. Appl. (Amsterdam, Netherlands)* **1982**, *114A*, 68−73.
(40) Bader, R. F. W. http://www.chemistry.mcmaster.ca/faculty/bader/aim/.
(41) Dye, J. L. *Inorg. Chem.* **1997**, *36*, 3816−3826.
(42) Wagner, M. J.; Dye, J. L. *Annu. Rev. Mater. Sci.* **1993**, *23*, 223−253.
(43) Dye, J. L. *Science (Washington, D.C.)* **1990**, *247*, 663−668.
(44) Sheldrick, G. M. *SHELXL97, SHELXS97, SHELXTL*; University of Göttingen: Göttingen, Germany, 1997.
(45) Dickinson, R. G.; Raymond, A. L. *J. Am. Chem. Soc.* **1923**, *45*, 22−29.
(46) Gossell, H. W.; Mark, H. *Z. Phys. Chem.* **1923**, *107*, 181−218.
(47) Shaffer, P. A., Jr. *J. Am. Chem. Soc.* **1947**, *69*, 1557−1561.
(48) Andresen, A. F. *Acta Crystallogr.* **1957**, *10*, 107−110.
(49) Becka, L. N.; Cruickshank, D. W. J. *Proc. R. Soc. (London)* **1963**, *273*, 455−465.
(50) Becka, L. N.; Cruickshank, D. W. J. *Proc. R. Soc. (London)* **1963**, *273*, 435−454.
(51) Duckworth, J. A. K.; Willis, B. T. M.; Pawley, G. S. *Acta Crystallogr., Sect. A: Cryst. Phys., Diffr., Theor. Gen. Crystallogr.* **1969**, *25*, 482−484.
(52) Willis, B. T. M.; Howard, J. A. K. *Acta Crystallogr., Sect. A: Cryst. Phys., Diffr., Theor. Gen. Crystallogr.* **1975**, *A31*, 514−520.
(53) Parini, E. V.; Tsirel'son, V. G.; Ozerov, R. P. *Kristallografiya* **1985**, *30*, 857−866.
(54) Chakhlov, A. N.; Ionov, S. P. *Kristallografiya* **1982**, *27*, 506−510.
(55) Gruchowski, J.; Serda, P.; Wilson, K. S.; Dauter, Z. *J. Appl. Crystallogr.* **1994**, *27*, 722−726.

(56) Kamperman, S. P.; Sabine, T. M.; Craven, B. M.; McMullan, R. K. *Acta Crystallogr., Sect. A: Found. Crystallogr.* **1995**, *A51*, 489–497.
(57) Spackman, M. A.; Byrom, P. G. *Acta Crystallogr., Sect. B: Struct. Sci.* **1997**, *B53*, 553–564.
(58) Terpstra, M.; Craven, B. M.; Stewart, R. F. *Acta Crystallogr., Sect. A: Found. Crystallogr.* **1993**, *A49*, 685–692.
(59) Rasing, H. A. *Mol. Cryst. Liq. Cryst.* **1969**, *9*, 101–132.
(60) Burgi, H. B., Capelli, S. C.; Birkedal, H. *Acta Crystallogr., Sect. A: Found. Crystallogr.* **2000**, *A56*, 425–435.
(61) Mak, T. C. W.; Ladd, M. F. C.; Povey, D. C. *J. Chem. Soc., Perkin Trans. 2: Phys. Org. Chem.* **1979**, 593–595.
(62) Bruno, I. J.; Cole, J. C.; Edgington, P. R.; Kessler, M.; Macrae, C. F.; McCabe, P.; Pearson, J.; Taylor, R. *Acta Crystallogr., Sect. B* **2002**, *B58*, 389–397.
(63) Allen, F. H.; Motherwell, W. D. S. *Acta Crystallogr., Sect. B* **2002**, *B58*, 407–422.
(64) Yu, P.-Y.; Mak, T. C. W. *Acta Crystallogr., Sect. B: Struct. Crystallogr. Cryst. Chem.* **1978**, *B34*, 3053–3056.
(65) Trotter, J.; Mak, T. C. W. *Acta Crystallogr., Sect. B: Struct. Crystallogr. Cryst. Chem.* **1979**, *B35*, 2367–2369.
(66) Mak, T. C. W.; Lam, Y.-S. *Acta Crystallogr., Sect. B: Struct. Crystallogr. Cryst. Chem.* **1978**, *B34*, 1732–1735.
(67) Lam, Y.-S.; Mak, T. C. W. *Acta Crystallogr., Sect. B: Struct. Crystallogr. Cryst. Chem.* **1978**, *B34*, 1915–1918.
(68) Lam, Y.-S.; Mak, T. C. W. *Aust. J. Chem.* **1978**, *31*, 1249–1253.
(69) Chesnut, D. B.; Savin, A. *J. Am. Chem. Soc.* **1999**, *121*, 2335–2336.
(70) Chesnut, D. B. *J. Am. Chem. Soc.* **1998**, *120*, 10504–10510.
(71) Cunningham, T. P.; Cooper, D. L.; Gerratt, J.; Karadakov, P. B.; Raimondi, M. *J. Chem. Soc., Faraday Trans.* **1997**, *93*, 2247–2254.
(72) Cunningham, T. P.; Cooper, D. L.; Gerratt, J.; Karadakov, P. B.; Raimondi, M. *Int. J. Quantum Chem.* **1996**, *60*, 393–400.
(73) Ra, U. S.; Symons, M. C. R. *J. Chem. Soc., Faraday Trans.* **1994**, *90*, 2649–2652.
(74) Gilhamy, D. G. *Chem. Rev.* **1994**, *94*, 1339–1374.
(75) Magnusson, E. *J. Am. Chem. Soc.* **1993**, *115*, 1051–1061.
(76) Reed, A. E.; Schleyer, P. v. R. *J. Am. Chem. Soc.* **1990**, *112*, 1434–1445.
(77) *Smart*, Version 5.044, Bruker: Madison, WI, 1997.
(78) *Saint*, Version 5.01, Bruker: Madison, WI, 1997.
(79) Larson, A. C.; Von Dreele, R. B. *General Structure Analysis System (GSAS)*; Los Alamos National Laboratory: Los Alamos, NM, 2000.
(80) Sheldrick, G. M. *SADABS*; University of Göttingen: Göttingen, Germany, 1996.
(81) Schultz, A. J.; Srinivasan, K., Teller, R. G.; Williams, J. M.; Lukehart, C. M. *J. Am. Chem. Soc.* **1984**, *106*, 999–1003.
(82) Schultz, A. J.; Carlin, R. L. *Acta Crystallogr., Sect. B Struct. Sci.* **1995**, *B51*, 43–47.
(83) Chattopadhyay, A.; Mikkelson, D.; Mikkelson, R.; Hammonds, J.; Worlton, T. *Appl. Phys. A: Mater. Sci. Process.* **2002**, *74*, S194–S197.
(84) Sears, V. F. *Methods of Experimental Physics*; Academic Press: New York, 1986; Vol. 23.
(85) Howard, J. A. K.; Johnson, O.; Schultz, A. J.; Stringer, A. M. *J. Appl. Crystallogr.* **1987**, *20*, 120–122.
(86) Taylor, R.; Macrae, C. F. *Acta Crystallogr., Sect. B* **2001**, *B57*, 815–817.
(87) Desiraju, G. R.; Steiner, T. *The Weak Hydrogen Bond*: Oxford University Press: New York, 2001: Vol. 9.
(88) Bondi, A. *J. Phys. Chem.* **1964**, *68*, 441–451.
(89) Steiner, T.; Desiraju, G. R. *Chem. Commun.* **1998**, 891–892.
(90) Wilson, C. C.; Goeta, A. E. *Angew. Chem., Int. Ed.* **2004**, *43*, 2095–2099.
(91) Nygren, C. L., Wilson, C. C.; Turner, J. F. C. Accepted for publication in *J. Phys. Chem. A*.
(92) Dunitz, J. D.; Schomaker, V.; Trueblood, K. N. *J. Phys. Chem.* **1988**, *92*, 856–867.
(93) Fenn, T. D.; Ringe, D.; Petsko, G. A. *J. Appl. Crystallogr.* **2003**, *36*, 944–947.
(94) Farrugia, L. J. *J. Appl. Crystallogr.* **1999**, *32*, 837–838.

Inorg. Chem. 2005, 44, 989–995



$Cu(HCO_2)_2(pym)$ (pym = pyrimidine): Low-Dimensional Magnetic Behavior and Long-Range Ordering in a Quantum-Spin Lattice

J. L. Manson,*,†,‡ T. Lancaster,§ L. C. Chapon,∥ S. J. Blundell,§ J. A. Schlueter,⊥ M. L. Brooks,§ F. L. Pratt,# C. L. Nygren,▽ and J. S. Qualls◆

Department of Chemistry and Biochemistry, Eastern Washington University, Cheney, Washington 99004, Condensed Matter Sciences Division, Oak Ridge National Laboratory, Oak Ridge, Tennessee 37831, Clarendon Laboratory, Department of Physics, Oxford University, Oxford, OX1 3PU, U.K., ISIS Department, Rutherford Appleton Laboratory, Chilton, Didcot, OX11 0QX, U.K., Materials Science Division, Argonne National Laboratory, Argonne, Illinois 60439, ISIS Muon Facility, Rutherford Appleton Laboratory, Chilton, Didcot, OX11 0QX, U.K., Department of Chemistry, University of Tennessee, Knoxville, Tennessee 37996, and Department of Physics and Geology, University of Texas-Pan American, Edinburg, Texas 78539

Received September 13, 2004

We synthesized and structurally and magnetically characterized the novel 3D coordination polymer $Cu(HCO_2)_2$(pym) (pym = pyrimidine). The compound crystallizes in the monoclinic space group $C2/c$ with a = 14.4639(8) Å, b = 7.7209(4) Å, c = 8.5172(5) Å, β = 126.076(2)°, and V = 768.76(7) Å^3. In the structure buckled layers of $Cu(HCO_2)_2$ are interconnected by pym ligands to afford 1D Cu–pym–Cu chains. Bulk magnetic susceptibility measurements show a broad maximum at 25 K that is indicative of short-range magnetic ordering. Between 12 and 300 K a least-squares fit of the $\chi(T)$ data to a mean-field-corrected antiferromagnetic chain model yielded excellent agreement for g = 2.224(3), J/k_B = −26.9(2) K, and zJ'/k_B = −1.1(3) K. Below ~3 K a transition to long-range magnetic ordering is observed, as suggested by a sharp and sudden decrease in $\chi(T)$. This result is corroborated by muon spin relaxation measurements that show oscillations in the muon asymmetry below T_N = 2.802(1) K and rapidly fluctuating moments above T_N.

Introduction

Small, multidentate anions such as CN^-,[1] $[N(CN)_2]^-$,[2] $[C(CN)_3]^-$,[2] N_3^-,[3] and $C_2O_4^{2-}$[4] have been utilized in the design and synthesis of novel compounds that exhibit long-range magnetic ordering, some with T_c's that exceed room temperature.[1] The dimensionality of the structures can be tuned by virtue of the metal ion selected and whether other ligands such as chelates are present. The ability to predict structural and physical properties of new materials has been a major challenge welcomed by chemists working in the area of molecular magnetism.

Currently, the smallest carboxylate building block, i.e., formate ion, HCO_2^-, is being actively studied, and it has proven to be an effective bridging ligand and superexchange mediator in transition-metal-containing coordination polymers. In addition to the various hydrate forms that have been known for many years,[5] other examples that contain organic ligands have begun to emerge. Several dimeric complexes

* To whom correspondence should be addressed. E-mail: jmanson@ewu.edu.
† Eastern Washington University.
‡ Oak Ridge National Laboratory.
§ Oxford University.
∥ ISIS Department, Rutherford Appleton Laboratory.
⊥ Argonne National Laboratory.
ISIS Muon Facility, Rutherford Appleton Laboratory.
▽ University of Tennessee.
◆ University of Texas-Pan American.

(1) (a) Hatlevik, O.; Buschmann, W. E.; Zhang, J.; Manson, J. L.; Miller, J. S. *Adv. Mater.* **1999**, *11*, 914. (b) Holmes, S. M.; Girolami, G. S. *J. Am. Chem. Soc.* **1999**, *121*, 5593. (c) Verdaguer, M.; Bleuzen, A.; Marvaud, V.; Vaissermann, J.; Seuleiman, M.; Desplanches, C.; Scuiller, A.; Train, C.; Garde, R.; Gelly, G.; Lomenech, C.; Rosenman, I.; Veillet, P.; Cartier, C.; Villain, F. *Coord. Chem. Rev.* **1999**, *192*, 1023.

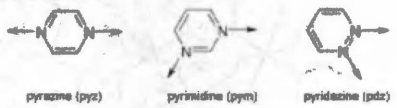
(2) Reviews: (a) Miller, J. S.; Manson, J. L. *Acc. Chem. Res.* **2001**, *34*, 563 and references therein. (b) Batten, S. R.; Murray, K. S. *Coord. Chem. Rev.* **2003**, *246*, 103 and references therein.

(3) See, for example: (a) Ray, U.; Jasimuddin, S.; Ghosh, B. K.; Monfort, M.; Ribas, J.; Mostafa, G.; Lu, T. H.; Sinha, C. *Eur. J. Inorg. Chem.* **2004**, 250. (b) Fu, A. H.; Huang, X. Y.; Li, J.; Yuen, T.; Lin, C. L. *Chem. Eur. J.* **2002**, *8*, 2239.

(4) See, for example: Decurtins, S.; Pellaux, R.; Antorrena, G.; Palacio, F. *Coord. Chem. Rev.* **1999**, *192*, 841.

10.1021/ic048723x CCC: $30.25 © 2005 American Chemical Society
Published on Web 01/15/2005

Scheme 1. Three Diazine Ligands Showing Possible Bidentate Coordination Modes



such as $Cu_2(HCO_2)_4L_2$ [L = urea,[6] dioxane,[7] dimethyl sulfoxide (DMSO),[7] and *N,N*-dimethylformamide (DMF)[8]] and the 1D chain compound $Cu(HCO_2)_2(py)_2 \cdot H_2O$[9] (py = pyridine) have been reported. The majority of reported structures though are inherently two-dimensional and include the aforementioned hydrates, $Co(HCO_2)_2(DMF)_2$[10] and $M(HCO_2)_2(urea)_2$ (M = Mn, Fe, Co, Ni, Cd, Zn).[11] Three-dimensional structures have been relatively unknown until recently and include $Cu(HCO_2)_2(pyz)$ (pyz = pyrazine),[12] $Cu(HCO_2)_2(4,4'\text{-bipy})$ (bipy = bipyridine),[12] $Mn_3(HCO_2)_6$,[13] $Mn(HCO_2)_3$,[14] and [AmineH][$Mn(HCO_2)_3$].[15]

In continuing our work on formate-based coordination polymers we extended our studies to include other diazine ligands such as pyrimidine (pym or 1,3-diazine). The corrugated 2D $Cu(HCO_2)_2$ layer found in $Cu(HCO_2)_2(pyz)$ offers the potential to accommodate a variety of molecules, thus producing an array of 3D lattice types. Specifically, the intralayer buckling affords an opposing 120° tilt of the CuO_4X_2 (X is a vacant axial position) chromophores, which allows successive layers to tightly pack together. Pyrimidine was chosen because the lone pairs on the sp^2 nitrogen atoms form a nominal 120° coordination angle (Scheme 1) that could lead to a network similar to $Cu(HCO_2)_2(pyz)$. From Scheme 1 it can be seen that the sp^2 nitrogen atoms in the other diazines, i.e., pyz and pyridazine (pdz), are arranged 180° and 60° apart, respectively, which profoundly affects the metal spacing, orbital orientations, and subsequent magnetic properties. By reacting $Cu(HCO_2)_2$ with pym, the anticipated $Cu(HCO_2)_2(pym)$ compound was formed which shows long-range magnetic ordering at low temperatures.

Table 1. X-ray Crystallographic Data for $Cu(HCO_2)_2(pym)$ Collected at 295 K

formula	$CuO_4N_2C_6H_6$
formula weight	233.67
space group	*C*2/*c*
a, Å	14.4639(8)
b, Å	7.7209(4)
c, Å	8.5172(5)
β, deg	126.076(2)
V, Å^3	768.76(7)
Z	4
ρ_{calc}, g/cm^3	2.019
λ, Å	0.71073
μ, mm^{-1}	2.821
$R^a(F)$	0.0297
$R_w{}^b(F)$	0.0799
GOF	0.870

$^a R = \sum[|F_o| - |F_c|]/\sum|F_o|$. $^b R_w = [\sum w[|F_o| - |F_c|]^2/\sum w[|F_o|^2]]^{1/2}$.

Table 2. Selected Bond Lengths (Å) and Bond Angles (deg) for $Cu(HCO_2)_2(pym)$ at 295 K

Cu–O(1)	2.398(1)	O(1)–Cu–O(2)	89.22(4)
Cu–O(2)	1.952(1)	N(1)–Cu–O(2)	89.31(5)
Cu–N(1)	2.060(1)	O(1)–Cu–N(1)	89.67(4)
C(1)–O(1)	1.238(2)	Cu–O(1)–C(1)	119.9(1)
C(1)–O(2)	1.250(2)	Cu–O(2)–C(1)	128.1(1)
N(1)–C(2)	1.337(2)	O(1)–C(1)–O(2)	125.7(1)
N(1)–C(4)	1.338(2)	N(1)–C(2)–C(3)	121.5(2)
C(2)–C(3)	1.381(2)	N(1)–C(4)–C(2)	117.5(1)

The structural and magnetic properties of $Cu(HCO_2)_2(pym)$ are described here and compared to $Cu(HCO_2)_2(pyz)$.

Experimental Section

Synthesis. In a typical synthesis a dilute aqueous solution of $Cu(HCO_2)_2 \cdot 3H_2O$ (Aldrich, 0.500 g, 3.3 mmol) is mixed with pyrimidine (Acros, 0.261 g, 3.3 mmol) to afford a deep blue solution. X-ray-quality single crystals are obtained in 42% yield by slow evaporation of the solvent over a period of 1−2 weeks depending on the dilution used. Selected IR data (Nujol, cm^{-1}): 3115 w, 3093 w, 1600 s, 1562 s, 1411 m, 1335 s, 1086 m, 1038 w, 1010 w, 836 m, and 796 s.

X-ray Crystallography. A blue block measuring 0.45 × 0.20 × 0.20 mm^3 was mounted on a Bruker AXS SMART 1000 X-ray diffractometer equipped with a CCD area detector. Monochromated Mo Kα radiation (*λ* = 0.710 73 Å) was used in the data collection. Approximately a hemisphere of data was measured to a resolution of 0.75 Å at 295 K. The area detector frames were integrated by use of the program SAINT.[16] and the resulting intensities were corrected for absorption by Gaussian integration (SHELXTL program suite).[17] The SHELXTL program package was employed in the structure solution using direct methods and full-matrix least-squares refinement on F^2 (using all data). Positions of aromatic H atoms were calculated by employing a 'riding' model. All non-hydrogen atoms were refined with anisotropic thermal parameters. Additional details of the data collection are given in Table 1, while selected bond lengths and angles are listed in Table 2. Further details are available in the CIF deposited as electronic Supporting Information.

Magnetic Measurements. AC susceptibility measurements were conducted on a Lake Shore Cryotronics 7000 series susceptometer equipped with a low-temperature helium subpot option (allowing

(5) (a) Flippen, R. B.; Friedberg, S. A. *J. Chem. Phys.* **1963**, *38*, 2652. (b) Abe, H. *Phys. Rev.* **1953**, *92*, 1572. (c) Shimada, J.; Abe, H.; Ono, K. *J. Phys. Soc. Jpn.* **1956**, *11*, 137. (d) Wagner, G. R.; Friedberg, S. A. *Phys. Lett.* **1964**, *9*, 11.
(6) Uekusa, H.; Ohba, S.; Saito, Y. *Acta Crystallogr.* **1989**, *C45*, 377.
(7) Sapina, F.; Burgos, M.; Escriva, E.; Folgado, J.-V.; Beltran, D.; Gomez-Romero, P. *Inorg. Chim. Acta* **1994**, *216*, 185.
(8) Cepeda, R.; Airuet, G.; Borras, J.; Lin-Gonzalez, M.; Sanz-Ruiz, F. *Polyhedron* **2002**, *21*, 1057.
(9) Cartwright, B. A.; Couchman, L.; Skapski, A. C. *Acta Crystallogr.* **1979**, *B35*, 824.
(10) Rettig, S. J.; Thompson, R. C.; Trotter, J.; Xia, S. *Inorg. Chem.* **1999**, *38*, 1360.
(11) See, for example: (a) Takeda, K.; Mito, M.; Nakajima, K.; Kakurai, K.; Yamagata, K. *Phys. Rev. B* **2001**, *63*, 024425. (b) Tokita, M.; Zasmyo, K.; Kubo, H.; Takeda, K.; Yamagata, K. *Physica B* **2000**, *284*, 1497. (c) Takeda, K.; Deguchi, H.; Hoshiko, T.; Yamagata, J. *J. Phys. Soc. Jpn.* **1989**, *58*, 3489.
(12) Manson, J. L.; Lecher, J. G.; Gu, J.; Geiser, U.; Schlueter, J. A.; Henning, R.; Wang, X.; Schultz, A. J.; Koo, H.-J.; Whangbo, M.-H. *J. Chem. Soc., Dalton Trans.* **2003**, 2905.
(13) Wang, Z.; Zhang, B.; Fujiwara, H.; Kobayashi, H.; Kurmoo, M. *Chem. Commun.* **2004**, 416.
(14) Cornia, A.; Caneschi, A.; Dapporto, P.; Fabretti, A. C.; Gatteschi, D.; Malavasi, W.; Sangregorio, C.; Sessoli, R. *Angew. Chem., Int. Ed.* **1999**, *38*, 1780.
(15) Wang, Z.; Zhang, B.; Otsuka, T.; Inoue, K.; Kobayashi, H.; Kurmoo, M. *J. Chem. Soc., Dalton Trans.* **2004**, 2209.
(16) Data Integration Software. *SAINT*, version 5.00; Bruker AXS, Inc.: Madison, WI, 1999.
(17) Structure Solution and Refinement Software. *SHELXTL*, version 5.0; Bruker AXS, Inc.: Madison, WI, 1996.

measurements to as low as 1.6 K to be achieved). A 1 Oe amplitude field oscillating at a frequency of 125 Hz was utilized for all measurements. A powder sample weighing ~187 mg was loaded into Delrin sample holders and affixed to the end of an aluminum rod. The samples were cooled from 300 to 4.5 K over a period of ~15 min and then further cooled to 1.5 K over a period of ~30 min. The real and imaginary components, χ' and χ'', respectively, of the volume AC susceptibility were recorded every 0.05 K.

For magnetization measurements a Quantum Design Physical Properties Measurement System (PPMS) ac/dc magnetometer equipped with a 9 T superconducting magnet and reciprocating sample option was used. Homogeneous powder samples were loaded into gelatin capsules and mounted on the end of a carbon fiber rod. For the broad temperature scan the sample was cooled in zero field to the lowest achievable temperature of 2 K, the magnet charged to 1 kOe, and data collected on warming to 300 K. Low-temperature zero-field-cooled $M(T)$ data were recorded for magnetic field strengths of 2, 3, 4, 5, 6, 7, 8, and 9 T. Isothermal $M(H)$ measurements were carried out at 1.3 K at the National High Magnetic Field Laboratory (Tallahassee, FL) in magnetic fields up to $\mu_0 H = 27$ T using a torque magnetometer. All magnetic data were corrected for core diamagnetism using Pascal's constants and temperature-independent paramagnetism (60×10^{-4} emu/mol for Cu^{2+} ion).

Muon Spin Relaxation. Zero-field muon spin relaxation (ZF μ^+SR) measurements have been made on a powder sample of $Cu(HCO_2)_2(pym)$ using the MuSR instrument at the ISIS facility, Rutherford Appleton Laboratory, U.K., using a standard orange cryostat. The sample was wrapped in silver foil and mounted on a silver sample holder.

In a μ^+SR experiment[18] spin-polarized positive muons are stopped in a target sample, where the muon usually occupies an interstitial position in the crystal. The observed property in the experiment is the time evolution of the muon spin polarization, the behavior of which depends on the local magnetic field at the muon site. Each muon decays, with a lifetime of 2.2 μs, into two neutrinos and a positron, the latter particle being emitted preferentially along the instantaneous direction of the muon spin. Recording the time dependence of the positron emission directions therefore allows determination of the spin polarization of the ensemble of muons. In our experiments positrons are detected by detectors placed forward (F) and backward (B) of the initial muon polarization direction. Histograms $N_F(t)$ and $N_B(t)$ record the number of positrons detected in the two detectors as a function of time following the muon implantation. The quantity of interest is the decay positron asymmetry function which is defined as

$$A(t) = \frac{N_F(t) - \alpha N_B(t)}{N_F(t) + \alpha N_B(t)} \quad (1)$$

where α is an experimental calibration constant. $A(t)$ is proportional to the spin polarization of the muon ensemble.

Results and Discussion

Crystal Structure. $Cu(HCO_2)_2(pym)$ crystallizes in the monoclinic space group $C2/c$ with four molecules per unit cell. The Cu^{2+} ion lies on an inversion center (Wyckoff position 4*c*), while C(3), H(3A), C(4), and H(4A) reside on the 2-fold axis (Wyckoff position 4*e*). All other atoms occupy general positions. Each Cu^{2+} ion is coordinated to four

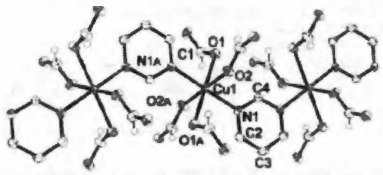


Figure 1. ORTEP diagram and atom-labeling scheme for $Cu(HCO_2)_2(pym)$ showing the dominant Cu−pym−Cu superexchange pathway. pym hydrogen atoms have been omitted for clarity. Thermal ellipsoids are drawn at the 50% probability level.

different formate oxygen atoms: two Cu−O(1) with bond distances of 2.398(1) Å are in axial positions, whereas two Cu−O(2) distances are 1.952(1) Å and occupy the equatorial plane along with two nitrogen atoms from the pym ligands [2× Cu−N(1) = 2.060(1) Å] (Figure 1). The Cu−O(1) bond length is similar to the Cu−O(2) distance found in $Cu(HCO_2)_2(pyz)$ [2.371(2)Å], while Cu−O(2) is much longer in $Cu(HCO_2)_2(4,4'\text{-bipy})$ [2.528(2)Å].[12] Aside from the Jahn−Teller elongation along the O(1)−Cu−O(1A) axis, the CuO_4N_2 octahedron in $Cu(HCO_2)_2(pym)$ is quite regular, the greatest deviation from 90° being 89.22(4)° for O(2)−Cu−O(1). The N(1)−Cu−N(1A), O(1)−Cu−O(1A), and O(2)−Cu−O(2A) bond angles are 180° as required by symmetry. Formate oxygen atoms coordinated to the Cu center, i.e., O(1) and O(2), form bond angles of 119.9(1)° and 128.1(1)° for Cu−O(1)−C(1) and Cu−O(2)−C(1), respectively. Comparing these bond angles to those of the pyz [120.5(2)° and 128.6(2)°] and 4,4'-bipy [117.2(2)° and 129.7(2)°] compounds reveals a clear similarity.[12] There is a larger difference, however, when we compare the Cu−O−C angles of 105.8(1)° and 133.5(2)° observed for the mixed-anion compound $Cu(HCO_2)(NO_3)(pyz)$.[19] All bond lengths and angles for the HCO_2^- and pym ligands are in accord with those generally observed.[12]

Anti−anti formate anions join Cu^{2+} ions together to form corrugated 2D layers (Figure 2) within the *bc* plane, while neutral pym ligands join them together along the *a* direction to afford a noninterpenetrating 3D lattice (Figure 3). Each CuO_4N_2 octahedron is tilted with respect to neighboring octahedra, meaning that the Jahn−Teller axes are tilted accordingly. Cu···Cu separations along the Cu−pym−Cu and Cu−O−C(H)−O−Cu pathways are, respectively, 5.845 and 5.748 Å, which leads to voids apparently too small to accommodate interstitial solvent molecules.

When the structure of $Cu(HCO_2)_2(pym)$ is viewed parallel to the *b* or *c* axes, its structure is indistinguishable from that of the pyz derivative. The only real difference between the two structures is the manner in which the Cu ions are linked by the diazine ligand, L, as shown in Scheme 2. In each case the Cu−L−Cu chains are linear with the Cu ions being equidistant. There are two types of chains in $Cu(HCO_2)_2(pyz)$, one running parallel to (110) and the other propagating along (1−10), with all chains in the same "layer" being aligned along a common direction. The Cu−L−Cu chains

(18) Blundell, S. J. *Contemp. Phys.* **1999**, *40*, 175.

(19) Manson, J. L.; Lancaster, T.; Schlueter, J. A.; Nygren, C., Blundell, S. J.; Brooks, M. L.; Pratt, F. L.; Koo, H.-J.; Whangbo, M.-H., manuscript in preparation.

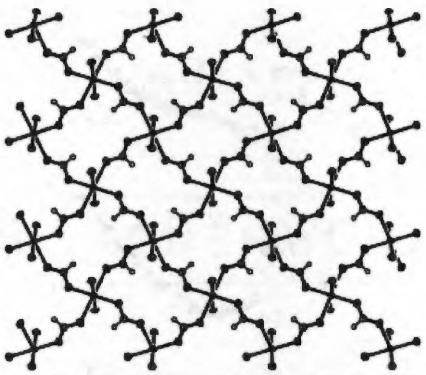


Figure 2. Portion of the corrugated 2D layers found in $Cu(HCO_2)_2(pym)$ showing the Cu−O−C(H)−O−Cu connectivity. Only the coordinated N atoms of the pym ligands are shown.

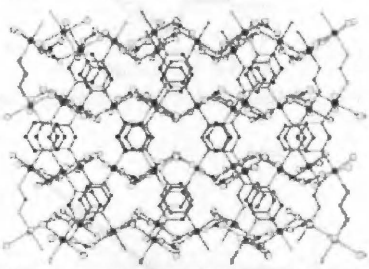
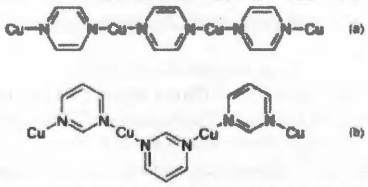


Figure 3. Three-dimensional framework of $Cu(HCO_2)_2(pym)$ viewed along the c axis. Pyrimidine hydrogen atoms have been omitted for clarity. Cu, O, N, and C atoms are depicted as heavily shaded, lightly shaded, open, and filled spheres, respectively.

Scheme 2. Schematic Comparing the Two Types of Linear Cu−L−Cu Chains Present in $Cu(HCO_2)_2L$ [L = pyz (a) and pym (b)][a]



[a] Note that in both cases the Cu ions are uniformly spaced and lie along a common axis.

in $Cu(HCO_2)_2(pym)$ possess a single orientation that runs roughly perpendicular to the bc plane, i.e., approximately 36° away from the crystallographic a axis.

Short- and Long-Range Magnetic Ordering. Temperature Dependence. A plot of χT (Figure 4) shows a continuous decrease from a value of 0.424 emu K/mol at 300 K to 0.010 emu K/mol at 2 K. The value of χT at 300 K exceeds the value of 0.375 emu K/mol predicted for uncoupled $S = {}^1/_2$ ions; however, owing to g-value anisotropy this is not unexpected. The nature of the χT curve strongly suggests that all magnetic exchange interactions are antiferromagnetic. This finding was verified by a mean-field-corrected fit to a $S = {}^1/_2$ antiferromagnetic chain model with intrachain J, interchain exchange J', with each chain having

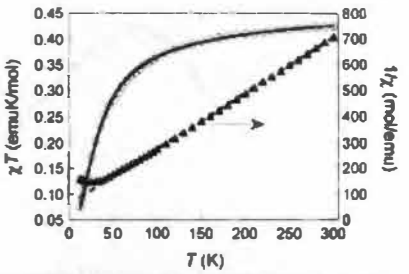


Figure 4. χT (○) and $1/\chi$ (▲) for $Cu(HCO_2)_2(pym)$ measured in a 1 kOe dc field. Solid and broken lines are theoretical fits to the Borner−Fisher chain model and Curie−Weiss expression, respectively, as described in the text.

Table 3. Comparison of Exchange Coupling Constants and pym Coordination Modes in Some Cu^{2+} Complexes

compound	J/k_B (K)	pym bonding mode[a]	ref
$Cu(HCO_2)_2(pym)$	−26.9	eq−eq	this work
$Cu(dca)(NO_3)(pym)(H_2O)$[b]	−42.6	eq−eq	25a
$Cu_3(dca)_6(pym)_2$	−69.4	eq−eq	25a
$Cu(dca)_2(pym)\cdot CH_3CN$	>−1	ax−ax	31
$Cu(NO_3)_2(pym)(H_2O)_2$	−18	eq−eq	25d
$Cu(NO_3)_2(pym)_3$	+0.9	ax−eq	25d
$Cu(hfac)_2(pym)$[c]	+0.2	ax−eq	25b,c

[a] eq−eq = equatorial−equatorial, ax−eq = equatorial−axial, ax−ax = axial−axial. [b] dca = dicyanamide = $[N(CN)_2]^-$. [c] hfac = hexafluoroacetylacetonate.

z nearest neighbors.[20] A least-squares fit of χT to the model generated excellent agreement for the following parameters: $g = 2.224(3)$, $J = -26.9(2)$, and $zJ' = -1.1(3)$ K.[21] J and zJ' are assigned to the Cu−pym−Cu and Cu−O−C(H)−O−Cu exchange interactions, respectively. A fit of $1/\chi$ to a Curie−Weiss expression afforded $g = 2.229(3)$ and $\theta = -28.2(5)$ K, the negative θ value indicating the presence of antiferromagnetic correlations between Cu^{2+} sites (Figure 4). Furthermore, the fitted J value is in very good agreement with the absolute value of 26.6 K calculated from the expression $k_BT_{max}/J = 1.12S(S+1) + 0.10$ that relates the J value of a 1D magnetic system to the temperature, T_{max}, where $\chi(T)$ reaches a maximum.[22] Table 3 compares the J values and corresponding pym coordination modes observed in other polymeric materials.

Analogous to that found in $Cu(HCO_2)_2(pyz)$, there is an alternation of the magnetic Cu $d_{x^2-y^2}$ orbitals that occupy the equatorial CuN_2O_2 plane within the 2D $Cu(HCO_2)_2$ layers. The small zJ' value is then likely due to a competition between antiferromagnetic and ferromagnetic exchange interactions where the net coupling is slightly antiferromagnetic. This finding is in contrast to the large exchange coupling, i.e., $J/k_B = -73.2$ K, observed in $Cu(HCO_2)_2(H_2O)_4$ which leads to $T_N = 16.54$ K.[5a,23] In the tetrahydrate the magnetic $d_{x^2-y^2}$ orbitals exclusively occupy the 2D $Cu(HCO_2)_2$ layers, which affords very good orbital overlap.

(20) (a) Borner, J. C.; Fisher, M. E. *Phys. Rev. A* **1964**, *135*, 640. (b) Ginsberg, A. P.; Lines, M. E. *Inorg. Chem.* **1972**, *11*, 2289.
(21) A least-squares fit of the $\chi(T)$ data to the same theoretical model as described in the text yielded parameters identical to those obtained for the $\chi T(T)$ analysis.
(22) Lines, M. E. *J. Phys. Chem. Solids* **1970**, *31*, 101.

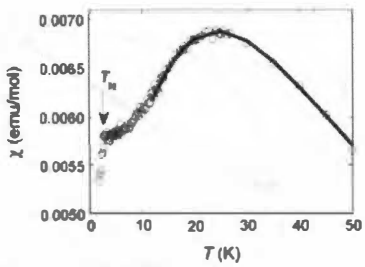


Figure 5. Low-temperature $\chi(T)$ plot of $Cu(HCO_2)_2(pym)$ showing the broad maximum and abrupt decrease in $\chi(T)$ associated with the short- and long-range magnetic orderings. The solid line is the theoretical curve generated from the $\chi J(T)$ fit.

Upon cooling from 300 K, $\chi(T)$ increases gradually, reaching a value of 0.00685 emu/mol at 25 K where a broad maximum is observed. Below χ_{max}, $\chi(T)$ decreases smoothly until ~3 K, where it decreases abruptly (Figure 5). AC measurements indicate that these features do not depend on the frequency of the oscillating magnetic field. The origin of the broad maximum is likely due to short-range magnetic ordering within the Cu−pym−Cu chains, while the origin of the sharp decline in $\chi(T)$ is not completely clear but may be due to a structural or magnetic phase transition. The only other example that we aware of which shows a similar response in $\chi(T)$ is the spin-Peierls compound $(TTF)Cu[S_4C_4(CF_3)_4]$ (TTF = tetrathiafulvalene).[24]

It is known that μ-bridging pym can stabilize either antiferromagnetic or ferromagnetic exchange interactions depending on the magnetic orbital configuration of the transition metal to which it is attached. In the case of $S = 1/2$ copper and vanadyl complexes, molecular orbital calculations suggest that equatorial−equatorial (eq−eq) and axial−axial (ax−ax) coordination favors orbital overlap, i.e., antiferromagnetic coupling, while a mixed axial−equatorial (ax−eq) situation leads to ferromagnetic interactions between Cu $d_{x^2-y^2}$ magnetic orbitals and nitrogen $n\sigma$ and $p\pi$ orbitals of pym.[25] Thus, the antiferromagnetic coupling observed in $Cu(HCO_2)_2(pym)$ can be understood in terms of its crystal structure, which shows eq−eq coordination of the pym ligand.

Field Dependence. The zero-field magnetization, $M(T)$, for $Cu(HCO_2)_2(pym)$ was measured in various external fields between 2 and 9 T, and selected data are presented in Figure 6. In a 2 T field the magnetization shows a subtle downward inflection near 4 K, and as the field is increased, the data

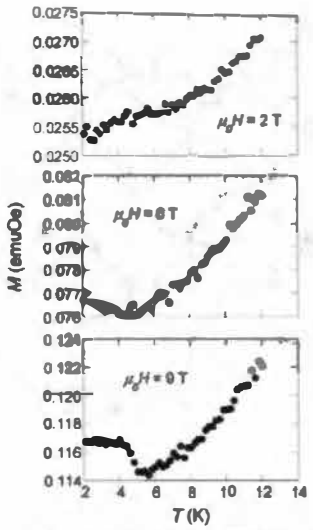


Figure 6. Zero-field-cooled $M(T)$ data for $Cu(HCO_2)_2(pym)$ measured at 2, 6, and 9 T.

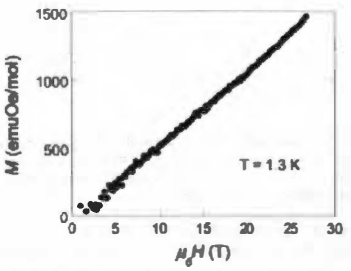


Figure 7. $M(H)$ plot for $Cu(HCO_2)_2(pym)$ recorded at 1.3 K.

begin to curve upward for H approaching 8 T. At $\mu_0H = 9$ T the data take on a different appearance in that there is a sudden rise in $M(T)$ at 5 K which then levels off below 4 K. This behavior may be due to a spin flip transition; however, detailed measurements on single crystals are planned to help sort this out.

The isothermal magnetization, $M(H)$, was measured at 1.3 K up to 27 T and is shown in Figure 7. It can be seen that $M(H)$ initially rises slowly with an almost linear slope. Near 12 T the data curve upward and thus continue to rise up to the highest attainable field. This type of behavior has been observed in other low-dimensional $S = 1/2$ quantum antiferromagnets.[26] At 27 T, M reaches a value of 1454 emu Oe/mol, which is ~77% below the predicted value of 6210 emu Oe/mol based on the fitted g value of 2.224. From the mean-field prediction of the zero-temperature saturation field, $H_{sat}(0)$, we can estimate the field necessary to overcome the antiferromagnetic interaction and fully align the Cu^{2+}

(23) (a) Kobayashi, H.; Haseda, T. *J. Phys. Soc. Jpn.* **1963**, *18*, 541. (b) Seehra, M. S. *Phys. Lett.* **1969**, *28A*, 754. (c) Koyama, K.; Nobumasa, H.; Matsuura, M. *J. Phys. Soc. Jpn.* **1987**, *56*, 1553.

(24) (a) Bray, J. W.; Hart, H. R.; Interrante, L. V.; Jacobs, I. S.; Kasper, J. S.; Watkins, G. D.; Wee, S. H.; Bonner, J.C. *Phys. Rev. Lett.* **1978**, *35*, 744. (b) Jacobs, I. S.; Bray, J. W.; Hart, H. R.; Interrante, L. V.; Kasper, J. S.; Watkins, G. D.; Prober, D. E.; Bonner, J.C. *Phys. Rev. B* **1976**, *14*, 3036.

(25) (a) Manson, J. L.; Gu, J.; Schlueter, J. A.; Wang, H-H. *Inorg. Chem.* **2003**, *42*, 3950. (b) Ishida, T.; Nakayama, K.; Nakagawa, M.; Sato, W.; Ishikawa, Y.; Yasui, M.; Iwasaki, F.; Nogami, T. *Synth. Met.* **1997**, *85*, 1655. (c) Yasui, M.; Ishikawa, Y., Ishida, T.; Nogami, T.; Iwasaki, F. *Acta Crystallogr.* **2001**, *B57*, 772. (d) Yasui, M.; Ishikawa, Y.; Akiyama, N.; Ishida, T.; Nogami, T.; Iwasaki, F. *Acta Crystallogr.* **2001**, *B57*, 288.

(26) See, for example: (a) Amaral, S.; Jansen, W. E.; Landee, C. P.; Turnbull, M. M.; Woodward, F. M. *Polyhedron* **2001**, *20*, 1317. (b) Bordallo, H. N.; Chapon, L.; Manson, J. L.; Ling, C. D.; Qualls, J. S.; Hall, D.; Argyriou, D. N. *Polyhedron* **2003**, *22*, 2045.

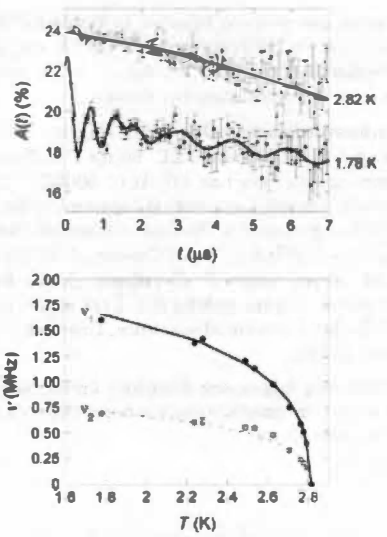


Figure 8. (a) ZF μ^+SR spectra measured at 1.78 and 2.82 K showing oscillations below the ordering temperature $T_N = 2.802(1)$ K. Data measured above T_N display a Gaussian form at high temperatures. (b) Temperature evolution of the two oscillation frequencies. The solid and dashed lines are fits to eq 4.

magnetic moments according to eq 2[26a]

$$\mu_0 H_{sat}(0) = 2zJ/(g\mu_B) \quad (2)$$

From this equation we derive $\mu_0 H_{sat}(0) = 48.4$ T for $z = 2$, $J/k_B = 26.9$ K, and $g = 2.224$. We note that since the Cu−pym−Cu "chains" in $Cu(HCO_2)_2(pym)$ are not completely isolated, the actual saturation field is likely higher than that estimated owing to additional interchain antiferromagnetic interactions. Hence, 48.4 T should be taken as the minimum saturation field.

Muon Spin Relaxation. We chose μ^+SR to further study the origin of the low-temperature anomaly because muons are especially sensitive to small magnetic moments. Figure 8a shows examples of ZF asymmetry spectra measured for this material. For temperatures $T \geq 2.82$ K, the observed asymmetry spectra show Gaussian relaxation, characteristic of the muon ensemble experiencing a static, random array of local magnetic fields. This field distribution is most likely due to the randomly oriented nuclear moments in the material, with the contribution from the fast-fluctuating electronic moments outside the muon time scale in this temperature regime. This hypothesis is consistent with our observation that an applied field of as little as 1 mT, directed parallel to the initial muon spin direction, repolarizes the muon ensemble [i.e., $\lim_{t\to\infty} A(t) = A(0)$], as expected for relaxation due to static, disordered field distribution.[27]

At temperatures $T < 2.82$ K oscillations in the positron asymmetry are clearly observable (Figure 8a). These oscillations are characteristic of a quasistatic local magnetic field at the muon site, which causes a coherent precession of the spins of those muons with a component of their spin polarization perpendicular to this local field. The frequencies of the oscillations (which are proportional to the order parameter in the broken symmetry phase) are given by $\nu_i = \gamma_\mu B_i/2\pi$, where γ_μ is the muon gyromagnetic ratio ($\equiv 2\pi \times 135$ MHz T^{-1}) and B_i is the local field at the ith muon site. The presence of oscillations in the muon asymmetry for $T < 2.82$ K provides strong evidence for the existence of long-range magnetic order (LRO) but not a spin-Peierls transition.

Two distinct precession frequencies are found in our data below T_N, suggesting the existence of two distinct muon stopping sites in $Cu(HCO_2)_2(pym)$. We note that two precession frequencies have been observed in muon studies of related materials.[19,28,29] To extract the temperature dependence of these frequencies, the spectra for $T < 2.82$ K were successfully fitted to a function of the form

$$A(t) = A_1 \exp(-\lambda_1 t)\cos(2\pi\nu_1 t + \phi_1) + A_2 \exp(-\lambda_2 t)\cos(2\pi\nu_2 t + \phi_2) + A_3 \exp(-\lambda_3 t) \quad (3)$$

where $\phi_{1,2}$ are phases and $\lambda_{1,2}$ are temperature-dependent relaxation rates. The parameters A_3 and λ_3 reflect a temperature-independent contribution to the signal from the component of the muon-spin polarization parallel to the local magnetic field and also from those muons which stop in the sample holder or cryostat tail.

The ratio of the contributions from the oscillating signals A_1:A_2 was found to be approximately 6:1, suggesting that the site associated with the frequency ν_1 is six times as probable as that associated with ν_2. The origin of the phase offsets ϕ_1 (≈−39°) and ϕ_2 (≈−31°) are unclear, although we note that similar phase offsets have also been observed in muon studies of related materials.[28] The magnitudes of the relaxation rates λ_i (which scale roughly with the frequencies ν_i) do not vary strongly with temperature but show a tendency to decrease as the magnetic phase transition is approached from below. This suggests that the spin relaxation is dominated by the magnitude of the local field at the muon site rather than the slowing of critical fluctuations.

The temperature dependence of the extracted precession frequencies is shown in Figure 8b. The lines shown are fits to the functional form

$$\nu_i(T) = \nu_i(0)\left[1 - \left(\frac{T}{T_N}\right)^\delta\right]^\beta \quad (4)$$

The paucity of data at low temperatures makes a reliable determination of the parameters in eq 4 problematic. If we make the assumption that $\delta = 2$, as would be expected for antiferromagnetic spin waves, we obtain $\nu_1(0) = 1.97(2)$ MHz (corresponding to a local field at the muon site of $B_1 = 14.5(1)$ mT), $\nu_2(0) = 0.844(1)$ MHz (or $B_2 = 6.23(1)$ mT),

(27) Hayano, R. S.; Uemura, Y. J.; Imazato, J.; Nishida, N.; Yamazaki, T.; Kubo, R. *Phys. Rev. B* **1979**, *20*, 850.

(28) Lancaster, T.; Blundell, S. J.; Pratt, F. L.; Brooks, M. L.; Manson, J. L.; Brechin, E. K.; Cadiou, C.; Low, D.; Melnikov, E. J. L.; Wimpenny, R. E. P. *J. Phys.: Condens. Matter* **2004**, *16*, S4563.

(29) Manson, J. L.; Lancaster, T.; Qu, Y.; Kenzelmann, M.; Blundell, S. J.; Brooks, M. L.; Pratt, F. L., manuscript in preparation.

$\beta = 0.33(1)$, and $T_N = 2.802(1)$ K. We note that the value of β is similar to that observed for $(C_2H_5NH_3)_2CuCl_4$ ($\beta = 0.32$), which is comparable to that calculated for a 3D Ising system ($\beta = 0.312$).[30]

Conclusions

$Cu(HCO_2)_2(pym)$ is a novel quasi-1D antiferromagnet that exhibits a transition to long-range ordering below $T_N = 2.8$ K as shown by magnetic susceptibility and muon spin relaxation measurements. The HCO_2^- anions adopt an anti–anti bridging mode between the $S = {}^1/_2$ Cu^{2+} ions which affords a weak antiferromagnetic coupling relative to the interaction along Cu–pym–Cu, which is much stronger ($J/k_B = -26.9$ K). The present work also clearly demonstrated the need for additional techniques to determine the nature of anomalous magnetic behavior, in this case μ^+SR. Future studies on $Cu(HCO_2)_2(pym)$ will involve use of neutron scattering to study spin excitations in the absence and presence of external magnetic fields.

Acknowledgment. Oak Ridge National Laboratory is managed by UT-Battelle, LLC, for the U.S. Department of Energy under contract no. DE-AC05-00OR22725. Work at Argonne National Laboratory is supported by the Office of Basic Energy Sciences, Division of Materials Science, U.S. Department of Energy, under Contract W-31-109-ENG-38. J.L.M. acknowledges R. Feyerherm (HMI) for helpful discussions. We are grateful to J. Lord and P. King at the ISIS facility for technical assistance. This work is supported by the EPSRC.

Supporting Information Available: Crystallographic data in CIF format. This material is available free of charge via the Internet at http://pubs.acs.org.

IC048723X

(30) de Jongh, L. J.; Miedema, A. R. *Adv. Phys.* 1974, *23*, 1.
(31) Riggio, I.; van Albada, G. A.; Ellis, D. D.; Spek, A. L.; Reedijk, J. *Inorg. Chim Acta* 2001, *313*, 120.

Acta Crystallographica Section C
Crystal Structure
Communications
ISSN 0108-2701

Tetrakis(tetrahydrofuran-κO)lithium *mer*-tris(carbazolyl-κN)-*trans*-dichloro(tetrahydrofuran-κO)zirconate

Cara L. Nygren,[a] M. E. T. Bragg[a] and John F. C. Turner[b]*

[a]406 Buehler Hall, Department of Chemistry, University of Tennessee, Knoxville, TN 37996, USA, and [b]409 Buehler Hall, Neutron Sciences Consortium and Department of Chemistry, University of Tennessee, Knoxville, TN 37996, USA
Correspondence e-mail: jturner@utk.chem.utk.edu

Received 10 November 2003
Accepted 8 January 2004
Online 31 January 2004

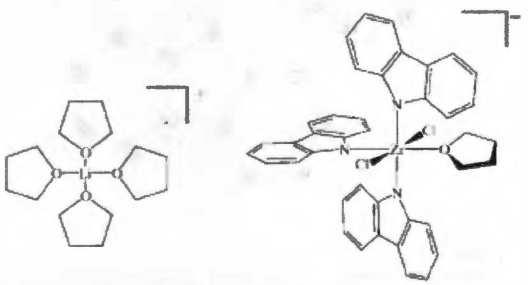
In the title compound, $[Li(C_4H_8O)_4][ZrCl_2(C_{12}H_8N)_3(C_4H_8O)]$, the environment of the Zr atom is pseudo-octahedral, with the three carbazolyl ligands in a *mer* configuration. The counter-ion of the zirconium complex is composed of an Li atom surrounded by four tetrahydrofuran (THF) molecules. The THF molecule attached to the Zr atom is disordered over two sites, as are two of the THF molecules in the lithium moiety. All bond distances and angles are consistent with those in complexes with similar structural entities. The Zr—N bond distances are 2.2185 (18) and 2.167 (3) Å.

Comment

Tris-amide complexes of transition metals show a wide and varied reactivity, and the synthesis and exploration of this class of compound have been the focus of considerable research in recent years in the inorganic community (Cummins *et al.*, 1988, 1991; Cummins, 1998*a*; Yandulov & Schrock, 2002). These studies have used electronically hard ligands, often for the formation of low-coordinate metal complexes, with a view to small-molecule activation (Cummins, 1998*a*,*b*). The merit of the study of complexes of this type has been demonstrated by the catalytic reduction of N_2 to NH_3 (Yandulov & Schrock, 2002, 2003). Recently, complexes with softer non-innocent ligands have been reported (Nygren *et al.*, 2003, 2004; Tanski & Parkin, 2003).

Structurally characterized carbazolyl complexes of transition metals that are σ-bound are rare (Lopez *et al.*, 2002); most of the known examples (Riley *et al.*, 1998, 1999, 2001) are for groups 4B and 5B. In most previous reports of group 4B metal complexes containing carbazolyl ligands, the metal center is surrounded by other nitrogen-containing ligands, such as dimethylamine (Riley *et al.*, 1999, 2001).

The molecular structure of the zirconium moiety of the title compound, (I), is shown in Fig. 1. Examination of the Cambridge Structural Database (CSD; Allen, 2002; Bruno *et al.*, 2002) revealed that the Zr—N bond lengths [mean Zr—N = 2.202 (3) Å; Table 1] of the carbazolyl ligands in (I) are well within the range of normal Zr—N bond lengths (mean Zr—N = 2.241 Å) reported in the literature. The Zr—Cl bond lengths are also well within the typical range (2.287–2.734 Å) reported for the first coordination sphere of zirconium consisting of two Cl atoms, three N atoms and one O-containing ligand. This search also revealed that the first coordination sphere of zirconium, consisting of three N atoms, one O atom and two Cl atoms, is rare in the structural chemistry of group 4B metals, with only eight examples in the database.



(I)

In the tetrahydrofuran (THF) molecule (Fig. 2) that ligates the zirconium center, atoms C20 and C20*A* are disordered over two sites, with relative occupancies of ~0.4 and ~0.6. Similarly, in the $Li(THF)_4$ moiety, the THF molecule containing atoms C25–C28, and the symmetry-generated THF molecule, are disordered over two sites, hereafter termed the THF and THF′ molecules, where the prime denotes a separate molecule with fractional population. The disorders in the C25 and C28 positions were treated identically, *i.e.* as a group, and the disorders in the C26 and C27 positions were treated in a similar manner. Atoms C25 and C28, and C25′ and C28′, were modeled with opposing populations, leading to occupancies of ~0.6 and ~0.4, respectively, for both atom sets. Atoms C26 and C27 were also modeled as being distributed over two sites, giving the pairs C26/C26′ and C27/C27′. The occupancies in this case are 0.5 for both sites of both atom pairs. The THF molecule composed of atoms O3 and C25–C28 has a bent conformation, the C25—C26—C27—C28 torsion angle being 4 (2)°, whereas for the second component of the disordered model, THF′, the torsion angle is 36 (3)°. These torsion angles are well within the normal range for THF coordinated to a metal center, as shown by a search of the CSD. For this torsion angle, 94.9% of the reported angles lie between +40 and −40° [mean 0.487 (8)°]. Although this solution may not be a perfect disorder model, it is the best fit given the quality of the data.

Recently, we reported the crystal structure of the related potassium salt (tetrahydrofuran)potassium *mer*-tris(carbazolyl)-*trans*-dichloro(tetrahydrofurano)zirconate (Nygren *et al.*, 2003). The *trans*-carbazolyl ligands in (I) deviate from linearity [167.49 (9)°] to a greater extent than those in the

 © 2004 International Union of Crystallography DOI 10.1107/S0108270104000605

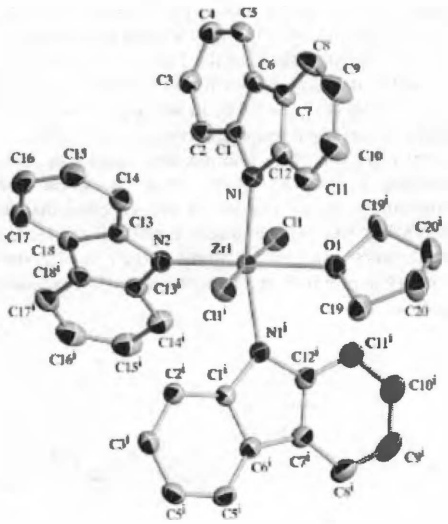


Figure 1
A view of the structure of the anion of (I), showing the atomic numbering scheme. All H atoms have been omitted for clarity, and only one of the disordered positions for each of atoms C20 and C20′ is shown. Displacement ellipsoids are drawn at the 50% probability level for non-H atoms. [Symmetry code: (i) $-x, y, \frac{1}{2}-z$.]

corresponding potassium complex [171.90 (7)°]. However, the Cl—Zr—Cl angle is closer to linearity [176.08 (3)°] in (I) than in the potassium analog [171.38 (2)°]. In (I), there is very little interaction between the tetrakis(tetrahydrofuran)lithium moiety of the structure and the zirconium fragment. The closest contact distance between the carbazolyl ligands and the cation is ~4.44 Å. By contrast, in the potassium complex, the cation is bound to two of the carbazolyl ligands in η^2 and η^6

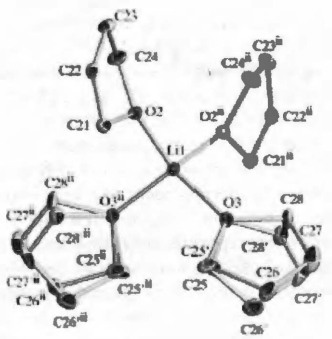


Figure 2
A view of the structure of the anion of (I), showing the atomic numbering scheme. Displacement ellipsoids are shown at the 50% probability level. [Symmetry code: (ii) $1-x, y, \frac{1}{2}-z$.]

fashions. This interaction, however, has very little effect on the structure of the zirconium anion. A slight difference may be seen in the intramolecular angles. The *cis*-carbazolyls that are most affected by the presence of the cation differ in their N—Zr—N angles by 3.03° [96.26 (5) and 93.23 (7)° for lithium and potassium, respectively]. Further comparison of the structures of the anions in the two structures shows that the type of cation has little influence on the overall anion structure. Given the close coordination of the K(THF) ion to the Zr complex, this result is surprising. However, the site between the rings that is occupied by the K atom is occupied by a THF moiety of the $Li(THF)_4$ cation in (I).

Experimental

Treatment of a suspension of $ZrCl_4$ (0.153 g, 0.656 mmol) in THF, chilled to 195 K, with a solution of lithiated carbazole (0.500 g, 2.00 mmol) in THF, previously formed by deprotonation of carbazole with a fourfold molar excess of lithium hydride, resulted in a reaction that, on warming to room temperature, afforded a yellow solution. After filtration and removal of solvent, a yellow powder was recovered. THF was added to a small portion of the yellow powder until a saturated solution resulted and, over a period of a week, large crystals grew from the recrystallization solution. The compound has been characterized by one- and two-dimensional ^1H and ^{13}C NMR spectroscopy at variable temperatures in solution. The spectroscopic data fully support the formation of this compound.

Crystal data

$[Li(C_4H_8O)_4][ZrCl_2(C_{12}H_8N)_3\cdot(C_4H_8O)]$
$M_r = 1028.16$
Monoclinic, $C2/c$
$a = 14.984\ (5)$ Å
$b = 27.435\ (9)$ Å
$c = 13.574\ (4)$ Å
$\beta = 113.220\ (5)°$
$V = 5128\ (3)$ Å^3
$Z = 4$
$D_x = 1.332$ Mg m^{-3}
Mo $K\alpha$ radiation
Cell parameters from 14 112 reflections
$\theta = 2.7–26.1°$
$\mu = 0.37$ mm^{-1}
$T = 173\ (2)$ K
Block, yellow
0.22 × 0.19 × 0.15 mm

Data collection

Bruker SMART CCD diffractometer
φ and ω scans
Absorption correction: multi-scan (*SADABS*; Sheldrick, 1996)
$T_{min} = 0.946$, $T_{max} = 0.946$
24 554 measured reflections
5069 independent reflections
4128 reflections with $I > 2\sigma(I)$
$R_{int} = 0.037$
$\theta_{max} = 26.1°$
$h = -18 \rightarrow 18$
$k = -33 \rightarrow 33$
$l = -16 \rightarrow 16$

Table 1
Selected geometric parameters (Å, °).

Li1—O2	1.939 (4)	O1—Zr1	2.261 (2)
Li1—O3	1.952 (4)	Zr1—N1	2.2185 (18)
N2—Zr1	2.167 (3)	Zr1—Cl1	2.4488 (9)
N2—Zr1—N1^i	96.26 (4)	Cl1—Zr1—Cl1^i	176.07 (3)
N1—Zr1—N1^i	167.49 (9)		
C25—C26—C27—C28	−4 (2)	C25′—C26′—C27′—C28′	−36 (3)

Symmetry code: (i) $-x, y, \frac{1}{2}-z$.

Refinement

Refinement on F^2	$w = 1/[\sigma^2(F_o^2) + (0.038P)^2 + 5.9992P]$
$R[F^2 > 2\sigma(F^2)] = 0.032$	where $P = (F_o^2 + 2F_c^2)/3$
$wR(F^2) = 0.088$	$(\Delta/\sigma)_{max} < 0.001$
$S = 1.07$	$\Delta\rho_{max} = 0.75$ e Å^{-3}
5069 reflections	$\Delta\rho_{min} = -0.47$ e Å^{-3}
357 parameters	
H-atom parameters constrained	

All H atoms were introduced at calculated positions and treated by applying a riding model [U_{iso}(H) = 1.2U_{eq}(C), and C—H = 0.99 (CH_2) and 0.95 Å (aromatic)].

Data collection: *SMART* (Bruker, 1997); cell refinement: *SAINT* (Bruker, 1997); data reduction: *SAINT*; program(s) used to solve structure: *SHELXS97* (Sheldrick, 1997); program(s) used to refine structure: *SHELXL97* (Sheldrick, 1997); molecular graphics: *SHELXTL* (Bruker, 1997); software used to prepare material for publication: *SHELXTL*.

The authors thank the University of Tennessee for supporting this research.

Supplementary data for this paper are available from the IUCr electronic archives (Reference: SQ1141). Services for accessing these data are described at the back of the journal.

References

Allen, F. H. (2002). *Acta Cryst.* B58, 380–388.

Bruker (1997). *SMART* (Version 5.044), *SAINT* (Version 5.01) and *SHELXTL*. Bruker AXS Inc., Madison, Wisconsin, USA.

Bruno, I. J., Cole, J. C., Edgington, P. R., Kessler, M., Macrae, C. F., McCabe, P., Pearson, J. & Taylor, R. (2002). *Acta Cryst.* B58, 389–397.

Cummins, C. C. (1998*a*). *Chem. Commun.* pp. 1777–1786.

Cummins, C. C. (1998*b*). *Prog. Inorg. Chem.* 47, 685–836.

Cummins, C. C., Baxter, S. M. & Wolczanski, P. T. (1988). *J. Am. Chem. Soc.* 110, 8731–8733.

Cummins, C. C., Schaller, C. P., Van Duyne, G. D., Wolczanski, P. T., Chan, A. W. E. & Hoffmann, R. (1991). *J. Am. Chem. Soc.* 113, 2985–2994.

Lopez, C., Bravo, G., Arevalo, A., Munoz-Hernandez, M. A. & Garcia, J. J. (2002). *J. Organomet. Chem.* 664, 170–175.

Nygren, C. L., Bragg, M. E. T. & Turner, J. F. C. (2003). *Acta Cryst.* C59, m275–m276.

Nygren, C. L., Bragg, M. E. T. & Turner, J. F. C. (2004). *Acta Cryst.* C60, m4–m6.

Riley, P. N., Fanwick, P. E. & Rothwell, I. P. (2001). *J. Chem. Soc. Dalton Trans.* pp. 181–186.

Riley, P. N., Parker, J. R., Fanwick, P. E. & Rothwell, I. P. (1999). *Organometallics*, 18, 3579–3583.

Riley, P. N., Profilet, R. D., Salberg, M. M., Fanwick, P. E. & Rothwell, I. P. (1998). *Polyhedron*, 17, 773–779.

Sheldrick, G. M. (1996). *SADABS*. University of Göttingen, Germany.

Sheldrick, G. M. (1997). *SHELXL97* and *SHELXS97*. University of Göttingen, Germany.

Tanski, J. M. & Parkin, G. (2003). *Inorg. Chem.* 42, 264–266.

Yandulov, D. V. & Schrock, R. R. (2002). *J. Am. Chem. Soc.* 124, 6252–6253.

Yandulov, D. V. & Schrock, R. R. (2003). *Science*, 301, 76–78.

Acta Crystallographica Section C
Crystal Structure
Communications
ISSN 0108-2701

A pair of epimeric 13-hydroxy-2,3,6,7-tetramethoxy-8b,11,12,12a,13,13a-hexahydro-9*H*-9a-azacyclopenta[*b*]-triphenylene-10-ones

Cara Nygren, Tianniu Chen, Sanbao Zhong, Conrad Kaczmarek, John F. C. Turner and David C. Baker*

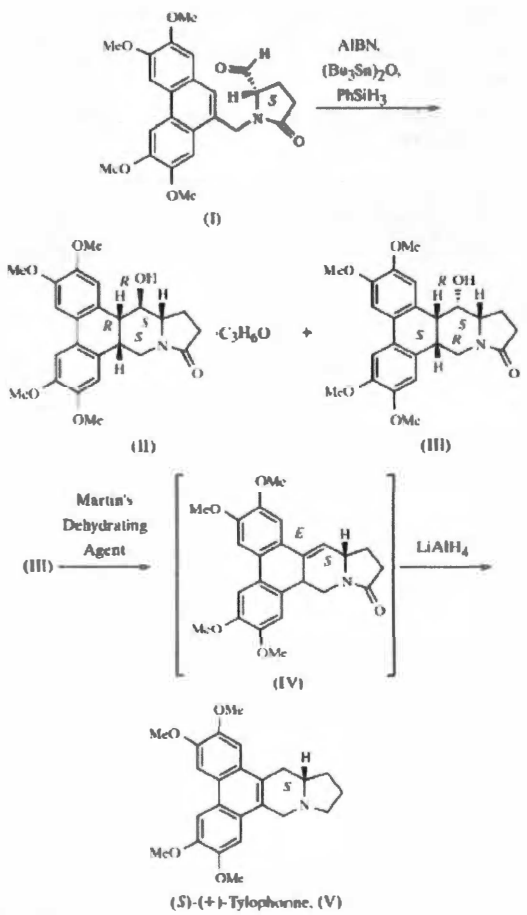
Department of Chemistry, University of Tennessee, Knoxville, TN 37996, USA
Correspondence e-mail: dcbaker@utk.edu

Received 20 October 2003
Accepted 22 January 2004
Online 19 February 2004

The structures of two compounds which are intermediates in the synthesis of phenanthroindolizidine alkaloids have been determined. (8b*S*,13a*S*,14*R*,14a*R*)-8b,9,11,12,13,13a,14,14a-Octahydro-14-hydroxy-2,3,6,7-tetramethoxydibenzo[*f*,*h*]pyrrolo[1,2-*b*]isoquinolin-11-one acetone solvate, $C_{24}H_{27}NO_6 \cdot C_3H_6O$, (II), crystallizes in a chiral space group with one solvent molecule (acetone) present in the asymmetric unit. On the other hand, (8b*S*,13a*S*,14*S*,14a*R*)-8b,9,11,12,13,13a,14,14a-octahydro-14-hydroxy-2,3,6,7-tetramethoxydibenzo[*f*,*h*]pyrrolo[1,2-*b*]isoquinolin-11-one, $C_{24}H_{27}NO_6$, (III), crystallizes in a centrosymmetric space group with two molecules in the asymmetric unit and with no solvent present. The two molecules in the asymmetric unit of (III) are structurally the same. Compounds (II) and (III) are epimers at the C atom carrying the OH group; otherwise they are very similar in structure.

Comment

In a project involving the synthesis and evaluation of a number of phenanthroindolizidine alkaloids (Li *et al.*, 2001) that are of interest as potential cancer chemotherapeutic agents, we have developed a synthetic route (Zhong *et al.*, 2004; see scheme) to this group of alkaloids *via* a pair of epimeric intermediates, *viz.* the title compounds, (II) and (III). Reductive ring closure of optically active (I) using free-radical chemistry (Hays & Fu, 1996, 1999) gives the intermediates (II) and (III) in an approximate 2.3:1 ratio. The key issue in this work was the determination of the relative stereochemistries for (II) and (III), as those epimers did not lend themselves to definitive NMR spectral analyses. Compound (III), with its *trans* H—C—C—OH arrangement that is necessary for the elimination of water, is readily converted to the 14-14a double-bonded intermediate (IV) (not analyzed due to instability). Reduction of the amide function and concomitant rearrangement of the double bond in (IV) produces the natural product tylophorine, (V), which is an antitumor agent (Gao *et al.*, 2004). Optical rotation measurements of bulk samples of (II) and (III) indicate that optical activity is maintained, giving the final product as (*S*)-(+)-tylophorine (Buckley & Rapoport, 1983; Norlander & Njoroge, 1987), with a single chiral center at the 13a position. However, the crystal of (II) was obtained as a racemate (see *Experimental*), indicating that at least a portion of the sample had racemized during ring closure or that the starting material, (I), was partially racemized at the outset. The issue of this apparent partial racemization is presently under study.



The structure of the molecule consists of a semiplanar aromatic system that is torsionally distorted, with an azacyclohexane ring in a chair configuration fused *cis* to atoms C14 and C17 of a dihydrophenanthrene system. The molecular structures of (II) and (III), apart from their epimeric relationship at C19, are very similar.

 © 2004 International Union of Crystallography DOI: 10.1107/S0108270104001659

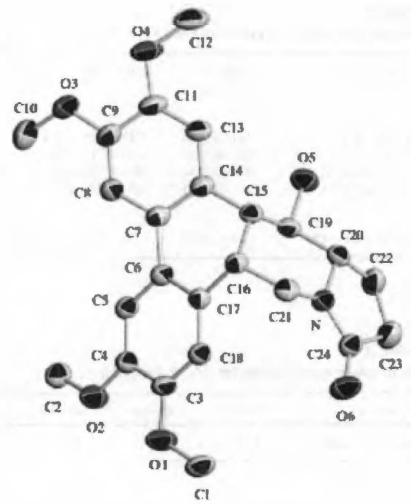


Figure 1
A view of the structure of (II), showing the atomic numbering scheme. Displacement ellipsoids are drawn at the 50% probability level. H atoms and the acetone solvent molecule have been omitted for clarity.

One major structural difference between (II) and (III) is the torsion angle between the aromatic rings, defined as the angle between the C5—C6 and C7—C8 bonds. For (II), this angle is 20.0 (3)°, whereas in (III), the corresponding value is found to be 11.0 (3)°. The torsion angles between the C14—C15 and C16—C17 bonds are 53.2 (2) and 48.18 (19)° for (II) and (III), respectively. Taken together, these values are in accord with the statistically observed relationship between these two parameters in these types of systems (Allen, 2002; Bruno *et al.*, 2002). Given the difference in unit-cell contents and the inclusion of acetone in the structure of (II), no straightforward comparison of the torsion angles may be made, although the values are not atypical for the dihydrophenanthrene ring system. We note that, in the presence of acetone in the lattice of (II), the number of intermolecular contacts is lower, and we speculate that this leads to the higher torsion value.

While the presence of a solvent of crystallization in (II) disturbs the intermolecular contacts, a direct comparison may be made between the interbond angles and lengths of the two structures. Inspection of the structures of (II) and (III) shows that all bond lengths and angles in the two structures are well within the normal reported ranges and are similar in both structures.

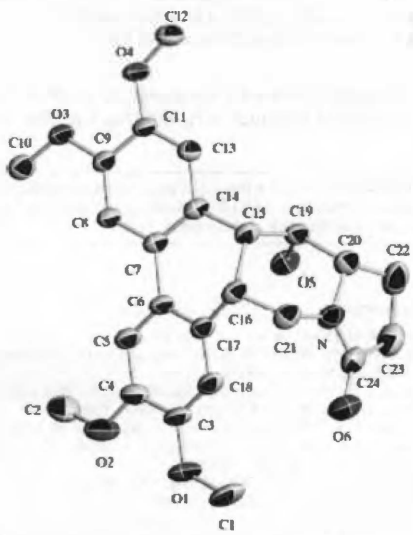


Figure 2
A view of the structure of (III), illustrating one of the two crystallographically independent molecules and showing the atomic numbering scheme. Displacement ellipsoids are drawn at the 50% probability level and H atoms have been omitted for clarity.

Experimental

To a solution of (I) (2.12 g, 5.00 mmol) in dry benzene (15 ml) in a 100 ml Schlenk tube were added bis(tributyltin) oxide [$(Bu_3Sn)_2O$, 0.38 ml, 0.75 mmol], $PhSiH_3$ (0.31 ml, 2.50 mmol), EtOH (0.585 ml, 2.00 mmol) and 2,2′-azobis(isobutyro)nitrile (90 mg, 0.548 mmol; AIBN) in benzene (2.0 ml). The vessel was sealed, shaken and placed in an oil bath at 353–358 K. After 12 h, thin-layer chromatographic analysis indicated that all of the starting material had been consumed. The mixture was allowed to cool to room temperature and tetrabutylammonium fluoride (30.0 ml of a 1.0 *M* solution in tetrahydrofuran, 30.0 mmol) was added with stirring for 2 h, at the end of which time 2 *M* HCl (15 ml) was added. The reaction mixture was extracted with CH_2Cl_2 (3 × 50 ml), and the combined organic extracts were dried ($MgSO_4$), filtered and concentrated. The residue was purified by flash chromatography (eluting with 3:1:0.01 CH_2Cl_2–EtOAc–MeOH) to give 827 mg (69%) of compound (II) in the non-solvated form. Analysis: $[\alpha]_D^{22}$ 78.3° (*c* 0.48, $CHCl_3$); HREIMS, calculated for $C_{24}H_{27}NO_6$: 425.1838; found: *m/z* 425.1842. Compound (III) was obtained as 30% of the final product. Analysis: $[\alpha]_D^{22}$ −84.5° (*c* 1.0, $CHCl_3$); HREIMS, calculated for $C_{24}H_{27}NO_6$: 425.1838; found: *m/z* 425.1842. Single crystals of (II) as the acetone solvate and of (III) were obtained from 2:1 acetone–methanol solutions after partial evaporation. The crystal of (II) was shown to be a racemic mixture, a fact which indicates that either the ring closure of (I) to (II) is accompanied by racemization, or that the starting material, (I), was partially racemized.

Compound (II)

Crystal data

$C_{24}H_{27}NO_6 \cdot C_3H_6O$
M_r = 483.54
Monoclinic, $P2_1/c$
a = 11.5790 (10) Å
b = 17.4011 (15) Å
c = 13.0453 (11) Å
β = 110.488 (2)°
V = 2462.2 (4) Å^3
Z = 4
D_x = 1.304 Mg m^{-3}
Mo $K\alpha$ radiation
Cell parameters from 3948 reflections
θ = 2.2–22.1°
μ = 0.09 mm^{-1}
T = 295 (2) K
Block, colorless
0.50 × 0.20 × 0.15 mm

Data collection

Bruker SMART 1000 CCD area-detector diffractometer
φ and ω scans
Absorption correction: multi-scan (*SADABS*; Sheldrick, 1996)
T_{min} = 0.881, T_{max} = 0.986
24 264 measured reflections

5059 independent reflections
2927 reflections with $I > 2\sigma(I)$
R_{int} = 0.053
θ_{max} = 26.4°
$h = -14 \rightarrow 14$
$k = -21 \rightarrow 21$
$l = -16 \rightarrow 16$

Refinement

Refinement on F^2
$R[F^2 > 2\sigma(F^2)]$ = 0.046
$wR(F^2)$ = 0.127
S = 1.01
5059 reflections
323 parameters
H-atom parameters constrained

$w = 1/[\sigma^2(F_o^2) + (0.0429P)^2 + 0.9647P]$ where $P = (F_o^2 + 2F_c^2)/3$
$(\Delta/\sigma)_{max} < 0.001$
$\Delta\rho_{max}$ = 0.18 e Å^{-3}
$\Delta\rho_{min}$ = −0.19 e Å^{-3}

Table 1
Selected geometric parameters (Å, °) for (II).

C15—C19	1.534 (3)	C19—C20	1.517(3)
C19—O5	1.421 (2)		
C5—C6—C7	121.80 (18)	C17—C16—C15	110.27 (16)
C8—C7—C6	122.32 (19)	C18—C17—C16	121.90 (18)
C14—C15—C16	110.11 (17)	O5—C19—C20	109.32 (16)
C21—C16—C17	115.18(16)	O5—C19—C15	108.68 (16)
C5—C6—C7—C8	20.0 (3)	C14—C15—C16—C17	53.2 (2)

Table 2
Hydrogen-bonding geometry (Å, °) for (II).

D—H···A	D—H	H···A	D···A	D—H···A
O5—H5···O8^{i}	0.82	1.92	2.737 (2)	174

Symmetry code: (i) $x, \frac{1}{2}-y, \frac{1}{2}+z$.

Compound (III)

Crystal data

$C_{28}H_{27}NO_4$
M_r = 425.47
Orthorhombic, $P2_12_12_1$
a = 13.0534 (16) Å
b = 14.9664 (18) Å
c = 21.356 (3) Å
V = 4172.1 (9) Å^3
Z = 8
D_x = 1.355 Mg m^{-3}

Mo $K\alpha$ radiation
Cell parameters from 8864 reflections
θ = 2.3–25.0°
μ = 0.10 mm^{-1}
T = 293 (2) K
Fragment, colorless
0.50 × 0.42 × 0.40 mm

Data collection

Bruker SMART 1000 CCD area-detector diffractometer
φ and ω scans
Absorption correction: multi-scan (*SADABS*; Sheldrick, 1996)
T_{min} = 0.953, T_{max} = 0.962
45 934 measured reflections

5663 independent reflections
4458 reflections with $I > 2\sigma(I)$
R_{int} = 0.035
θ_{max} = 28.3°
$h = -17 \rightarrow 17$
$k = -19 \rightarrow 19$
$l = -27 \rightarrow 28$

Refinement

Refinement on F^2
$R[F^2 > 2\sigma(F^2)]$ = 0.033
$wR(F^2)$ = 0.086
S = 0.98
5663 reflections
567 parameters

H-atom parameters constrained
$w = 1/[\sigma^2(F_o^2) + (0.0549P)^2]$ where $P = (F_o^2 + 2F_c^2)/3$
$(\Delta/\sigma)_{max} < 0.001$
$\Delta\rho_{max}$ = 0.19 e Å^{-3}
$\Delta\rho_{min}$ = −0.18 e Å^{-3}

Table 3
Selected geometric parameters (Å, °) for (III).

C15—C19	1.544 (3)	C19—C20	1.526 (3)
C19—O5	1.417 (2)		
C5—C6—C7	121.28 (16)	C17—C16—C15	112.09 (15)
C8—C7—C6	121.10 (16)	C18—C17—C6	118.88 (18)
C14—C15—C16	110.63(15)	O5—C19—C20	108.21 (15)
C17—C16—C21	115.78 (15)	O5—C19—C15	112.80 (15)
C5—C6—C7—C8	11.0 (3)	C14—C15—C16—C17	48.18(19)

Table 4
Hydrogen-bonding geometry (Å, °) for (III).

D—H···A	D—H	H···A	D···A	D—H···A
O5—H5A···O12	0.82	2.00	2.818 (2)	179

Most H atoms were introduced at calculated positions and refined by applying a riding model [C—H = 0.93–0.98 Å and U_{iso}(H) = 1.2U_{eq}(C); O—H = 0.82 Å and U_{iso}(H) = 1.5U_{eq}(O)]. The hydroxyl H atoms in (III) were located in difference Fourier maps and were refined with constraints on their positions and U_{iso} values. Friedel equivalents were merged before the final refinement.

For both compounds, data collection: *SMART* (Bruker, 1997); cell refinement: *SAINT* (Bruker, 1997); data reduction: *SAINT*; program(s) used to solve structure: *SHELXS97* (Sheldrick, 1997); program(s) used to refine structure: *SHELXL97* (Sheldrick, 1997); molecular graphics: *SHELXTL* (Sheldrick, 1997); software used to prepare material for publication: *SHELXTL*.

Support for this work was provided, in part, by a grant from the National Institutes of Health (No. CA-87863).

Supplementary data for this paper are available from the IUCr electronic archives (Reference: FR1452). Services for accessing these data are described at the back of the journal.

References

Allen, F. H. (2002). *Acta Cryst.* B58, 380–388.
Bruker (1997). *SMART* (Version 5.044) and *SAINT* (Version 5.01). Bruker AXS Inc., Madison, Wisconsin, USA.
Bruno, I. J., Cole, J. C., Edgington, P. R., Kessler, M., Macrae, C. F., McCabe, P., Pearson, J. & Taylor, R. (2002). *Acta Cryst.* B58, 389–397.
Buckley, T. F. & Rapoport, H. (1983). *J. Org. Chem.* 48, 4222–4232.
Gao, W., Lam, W., Zhong, S., Kaczmarek, C., Baker, D. C. & Cheng, Y.-C. (2004). *Cancer Res.* 64, 678–688.
Hays, D. S. & Fu, G. C. (1996). *J. Org. Chem.* 61, 4–5.
Hays, D. S. & Fu, G. C. (1999). *Tetrahedron*, 55, 8815–8832.
Li, Z., Jin, Z. J. & Huang, R. (2001). *Synthesis*, pp. 2365–2378.
Norlander, J. E. & Njoroge, F. G. (1987). *J. Org. Chem.* 52, 1627–1630.
Sheldrick, G. M. (1996). *SADABS*. University of Göttingen, Germany.
Sheldrick, G. M. (1997). *SHELXS97*, *SHELXL97* and *SHELXTL*. University of Göttingen, Germany.
Zhong, S., Kaczmarek, C., Welsh, K., Cheng, Y.-C. & Baker, D. C. (2004). In preparation.

Acta Crystallographica Section C
Crystal Structure
Communications
ISSN 0108-2701

trans-Dichloro-*cis*-bis(3,6-dimethylcarbazolyl)-*cis*-bis(tetrahydrofuran)zirconium(IV) benzene sesquisolvate

Cara L. Nygren,[a] M. E. T. Bragg[a] and John F. C. Turner[b]*

[a]Department of Chemistry, 406 Buehler Hall, University of Tennessee, Knoxville, TN 37996, USA, and [b]Neutron Sciences Consortium and Department of Chemistry, 409 Buehler Hall, University of Tennessee, Knoxville, TN 37996, USA
Correspondence e-mail: jturner@atom.chem.utk.edu

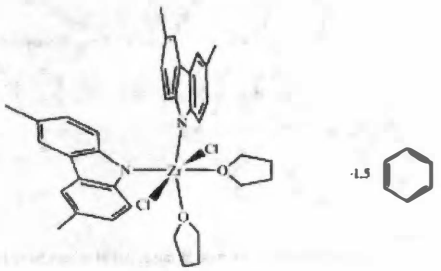
Received 10 November 2003
Accepted 13 November 2003
Online 6 December 2003

In the title compound, $[ZrCl_2(C_{14}H_{12}N)_2(C_4H_8O)_2]\cdot 1.5C_6H_6$, the Zr atom is pseudo-octahedral, with two Cl atoms in *trans* positions and two tetrahydrofuran molecules in *cis* positions. The two 3,6-dimethylcarbazolyl ligands are in *cis* positions and are canted with respect to one another. The two Zr—N distances are 2.1148 (18) and 2.1236 (18) Å, and the N—Zr—N angle is 95.08 (7)°. The title compound crystallizes as the benzene solvate, with one of the benzene molecules positioned on an inversion center.

Comment

Amide complexes of transition metals are known to display reactivity that is often unusual. This fact has been highlighted recently by the reduction of N_2 to NH_3 using a trisamide complex of Mo (Yandulov & Schrock, 2002, 2003). One of the major goals of inorganic chemistry has been attained with the application of the electronic properties of hard amide ligands, an area that has been reviewed recently (Cummins, 1998; Schrock, 1997*a*,*b*). In contrast, recent work by ourselves (Nygren *et al.*, 2003, 2004) and others (Riley *et al.*, 1998, 1999, 2001; Tanski & Parkin, 2003) has been based on the exploration of the chemistry of amide ligands in which the π interaction is uncertain with respect to the donation to the metal center. These amides with a lower π basicity (Tanski & Parkin, 2003) form a class of non-innocent ligands in coordination chemistry that differ from the non-innocent ligands described by Gray *et al.* (1967), in that the oxidation state is not uncertain, only the degree of electronic coupling between the π-donating ligating atom and the metal center. Although formally an *LX* ligand (Green, 1995), the carbazolyl ligand is related to the N-heterocyclic carbenes (Arduengo, 1999; Herrmann, 2002; Tulloch *et al.*, 2003), which are known to be almost pure σ donors, although in the case of carbazolyl there is some π basicity. In this structure report, we describe a neutral biscarbazolyl zirconium dichloride, *viz.* the title compound, (I), that will serve as a useful synthetic entrance into this area.

Carbazolyl complexes of transition metals that are σ-bound are rare (Lopez *et al.*, 2002); most of the known examples (Riley *et al.*, 1998, 1999, 2001) involve group 4B and 5B metals. A few biscarbazolyl structures are known for the group 4B metals (mostly containing titanium; Riley *et al.*, 2001). There are also a few known complexes for the group 5B metals (Riley *et al.*, 1999).



(I)

Recently, the crystal structures of (tetrahydrofuran)potassium *mer-trans*-tris(carbazolyl)dichloro(tetrahydrofuran)zirconate and tetrakis(tetrahydrofuran)lithium *mer-trans*-tris(carbazolyl)dichloro(tetrahydrofuran)zirconate have been reported (Nygren *et al.*, 2003, 2004).

The molecular structure of (I) (Fig. 1) consists of a pseudo-octahedral zirconium center bearing *trans* chloro ligands, *cis* carbazolyl moieties and *cis*-coordinated tetrahydrofuran (THF) molecules. Examination of the Cambridge Structural Database (Allen, 2002; Bruno *et al.*, 2002) reveals that this composition of the first coordination sphere, consisting of two

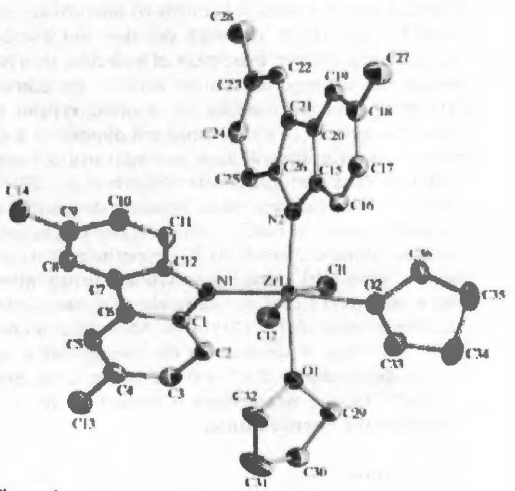


Figure 1
A view of the structure of (I), showing the atomic numbering scheme. All H atoms and solvent molecules have been omitted for clarity. Displacement ellipsoids are drawn at the 50% probability level.

 © 2004 International Union of Crystallography DOI: 10.1107/S0108270103026258

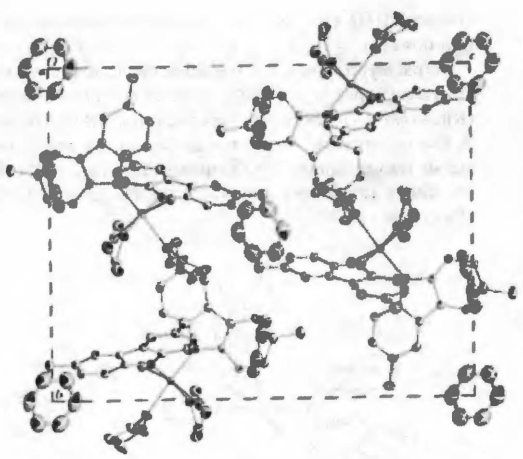


Figure 2
The crystal packing of (I), viewed along *a*. All H atoms have been omitted for clarity.

N atoms, two O atoms and two chloro ligands, is quite common for group 4B metals, and all bond lengths and angles in (I) (Table 1) are typical of those observed in zirconium complexes.

Examination of the intermolecular correlations reveals several interactions that are shorter than the sum of the van der Waals radii. Interestingly, the benzene molecules located at the cell corners do not participate in any of these short contacts, whereas the internal benzene molecules bridge the carbazolyl group of one molecule and the THF group coordinated to the Zr atom of another, *via* atoms H10, C38 and H35*A* (Fig. 2). Another long-range interaction pairs two molecules together through mutually *cis* interactions between atoms C12 and H27*B*. Although this does not constitute a strongly bonded dimer, these pairs of molecules then interact through shorter-range interactions between the coordinated THF group and the mutually *cis* aromatic systems of the carbazolyl moieties. A similar structural disposition is seen in tetrakis(tetrahydrofuran)lithium *mer-trans*-tris(carbazolyl)dichloro(tetrahydrofuran)zirconate (Nygren *et al.*, 2004). The final set of interactions occur between the methyl group (containing atom C14) and the aromatic ring of a neighboring molecule (atoms C21 and C26). The opposite methyl group on the same carbazolyl ligand is involved in a strong interaction with a carbazolyl ligand on a different zirconium center of a neighboring molecule [2.7420 (14) Å; Allen, 2002; Bruno *et al.*, 2002]. The range of distances for the intermolecular interactions is approximately 2.372–3.811 Å (Allen, 2002; Bruno *et al.*, 2002). Thus, a zigzag chain is formed in the *bc* plane throughout the extended lattice.

Experimental

Dropwise addition of dry THF to a mixture of $ZrCl_4$(s) (0.43 g, 0.0018 mol) and previously prepared carbazolyltetrahydrofuranlithium(s) (1.01 g, 0.0037 mol) at 195 K resulted in a slow reaction that, on warming to room temperature, afforded a yellow solution. After filtration, THF was evacuated and the product was washed with pentane. Benzene was added to the resulting compound, and large orange rectangular crystals formed spontaneously at room temperature over a period of one week. This compound was characterized by one- and two-dimensional ^{1}H and ^{13}C NMR spectroscopy at variable temperature in solution, and the spectroscopic data fully support formation of the title compound.

Crystal data

$[ZrCl_2(C_{16}H_{12}N)_2(C_4H_8O)_2]\cdot 1.5C_6H_6$
M_r = 811.98
Monoclinic, $P2_1/c$
a = 10.200 (3) Å
b = 17.594 (5) Å
c = 22.760 (7) Å
β = 100.200 (5)°
V = 4020 (2) Å^3
Z = 4
D_x = 1.342 Mg m^{-3}
Mo $K\alpha$ radiation
Cell parameters from 21 512 reflections
θ = 2.3–26.5°
μ = 0.45 mm^{-1}
T = 173 (2) K
Block, orange
0.30 × 0.18 × 0.17 mm

Data collection

Bruker SMART CCD diffractometer
φ and ω scans
Absorption correction: multi-scan (*SADABS*; Sheldrick, 1996)
T_{min} = 0.891, T_{max} = 0.927
39 916 measured reflections
8342 independent reflections
6645 reflections with $I > 2\sigma(I)$
R_{int} = 0.041
θ_{max} = 26.5°
$h = -12 \rightarrow 12$
$k = -22 \rightarrow 22$
$l = -28 \rightarrow 28$

Refinement

Refinement on F^2
$R[F^2 > 2\sigma(F^2)]$ = 0.032
$wR(F^2)$ = 0.085
S = 1.08
8342 reflections
473 parameters
H-atom parameters constrained
$w = 1/[\sigma^2(F_o^2) + (0.0347P)^2 + 2.6992P]$ where $P = (F_o^2 + 2F_c^2)/3$
$(\Delta/\sigma)_{max}$ = 0.041
$\Delta\rho_{max}$ = 0.44 e Å^{-3}
$\Delta\rho_{min}$ = −0.31 e Å^{-3}

Table 1
Selected geometric parameters (Å, °).

Cl1—Zr1	2.4473 (7)	N2—Zr1	2.1236 (18)
Cl2—Zr1	2.4413 (7)	O1—Zr1	2.2624 (15)
N1—Zr1	2.1148 (18)	O2—Zr1	2.2659 (15)
N1—Zr1—N2	95.08 (7)	Cl2—Zr1—Cl1	165.44 (2)
O1—Zr1—O2	82.83 (6)		

All H atoms were introduced at calculated positions and treated using a riding model [U_{iso}(H) = 1.2U_{eq}(C), and C—H = 0.98 (CH_3), 0.99 (CH_2) and 0.95 Å (aromatic)].

Data collection: *SMART* (Bruker, 1997); cell refinement: *SAINT* (Bruker, 1997); data reduction: *SAINT*; program(s) used to solve structure: *SHELXS97* (Sheldrick, 1997); program(s) used to refine structure: *SHELXL97* (Sheldrick, 1997); molecular graphics: *SHELXTL* (Sheldrick, 1997); software used to prepare material for publication: *SHELXTL*.

The authors thank the University of Tennessee for supporting this research.

Supplementary data for this paper are available from the IUCr electronic archives (Reference: FR1455). Services for accessing these data are described at the back of the journal.

References

Allen, F. H. (2002). *Acta Cryst.* B58, 407–422.
Arduengo, A. J. III (1999). *Acc. Chem. Res.* 32, 913–921.
Bruker (1997). *SMART* (Version 5.044) and *SAINT* (Version 5.01). Bruker AXS Inc., Madison, Wisconsin, USA.
Bruno, I. J., Cole, J. C., Edgington, P. R., Kessler, M., Macrae, C. F., McCabe, P., Pearson, J. & Taylor, R. (2002). *Acta Cryst.* B58, 389–397.
Cummins, C. C. (1998). *Prog. Inorg. Chem.* 47, 685–836.
Gray, H. B., Eisenberg, R. & Stiefel, E. I. (1967). *Adv. Chem. Ser.* 62, 641–650.
Green, M. L. H. (1995). *J. Organomet. Chem.* 500, 127–148.
Herrmann, W. A. (2002). *Angew. Chem. Int. Ed.* 41, 1363–1365.
Lopez, C., Baron, G., Arevalo, A., Munoz-Hernandez, M. A. & Garcia, J. J. (2002). *J. Organomet. Chem.* 664, 170–175.
Nygren, C. L., Bragg, M. E. T. & Turner, J. F. C. (2003). *Acta Cryst.* C59, m275–m276.
Nygren, C. L., Bragg, M. E. T. & Turner, J. F. C. (2004). *Acta Cryst.* Submitted.
Riley, P. N., Fanwick, P. E. & Rothwell, I. P. (2001). *J. Chem. Soc. Dalton Trans.* pp. 181–186.
Riley, P. N., Parker, J. R., Fanwick, P. E. & Rothwell, I. P. (1999). *Organometallics*, 18, 3579–3583.
Riley, P. N., Profilet, R. D., Salberg, M. M., Fanwick, P. E. & Rothwell, I. P. (1998). *Polyhedron*, 17, 773–779.
Schrock, R. R. (1997*a*). *Acc. Chem. Res.* 30, 9–16.
Schrock, R. R. (1997*b*). *Pure Appl. Chem.* 69, 2197–2203.
Sheldrick, G. M. (1996). *SADABS*. University of Göttingen, Germany.
Sheldrick, G. M. (1997). *SHELXL97*, *SHELXS97* and *SHELXTL*. University of Göttingen, Germany.
Tanski, J. M. & Parkin, G. (2003). *Inorg. Chem.* 42, 264–266.
Tulloch, A. A. D., Winston, S., Danopoulos, A. A., Eastham, G. & Hursthouse, M. B. (2003). *J. Chem. Soc. Dalton Trans.* 4, 699–708.
Yandulov, D. V. & Schrock, R. R. (2002). *J. Am. Chem. Soc.* 124, 6252–6253.
Yandulov, D. V. & Schrock, R. R. (2003). *Science*, 301, 76–78.

ACADEMIC PRESS

Available online at www.sciencedirect.com
SCIENCE DIRECT®

Journal of Solid State Chemistry 176 (2003) 175–179

JOURNAL OF SOLID STATE CHEMISTRY

http://elsevier.com/locate/jssc

A novel germanate, $Cu_2Fe_2Ge_4O_{13}$, with a four tetrahedra oligomer

Takatsugu Masuda,[a] Bryan C. Chakoumakos,[a,*] Cara L. Nygren,[b] Suguru Imai,[c] and Kunimitsu Uchinokura[c]

[a] *Condensed Matter Sciences Division, Oak Ridge National Laboratory, P.O. Box 2008, Building 7962, Oak Ridge, TN 37831-6393, USA*
[b] *Department of Chemistry, University of Tennessee, Knoxville, TN 37996-1600, USA*
[c] *Department of Advanced Materials Science, The University of Tokyo, 7-3-1 Hongo, Bunkyo-ku, Tokyo 113-8656, Japan*

Received 15 April 2003; received in revised form 10 June 2003; accepted 14 July 2003

Abstract

The structure of $Cu_2Fe_2Ge_4O_{13}$, previously thought to be $CuFeGe_2O_6$, has been determined from single-crystal X-ray diffraction data to be monoclinic, $P2_1/m$, $a = 12.1050(6)$, $b = 8.5073(4)$, $c = 4.8736(2)$ Å, $\beta = 96.145(1)°$, $Z = 2$, with $R1 = 0.0231$ and $wR2 = 0.0605$. The unique structure has an oligomer of four germanate tetrahedra, cross-linked laterally by square-planar copper ions, joined end-to-end by a zigzag chain of edge-sharing iron oxide octahedra. Running along the a-direction the metal oxide chain consists of alternating Cu–Cu and Fe–Fe dimers. A hypothetical series of homologous structures ($Cu_{n-2}Fe_2Ge_nO_{2n+1}$ with $n = 3,4, \ldots, \infty$) with different length germanate oligomers is proposed, where as n increases, the infinite chain of the $CuGeO_3$ is approached. In this context, $Cu_2Fe_2Ge_4O_{13}$ is viewed as being built from blocks of $CuGeO_3$ and the Fe oxide chains. This material has significance to the study of low-dimensional mixed-spin systems.
© 2003 Elsevier Inc. All rights reserved.

Keywords: Germanate; $Cu_2Fe_2Ge_4O_{13}$; Crystal structure; Mixed-spin system; $CuGeO_3$; Low-dimensional magnet

1. Introduction

Quantum spin systems have been studied extensively in condensed matter physics, which has resulted in a good understanding of simple model systems. One of the new challenges in this area is greater complexity, such as that offered by mixed-spin systems. The mixed spins chain with period 4, such that the spins are arrayed as $s_a - s_a - s_b - s_b$ in the unit cell, has been a focus of theoretical interest [1–4] and rich phase diagrams of the ground states have been presented. A model material of this system; however, has not been reported.

Many low-dimensional spin materials are reported in germanates, where a tetrahedral germanate chain separates the transition metal spin chain, such as the spin Peierls materials $CuGeO_3$ [5,6]. Therefore, a trial germanate which contains two different $3d$ transition metals would seem to be a good strategy to discover a mixed-spins chain material.

Previously, $Cu_2Fe_2Ge_4O_{13}$ was thought to be $CuFeGe_2O_6$, but the crystal structure had not been determined. It is the only known ternary phase in the CuO–GeO_2–$(1/2)Fe_2O_3$ system. Here we report the crystal structure, describe its relationship to $CuGeO_3$, and discuss its possibility as a low-dimensional mixed-spin system.

2. Experimental

A rod-shaped polycrystalline sample of the title compound was synthesized by solid state reaction methods. The mixture of starting materials, CuO, Fe_2O_3 and GeO_2, was heated at 1000°C in air for 50 h. This compound melts congruently and a large single crystal was easily grown from the polycrystalline starting material by the floating zone method using an infrared image furnace. The size of the crystal grown was about 3 mm in diameter by 3 cm in length. A small slice of one end of the boule was cut off, and broken to obtain a small crystal suitable for X-ray diffraction measurements. The cleavage fragment selected exhibited uniform optical properties and is pleochroic, green to darker green. The one good cleavage plane was later

*Corresponding author. Fax: +1-865-574-6268.
E-mail address: kou@ornl.gov (B.C. Chakoumakos).

0022-4596/$ - see front matter © 2003 Elsevier Inc. All rights reserved.
doi:10.1016/S0022-4596(03)00387-6

determined to be {110}. Single-crystal X-ray diffraction data were collected at room temperature using a Bruker AXS SMART 1000 diffractometer equipped with a CCD area detector and a graphite monochromatized Mo source ($K\alpha$, 0.71073 Å). The crystal-to-detector distance was 5 cm. More than a hemisphere of data were collected over the angular range $3° \leqslant 2\Theta \leqslant 56.7°$. Frame widths of 0.2° were used for the data collection, counting 20 s per frame. The three dimensional data were integrated and corrected for Lorentz, polarization, and background effects using the Bruker program SAINT. Unit cell dimensions were refined on the basis of 4678 reflections by least-squares methods. An empirical absorption correction was made using SADABS [7]. Systematic absences were consistent with the space group $P2_1/m$. A total of 5151 reflections was collected, and merging of equivalent reflections gave 1283 unique reflections ($R_{int} = 3.3\%$), with 1233 classed as observed ($|F_o| \geqslant 4\sigma_F$). The structure was solved by direct methods using SIR97 [8]. Crystal structure refinement was made using SHELX [9] packaged in the WinGX suite [10]. Data collection parameters and refinement results are given in Table 1. Scattering factors for neutral atoms, together with anomalous dispersion corrections, were taken from *International Tables for Crystallography* [11]. Refinement with anisotropic atomic displacement parameters was made, but only the refinement with equivalent isotropic displacement parameters is reported. Polyhedral drawings projected on the principal planes are displayed in Fig. 1a and the probability ellipsoids for the root-mean-square atomic displacements are show in Fig. 1b along with the atomic numbering scheme. The atomic positions and isotropic displacement parameters are given in Table 2 and selected bond lengths and angles particularly relevant to the mixed-spin system geometry are given in Table 3. The anisotropic displacement parameters are archived with the crystallographic information file.

Table 1
Data collection parameters and refinement results for $Cu_2Fe_2Ge_4O_{13}$

a (Å)	12.1050(6)
b (Å)	8.5073(4)
c (Å)	4.8736(2)
β (deg)	96.145(1)
V (Å^3)	499.00(4)
Space group	$P2_1/m$
Z	2
Formula	$Cu_2Fe_2Ge_4O_{13}$
Formula weight (g)	737.14
Crystal dimensions (mm)	0.10 × 0.10 × 0.02
μ (mm^{-1})	18.95
Color	green
Cleavage	{110} good
Density calc. (g/cm^3)	4.906
F (000)	684
Number of variables	110
Extinction coefficient	0.062(1)
Measured reflections	5151
Unique reflections	1283
Unique reflections $I > 4\sigma_F$	1233
Goof = S	1.14
R_{int}	0.033
$R1_{obs}$	0.0231
$wR2$	0.0605
Weight	$1/[\sigma^2(F_o^2) + (0.0357P)^2 + 0.1616P]$ $P = (F_o^2 + 2F_c^2)/3$
Max., min., $\Delta\rho$ e Å^{-3}	−1.22, 1.23

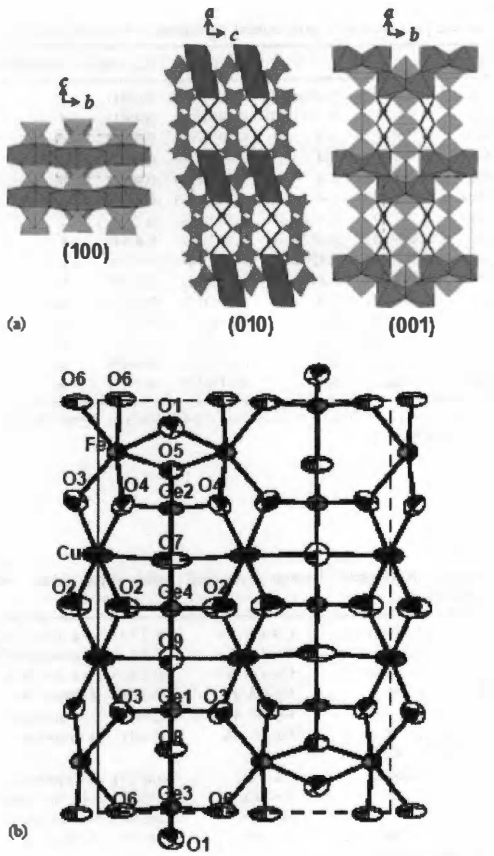


Fig. 1. (a) Crystal structure projections of $Cu_2Fe_2Ge_4O_{13}$, with the iron oxide octahedra darkly shaded and the germanate tetrahedra lightly shaded. The square-planar Cu oxide units are shown as ball-and-stick. The unit cell is outlined by a dashed box for each projection. (b) Probability (99%) density ellipsoids showing the root-mean-square displacements of the atoms in a (001) projection of the unit cell outlined by the dashed line.

Table 2
Atomic positional and displacement parameters for $Cu_2Fe_2Ge_4O_{13}$

Atom	x	y	z	U_{eq} (nm^2)	Symmetry
Cu	0.62557(2)	0.49662(3)	0.54329(6)	1.00(1)	1
Fe	0.87587(2)	0.56133(4)	0.54825(6)	0.49(1)	1
Ge1	0.73996(3)	3/4	0.99333(7)	0.48(1)	*m*
Ge2	0.90508(3)	1/4	0.09433(8)	0.60(1)	*m*
Ge3	0.75264(3)	1/4	0.16240(8)	0.49(1)	*m*
Ge4	0.98773(3)	1/4	0.89357(7)	0.45(1)	*m*
O1	0.7477(1)	0.5840(2)	0.7848(4)	0.79(4)	1
O2	0.4969(1)	0.5828(3)	0.7025(4)	1.43(4)	1
O3	0.7578(1)	0.4201(2)	0.3655(4)	0.82(4)	1
O4	0.9963(1)	0.4253(2)	0.7081(4)	0.71(4)	1
O5	0.8315(1)	3/4	0.2951(5)	0.66(5)	*m*
O6	0.3869(1)	1/4	0.8547(5)	0.83(5)	*m*
O7	0.8465(2)	1/4	0.9275(6)	1.37(6)	*m*
O8	0.6274(1)	1/4	0.9338(5)	0.90(6)	*m*
O9	0.0642(2)	1/4	0.2198(5)	0.75(5)	*m*

$P2_1/m$, $a=12.1050(6)$, $b=8.5073(4)$, $c=4.8736(2)$ Å, $\beta=96.145(1)°$, $V=499.00(4)$ Å^3.

Table 3
Selected interatomic distances (Å) and bond angles (deg) for $Cu_2Fe_2Ge_4O_{13}$

Ge1–O1	1.748(1) × 2	Cu–O1–Fe	101.39(8)	(~*a* direction)
Ge1–O5	1.745(2)	Cu–O2–Cu × 2	102.38(9)	(~*a* direction)
Ge1–O6	1.776(2)	Cu–O3–Fe	100.23(8)	(~*a* direction)
Mean	1.754	Fe–O4–Fe	107.29(8)	(*b* direction)
		Fe–O5–Fe × 2	102.3(1)	(~*a* direction)
Ge2–O2	1.735(2) × 2	Fe–O9–Fe	103.0(1)	(*b* direction)
Ge2–O6	1.747(2)			
Ge2–O8	1.748(2)	Cu···Cu	3.0247(3)	(*a* direction)
Mean	1.741	Fe···Cu	3.0770(3)	(~*a* direction)
		Fe···Fe	3.2625(4)	(~*a* direction)
Ge3–O3	1.750(1) × 2	Fe···Fe	3.2101(6)	(*b* direction)
Ge3–O7	1.697(3)			
Ge3–O8	1.782(2)			
Mean	1.744			
Ge4–O4	1.753(1) × 2			
Ge4–O7	1.735(2)			
Ge4–O9	1.751(2)			
Mean	1.748			
Fe–O1	2.038(1)			
Fe–O3	2.001(1)			
Fe–O4	1.956(1)			
Fe–O4	2.092(1)			
Fe–O5	2.060(1)			
Fe–O9	2.050(1)			
Mean	2.032			
Cu–O1	1.937(1)			
Cu–O2	1.926(1)			
Cu–O2	1.955(1)			
Cu–O3	2.008(1)			
Cu–O6	2.892(1)			
Cu–O8	2.831(1)			
Mean	1.964 (CN 4)			
Mean	2.258 (CN 4+2)			

3. Results

Based on the chemical formula, $CuFeGe_2O_6$, and lattice parameters ($a=12.08$, $b=8.502$, $c=4.878$ Å, $\beta=96.25°$) given on the PDF card 38-1177 by M. Behruzzi and Th. Hahn, it was thought that the crystal structure might be a distorted pyroxene; however, this is not the case. The correct structural formula is $Cu_2Fe_2Ge_4O_{13}$. The structure is unique in having an oligomer of four germanate tetrahedra, cross-linked laterally by square-planar copper ions, joined end-to-end by a zigzag chain of edge-sharing iron oxide octahedra. The square-planar coordination geometry of Cu has four bond lengths between 1.926(1) and 2.008(1) Å; the next-nearest oxygen atoms at 2.831(1) and 2.892(1) Å complete a (4+2) coordination due to a large Jahn–Teller distortion. The transition metal oxide polyhedra form edge-sharing chains. Running along the *a*-direction the metal oxide chain consists of alternating Cu–Cu and Fe–Fe dimers. The chains are linked along the *b*-direction by a zigzag Fe oxide chain. All of the anions belong to the germanate tetrahedra, $[Ge_4O_{13}]^{10-}$, making the tetrahedral sharing coefficient according to Zoltai [12] equal to 1.375. The bond valence sums to all of the oxygen atoms are perfectly satisfied only if the valence of the Cu and Fe are +2 and +3, respectively. The ternary phase diagram, CuO–GeO_2–$(1/2)Fe_2O_3$, appropriately contoured with different values of Zoltai's tetrahedral sharing coefficient [13] (Fig. 2), shows the compositional range of a hypothetical series

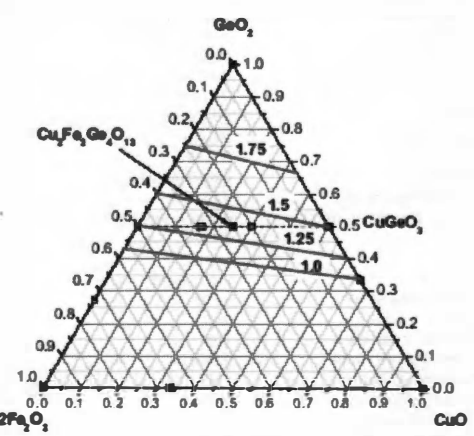


Fig. 2. The ternary phase diagram, CuO–GeO_2–$(1/2)Fe_2O_3$, in molar quantities. The bold lines are contours for different values of Zoltai's tetrahedral sharing coefficient [12,13] and are so labeled. Hypothetical (open symbols) and observed (solid symbols) compounds of the hypothetical homologous structural series ($Cu_{n-2}Fe_2Ge_nO_{3n+1}$ with $n=2,3,4,\ldots,\infty$) plot along the dashed line between hypothetical $Fe_2Ge_2O_7$ and the well-known $CuGeO_3$.

of homologous structures ($Cu_{n-2}Fe_2Ge_nO_{3n+1}$ with $n = 3,4, \ldots, \infty$) with different length germanate oligomers. As the oligomer length, n, increases, the infinite chain of the $CuGeO_3$ is approached. The hypothetical structures of $n = 3, 5, 6, \ldots$ are crystal chemically reasonable in terms of Pauling's electrostatic neutrality principle; however, their realization might only be possible in engineered thin film superlattices. The $n = 2$ member, containing no copper, is problematic because it would require the condensation of the iron oxide octahedral chains into a trioctahedral (gibbsite-type) sheet, which would result in some of the oxygen atoms being underbonded. The symmetry of the $n = 3$ phase is expected to also be monoclinic with a slightly larger β angle than for the $n = 4$ phase. For the $n = 5$ and higher phases the β angle is expected to gradually change towards 90°. The $d(100)$-spacings of the hypothetical phases will be commensurate with the reduction or increase of multiples of the $CuGeO_3$ layer module thickness (Fig. 3); 2.9349(4) Å in $CuGeO_3$ [14] compared to 3.0088 Å for the same layer module in $Cu_2Fe_2Ge_4O_{13}$. Indeed the b and c lattice parameters, 8.5073(4) and 4.8736(2) Å, of $Cu_2Fe_2Ge_4O_{13}$ are only slightly expanded as compared to their corresponding c and b lattice parameters, 8.449(2) and 4.786(1) Å, of $CuGeO_3$ [14]. The Jahn–Teller coordination geometry of the Cu in $CuGeO_3$ (1.934 and 2.746 Å) is also slightly less distorted than in $Cu_2Fe_2Ge_4O_{13}$ (Table 3). Preliminary attempts to synthesize the $n = 3$ and 5 members by solid-state methods were not successful.

The oligomeric germanate anion in this structure is unusual and hitherto has rarely been observed in either germanates or silicates. Stabilization of the germanate oligomers seems to be achieved by the size and charge match of the edge-sharing, (4 + 2)-coordinated copper oxide groups which join them together, as in $CuGeO_3$. The mineral kinoite, $Ca_2Cu_2Si_3O_{10}(H_2O)$ [15], has a triple-tetrahedra silicate oligomer in which a square-pyramidal, edge-sharing, copper oxide chain is present,

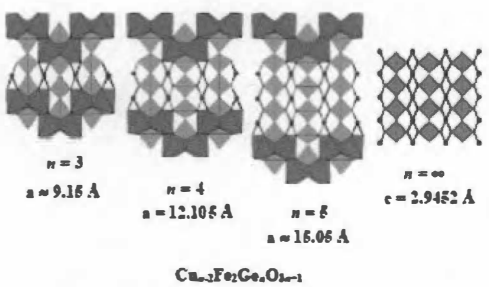


Fig. 3. (001) Crystal structure projections of the proposed homologous series $Cu_{n-2}Fe_2Ge_nO_{3n+1}$ for $n = 3, 4, 5$, and ∞. Coordinates for $CuGeO_3$ ($n = \infty$) were taken from Braden et al. [14].

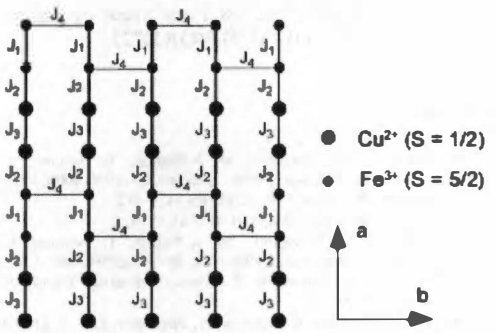


Fig. 4. Topology of the possible spin structure of $Cu_2Fe_2Ge_4O_{13}$ built from the Fe^{3+} ($S = 5/2$) and Cu^{2+} ($S = 1/2$) projected on (001).

but the structure is topologically quite different from that of $Cu_2Fe_2Ge_4O_{13}$ and would not be a member of the proposed homologous series. A four-tetrahedra oligomer is found in the crystal structure of the silicate $Nd_2Ba_2Si_4O_{13}$ [16] as well as several other phosphates, vanadates, and chromates.

From the point of view of quantum spin systems, spin $S = 1/2$ is localized at the Cu^{2+} ($3d^9$) ion and spin $S = 5/2$ is localized at the Fe^{3+} ($3d^5$) ion. Through anion superexchange, interaction exists between the magnetic ions in general. A mixed-spins chain with period 4, such that the spins are arrayed as $S = 1/2, S = 1/2, S = 5/2, S = 5/2$, extends in the a-direction and a zigzag $S = 5/2$ is along the b-direction, which together form a two-dimensional spin plane (Fig. 4). Four different spin interactions (J_1, J_2, J_3, and J_4) are expected. The spin plane is separated by oligomers of four germanate tetrahedra, $[Ge_4O_{13}]^{10-}$, and therefore, this compound is a model material for a low-dimensional mixed-spin system.

Success in the synthesis of $Cu_{n-2}Fe_2Ge_nO_{3n+1}(n \geq 5)$ will give us model materials for the study of finite chain effects in the spin-Peierls system. There are many studies of impurity effects in doped spin-Peierls materials, e.g., $Cu_{1-x}Zn_xGeO_3$ [17], $CuGe_{1-x}Si_xO_3$ [18], $Cu_{1-x}Mg_xGeO_3$ [19,20]. In these cases, impurities are distributed randomly and therefore both randomness and finite chain effects have to be considered. In contrast, for $Cu_{n-2}Fe_2Ge_nO_{3n+1}(n \geq 5)$ it will be possible to study the finite chain effect systematically.

Acknowledgments

The authors (T.M., S.I., and K.U.) thank H. Sawa and J. Yamaura for discussions about this structure at the early stages of this work. ORNL is managed by

UT-Battelle, LLC for the US Department of Energy under Contract No. DE-AC05-00OR22725.

References

[1] T. Tonegawa, T. Hikihara, M. Kaburagi, T. Nishino, S. Miyashita, H.-J. Mikeska, J. Phys. Soc. Jpn. 67 (1998) 1000–1003.
[2] K. Takano, Phys. Rev. Lett. 82 (1999) 5124–5127.
[3] K. Takano, Phys. Rev. B 61 (2000) 8863–8870.
[4] T. Hikihara, T. Tonegawa, M. Kaburagi, T. Nishino, S. Miyashita, H.-J. Mikeska, J. Phys. Soc. Jpn. 69 (2000) 1207–1209.
[5] H. Vollenkle, A. Wittmann, H. Nowny, Monatsh. Chem. 98 (1967) 1352–1358.
[6] M. Hase, I. Terasaki, K. Uchinokura, Phys. Rev. Lett. 70 (1993) 3651–3654.
[7] G.M. Sheldrick, SADABS, Program for empirical absorption correction of area detector data, Institüt fur Anorganische Chemie der Universität, Tammannstrasse 4, D-3400 Göttingen, Germany, 1996.
[8] A. Altomare, M.C. Burla, M. Camalli, G.L. Cascarano, C. Giacovazzo, A. Guagliardi, A.G.G. Moliterni, G. Polidori, R. Spagna, J. Appl. Crystallogr. 32 (1999) 115–119.
[9] G.M. Sheldrick, SHELX97 programs for crystal structure analysis, Release 97-2, Institüt fur Anorganische Chemie der Universität, Tammannstrasse 4, D-3400 Göttingen, Germany, 1997.
[10] L.J. Farrugia, WinGX suite for small-molecule single-crystal crystallography, J. Appl. Crystallogr. 32 (1999) 837–838.
[11] A.J.C. Wilson, in: International Tables for Crystallography, Vol. C, Kluwer Academic Press, London, 1992.
[12] T. Zoltai, Am. Mineral. 45 (1960) 960–973.
[13] B.C. Chakoumakos, J. Mater. Res. 10 (1995) 1772–1778.
[14] M. Braden, E. Resaouche, B. Buechner, R. Kessler, G. Heger, G. Dhalenne, A. Revcolevschi, Phys. Rev. B 57 (1998) 11497–11503.
[15] R.B. Laughon, Am. Mineral. 56 (1971) 193–199.
[16] R.A. Tamazyan, Yu.A. Malinovskii, Dokl. Akad. Nauk SSSR 285 (1985) 124–128.
[17] M. Hase, I. Terasaki, Y. Sasago, K. Uchinokura, H. Obara, Phys. Rev. Lett. 71 (1993) 4059–4062.
[18] L.P. Regnault, J.P. Renard, G. Dhalenne, A. Revcolevschi, Europhys. Lett. 32 (1995) 579–581.
[19] T. Masuda, A. Fujioka, Y. Uchiyama, I. Tsukada, K. Uchinokura, Phys. Rev. Lett. 80 (1998) 4566–4569.
[20] T. Masuda, I. Tsukada, K. Uchinokura, Y. Wang, V. Kiryukhin, R. Birgeneau, Phys. Rev. B 61 (2000) 4103–4108.

Acta Crystallographica Section C
Crystal Structure
Communications
ISSN 0108-2701

(Tetrahydrofuran)potassium *mer-trans*-tris(carbazolyl)dichloro-(tetrahydrofuran)zirconate

Cara L. Nygren,[a] M. E. T. Bragg[a] and John F. C. Turner[a,b]*

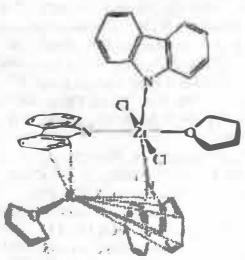
[a]406 Buehler Hall, Department of Chemistry, University of Tennessee, Knoxville, TN 37996, USA, and [b]409 Buehler Hall, Neutron Sciences Consortium, University of Tennessee, Knoxville, TN 37996, USA
Correspondence e-mail: jturner@atom.chem.utk.edu

Received 10 April 2003
Accepted 12 May 2003
Online 20 June 2003

In the title compound, $[K(C_4H_8O)][ZrCl_2(C_{12}H_8N)_3(C_4H_8O)]$, the Zr atom is pseudo-octahedral, with two Cl ligands in *trans* positions. There is extensive interaction between the potassium cation and two of the aromatic carbazolyl ligands in η^6 [C···K = 3.167 (3)–3.331 (3) Å] and η^2 [C···K = 3.147 (3)–3.268 (2) Å] fashions.

Comment

Trisamide complexes of transition metals show a wide range of reactivity, and the synthesis and exploration of this class of compound has been the focus of considerable research in recent years within the inorganic community (Cummins *et al.*, 1988, 1991; Schrock, 1997; Cummins, 1998*a*). The majority of these complexes contain hard electronic ligands (Cummins, 1998*b*). Recently, complexes with softer non-innocent ligands have been reported (Tanski & Parkin, 2003).



(I)

The electronic properties of the carbazolyl anion should predispose it to non-innocence when acting as a ligand at a transition metal center. Moreover, carbazolyl complexes of transition metals that are σ-bound are rare (Lopez *et al.*, 2002), and most of the known examples (Riley *et al.*, 1998, 1999, 2001) involve groups IV and V. In this paper, brief details of the synthesis and full details of the structure of the first carbazolylzirconium anion, namely *mer-trans*-tris(carbazolyl)-dichloro(tetrahydrofuran)zirconate as the (tetrahydrofuran)-potassium adduct, (I), are reported. Examination of the Cambridge Structural Database (CSD; Allen & Motherwell, 2002; Bruno *et al.*, 2002) revealed that the first coordination sphere, consisting of three N atoms, one O atom and two Cl atoms, is unique in the structural chemistry of zirconium.

The molecular structure of (I) is shown in Fig. 1. Examination of the CSD revealed that the Zr—N bond lengths [mean Zr—N = 2.188 (17) Å; Table 1] of the carbazolyl ligands are shorter than the mean Zr—N single-bond length (2.241 Å) reported in the literature, although the Zr—N bonds in (I) are not outside the range of typical distances. The Zr—Cl bond lengths are well within the typical range of 2.379–2.776 Å (Allen & Motherwell, 2002; Bruno *et al.*, 2002), although the Zr—Cl bond in (I) is slightly shorter than the mean of these distances, *i.e.* 2.514 Å [Zr—Cl1 = 2.4276 (7) Å and Zr—Cl2 = 2.4914 (6) Å].

There are close interactions between the potassium cation and two of the carbazolyl ligands. One of the carbazolyl ligands is coordinated in a η^6 fashion, and the average distance of this interaction is 3.248 (3) Å. There is also a η^2 interaction with a carbazolyl ligand, in which the average distance is 3.208 (3) Å. This type of close interaction between a transition metal anionic complex and the counter-ion is not uncommon. However, the fact that crystallization from tetrahydrofuran (THF) results in a coordination sphere composed not solely of this ether but rather of a mixture of hard and soft bases (Pearson, 1963, 1969) was surprising, given that K^+ is considered a hard acid. The mixed nature of the coordination sphere prompted a further examination of the CSD. The search was based on all K^+–arene interactions and revealed that potassium may coordinate in a η^2, η^3 or η^6 fashion, with a range of distances, over all hapticities, of 2.856–3.927 Å.

Given the mixed hard–soft coordination sphere, we chose to compare the structure with a soft ion of similar ionic radius and equal formal charge, namely the Ag^+ ion, an archetypal soft acid. Surprisingly, very few Ag^+–arene interactions were

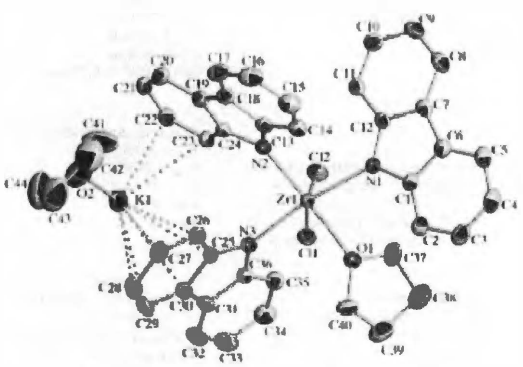


Figure 1
A view of the structure of (I), showing the atomic numbering scheme. All H atoms have been omitted for clarity, and displacement ellipsoids are drawn at the 50% probability level for non-H atoms.

 DOI: 10.1107/S0108270103010321 © 2003 International Union of Crystallography

found. In the Pearson acid–base classification (Pearson, 1963, 1969), K^+ is a hard acid, whereas Ag^+ is a soft acid; soft bases, such as arene π-electron density, would be assumed to bind more strongly to the soft acid than to the hard acid. Moreover, the Ag^+ ion is used in chromatographic separations of alkenes and other unsaturated hydrocarbons (Williams & Mander, 2001) because of this interaction of Ag^+ with the unsaturated π density, and several salts of Ag^+ are soluble in aromatic hydrocarbons, in contrast to the K^+ congeners. The dearth of structural data on arene–Ag^+ interactions and the number of arene–K^+ interactions is therefore surprising. We speculate that the formally charge-separated nature of (I), and possibly the distribution of the negative charge in the carbazolyl portion of the anion, may play a role in ensuring that the observed structure is favorable. Theoretical and experimental studies are in progress to explore this possibility.

Experimental

Treatment of a suspension of $ZrCl_4$ (2.32 g, 0.01 mol) in Et_2O, chilled to 195 K, with a freshly prepared concentrated tetrahydrofuran solution of carbazolyl potassium, formed by deprotonation of carbazole (5 g, 0.030 mol) with an excess of potassium hydride (2.4 g, 0.060 mol), resulted in a slow reaction that, on warming to room temperature, afforded a golden-yellow solution. Large leaf-like golden-yellow crystals of (I) grew spontaneously from the unstirred reaction mixture over a period of 3 d from which a block was cut for X-ray analysis. The crystal growth occurred with precipitation of a quantity of bright-yellow powder, which gave identical spectroscopic data to the crystals. The compound has been characterized by one- and two-dimensional ^1H and ^{13}C NMR spectroscopy at variable temperatures in solution and by CP–MAS ^{13}C NMR in the solid state. The spectroscopic data fully support the formulation of (I) as {K(THF)}{*mer*-(carbazolyl)$_2$ZrCl$_2$·THF}.

Crystal data

{K(C$_4$H$_8$O)}{ZrCl$_2$(C$_{12}$H$_8$N)$_2$-(C$_4$H$_8$O)}	D_x = 1.457 Mg m^{-3}
M_r = 844.01	Mo $K\alpha$ radiation
Orthorhombic, $P2_12_12_1$	Cell parameters from 7774 reflections
a = 14.158 (3) Å	θ = 2.3–28.3°
b = 15.486 (3) Å	μ = 0.58 mm^{-1}
c = 17.548 (3) Å	T = 173 (2) K
V = 3847.4 (13) Å^3	Block, yellow
Z = 4	0.40 × 0.35 × 0.25 mm

Data collection

Bruker CCD diffractometer	8608 reflections with $I > 2\sigma(I)$
φ and ω scans	R_{int} = 0.029
Absorption correction: multi-scan (*SADABS*, Sheldrick, 1996)	θ_{max} = 28.3°
T_{min} = 0.882, T_{max} = 0.890	$h = -18 \rightarrow 18$
41 736 measured reflections	$k = -19 \rightarrow 19$
9248 independent reflections	$l = -23 \rightarrow 23$

Refinement

Refinement on F^2	$w = 1/[\sigma^2(F_o^2) + (0.0454P)^2 + 1.0517P]$ where $P = (F_o^2 + 2F_c^2)/3$
$R[F^2 > 2\sigma(F^2)]$ = 0.028	$(\Delta/\sigma)_{max}$ = 0.005
$wR(F^2)$ = 0.078	$\Delta\rho_{max}$ = 0.75 e Å^{-3}
S = 1.07	$\Delta\rho_{min}$ = −0.34 e Å^{-3}
9248 reflections	Absolute structure: Flack (1983), 5169 Friedel Pairs
479 parameters	Flack parameter = −0.04 (2)
H-atom parameters constrained	

Table 1
Selected geometric parameters (Å, °).

C22—K1	3.147 (3)	C30—K1	3.263 (2)
C23—K1	3.268 (2)	Cl1—Zr1	2.4276 (7)
C25—K1	3.202 (2)	Cl2—Zr1	2.4914 (6)
C26—K1	3.167 (3)	N1—Zr1	2.2056 (16)
C27—K1	3.221 (3)	N2—Zr1	2.1374 (18)
C28—K1	3.302 (3)	N3—Zr1	2.2224 (18)
C29—K1	3.331 (3)	O1—Zr1	2.2659 (16)
N2—Zr1—N1	94.61 (7)	N3—Zr1—Cl1	88.77 (5)
N2—Zr1—N3	93.23 (7)	O1—Zr1—Cl1	85.69 (5)
N1—Zr1—N3	171.90 (7)	N2—Zr1—Cl2	94.24 (5)
N2—Zr1—O1	177.06 (6)	N1—Zr1—Cl2	89.39 (5)
N1—Zr1—O1	88.34 (6)	N3—Zr1—Cl2	92.07 (5)
N3—Zr1—O1	83.83 (6)	O1—Zr1—Cl2	85.87 (5)
N2—Zr1—Cl1	94.27 (5)	Cl1—Zr1—Cl2	171.38 (2)
N1—Zr1—Cl1	88.62 (5)		

All H atoms were introduced at calculated positions and treated as riding [U_{iso}(H) = 1.2U_{eq}(C) and C—H = 0.98 Å]. Friedel pairs were not merged.

Data collection: *SMART* (Bruker, 1997); cell refinement: *SAINT* (Bruker, 1997); data reduction: *SAINT*; program(s) used to solve structure: *SHELXS97* (Sheldrick, 1997); program(s) used to refine structure: *SHELXL97* (Sheldrick, 1997); molecular graphics: *SHELXTL* (Bruker, 1997); software used to prepare material for publication: *SHELXTL*.

The authors thank the University of Tennessee for supporting this research.

Supplementary data for this paper are available from the IUCr electronic archives (Reference: FR1422). Services for accessing these data are described at the back of the journal.

References

Allen, F. H. & Motherwell, W. D. S. (2002). *Acta Cryst.* B58, 407–422.
Bruker (1997). *SMART* (Version 5.044), *SAINT* (Version 5.01) and *SHELXTL*. Bruker AXS Inc., Madison, Wisconsin, USA.
Bruno, I. J., Cole, J. C., Edgington, P. R., Kessler, M., Macrae, C. F., McCabe, P., Pearson, J. & Taylor, R. (2002). *Acta Cryst.* B58, 389–397.
Cummins, C. C. (1998*a*). *Chem. Commun.* pp. 1777–1786.
Cummins, C. C. (1998*b*). *Prog. Inorg. Chem.* 47, 685–836.
Cummins, C. C., Baxter, S. M. & Wolczanski, P. T. (1988). *J. Am. Chem. Soc.* 110, 8731–8733.
Cummins, C. C., Schaller, C. P., Van Duyne, G. D., Wolczanski, P. T., Chan, A. W. E. & Hoffmann, R. (1991). *J. Am. Chem. Soc.* 113, 2985–2994.
Flack, H. D. (1983). *Acta Cryst.* A39, 876–881.
Lopez, C., Baron, G., Arevalo, A., Munoz-Hernandez, M. A. & Garcia, J. J. (2002). *J. Organomet. Chem.* 664, 170–175.
Pearson, R. G. (1963). *J. Am. Chem. Soc.* 85, 3533–3539.
Pearson, R. G. (1969). *Surv. Prog. Chem.* 5, 1–52.
Riley, P. N., Fanwick, P. E. & Rothwell, I. P. (2001). *J. Chem. Soc., Dalton Trans.* pp. 181–186.
Riley, P. N., Parker, J. R., Fanwick, P. E. & Rothwell, I. P. (1999). *Organometallics*, 18, 3579–3583.
Riley, P. N., Profilet, R. D., Salberg, M. M., Fanwick, P. E. & Rothwell, I. P. (1998). *Polyhedron*, 17, 773–779.
Schrock, R. R. (1997). *Acta Chem. Res.* 30, 9–16.
Sheldrick, G. M. (1996). *SADABS*. University of Göttingen, Germany.
Sheldrick, G. M. (1997). *SHELXL97* and *SHELXS97*. University of Göttingen, Germany.
Tanski, J. M. & Parkin, G. (2003). *Inorg. Chem.* 42, 264–266.
Williams, C. M. & Mander, L. N. (2001). *Tetrahedron*, 57, 425–447.

VITA

Cara Nygren was born in Sweet Valley, Pennsylvania in 1977. She graduated from Lake Lehman High School in 1995. She attended the University of Maryland for a year and a half before taking two semesters off from college. During her return to college at Wilkes University in Pennsylvania, she was employed as a bartender, waitress and fork-lift driver. She graduated from Wilkes in 2000 with a B.A. in Chemistry.

2094 9169 36
08/17/05 MRB